PRE-ERUPTIVE CONDITIONS AT LONQUIMAY AND PUYEHUE - CORDÓN CAULLE VOLCANOES, CHILE: FRAMEWORK FOR TECTONIC INFLUENCES

DISSERTATION

zur Erlangung des Doktorgrades

an der Mathematisch-Naturwissenschaftlichen

Fakultät der Christian-Albrechts-Universität zu Kiel

vorgelegt von

David Johann Gilbert

Kiel, Donnerstag den 12. Juli 2012

Referent: ..... PD Dr. Armin Freundt

Koreferent: ..... Professor Dr. Kaj Hoernle

Tag der mündlichen Prüfung: 13.09.2012

Zum Druck genehmigt: 13.09.2012

……..

Der Dekan

"*Gas is the active agent and the magma is its vehicle*"

F.A. Perrett (1929)

This thesis is typeset using the font Bembo. Bembo is the revival of an old style serif cut by Francesco Griffo around 1495 in Venice. It was first used to print the book De Aetna about Pietro Bembo´s journey to volcano Etna on Sicily.

Hiermit erkläre ich, dass ich die vorliegende Doktorarbeit selbständig und ohne Zuhilfenahme unerlaubter Hilfsmittel erstellt habe. Weder diese noch eine ähnliche Arbeit wurde an einer anderen Hochschule im Rahmen eines Prüfungsverfahrens vorgelegt, veröffentlicht oder zur Veröffentlichung vorgelegt. Ferner versichere ich, dass die Arbeit unter Einhaltung der Regeln guter wissenschaftlicher Praxis der Deutschen Forschungsgemeinschaft entstanden ist.

Kiel, den……..

David Johann Gilbert

Contents

Additional electronic supplementary material on enclosed CD

ABSTRACT

Vivid tectonic conditions - typical for subduction zones - affect the associated volcanism in many ways. Upper plate tectonic faults control not only the location of volcanoes but magnitude and orientation of tectonic stress along fault systems particularly control magma plumbing dynamics, i.e. the ascent, storage and eruption of magmas. For instance, bimodal volcanism in the central Andes is closely linked to the orientation and kinematics of regional faults and time-predictability may be a fundamental property of volcanism controlled by regional tectonic strain. While some eruption records show fairly uniform behavior through time, erratic evolution at other volcanoes may be controlled by either inherent change in the magmatic system or external forcing, or by complex coupling of both. Tectonic influence on volcanism on longer time scales is commonly implied from observed spatial correlations between tectonic and volcanic structures but may also be inferred from the pattern of temporal evolution of a volcano. On much shorter time scales, it is commonly believed that regional earthquakes are capable of triggering volcanic eruptions even though the particular processes involved are still under debate.

The aim of this PhD thesis is to unravel a possible linkage between magmatic processes, regional tectonic stress and volatile inventories of two exemplary magmatic systems in the Southern Volcanic Zone (SVZ) of the Andes: **Lonquimay** (LVC; 38°23'S, 71°36'W) and **Puyehue-Cordón Caulle** (PCCVC; 40°35'S, 72°7'W) volcanic complexes. While the pre-eruptive inherent conditions of magmatic systems are in principle "visible" in the eruption products, the possible influence of tectonic stresses is commonly inferred by indirect evidence. Therefore, my work has focused on the control of post-glacial volcanism by petrogenesis (e.g. fractional crystallization, magma mixing) and stress regime; and in particular how the resulting volatile budgets ruled the eruptive activity by controlling the criticality of the investigated volcanic systems, i.e. their susceptibility to external forcing.

The **Lonquimay Volcanic Complex (LVC)** in the high Southern Andes comprises a stratocone and two NE-trending flank-cone alignments that are associated with the arc-wide Liquiñe-Ofqui Fault Zone. Numerous effusive and explosive volcanic eruptions characterize its post-glacial magmatic activity. LVC's tephrostratigraphy that comprises 22 dated pyroclastic deposits, was studied in order to investigate eruptive behavior through time. Statistical examination of the eruption time series yields two distinct repose time regimes. This change in recurrence times around 6000 b2k (years before 2000 AD) is also reflected in a change of magmatic products tapped during eruptions. In general, the LVC tephra deposits can be

subdivided into three petrographic groups: a felsic group (Lonquimay Colored Pumice Tephra, LCPT), an intermediate population (Lonquimay Grey Pumice Tephra, LGPT) and a mafic member (Lonquimay Dark Scoria Tephra, LDST). LDST deposits as well as deposits compositionally zoned from LCPT to LGPT dominate the lower part of the stratigraphy for which recurrence times are short (RT_{mean}=417±169 a). Deposits younger than 6000 b2k have dominantly LCPT and minor LDST compositions, no longer contain LGPT, and repose times are significantly longer (RT_{mean}=1350±310 a). This change in eruption regime is interpreted to result from a tectonically driven rearrangement in the magma storage and plumbing system.

To better constrain the plumbing system dynamics, thermobarometric calculations were performed using several complementary mineral liquid equilibria. The obtained P-T-X results reveal distinct magma storage levels for each petrographic group: the mafic LDST derive from mid crustal storage (P_{mean}≈440±100 MPa, T_{mean}≈1065±25°C), felsic LCPT mainly erupted from upper-crustal level (P_{mean}≈80±25 MPa, T_{mean}=935±20°C) whereas LGPT samples yield intermediate storage depths (P_{mean}=240±110 MPa, T_{mean}=1010±15°C). Magma contributions from this intermediate reservoir are restricted to >6000 b2k when the Lonquimay plumbing system was in a regime of short repose times; disappearance of the intermediate reservoir coincides with the change to longer repose times between eruptions. Despite the distinct storage levels, LVC's magmatic products record a complex history of component magmas interacting within the plumbing system, thereby affecting the involved magmas and their volatile inventories and hence LVC's eruptive behavior.

Two independent levels of volatile saturation are documented in LVC magmatic products. A first deep level (~14 km) of volatile-saturation was reached by LDST melts during ascent, leading to the formation of a S-rich fluid phase and therefore strong depletion of S in the melt. A second level of H_2O-saturation was reached between 1.5 and 6 km in the shallow reservoir. The stagnation of LCPT melts at this level led to their H_2O-oversaturation and hence exsolution of an aqueous fluid phase. The frequent injections of primitive melt batches into the LDST reservoir, as documented in the pheno- and xenocryst assemblages, may have triggered the mafic LDST eruptions. The occurrence of compositionally zoned, amphibole-bearing deposits that is limited to LCPT deposits older 6000 b2k indicates the occurrence of compositionally zoned magma bodies and hence stronger interaction between the three distinct reservoirs prior to this threshold. In contrast, the matrix glass and crystal records of most felsic eruptions younger than 6000 b2k do not show such a strong influence of mafic replenishment. I therefore propose that these eruptions may

have been triggered by H_2O-saturation, giving a possible explanation for the longer repose times between these eruptions.

While statistically significant correlations between major regional earthquakes and eruptions within days or even months have been reported by several studies, the 1960 eruption of the **Puyehue-Cordón Caulle Volcanic Complex (PCCVC)** is one of the most renowned examples thought to be susceptible to seismic triggering, because it occurred only 37h after the largest ever instrumentally recorded earthquake (M_S=9.5). Its recent eruption that started on June 4th 2011 raised the question, if it was possibly related to the preceding M_W 8.8 Maule earthquake of 2010. To determine the pre-eruptive criticality, thermobarometric and volatile studies were performed for the remarkably homogeneous rhyodacitic 2011, 1960 and four older post-glacial eruptions. The use of several independent methods allows us to give robust estimates of pre-eruptive P-T-X-conditions and how the volatile saturation state evolved over time. Several independent estimates for crystallization temperatures and pressures as well as pre-eruptive H_2O-contents yield shallow magma storage (P=50-250 MPa, T=885-915°C) for all PCCVC eruptions studied. Pre-eruptive H_2O contents of 4-5 wt% and the occurrence of water-dominated magmatic fluid inclusions indicate the exsolution of an aqueous fluid phase ($salinity_{mean}$=3.2±0.1 wt% NaCl equivalent) at pressures of ~135 MPa for the 2011 eruption. Such pre-eruptive H_2O-saturation in the upper part of the plumbing system appears to be typical for explosive eruptions at this volcanic system. I propose that due to volatile-supersaturation the system was due to erupt when it was eventually triggered by seismic activity. PCCVC's position astride a NW fissure zone of the arc-wide Liquiñe Ofqui Fault Zone system (along which seismic energy/strain may be transmitted particularly effectively) as well as its ability to repeatedly reach critical magmatic conditions probably are the two factors that facilitate tectonic triggering of eruptions at this particular volcanic system.

Although presenting case studies based on conditions valid for LVC and PCCVC, the general implication from this thesis may be applicable to other volcanic systems with similar prerequisites. Particularly in evolved subduction-related systems shallow storage and hence volatile saturation are common features, as are arc-wide fault systems in the upper plate due to oblique convergence in other subduction zones. I therefore infer that tectonic forcing of volcanic systems may be more common than usually assumed and is probably not only confined to dictating the structural features but also affects eruptive behavior. But more studies of the petrogenetic processes determining the saturation state and finally the criticality of volcanic systems that are discussed to be tectonically influenced are needed to better constrain the actual effects of internal and external forcing.

KURZFASSUNG

Subduktionszonenvulkanismus wird in vielfältiger Weise durch tektonische Rahmenbedingungen beeinflusst. Dabei bestimmen Störungszonen in der Oberplatte nicht nur das räumliche Auftreten von Vulkanen, sondern ebenso die Stärke und Orientierung des tektonischen Spannungsfeldes, welches wiederum die Dynamik von Magmenfördersystemen kontrolliert (d.h. Aufstieg, Speicherung und Eruption). Der bimodale Vulkanismus der Zentralanden beispielsweise ist eng verknüpft mit der Ausrichtung und Bewegungsrichtung regionaler Störungssysteme. Eine grundlegende Eigenschaft solcher tektonisch kontrollierter Vulkansysteme ist die zeitliche Kontinuität in ihrem Eruptionsverhalten. Während einige Vulkane eine zeitlich gleichförmige Eruptionstätigkeit aufweisen, zeigen andere ein sprunghaft wechselndes Eruptionsverhalten welches sich auf Magmensystem-inhärente Veränderungen oder externe Beeinflussung zurückführen lässt - oder aber auf eine komplexe Kopplung beider Prozesse. Der tektonische Einfluss auf Vulkanaktivität über längere Zeiträume wird für gewöhnlich aus der räumlichen Übereinstimmung zwischen tektonischen und vulkanischen Strukturen abgeleitet, lässt sich aber auch aus der zeitlichen Entwicklung eines Vulkansystems erschließen. Auf sehr kurzer Zeitskala können regionale Erdbeben Vulkaneruptionen auslösen, wie man gemeinhin annimmt, ohne dass die speziellen, dem zu Grund liegenden Prozesse bereits verstanden sind.

Das Ziel dieser Doktorarbeit ist es daher eine mögliche Verknüpfung zwischen magmatischen Prozessen, regionalen tektonischen Spannungen und diversen Volatilinventaren zweier exemplarischer Vulkane in der südlichen Vulkanzone der Anden zu untersuchen: des Lonquimay Vulkankomplexes (LVC; 38°23'S, 71°36'W) und des Puyehue-Cordón Caulle Vulkankomplexes (PCCVC; 40°35'S, 72°7'W). Meine Arbeit hat sich dabei auf die Untersuchung der Mechanismen welche die Petrogenese und Eruptionstätigkeit des nacheiszeitlichen Vulkanismus bestimmen (bspw. fraktionierte Kristallisation, Krustenassimilation und Magmenmischung), konzentriert, da sich die prä-eruptiven Bedingungen aus den Ablagerungen rekonstruieren lassen. Im Gegensatz dazu muss der Einfluss von tektonischem Stress meist indirekt abgeleitet werden. Von besonderem Interesse war in welcher Weise die resultierenden Volatilgehalte den kritischen Zustand und damit die Empfindlichkeit gegenüber externen Störungen und folglich die Eruptionstätigkeit beider Systeme bestimmt haben.

Der **Lonquimay Vulkankomplex** in den südlichen Hochanden besteht aus einem Stratovulkan und zwei nordost-streichenden Aneinanderreihungen von Eruptionszentren die mit der regionalen Liquiñe Ofqui Störungszone zusammenhängen. Zahlreiche effusive und explosive Eruptionen charakterisieren seine postglaziale Aktivität. Ich habe zunächst die LVC

Tephrostratigraphie untersucht. Diese Ergebnisse wurden dann genutzt um die zeitliche Entwicklung der Eruptionstätigkeit zu untersuchen. Die statistische Auswertung der stratigraphie-basierten Eruptionszeitreihen ergab innerhalb der Holozänen Eruptionsgeschichten zwei unterscheidbare Phasen mit unterschiedlich lang andauernde Ruhezeiten zwischen zwei aufeinanderfolgenden Eruptionen. Der Wechsel in der Eruptionsfrequenz spiegelt sich ebenso in der Zusammensetzung der geförderten magmatischen Produkte wider. Generell lassen sich die LVC Tephren in drei unterschiedliche Lithologien einteilen: eine felsische Gruppe (farbige Lonquimay Bimse, LCPT), eine Gruppe intermediärer Zusammensetzung (graue Lonquimay Bimse, LGPT) und eine undifferenzierte mafische Gruppe (dunkle Lonquimay Schlacke, LDST). Der untere Teil des stratigraphischen Profils wird durch LDST Ablagerungen sowie chemisch zonierte Fallablagerungen mit basalen LCPT und einem Oberteil aus LGPT Pyroklasten dominiert. Die mittlere Eruptionsfrequenz dieser Ablagerugnen beträgt dabei rund 417±169 Jahre. Ablagerungen jünger als 6000 b2k (Jahre bevor 2000 AD) werden demhingegen dominiert durch LCPT und untergeordnet LDST Ablagerungen. LGPT Ablagerungen sind jedoch nicht mehr zu finden und die Eruptionshäufigkeit ist seltener (RT_{mean}=1350±310a). Diese Unterschiede im Eruptionsverhalten lassen sich auf eine grundlegende, wahrscheinlich tektonisch verursachte Reorganisation des Magmenspeicher- und Fördersystems zurückführen.

Um die dem Magmensystem innewohnende Dynamik besser charakterisieren zu können wurden thermobarometrische Berechnungen unter Nutzung mehrerer komplementärer Mineral-Schmelzgleichgewichte durchgeführt. Die erhaltenen P-T-X Abschätzungen decken klar abgegrenzte Niveaus der Magmenspeicherung für jede petrographische Gruppe auf: die mafischen LDST Ablagerungen stagnierten in der mittleren Kruste (P_{mean}≈440±100 MPa, T_{mean} ≈1065±25°C), die felsischen LCPT-Ablagerungen eruptierten aus einer Magmenkammer in der Oberkruste (P_{mean}≈80±25 MPa, T_{mean}=935±20°C) während die intermediären LGPT Proben intermediäre Speichertiefen (P_{mean}=240±110 MPa, T_{mean}=1010±15°C) dokumentieren. Eine Beteiligung dieses intermediären Reservoirs ist auf Ablagerungen älter 6000 b2k beschränkt. Während der Zeiten als alle drei Reservoire in die Magmenförderugn involviert waren, war das Lonquimay Magmensystem in einem Zustand hoher Eruptionsfrequenz. Das Ende der Magmenförderung aus dem mittleren Reservoir fällt mit dem Übergang zu geringerer Eruptionshäufigkeit zusammen. Obwohl drei voneinander abgegrenzte Speicherniveaus existiert haben dokumentieren die LVC-Tephren eine komplexe Geschichte miteinander wechselwirkender Magmakomponenten innerhalb des Magmenfördersystems welche die Entwicklung der beteiligten Magmen sowie deren Volatileninventare und dadurch das Eruptionverhalten des Vulkans Lonquimay beeinflusst haben.

Zwei unabhängige krustale Niveaus der Volatilsättigung sind durch die LVC-Tephren dokumentiert. Ein tiefes Sättigungsniveau wurde durch LDST-Schmelzen während ihres Aufstiegs in rund 14 km Tiefe erreicht. Die resultierende Freisetzung einer schwefelreichen Fluidphase aus der Schmelze führte zu einer starken Abreicherung von Schwefel in dieser. Die Stagnation von LCPT-Schmelzen in Tiefen zwischen 1.5 und 6km führte zu deren Wasserübersättigung und als Folge dessen zur Entmischung einer wässrigen Fluidphase. Die häufige Injektion primitiver Schmelzen in das LDST-Reservoir ist in der Zusammensetzung der LDST Phäno- und Xenokristalle überliefert. Dieser häufige Magmennachschub könnte der Auslöser für die relativ häufigen LDST-Eruptionen gewesen sein. Das Auftreten von kompositionell zonierten, amphibolführenden Tephren ist auf Ablagerungen älter als 6000 b2k beschränkt. Dies kann als ein Hinweis für chemisch zonierte Magmenkammern interpretiert werden und weist auf eine möglicherweise stärkere Interaktion zwischen den einzelnen Magmenkörpern hin. Im Gegensatz dazu dokumentieren die Matrixgläser und Mineralzusammensetzungen der meisten felsischen LCPT-Tephren jünger 6000 b2k keinen signifikanten Einfluss mafischer Injektionen. Daraus lässt sich ableiten, dass diese Eruptionen vermutlich intern durch Volatilübersättigung ausgelöst wurden, was wiederum auch gut zu den niedrigeren Eruptionsfrequenzen dieser Eruptionen passt.

Zahlreiche Studien haben einen statistisch signifikanten Zusammenhang zwischen starken regionalen Erdbeben und sich innerhalb weniger Tage bis Monaten danach ereignenden Vulkaneruptionen belegt. Die Eruption des Vulkans Puyehue-Cordón Caulle aus dem Jahre 1960 ist vermutlich die bekannteste der als tektonisch ausgelöst geltenden Eruptionen da sie nur 37h nach dem größten jemals gemessenen Erdbeben (M_W 9.5) begonnen hat. Die letzte Eruption, die am 4. Juni 2011 begann wirft daher die Frage auf ob diese möglicherweise mit dem M_W 8.8 Erdbeben von 2010 in Zusammenhang steht. Um zu bestimmen in welchem kritischen Zustand sich das Magmensystem vor der Eruption befand, wurden thermobarometrische und Volatilstudien der außergewöhnlich homogenen rhyodazitischen Eruptionen der Jahre 2011 und 1960 sowie vier älterer Eruptionen durchgeführt. Die Anwendung mehrerer unabhängiger Methoden zur Bestimmung von Kristallisationsdrucken und -temperaturen sowie prä-eruptiven Wassergehalten ergeben flache Magmenspeicherbedingungen (P=50-250 MPa, T=885-915°C) für alle untersuchten Eruptionen. Prä-eruptive Wassergehalte von 4-5 wt% und vorkommende Fluideinschlüsse belegen die Entmischung einer wässrigen Fluidphase bei Drucken von ~135 MPa kurz vor der 2011 Eruption. Eine derartige Wassersättigung im oberen Bereich des Magmenzufuhrsystems scheint typisch für explosive Eruptionen dieses Vulkansystems zu sein. Es lässt sich daher schlussfolgern, dass eine Eruption des Magmensystems überfällig war als diese möglicherweise durch seismische Aktivität ausgelöst wurde. Die Position des Puyehue-Cordón

Caulle Vulkankomplex direkt auf einem nordwest-streichenden Seitenarm des regionalen Liquiñe-Ofqui Störungssystems - entlang dessen sich seismische Energie besonders effektiv ausbreiten kann - als auch die Eigenschaft des Systems wiederholt kritische prä-eruptive Bedingungen zu erreichen sind die notwendigen Randbedingungen, die eine tektonische Kontrolle dieses Vulkansystems ermöglichen.

Obwohl die vorliegende Arbeit Fallstudien in Abhängigkeit der speziellen Bedingungen der Vulkansysteme LVC und PCCVC enthält sind die Hauptergebnisse dieser Arbeit möglicherweise übertragbar auf andere ähnlich geartete Vulkane. Besonders in entwickelten Subduktionszonen-Vulkanen sind flache Magmenkammern und dadurch bedingt Volatilsättigung häufige Merkmale. Ebenso treten weitspannende regionale Störungssysteme auch in anderen Subduktionszonen auf. Daraus lässt sich ableiten, dass Vulkane vermutlich häufiger tektonisch kontrolliert werden als gemeinhin angenommen wird, und dass sich dies nicht nur auf die Ausbildung struktureller Merkmale sondern ebenso auf deren Eruptionsverhalten auswirken kann. Um diese Frage besser beantworten zu können bedarf es noch weiterer Detailstudien der petrogenetischen Prozesse die die Volatilsättigung und daduch den prä-eruptiven Zustand von Vulkansystemen bestimmen, von denen man annimmt, dass sie tektonisch kontrolliert sind.

Chapter 1

General Introduction

1.1 INTRODUCTION

The collision zones of convergent tectonic plates host the loci of most paroxysmal phenomena on the Earth's surface, including explosive volcanic activity, high-magnitude earthquakes, fast morphological evolution, and deeply contrasting thermal fields. The Earth's largest mountain chains such as the Alps and the Himalaya are produced by the collision of continental plates. Subduction zones are the primary sites on Earth where continental crust is formed and crustal material, as well as volatiles are recycled back into the Earth's mantle. It is a longstanding knowledge that more than 90% of global earthquake activity and more than 80% of explosive volcanic activity (e.g. Siebert and Simkin, 2002; Simkin, 1993) are associated with the collision of tectonic plates. If collision involves an oceanic plate, the colder and denser oceanic plate subducts below the less dense continental (Fig. 1.1) or oceanic plate resulting in the recycling of oceanic lithosphere. Thereby, plate tectonic motion is mainly driven by excess density that results from the temperature difference and prograde metamorphic reactions of the cold and dense subducting lithosphere, contrasting the warm and less dense underlying asthenosphere (e.g. Stern, 2002).

Volatile elements can be defined as those elements that prefer to be distributed in a vapor or in a supercritical fluid phase rather than into a solid or molten phase. Commonly, the more generic term "volatiles" is not only used as shorthand for volatile elements, but also includes the commonly occurring molecular species of these elements. Of these, H_2O is by far the most abundant, accompanied by less abundant species such as CO_2, SO_2, H_2S, HCl, HF or noble gases.

The consumption of lithospheric material into the mantle at subduction zones involves the entrainment of significant amounts of volatile components through various mechanisms (cf. 1.2). Subducted volatile elements play a key role in the generation of subduction zone magmatism. They are engaged in the transfer of material from the subducting slab to the mantle wedge, lowering the solidus of mantle peridotite causing partial melting, and catalyze the ore-forming hydrothermal processes in the vicinity of magma bodies. Further, the presence of volatiles facilitates the ascent of silicic melts, and in the first order dictates the driving mechanisms and explosivity of volcanic eruptions. When being emitted into the atmosphere during large volcanic eruptions, volatiles may impact atmospheric chemistry and as a consequence global climate.

Understanding the behavior of volatiles in subduction zone processes and in particular arc volcanism is crucial for understanding global cycles of matter but is also important for the understanding of connections between the natural environment and its impact on human society.

1.2 SUBDUCTION ZONE DYNAMICS AND MAGMATISM

1.2.1. Metamorphism and fluid release from the subducting slab

Subduction into the Earth's mantle exposes the down-going slab, hydrated with free pore water and chemically bound water in sediments, crust and lithospheric mantle to progressive heating and squeezing due to increasing heat and pressure. Hydration of oceanic crust and underlying lithospheric mantle occurs during its formation at mid-ocean ridges (Mével, 2003) as well as due to bending of the oceanic plate at subduction zones (Ranero and Sallarès, 2004). During the progressive course of subduction, fluids in the hydrated slab are released in a series of metamorphic reactions (Jödicke et al., 2006; Rüpke et al., 2004; Schmidt and Poli, 1998). Involved processes comprise the release of volatiles from the crust, its sediment cover, and the lithospheric mantle as well as progressive alteration (metamorphism and metasomatism) of the slab mineralogy. Recent studies (Poli and Schmidt, 2002; Schmidt and Poli, 1998) suggest that the slab which consists of lithospheric mantle, crust, and sedimentary cover releases volatiles continuously, because many dehydration reactions occur simultaneously. However, magnetotelluric studies (e.g. Brasse et al., 2002; Schwalenberg et al., 2002; Worzewski et al., 2011) suggest, that accumulation of fluids is a global phenomenon of subduction zones and results in a significant change of electrical conductivity at distinct zones. Dewatering due to tectonic shortening and associated sediment compaction starts at the deformation front, and most sediment dewatering occurs in the first 10-20 km of the fore-arc (Moore and Vrolijk, 1992; Saffer et al., 2000). With increasing depth, contribution of sediments ceases and the influence of devolatilization of the oceanic crust increases. At depths greater than 100 km, the main fluid source is the dehydrating serpentinized lithospheric mantle that underlies the already dehydrated oceanic crust. One important reaction that releases significant amounts of water (13 wt%; Peacock, 2001) is the breakdown of serpentinite into olivine, orthopyroxene and water. Because the addition of aqueous fluids significantly lowers the solidus of the mantle peridotite (Stern, 2002), metamorphic devolatilization and fluxing of the mantle wedge are of prime importance for generating arc magmas. Additional water may be transported to deeper mantle regions by serpentinites formed above the slab (cf. Fig. 1.1) from fluids that are squeezed out of subducted sediments and the upper crust.

1.2.2. Subduction zone magmatism

The extrusive part of subduction zone magmatism accounts for the majority (>80%) and for the most violent events of explosive eruptions on Earth. This explosive, eruptive behavior is directly related to the high amounts of incorporated volatile elements, which in turn are directly related to the devolatilization of the subducted oceanic crust that lies beneath the volcanic arc (cf. section 1.2.1 for a more detailed discussion). Magmatic suites of destructive margins are compositionally distinct from constructive margins or intra-plate settings (Basaltic Volcanism Study Project, 1981). The characteristic enrichment of trace alkalis, alkaline earths, U, Th, and Pb are a consequence of the involvement of a fluid component in the upper mantle during magma formation (e.g. Hofmann et al., 1986; McBirney, 1969).

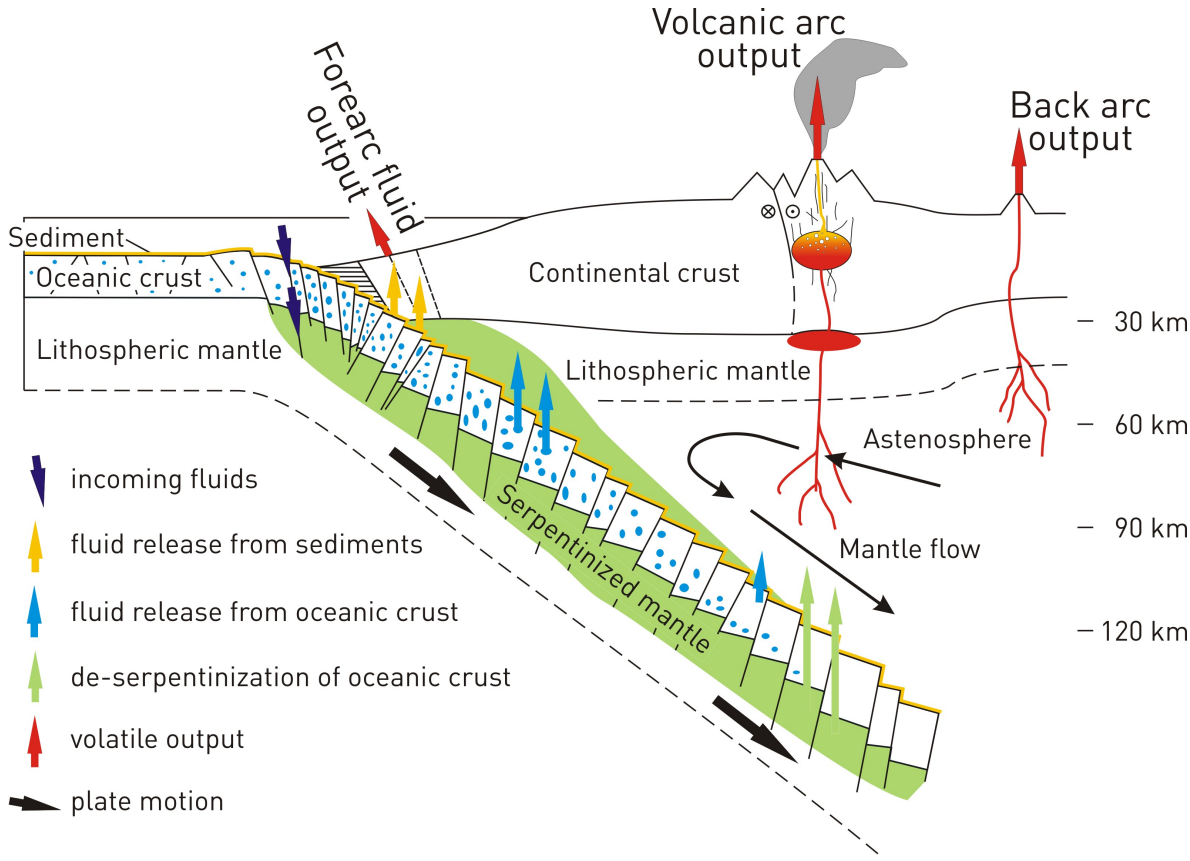

Fig. 1.1 Schematic view of volatile recycling and magma generation in subduction zones. Sediment and altered basaltic oceanic crust transport volatiles into subduction zones. Pore water is largely expelled from rock and sediment within the first 5-20 km depth (e.g., Moore and Vrolijk, 1992) On bending, the oceanic lithosphere is hydrated and serpentinized to upper-mantle depths (Ivandic et al., 2008). Structurally bound H_2O and other volatiles can be transported to greater depth and partially to completely released through metamorphic devolatilization reactions. Afterwards, they ascend into the overlying mantle, resulting in hydration and partial melting of the mantle peridotite. Ascending magmas carry volatiles back to the atmosphere (Volcanic arc and Back-arc output). Some portion of subducted volatiles may be retained by minerals in the slab and transported to the deep mantle (Rüpke et al., 2004).

The obvious Nb-Ta trough of volcanic-arc basalts, observable in multi-element diagrams of incompatible elements, has been explained by the retention of these elements in the source during partial melting.

Subduction of sediments accounts for most of the flux of incompatible elements that are transferred into the mantle at subduction zones. Trace element (Elliot et al., 1997) and isotopic systematics (Hawkesworth et al., 1997) suggest that sediment melting may occur in subduction zones (Johnson and Plank, 1999; Nichols et al., 1996; Plank, 2005) and affects magma composition (Stern, 2002).

1.2.3 Magmatic systems and volatiles

Many different species of gases (e.g. H_2O, CO_2, F, Cl, and S species) can dissolve in a silicate melt in the same way that CO_2 is dissolved in sparkling table water. Such gas species are referred to as magmatic volatiles. Of the volumetrically significant magma types on Earth, those emplaced in arc settings at convergent margins typically show the highest contents of dissolved volatiles. Magmatic volatiles are products of large-scale recycling processes involving devolatilization of variably hydrated and carbonated, sediment-covered, subducted oceanic lithosphere. These slab-derived fluids enter the overlying mantle wedge and lower its solidus, causing partial melting. However, several authors (e.g. Hilton et al., 2002; Sano and Williams, 1996) suggest that a significant portion of volatiles in arc magmas must be derived from the mantle wedge. Regardless of their origin, volatiles are incorporated in resulting magmas and transported towards the surface. The solubility of volatile components (e.g. H_2O) is a function of bulk melt composition (including dissolved volatile species), temperature and pressure. Interaction between magmas and transported volatile components during their ascent controls the final volatile inventory of volcanic products. Investigation of these volatile inventories allows for the determination of a number of pre-eruptive processes (e.g. storage history, fractionation, magma mixing, quiet degassing).

Chemical evolution of hydrous arc magmas

An empirical observation within arc magmas is that they are generally more hydrous and oxidized (i.e. high Fe_2O_3/FeO, Arculus, 1985; Arculus, 1994; Carmichael, 1991) than those of other tectonic settings (ridges and hot-spots). Although the discussion about the origin of the oxidized character is longstanding and still controversial (e.g. Arculus, 1985; Frost and McCammon, 2008; Kelley and Cottrell, 2009), these characteristics significantly impact magma genesis of arc magmas compared to dry and more reduced magma types (mid ocean ridge basalts (MORB) and ocean island basalts (OIB)). The most important effect of relatively high

concentrations of H_2O and Fe_2O_3/FeO on the crystallization of mafic melts are (Fig. 1.2) are: 1) the decrease of liquidus temperature and the suppression of plagioclase crystallization (Danyushevsky, 2001) associated with a shift towards more Ca-rich, Si-poor compositions; 2) stabilization of olivine towards higher melt SiO_2-contents (at the expense of plagioclase and orthopyroxene); 3) early appearance and persistence of a spinel phase (solid solution formula $(Mg,Fe^{2+})/(Cr,Al,Fe^{3+},Ti)_2O_4$) throughout the entire crystallization interval (Arculus, 2004). The crystallization of this mineral assemblage results in a strong increase of SiO_2 content accompanied by depletion of FeO_{tot} and MgO, as well as enrichment in K_2O, Na_2O and Al_2O_3.

Fractional crystallization of such mineral assemblages results in the formation of cumulates complementary to the previously described general evolution of arc melts. These cumulates, such as wehrlite (spinel, olivine, and clinopyroxene), dunite (spinel and olivine), and gabbro (spinel, clinopyroxene, anorthite, ±olivine, ±orthopyroxene, ±amphibole) are described to exist in some exhumed lower crustal arc segments (e.g. DeBari and Coleman, 1989; Khan et al., 1993; Spandler et al., 2003) as well as in volcanic deposits, where they are found as xenolithic cumulates (e.g. Dungan and Davidson, 2004; Rodríguez et al., 2007).

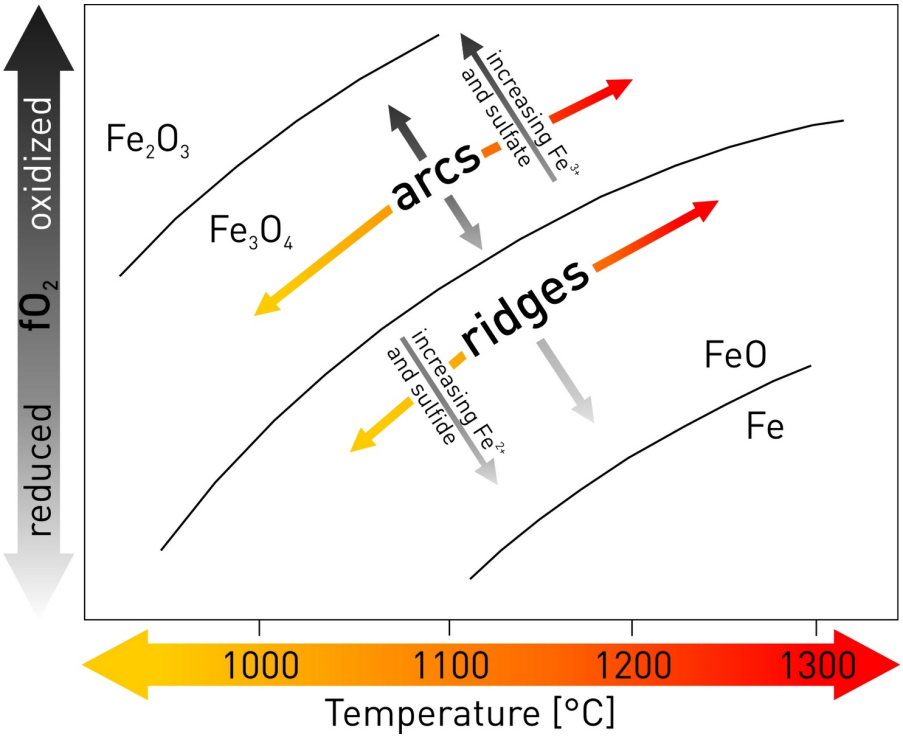

Fig. 1.2 Schematic illustration (modified from Arculus, 2004) of the range of redox states commonly covered by arc and mid-ocean ridge magmas. Redox conditions are reflected by Fe^{2+}/Fe^{3+} (i.e. FeO/Fe_2O_3) and SO_4^{2-}/S^{2-} (i.e. sulfate/sulfide) and shown here as relative oxygen fugacity (f02) versus temperature. Solid black lines indicate the stability curves of Fe_2O_3 and FeO in fO_2-T space. The intermediate field is characterized by stability and hence coexistence of Fe^{2+} and Fe^{3+} and corresponding solid solutions. The division between arc and ridge fields corresponds to a synthetic buffer reaction ($3Fe_2SiO_4 + O_2 \leftrightarrow 2\ Fe_3O_4 + 3\ SiO_2$).

The relatively low density of continental crust causes mantle-derived magmas to stagnate within the crust or at its base (Herzberg et al., 1983), encouraging fractionation, assimilation and degassing. These account for the fairly evolved compositions of arc magmas compared to other tectonic settings. Beside the differentiation trends (basalt-andesite-dacite-rhyolite) that mainly result from fractional crystallization of parental hydrous basalts, the presence of volatiles moderates several additional processes that control the petrogenesis of arc magmas including: 1) mingling of magma bodies with different degrees of fractionation; 2) assimilation of hydrated (and accordingly lowered solidus) rocks surrounding the plumbing system; 3) partial remelting of previously crystallized intrusives; 4) degassing and associated extensive crystallization that most probably accounts for the plagioclase-phyric nature, that is common for most arc magmas (Cashman, 2004).

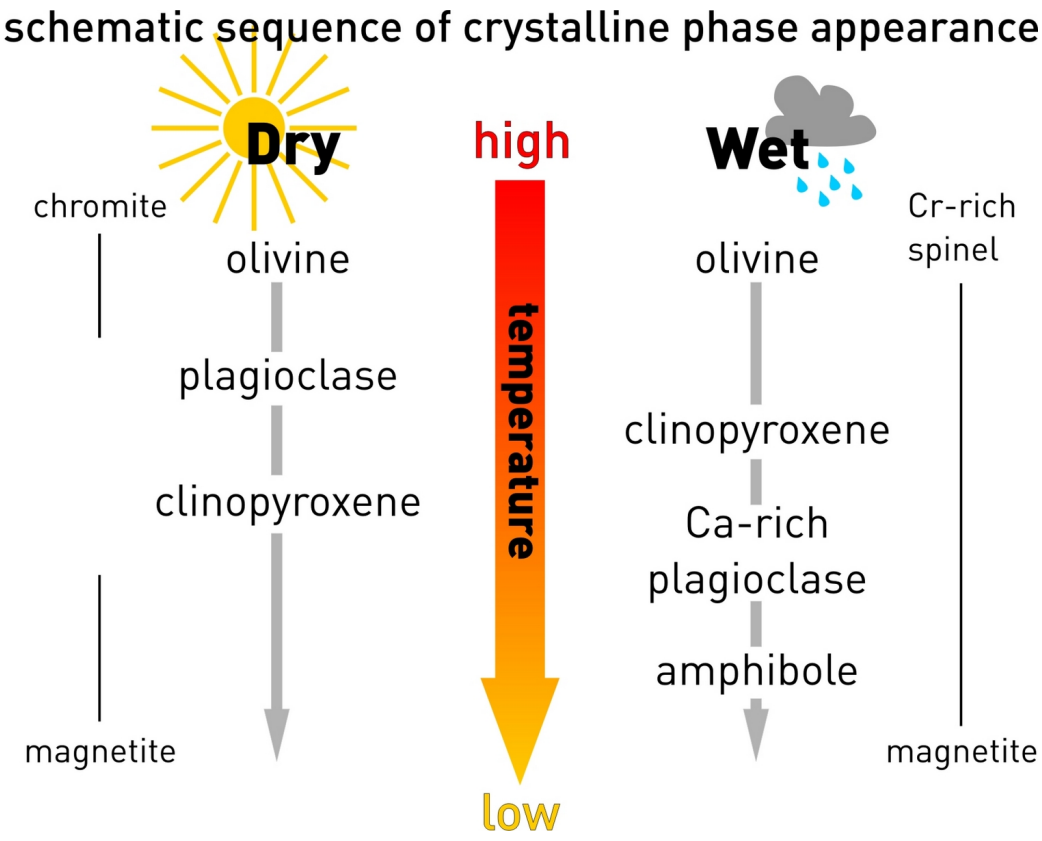

Fig. 1.3 Schematic depiction of the differences in progressive crystallization sequences between dry and hydrous subalkaline basaltic magmas. Arc magmas follow the wet crystallization sequence, whereas crystallization of MORBs adheres to the dry sequence. The continuous line on the wet path indicates the crystallization of a spinel phase throughout the whole differentiation sequence. In contrast, the intermittent line on the dry trend represents the early crystallization of a low Fe^{2+}-Cr-rich spinel phase (chromite), the absence of a spinel phase during the course of differentiation and the late onset of magnetite precipitation in anhydrous magmas. Redrawn from Arculus (2004).

Physical properties of hydrous arc magmas

The presence of a volatile phase does not only affect phase relations (melt generation and chemical evolution), but also rheology and fluid dynamics of magmas. Volatile species dissolve in silicate melts under high pressures, but form a vapor phase at low pressures. The formation of a gas phase generates overpressures in magma reservoirs and drives magma ascent through buoyancy. Rapid near-surface gas expansion results in excess kinetic energy, sufficient to sustain explosive eruptions. Therefore, exsolved magmatic volatiles provide the primary driving force for volcanic eruptions. Accumulation of a gas phase at the roof of a magma chamber might generate an overpressure that is capable to fracture wall rocks and trigger rapidly propagating, vapor-driven fractures (Carrigan, 2000; Lister, 1990; Rubin, 1993). Such gas-driven fractures may precede actual magma transfer from the storage level to the surface prior to the eruption (Menand and Tait, 2001).

In the last years, numerous studies using numerical (e.g. Melnik and Sparks, 2005) and experimental techniques were published addressing the description of the complex dynamics of magma ascent (e.g. disequilibrium degassing (Jaupart and Allègre, 1991; Papale et al., 1998; Woods and Koyaguchi, 1994), compressible fluid flow (Massol and Jaupart, 1999; Massol et al., 2001; Melnik et al., 2005) and surrounding wall rocks (Costa et al., 2009), phase changes (Mastin and Ghiorso, 2001; Mastin and Ghiorso, 2000), open system degassing (Burgisser and Gardner, 2004) and crystallization (Melnik and Sparks, 1999, 2002a, b), and bubble nucleation kinetics (Massol and Koyaguchi, 2005; Papale, 2001)). Altogether, these studies suggest that the state of a rising magma body is highly susceptible to changes in the kinetics of crystallization and vesiculation as well as associated changes in rheology of vesicular and crystal-bearing melts, the fluid dynamics of viscous magma flowing through conduits, and the explosivity of eruptions. All of these processes are controlled by the presence and behavior of magmatic volatiles.

Having summarized the internal controls on generation, evolution and eruption of arc magmas, there is a growing amount of evidence that external forcing is also a relevant factor (e.g. Cembrano and Lara, 2009). Arc volcanoes by nature lie in tectonically highly active regions where large-magnitude earthquakes transmit seismic energy over considerable distances. The various ways in which such external forcing may affect magmatic systems do, in turn, depend on the internal state of the system (i.e. volatile saturation state controlling the criticality of the system; e.g. Manga and Brodsky, 2006; Watt et al., 2009). A major theme of this thesis is to define the petrologic conditions that set the stage for the influence of external forces on volcano-magma-systems using examples from the Southern Andes.

1.3 STUDY AREA AND SAMPLE SELECTION

1.3.1 Justification of the study area

The role of external and internal factors in controlling eruptive behavior has become a major subject in research on volcanic hazards. The selected target area in Southern Chile between 32°-42°S provides an excellent opportunity to investigate the interplay between tectonic structures and stresses in the upper plate, seismic activity, and styles, magnitudes and frequencies of volcanic eruptions.

Melts, generated in the mantle wedge, which inherit some of the subducted volatiles, differentiate while rising through the crust. Differentiation processes, involving fractional crystallization, magma mixing and crustal contamination, which all affect the volatile inventory, are partly controlled by crustal tectonics that determine magma storage levels and ascent rates and may also affect eruptive behavior. Understanding how the interaction of all these processes affects the magmatic volatile inventory is essential to better constrain the turnover of volatiles through subduction zones and finally the potentially climate active emission into the atmosphere. Temporal variations in differentiation processes and volatile inventories at individual volcanic systems might reveal how (un)steady such processes are through time.

1.3.2 Sample selection

To explore the within-suite systematics/variations of magmatic volatile inventories, two volcanic systems - the Lonquimay and Puyehue-Cordón Caulle Volcanic Complexes - were chosen for a detailed investigation. Both sites were chosen because they cover an unusually wide range in composition (basalts to rhyodacites/rhyolites; e.g. Gerlach et al., 1988; Polanco, 1998) that facilitate the investigation of differentiation processes. All samples used in this study were collected during three extensive field campaigns in 2009 and 2010. Field work in 2009 mainly concentrated on the establishment of post-glacial tephrostratigraphic correlations for both volcanic systems. Together with obtained radiocarbon age dating results, this ensured the collection of stratigraphically well-controlled sample suites from both volcanic complexes during subsequent 2010 field campaigns. Due to rapid syn-eruptive quenching, collected tephra samples facilitate the investigation of pre-eruptive melt compositions (using matrix glasses of tephra clasts) and volatile contents (using glass and fluid inclusions trapped in phenocrysts).

1.3.3 The Chilean Subduction zone

The world's longest exposed mountain chain - the Andean orogen - extends 8000 km along the Western continental margin of South America: from the Caribbean Coast in the North to Cape Horn at its Southern end (Ramos, 1999; Ramos, 2009; Stern, 2004). The continental margin is characterized by the subduction of the Nazca plate beneath the South American continental plate, forming the Peru-Chile-Trench at the convergent plate boundary. The subduction geometry defines four distinct zones of active volcanism (e.g. Stern, 2004): the Northern Volcanic Zone (NVZ, 5°N-2°S), the Central Volcanic Zone (CVZ, 14°-27°S), the Southern Volcanic Zone (SVZ, 33°-46°S) and the Austral Volcanic Zone (AVZ, 49°-55°S). They are all divided by flat slab segments (dip angle <10°) that each account for a gap in the magmatic activity. Since this study is restricted to magmatic systems of the SVZ, the following section concentrates on the geological setting of this arc segment.

1.3.4 Southern Volcanic Zone (SVZ)

The north-eastward subduction (6.6 mm/a with azimuthal direction 80.1°; Angermann et al., 1999; Oncken et al., 2006) of the oceanic Nazca plate beneath the Southern part of the South American plate between 33° and 46°S results in the formation of the Quaternary Southern Volcanic Zone of the Andes (SVZ). The age of the oceanic Nazca Plate increases northwards along the trench from zero at the Chile Triple Junction, where the Chile Ridge subducts (46°S), to about 35 Ma at 33°S (Tebbens et al., 1997). The thickness of the continental crust continually decreases from 55-60 km in the North to only 30-35 km South of 37°S (Lowrie and Hey, 1981).

The volcanic front of the SVZ consists of at least 60 late Cenozoic to historically active volcanic centers (Ramos, 1999), including three giant silicic caldera systems and multitudinous minor eruptive centers (MECs). Based on petrographic, geochemical and tectonic observations, several authors (López-Escobar et al., 1995; Hildreth and Moorbath, 1988; López-Escobar et al., 1993; Stern, 2004; Tormey et al., 1991) propose a further subdivision of the SVZ into four domains: the Northern (NSVZ; 33°-34°30'S), Transitional (TSVZ; 34°30'-37°S), Central (CSVZ; 37°-41°30'S) and Southern (SSVZ; 41°30'-46°S) Volcanic Zones.

Magmatism of the NSVZ and TSVZ is dominated by andesitic and dacitic rocks, showing stronger influence of crustal assimilation (e.g. López-Escobar et al., 1995) than the volcanic province South of 37°S. Volcanic products of the Southern part of the SVZ are predominantly basalts and basaltic andesites with the notable exception of its largest volcanic center, Puyehue-Cordón Caulle (Gerlach et al., 1988; Lara et al., 2006; Völker et al., 2011), that discharged

significant amounts of rhyodacitic to rhyolithic melts. Oblique convergence (22°-30°NE) between the Chile Triple Junction at 46.2°S and the Copahue volcano at 38°S (Rosenau et al., 2006) causes dextral slip along the arc-parallel deep-rooted Liquiñe-Ofqui Fault Zone (Arancibia et al., 1999; Cembrano et al., 2000; Lavenu and Cembrano, 1999). The architecture of the intraarc region in the Southern province (37°-46°S) is heavily controlled by the onset of this long-lived transpressional dextral strike slip system (Cembrano et al., 2000; Hervé, 1994; Rosenau et al., 2006; Thomson, 2002). This tectonic control is most prominently expressed by the position of most of the larger volcanic and minor eruptive centers in the CSVZ and SSVZ (López-Escobar et al., 1995; Cembrano and Lara, 2009). In addition, several authors (Cembrano and Lara, 2009; Soyer, 2002) argue that tectonics do not only control the loci, but also the chemical evolution of volcanic systems by dominating crustal residence time through providing (transtensive regime) or blocking (transpressive regime) pathways.

Fig. 1.4 (next page) Overview map of the Southern Volcanic Zone (data from GEBCO_08 Grid; version 20091120, http://www.gebco.net). Positions of major upper plate faults (black lines) are redrawn from Melnick et al. (2009) and Melnick and Echtler (2006). The convergence directions of the Chiloe Microplate and the Nazca Plate are indicated by arrows. Magenta and purple stars mark the epicenter locations of the 1960 Mw 9.5 Great Chile and the 2010 Mw 8.8 Maule earthquakes. Approximate rupture zones of both earthquakes are given by dashed ellipses.

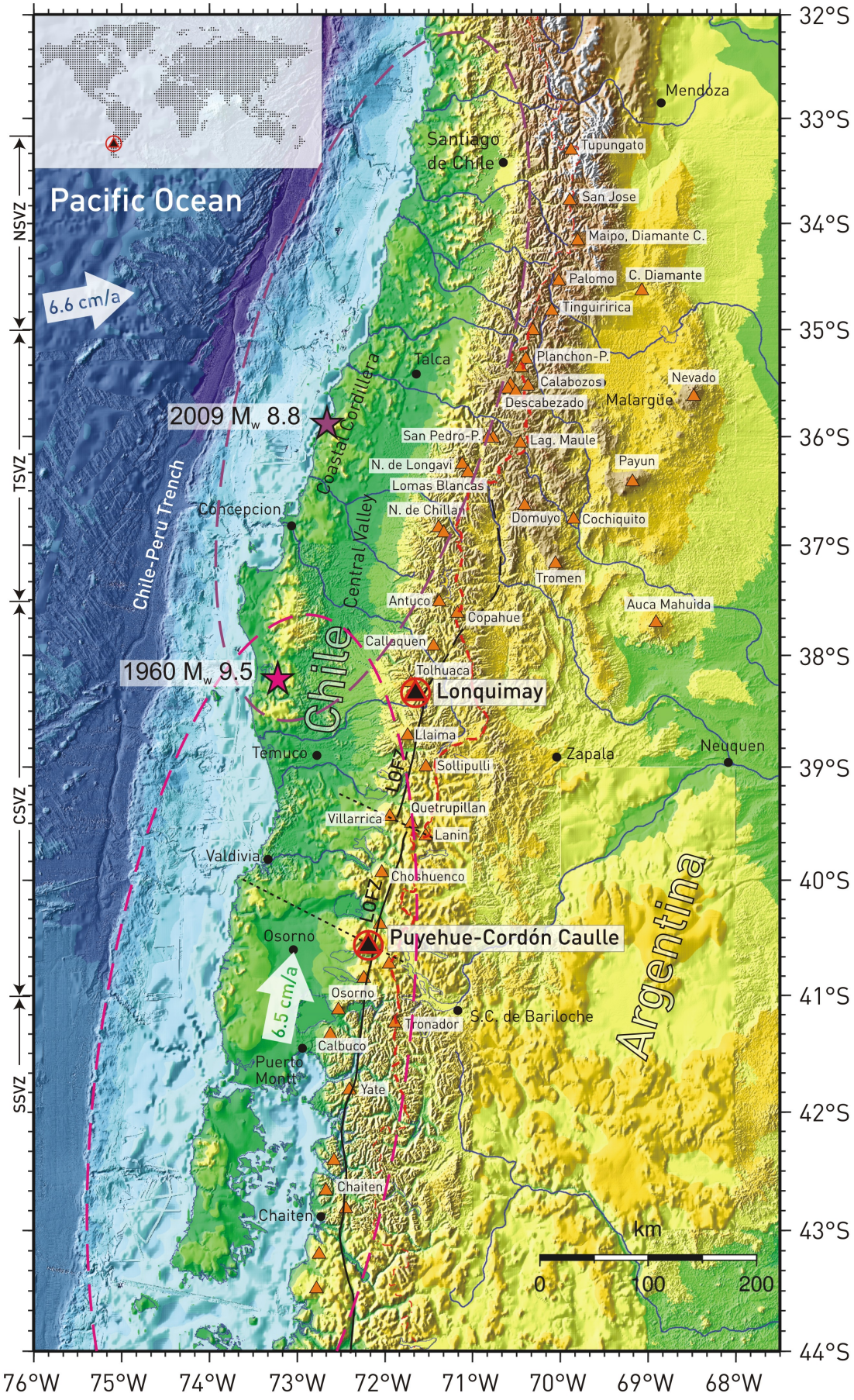
Pacific Ocean
6.6 cm/a
6.5 cm/a
2009 M$_w$ 8.8
1960 M$_w$ 9.5
Chile-Peru Trench
Coastal Cordillera
Central Valley
Chile
Argentina
LOFZ
NSVZ
TSVZ
CSVZ
SSVZ
Santiago de Chile
Mendoza
Concepcion
Temuco
Valdivia
Osorno
Puerto Montt
Chaiten
Talca
Neuquen
Zapala
S.C. de Bariloche
Tupungato
San Jose
Maipo, Diamante C.
Palomo
C. Diamante
Tinguiririca
Planchon-P.
Calabozos
Descabezado
Malargüe
Nevado
San Pedro-P.
Lag. Maule
Payun
N. de Longavi
Lomas Blancas
N. de Chillan
Domuyo
Cochiquito
Tromen
Antuco
Copahue
Auca Mahuida
Callaquen
Tolhuaca
Lonquimay
Llaima
Sollipulli
Quetrupillan
Villarrica
Lanin
Choshuenco
Puyehue-Cordón Caulle
Osorno
Tronador
Calbuco
Yate
Chaiten
km
0
100
200
32°S
33°S
34°S
35°S
36°S
37°S
38°S
39°S
40°S
41°S
42°S
43°S
44°S
76°W
75°W
74°W
73°W
72°W
71°W
70°W
69°W
68°W

1.4 SCOPE AND ORGANIZATION OF THIS STUDY

Chapters 2, 3 and 4 represent stand-alone manuscripts published, submitted or prepared for publication. They focus on individual aspects related to petrogenetic and tectonic controls on temporally changing volatile inventories of volcanic systems in the SVZ. Investigations are focused on two exemplary systems: the **Lonquimay** and **Puyehue-Cordón Caulle** volcanic complexes. Chapter 5 summarizes the results of the three stand-alone articles and evaluates the results in the context of subduction zone magmatism research.

In Chapter 2 tephrostratigraphic results from three field campaigns were integrated to establish a general post-glacial tephrostratigraphy for the Lonquimay Volcanic Complex in the high Southern Andes. Statistical time series analyses were used to calculate future eruption probabilities and investigate eruptive behavior through time. Furthermore, the results from time series analyses in combination with thermobarometric investigations were used to investigate the temporally changing systematics between eruption frequency and associated changes in the plumbing system.

Chapter 3 uses the stratigraphic framework established in chapter 2 to investigate the temporal variation of volatile inventories, melt evolution (based on crystal compositions, matrix glass and melt inclusion data), and plumbing system dynamics (i.e. mafic replenishments, magma mixing). The motivation was to clarify how these petrogenetic parameters controlled the volatile inventory (derived from melt inclusion analyses) of Lonquimay Volcanic Complex (LVC) through time.

Since its 1960 eruption, Puyehue-Cordón Caulle Volcanic Complex (PCCVC) - that woke in 2011 after 51 years of dormancy - is one of the most renowned volcanic systems thought to be susceptible to seismic triggering. The study presented in **chapter 4** uses a combination of thermobarometric and volatile investigations based on melt- and fluid inclusions in order to determine the pre-eruptive criticality of the magma chambers for the 2011, 1960 and four older post-glacial explosive eruptions. The results document that H_2O-saturation in relatively shallow reservoirs appears to be a typical feature of explosive eruptions at this volcanic system. This implies that due to volatile supersaturation the system was due to erupt when it was eventually triggered by seismic activity. PCCVC's ability to repeatedly restore critical magmatic conditions and its position astride the arc-wide Liquiñe-Ofqui Fault Zone system, along which seismic energy/strain may be transmitted particularly effectively, probably are the two factors that facilitate tectonic triggering of eruptions at this particular volcanic system.

REFERENCES

Angermann, D., Klotz, J., and Reigber, C., 1999, Space-geodetic estimation of the Nazca-South American Euler vector: Earth and Planetary Science Letters, v. Vol. 171, p. p. 329-334.

Arancibia, G., Cembrano, J., and Lavenu, A., 1999, Transpresión dextral y partición de la deformación en la Zona de Falla Liquiñe-Ofqui, Aisén, Chile (44-45°S): Revista Geológica de Chile, v. 26, p. 3-22.

Arculus, R.J., 1985, Oxidation Status of the Mantle: Past and Present: Annual Review of Earth and Planetary Sciences, v. 13, p. 75-95.

Arculus, R.J., 1994, Aspects of magma genesis in arcs: Lithos, v. 33, p. 189-208.

Arculus, R.J., 2004, Evolution of arc magmas and their volatiles, state of the planet: frontiers and challenges in geophysics, Volume 150: Washington, DC; USA, American Geophysical Union Monograph, p. 95-108.

Basaltic Volcanism Study Project, 1981, Basaltic Volcanism on the Terrestrial Planets: New York, Pergamon Press, Inc., p. 1286.

Brasse, H., Lezaeta, P., Rath, V., Schwalenberg, K., Soyer, W., and Haak, V., 2002, The Bolivian Altiplano conductivity anomaly: Journal of Geophysical Research, v. 107, p. 20-96.

Burgisser, A., and Gardner, J.E., 2004, Experimental constraints on degassing and permeability in volcanic conduit flow: Bulletin of Volcanology, v. 67, p. 42-56.

Carmichael, I.S.E., 1991, The redox states of basic and silicic magmas: a reflection of their source regions?: Contributions to Mineralogy and Petrology, v. 106, p. 129-141.

Carrigan, C.R., 2000, Plumbing systems, *in* Sigurdsson, H., Houghton, B.F., McNutt, S.R., Rymer, H., Stix, J., and McBirney, A.R., eds., Encyclopedia of Volcanoes, Volume 53: San Diego, USA, Academic Press, p. 149-170.

Cashman, K., 2004, Volatile Controls on Magma Ascent and Eruption, state of the planet: frontiers and challenges in geophysics, Volume 150: Washington, DC; USA, American Geophysical Union Monograph, p. 109-124.

Cembrano, J., and Lara, L., 2009, The link between volcanism and tectonics in the southern volcanic zone of the Chilean Andes: A review: Tectonophysics, v. 471, p. 96-113.

Cembrano, J., Schermer, E., Lavenu, A., and Sanhueza, A., 2000, Contrasting nature of deformation along an intra-arc shear zone, the Liquiñe-Ofqui fault zone, southern Chilean Andes: Tectonophysics, v. 319, p. 129-149.

Costa, A., Sparks, R.S.J., Macedonio, G., and Melnik, O., 2009, Effects of wall-rock elasticity on magma flow in dykes during explosive eruptions: Earth and Planetary Science Letters, v. 288, p. 455-462.

Danyushevsky, L.V., 2001, The effect of small amounts of H2O on crystallisation of mid-ocean ridge and backarc basin magmas: Journal of Volcanology and Geothermal Research, v. 110, p. 265-280.

DeBari, S.M., and Coleman, R.G., 1989, Examination of the deep levels of an island arc: evidence from the tonsina ultramafic-mafic assemblage, Tonsina, Alaska: Journal of Geophysical Research, v. 94, p. 4373-4391.

Dungan, M.A., and Davidson, J., 2004, Partial assimilative recycling of the mafic plutonic roots of arc volcanoes: An example from the Chilean Andes: Geology, v. 32, p. 773-776.

Elliot, T., Plank, T., Zindler, A., White, W., and Bourdon, B., 1997, Element transport from slab to volcanic front at the Mariana arc: Journal Geophysical Research, v. 102, p. 14991-15019.

Frost, D.J., and McCammon, C.A., 2008, The Redox State of Earth's Mantle: Annual Review of Earth and Planetary Sciences, v. 36, p. 389-420.

Gerlach, D.C., Frey, F.A., Moreno-Roa, H., and Lopez-Escobar, L., 1988, Recent Volcanism in the Puyehue-Cordón Caulle Region, Southern Andes, Chile (40·5°S): Petrogenesis of Evolved Lavas: Journal of Petrology, v. 29, p. 333-382.

Hawkesworth, C.J., Turner, S.P., McDermott, F., Peate, D.W., and van Calsteren, P., 1997, U-Th Isotopes in Arc Magmas: Implications for Element Transfer from the Subducted Crust: Science, v. 276, p. 551-555.

Hervé, F., 1994, The southern Andes between 39° and 44°S latitude: The geological signature of a transpressive tectonic regime related to a magmatic arc, *in* Reuter, K.J., Scheuber, E., and Wigger, P.J., eds., Tectonics of the Southern Central Andes: Berlin, Springer, p. 243-248.

Herzberg, C., Fyfe, W., and Carr, M., 1983, Density constraints on the formation of the continental Moho and crust: Contributions to Mineralogy and Petrology, v. 84, p. 1-5.

Hildreth, W., and Moorbath, S., 1988, Crustal contributions to arc magmatism in the Andes of Central Chile: Contributions Mineralogy Petrology, v. 98, p. 455-489.

Hilton, D.R., Fischer, T.P., and Marty, B., 2002, Noble Gases and Volatile Recycling at Subduction Zones: Reviews in Mineralogy and Geochemistry, v. 47, p. 319-370.

Hofmann, A.W., Jochum, K.P., Seufert, M., and White, W.M., 1986, Nb and Pb in oceanic basalts: new constraints on mantle evolution: Earth and Planetary Science Letters, v. Vol. 79, p. p. 33-45.

Ivandic, M., Grevemeyer, I., Berhorst, A., Flueh, E.R., and McIntosh, K., 2008, Impact of bending related faulting on the seismic properties of the incoming oceanic plate offshore of Nicaragua: Journal of Geophysical Research, v. 113.

Jaupart, C., and Allègre, C.J., 1991, Gas content, eruption rate and instabilities of eruption regime in silicic volcanoes: Earth and Planetary Science Letters, v. 102, p. 413-429.

Jödicke, H., Jording, A., Ferrari, L., Arzate, J., Mezger, K., and Rüpke, L., 2006, Fluid release from the subducted Cocos plate and partial melting of the crust deduced from magnetotelluric studies in southern Mexico: Implications for the generation of volcanism and subduction dynamics: Journal of Geophysical Research, v. 111, p. B08102.

Johnson, M.C., and Plank, T., 1999, Dehydration and melting experiments constrain the fate of subducted sediments: Geochemistry Geophysics Geosystems, v. 1, p. 1-26.

Kelley, K.A., and Cottrell, E., 2009, Water and the Oxidation State of Subduction Zone Magmas: Science, v. 325, p. 605-607.

Khan, M.A., Jan, M.Q., and Weaver, B.L., 1993, Evolution of the lower arc crust in Kohistan, N. Pakistan: temporal arc magmatism through early, mature and intra-arc rift stages: Geological Society, London, Special Publications, v. 74, p. 123-138.

Lara, L.E., Moreno, H., Naranjo, J.A., Matthews, S., and Pérez de Arce, C., 2006, Magmatic evolution of the Puyehue-Cordón Caulle Volcanic Complex (40° S), Southern Andean Volcanic Zone: From shield to unusual rhyolitic fissure volcanism: Journal of Volcanology and Geothermal Research, v. 157, p. 343-366.

Lavenu, A., and Cembrano, J., 1999, Compressional and transpressional stress pattern for Pliocene and Quaternary brittle deformation in fore-arc and intra-arc zones (Andes of Central and Southern Chile): Journal of Structural Geology, v. 21, p. 1669-1691.

Lister, J.R., 1990, Buoyancy-driven fluid fracture: the effects of material toughness and of low-viscosity precursors: Journal of Fluid Mechanics, v. 210, p. 263-280.

López-Escobar, L., Cembrano, J., and Moreno, H., 1995, Geochemistry and tectonics of the chilean Southern Andes basaltic Quaternary volcanism (37°-46°S). Revista Geológica de Chile, v. 22, p. 219-234.

López-Escobar, L., Killian, R., Kempton, P., and Tagiri, M., 1993, Petrography and geochemistry of Quaternary rocks from the Southern Volcanic Zone between 41°30' and 46°00' S: Revista Geológica de Chile, v. 20, p. 35-55.

Lowrie, A., and Hey, R., 1981, Geological and geophysical variations along the western margin of Chile near latitude 33° to 36°S and their relation to Nazca Plate subduction. In Nazca Plate; crustal formation and Andean convergence: Geological Society of America Memoirs, v. 154, p. 741-754.

Manga, M., and Brodsky, E., 2006, Seismic Triggering of Eruptions in the Far Field: Volcanoes and Geysers. : Annual Review of Earth and Planetary Sciences, v. 34, p. 263-291.

Massol, H., and Jaupart, C., 1999, The generation of gas overpressure in volcanic eruptions: Earth and Planetary Science Letters, v. 166, p. 57-70.

Massol, H., Jaupart, C., and Pepper, D.W., 2001, Ascent and decompression of viscous vesicular magma in a volcanic conduit: J. Geophys. Res., v. 106, p. 16223-16240.

Massol, H., and Koyaguchi, T., 2005, The effect of magma flow on nucleation of gas bubbles in a volcanic conduit: Journal of Volcanology and Geothermal Research, v. 143, p. 69-88.

Mastin, L., and Ghiorso, M., 2001, Adiabatic temperature changes of magma-gas mixtures during ascent and eruption: Contributions to Mineralogy and Petrology, v. 141, p. 307-321.

Mastin, L.G., and Ghiorso, M.S., 2000, A Numerical Program for Steady-State Flow of Magma-Gas Mixtures Through Vertical Eruptive Conduits, U.S. Geological Survey Open-File Report, Volume 00-209: Washington DC, Department of the interior, p. 1-59.

McBirney, A., 1969, Compositional variations in Cenozoic calc-alkaline suites of Central America, Proceedings of the Andesite Conference, Volume 65: State of Oregon, Department of Geology and Mineral Industries, Bulletin, p. 185-189.

Melnick, D., Bookhagen, B., Strecker, M.R., and Echtler, H.P., 2009, Segmentation of megathrust rupture zones from fore-arc deformation patterns over hundreds to millions of years, Arauco peninsula, Chile: Journal of Geophysical Research, v. 114, p. 1-23.

Melnick, D., and Echtler, H.P., 2006, Morphotectonic and Geologic Digital Map Compilations of the South-Central Andes (36°-42°S), *in* Oncken, O., Chong, G., Franz, G., Giese, P., Götze, H.-J., Ramos, V.A., Strecker, M.R., and Wigger, P., eds., The Andes – active subduction orogeny: Frontiers in Earth Sciences: Berlin, Springer Berlin Heidelberg, p. 565-568.

Melnik, O., Barmin, A.A., and Sparks, R.S.J., 2005, Dynamics of magma flow inside volcanic conduits with bubble overpressure buildup and gas loss through permeable magma: Journal of Volcanology and Geothermal Research, v. 143, p. 53-68.

Melnik, O., and Sparks, R.S.J., 1999, Nonlinear dynamics of lava dome extrusion: Nature, v. 402, p. 37-41.

Melnik, O., and Sparks, R.S.J., 2002a, Dynamics of magma ascent and lava extrusion at Soufrière Hills Volcano, Montserrat: Geological Society, London, Memoirs, v. 21, p. 153-171.

Melnik, O., and Sparks, R.S.J., 2002b, Modelling of conduit flow dynamics during explosive activity at Soufrière Hills Volcano, Montserrat: Geological Society, London, Memoirs, v. 21, p. 307-317.

Melnik, O., and Sparks, R.S.J., 2005, Controls on conduit magma flow dynamics during lava dome building eruptions: Journal of Geophysical Research, v. 110, p. B02209.

Menand, T., and Tait, S.R., 2001, A phenomenological model for precursor volcanic eruptions: Nature, v. 411, p. 678-680.

Mével, C., 2003, Serpentinization of abyssal peridotites at mid-ocean ridges: Comptes Rendus Geoscience, v. 335, p. 825-852.

Moore, J.C., and Vrolijk, P., 1992, Fluids in accretionary prisms: Reviews of Geophysics, v. 30, p. 113-135.

Nichols, G.T., Wyllie, P.J., and Stern, C.R., 1996, Experimental melting of pelagic sediment, constraints relevant to subduction, *in* E., B.G., ed., Subduction from Top to Bottom Volume 96: Geophysical monograph Washington DC, USA, American Geophysical Union, , p. 293-298.

Oncken, O., Hindle, D., Kley, J., Elger, K., Victor, P., and Schemmann, K., 2006, Deformation of the Central Andean Upper Plate System – Facts, Fiction, and Constraints for Plateau Models, *in* Oncken, O., Chong, G., Franz, G., Giese, P., Götze, H.-J., Ramos, V.A., Strecker, M.R., and Wigger, P., eds., The Andes – active subduction orogeny: Berlin, Springer, p. 3-27.

Papale, P., 2001, Dynamics of magma flow in volcanic conduits with variable fragmentation efficiency and nonequilibrium pumice degassing: Journal of Geophysical Research, v. 106, p. 11043-11065.

Papale, P., Neri, A., and Macedonio, G., 1998, The role of magma composition and water content in explosive eruptions: 1. Conduit ascent dynamics: Journal of Volcanology and Geothermal Research, v. 87, p. 75-93.

Peacock, S.M., 2001, Are the lower planes of double seismic zones caused by serpentine dehydration in subducting oceanic mantle?: Geology, v. 29, p. 299-302.

Plank, T., 2005, Constraints from Thorium/Lanthanum on Sediment Recycling at Subduction Zones and the Evolution of the Continents: Journal of Petrology, v. 46, p. 921-944.

Polanco, E., 1998, Volcanismo Explosivo Postglacial de la Cuenca del Alto Biobío, Andes del Sur (37º45'-38º30') [Master thesis]: Santiago de Chile, Universidad de Chile.

Poli, S., and Schmidt, M.W., 2002, Petrology of Subducted Slabs: Annual Review of Earth and Planetary Sciences, v. 30, p. 207-235.

Ramos, V.A., 1999, Plate tectonic setting of the Andean Cordillera: Episodes, v. 22, p. 183-190.

Ramos, V.A., 2009, Anatomy and global context of the Andes: Main geologic features and the Andean orogenic cycle: Geological Society of America Memoirs, v. 204, p. 31--65.

Ranero, C.R., and Sallarès, V., 2004, Geophysical evidence for hydration of the crust and mantle of the Nazca plate during bending at the north Chile trench: Geology, v. 32, p. 549-552.

Rodríguez, C., Sellés, D., Dungan, M., Langmuir, C., and Leeman, W., 2007, Adakitic Dacites Formed by Intracrustal Crystal Fractionation of Water-rich Parent Magmas at Nevado de Longaví Volcano (36·2°S; Andean Southern Volcanic Zone, Central Chile): Journal of Petrology, v. 48, p. 2033-2061.

Rosenau, M., Melnick, D., and Echtler, H., 2006, Kinematic constraints on intra-arc shear and strain partitioning in the southern Andes between 38°S and 42°S latitude: Tectonics, v. 25, p. TC4013.

Rubin, A.M., 1993, On the thermal viability of dikes leaving magma chambers: Geophysical Research Letters, v. 20, p. 257-260.

Rüpke, L.H., Morgan, J.P., Hort, M., and Connolly, J.A.D., 2004, Serpentine and the subduction zone water cycle: Earth and Planetary Science Letters, v. 223, p. 17-34.

Saffer, D.M., Silver, E.A., Fisher, A.T., Tobin, H., and Moran, K., 2000, Inferred pore pressures at the Costa Rica subduction zone: implications for dewatering processes: Earth and Planetary Science Letters, v. 177, p. 193-207.

Sano, Y., and Williams, S.N., 1996, Fluxes of mantle and subducted carbon along convergent plate boundaries: Geophysical Research Letters, v. 23, p. 2749-2752.

Schmidt, M.W., and Poli, S., 1998, Experimentally based water budgets for dehydrating slabs and consequences for arc magma generation: Earth and Planetary Science Letters, v. 163, p. 361-379.

Schwalenberg, K., Rath, V., and Haak, V., 2002, Sensitivity studies applied to a two-dimensional resistivity model from the Central Andes: Geophysical Journal International, v. 150, p. 673-686.

Siebert, L., and Simkin, T., 2002, Volcanoes of the World: an Illustrated Catalog of Holocene Volcanoes and their Eruptions, internet database.

Simkin, T., 1993, Terrestrial Volcanism in Space and Time: Annual Review of Earth and Planetary Sciences, v. 21, p. 427-452.

Soyer, W., 2002, Analysis of geomagnetic variations in the Central and Southern Andes [PhD thesis]: Berlin, Freie Universität Berlin.

Spandler, C., Arculus, R., Eggins, S., Mavrogenes, J., Price, R., and Reay, A., 2003, Petrogenesis of the Greenhills Complex, Southland, New Zealand: magmatic differentiation and cumulate formation at the roots of a Permian island-arc volcano: Contributions to Mineralogy and Petrology, v. 144, p. 703-721.

Stern, C.R., 2004, Active Andean volcanism: its geological and tectonic setting: Revista geológica de Chile, v. Vol. 31, p. p. 161-206.

Stern, R.J., 2002, Subduction zones: Reviews of Geophysics, v. 40, p. 1012.

Tebbens, S.F., Cande, S.C., Kovacs, L., Parra, J.C., LaBrecque, J.L., and Vergara, H., 1997, The Chile ridge: A tectonic framework: Journal of Geophysical Research, v. 102, p. 12035-12059.

Thomson, S.N., 2002, Late Cenozoic geomorphic and tectonic evolution of the Patagonian Andes between latitudes 42°S and 46°S: An appraisal based on fission-track results from the transpressional intra-arc Liquiñe-Ofqui fault zone: Geological Society of America Bulletin, v. 114, p. 1159-1173.

Tormey, D.R., Hickey-Vargas, R., Frey, F.A., and López-Escobar, L., 1991, Recent lavas from the Andean front (33° to 42°S): interpretations of along-arc compositional variations. , *in* Harmon, R.S., and Rapela, C.W., eds., Andean Magmatism and its Tectonic Setting, Volume 265: Special Paper, Geological Society of America, p. 57-77.

Völker, D., Kutterolf, S., and Wehrmann, H., 2011, Comparative mass balance of volcanic edifices at the southern volcanic zone of the Andes between 33°S and 46°S: Journal of Volcanology and Geothermal Research, v. 205, p. 114-129.

Watt, S.F.L., Pyle, D.M., and Mather, T.A., 2009, The influence of great earthquakes on volcanic eruption rate along the Chilean subduction zone: Earth and Planetary Science Letters, v. 277, p. 399-407.

Woods, A.W., and Koyaguchi, T., 1994, Transitions between explosive and effusive eruptions of silicic magmas: Nature, v. 370, p. 641-644.

Worzewski, T., Jegen, M., Kopp, H., Brasse, H., and Taylor Castillo, W., 2011, Magnetotelluric image of the fluid cycle in the Costa Rican subduction zone: Nature Geosci, v. 4, p. 108-111.

Chapter 2

Post-glacial time series of explosive eruptions and associated changes in the magma plumbing system of Lonquimay volcano, south central Chile

This chapter was accepted for publication in *International Journal of Earth Sciences* on 11 June 2012. Co-authors: A. Freundt, S. Kutterolf, C. Burkert

2.1 ABSTRACT

The Lonquimay Volcanic Complex (LVC) in the high Southern Andes comprises a stratocone and NE-trending flank-cone alignments. Numerous effusive and explosive volcanic eruptions characterize its post-glacial magmatic activity. Our tephrostratigraphic record, pre-dating the four historically documented eruptions, comprises 22 dated pyroclastic deposits that are used to constrain repose time distribution and eruption probability of the LVC magmatic system. Statistical examination of the stratigraphy-based eruption time series yields probabilities of 20-50% for at least one explosive (VEI≥3) eruption within the next 100 years as of 2011.

The tephra deposits are subdivided into three petrographic groups: a felsic group (Lonquimay Colored Pumice Tephra, LCPT), an intermediate population (Lonquimay Grey Pumice Tephra, LGPT) and a mafic member (Lonquimay Dark Scoria Tephra, LDST). The distribution of these petrographic groups through the LVC tephrostratigraphy is linked to the observed changes in repose times. LDST deposits as well as deposits compositionally zoned from LCPT to LGPT dominate the lower part of the stratigraphy for which recurrence times are short (RT_{mean}=417±169 a). Deposits younger than 6000 b2k (years before 2000 AD) have dominantly LCPT and minor LDST compositions, no longer contain LGPT, and repose times are significantly longer (RT_{mean}=1350±310 a). We interpret the change in eruption regime to result from a rearrangement in the magma storage and plumbing system.

Thermobarometric calculations based on cpx liquid equilibria and amphibole compositions reveal three distinct magma storage levels: the mafic LDST derive from mid crustal storage (P_{mean}=476±95 MPa, T_{mean}=1073±24°C), felsic LCPT mainly erupted from upper-crustal level (P_{mean}=86±49 MPa, T_{mean}=936±24°C), whereas LGPT samples yield intermediate storage depths (P_{mean}=239±100 MPa, T_{mean}=1013±17°C). Magma contributions from this intermediate reservoir are restricted to >6000 b2k when the Lonquimay plumbing system was in a regime of short repose times; disappearance of the intermediate reservoir coincides with the change to longer repose times between eruptions.

2.2 INTRODUCTION

Volcanism is affected by tectonic conditions in many ways. Crustal tectonic faults control the position of volcanoes (e.g. Hill, 1977; Kienle et al., 1980; Freundt et al., 2010) and regional earthquakes apparently have the capacity to trigger volcanic eruptive activity (La Femina et al., 2004; Lara et al., 2006b). Orientation and magnitude of tectonic stress associated with fault systems particularly control magma plumbing dynamics, that is the ascent, storage and eruption of magmas (e.g. Watanabe et al., 1999; Lara et al., 2006a; Lara et al., 2006b; Gevrek and Kazanci, 2000). For example, magma withdrawal along active faults of different stress orientation has tapped reservoirs of different composition and depth during the Etna 2001-2003 eruptions (Monaco et al., 2005). Bimodal volcanism in the central Andes is closely linked to the orientation and kinematics of regional faults (Petrinovic et al., 2006). Valentine and Perry (2007) suggested that time-predictability may be a fundamental property of volcanism controlled by regional tectonic strain.

Time predictions of future activity using statistical analysis are typically based on historic eruption records because these provide the most precise time resolution (e.g. Hill et al., 1998; Dzierma and Wehrmann, 2010a). Applying such methods to prehistoric, geologic eruption records (e.g. Jones et al., 1999) involves greater uncertainties arising from errors in radiometric ages, the necessity to estimate ages of undated eruptions, and the possibility that the record does not include all eruptions that occurred.

While some eruption records show fairly uniform behavior of volcanoes through their recorded history (e.g. Hill et al., 1998; Clark et al., 2006), erratic evolution at other volcanoes may be controlled by either inherent changes in the magmatic system (such as changing magma production conditions at depth) or by external forcing (such as changing tectonic strain). Tectonic influence on volcanism is commonly implied from observed spatial correlations between tectonic and volcanic structures but may also be inferred from the pattern of temporal evolution of a volcano.

Here, we revise and extend earlier work to establish a detailed, well age-constrained tephrostratigraphy of Lonquimay Volcanic Complex, Southern Chile, which lies on the Liquiñe-Ofqui Fault Zone. We obtain a time series of explosive eruptions and intervening repose times that reveals two successive regimes of different eruption frequencies that correlate with changes in the plumbing system inferred from geochemical and thermobarometric results. We discuss the rather sudden change in plumbing conditions as a result of a tectonic event, and we investigate the implications for the probabilistic estimation of future explosive activity at Lonquimay.

2.2.1 Geological setting of the Lonquimay Volcanic Complex

The Quaternary Southern Volcanic Zone of the Andes (SVZ) is a result of the north-eastward subduction of the 0-45 Ma old oceanic Nazca plate beneath the continental South American plate. The Northern end of the SVZ (33°S) coincides with the location of the subducted Juan Fernandez Ridge under the continental margin at 32°S, while the Chile Rise triple junction at 46.2°S marks the Southern end of the SVZ. Oblique convergence (22-30° NE) between the Chile Triple Junction and the Copahue volcano at 38°S (Rosenau et al., 2006) causes dextral slip along the arc-parallel (~10° NE) Liquiñe-Ofqui Fault Zone (Arancibia et al., 1999; Cembrano et al., 2000; Lavenu and Cembrano, 1999). This right lateral strike slip system controls the architecture of the intra-arc region and thus the location of many of the larger volcanic centers as well as smaller monogenetic cones in the Central (CSVZ) and Southern (SSVZ) Volcanic Zones (López-Escobar et al., 1995; Cembrano and Lara, 2009). The thickness of the continental crust continually decreases from 55-60 km in the NSVZ to only 30-35 km South of 37°S below the CSVZ and SSVZ (Lowrie and Hey, 1981).

The Lonquimay Volcanic Complex (LVC, 38°22'S-71°35'W) is part of the volcanic front of the Quaternary CSVZ (López-Escobar et al., 1995; Hildreth and Moorbath, 1988; López-Escobar et al., 1993; Stern, 2004; Tormey et al., 1991) and is of Late Pleistocene to Holocene age. The principal stratocone - the Volcán Lonquimay - is accompanied by several adjacent eruptive centers that are aligned along two fissure zones (Moreno Roa and Gardeweg, 1989) and thus seem to be controlled by regional tectonics. The shape of Lonquimay's truncated stratocone is slightly elongated in WSW-ENE direction and elevates up to 2865 m asl and approximately 1420 m above its base (Völker et al., 2011). Estimates of the edifice volume range from $Vol_{edifice}$=22 km^3 up to Vol_{max}=106.5 km^3, the large uncertainty being caused by the difficult definition of a proper baseplane due to the high relief in this area (Völker et al., 2011). These dimensions show that Lonquimay's edifice is quite small compared to other SVZ volcanoes. Its small size can mainly be attributed to its adolescent state of postglacial evolution that is inferred from the absence of any traces of glacial erosion (Völker et al., 2011). The oldest magmatic products dated so far do not exceed 10200±70 a BP (Polanco 1998).

Lonquimay's nearest volcanic neighbors are Tolhuaca to the Northwest and Llaima in the South. The distance to Llaima is 36.5 km, the volcano Tolhuaca is situated 6.5 km NNW of Lonquimay. The glacially eroded surface attests Tolhuaca's older (pre-glacial) age and contrasts with the smooth, younger postglacial surface of Lonquimay. The volcanic activity of basaltic-andesitic Tolhuaca during historical time is limited to fumarolic activity around its summit (Moreno Roa and Gardeweg, 1989) and rare, spatially limited deposits of small Holocene

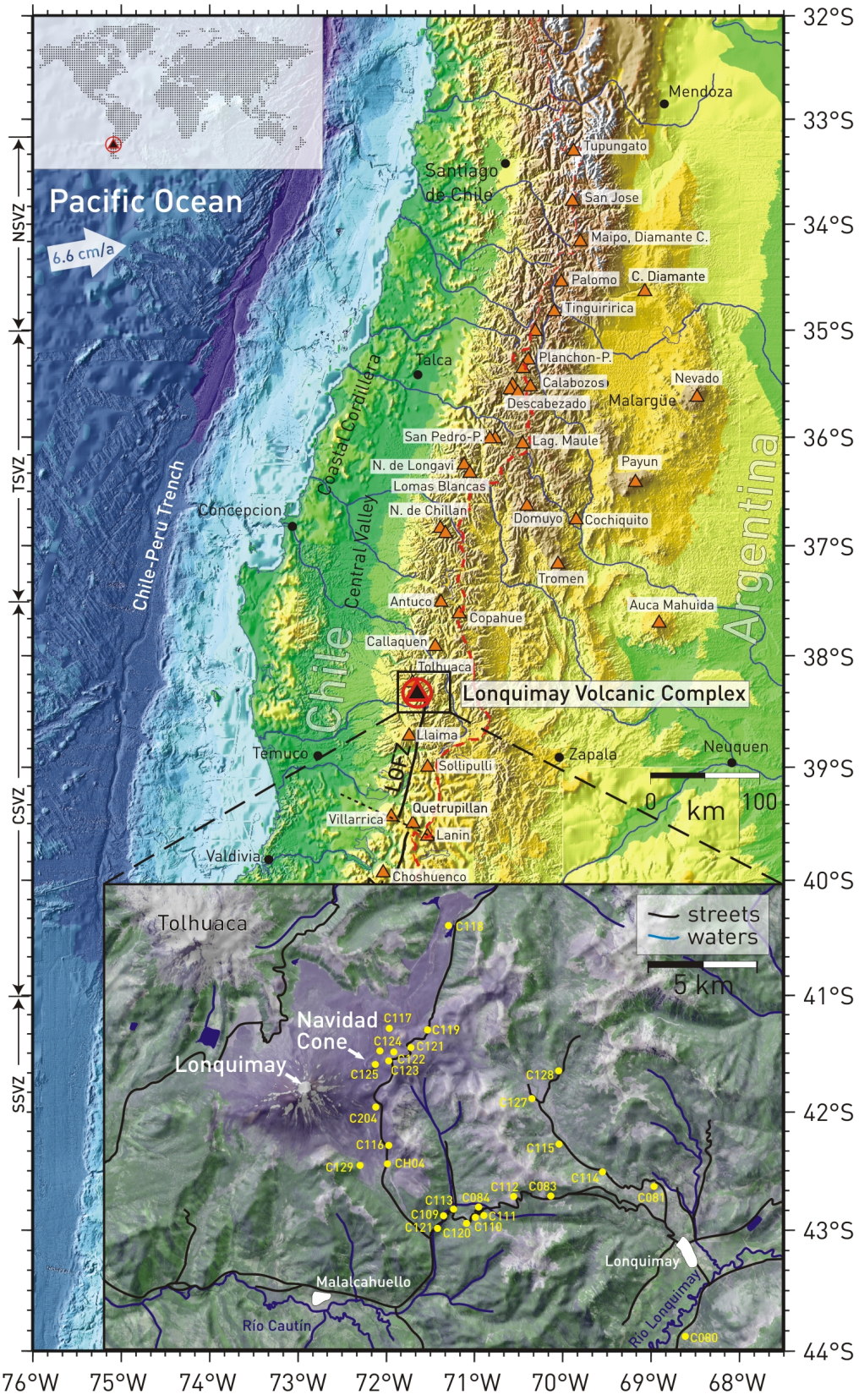

Fig. 2.1 Overview map (data from GINA, Lindquist et al., 2004) of the Southern Volcanic Zone (SVZ) emphasizing the location of the Lonquimay Volcanic Complex. Based on petrographic, geochemical and tectonic observations the SVZ has been further subdivided into four domains: the Northern (NSVZ; 33°-34°30'S), Transitional (TSVZ; 34°30'-37°S), Central (CSVZ; 37°-41°30'S), and Southern (SSVZ; 41°30'-46°S) Volcanic Zones. The Inset map shows the location of logged outcrops downwind from the volcano. LOFZ=Liquiñe-Ofqui Fault Zone.

explosive eruptions (Polanco, 1998). Seismological investigations of Barrientos and Acevedo-Aránguiz (1992) during the last eruptive period of LVC indicate that the magmatic systems ofLonquimay and Tolhuaca are distinct from each other despite their spatial vicinity. This is further supported by observation of distinct differentiation paths for Tolhuaca and LVC samples (Vergara Sáez, 2010).

The morphology of the LVC is apparently affected by regional tectonics (Polanco, 1998; Polanco, 2010; Vergara-Sáez, 2010; Moreno and Gardeweg, 1989; Fig. 2.2). The location of the eruptive centers in the area of Tolhuaca and Lonquimay is controlled by four tectonic lineaments (Fig. 2). A NW-SE trending fault zone defined by the volcanoes Lonquimay and Tolhuaca and some smaller eruptive centers (two craters and three cinder cones) extends into the valley of the Rio Colorado and is accompanied by a 20° NNE directed lineament that is well-defined by the valley of Rio Lolthe. Additionally, two (sub-)parallel fault zones are documented by 60-70° NE aligned eruptive centers. A lineament is formed by four independent intermediate-sized cones (Fig. 2.1) and a Southern, WSW-ENE striking, fissure zone (Cordón Fissural Oriental) extends east- and westward from the main stratocone of Lonquimay. East of the main edifice, the Cordón Fissural Oriental is an alignment of approximately twelve cinder cones, craters and domes straddling over a distance of 8-10 km. At the Western flank of Lonquimay stratocone, the Cordón Fissural Oriental is marked by an alignment of several flank vents and collapse structures.

The eruptive history of the LVC shows both, explosive and effusive activity, covering a range of magmatic compositions from basaltic andesite to dacite (Polanco, 1998; Vergara Sáez, 2010). Historic eruptive activity of the LVC was recorded 1853, 1887-1890, 1936, 1940, and 1988-1990. The 1887-1890 eruption produced two andesitic lava flows originating from two eruptive sites along the Cordon Fissural Oriental (Naranjo et al., 1992). The 1988-1990 strombolian "Navidad"-eruption discharged two andesitic lava flows (VEI=3; 58 wt% SiO_2; Moreno Roa and Gardeweg, 1989) and a widespread tephra blanket. Polanco, (1998) presented a first investigation of the tephrostratigraphy of the prehistoric deposits of LVC. He proposed a total of 24 stratigraphic units organized in two sequences: "Sequença Piroclastíca Inferior" and "Sequença Piroclastíca Superior" that are separated by a widespread paleosol horizon.

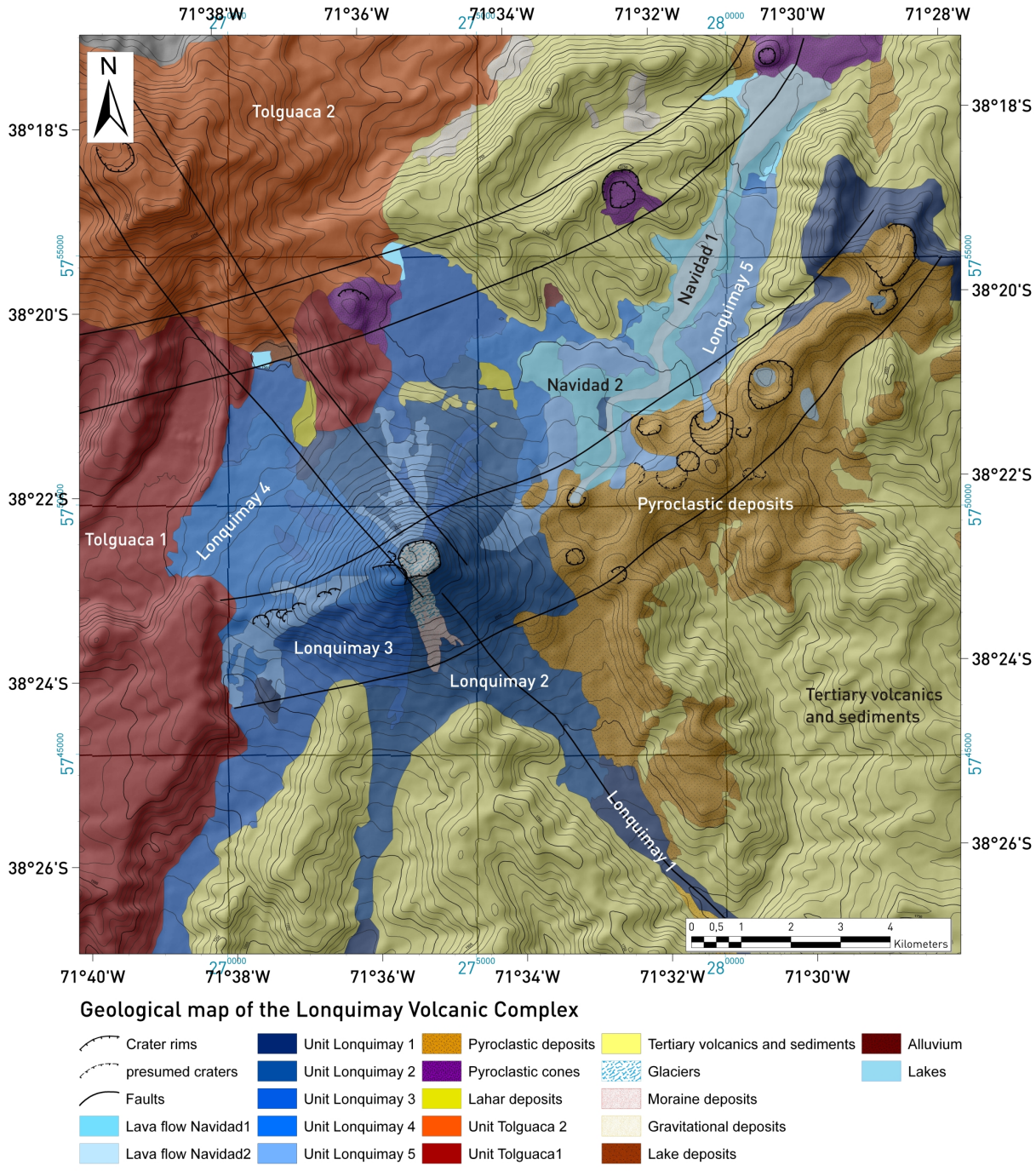

Fig. 2.2 Geological map of the Lonquimay Volcanic complex based on previous work of Moreno Roa and Gardeweg (1989), remote sensing using ASTER satellite data and own field observations. The Lonquimay and Tolhuaca units represent lava flow units. Black lines outline fault zones invoked from volcanic vent alignments.

2.3 METHODS AND APPROACHES

During our field work we reinvestigated and complemented the LVC tephrostratigraphy as originally established by Polanco (1998) by detailed logging of 25 outcrops and collecting 135 stratigraphically controlled samples. We focused on the identification, characterization, and correlation of pyroclastic fallout deposits in order to establish a general tephrostratigraphy for the LVC. Our field correlations are based upon modal compositions and textures of the pumice clasts, sedimentary structures of the deposits, relative stratigraphic position, and the occurrence of unconformities and soil horizons. The correlations are supported by radiometric ages (^{14}C-dating), including thirteen new radiocarbon ages, and by chemical compositions of matrix glasses, phenocrysts and juvenile bulk rock samples. The resulting LVC tephrostratigraphy comprises 23 stratigraphic units (Units A-W), and provides a framework for ongoing investigations of the petrogenetic evolution of the LVC. A detailed composite stratigraphic column including interpreted pictures of every unit is available as electronic supplement (Appendix A).

2.3.1 Radiocarbon dating

Thirteen stratigraphically collected samples of charcoal were analyzed for their radiocarbon ages at the Leibniz Laboratory for Radiometric Dating and Isotope Research at the University of Kiel. Chosen samples were visually checked for pollutants, mechanically cleaned under a microscope, and a suitable amount of charcoal was extracted from the sample. Conventional ^{14}C-ages were calculated following the procedures described by Stuiver and Polach, (1977). The isotopic fractionation was equalized with δ^{13}C based on ^{13}C/^{12}C- and ^{14}C/^{12}C-ratios simultaneously measured with an Accelerator Mass Spectrometer (AMS). Apart from the analytical uncertainty (statistics, instability of the AMS-system, and uncertainty of the subtracted background) possible contamination (meteoric water or reworking of older material) adds some uncertainty to the dating results. The radiometric ages were converted to calibrated ages using the software Calib 6.01 (Stuiver and Reimer, 1993). Southern hemisphere correction was applied according to McCormac et al (2004). Our new ^{14}C-ages and errors, as well as the resulting calibrated ages, and interpolated age estimates are given in Tab. 1 and Fig. 3. In the following, calibrated ages are rounded to five year intervals and reported as years before 2000 (b2k).

Tab. 2.1 (next page) Age dating for LVC stratigraphic units. *=radiometric age from Polanco (1998); ^=Navidad eruption 1988-1990; ^{14}C=radiocarbon; ip=interpolated; hr=historic record.

stratigraphic sequence	Unit	Sample#	dating method	Sample type	sample weight [mg C]	depth below surface [m]	Date ^{14}C [a BP]	Error [2σ]	Date interpolated [a BP]	Error	Date calibrated [years b2k]	PMC (corrected)	Error [2σ]	δ^{13}C [‰]	Error [2σ]	Lab#	Sample location UTM Zone 19 H E	Sample location UTM Zone 19 H N
ULS	W		hr^				1988 AD	±1			12							
	V	C-521	^{14}C	charcoal	5.10	1.50	365	± 25			435	95.55	± 0.27	-22.86	± 0.11	KIA43960	282147	5742537
	U	BB-15M★	^{14}C	charcoal			1430★	± 70			1300							
			ip						1485	± 1120								
	T	C-505	^{14}C	charcoal	4.00	0.80	2620	± 25			2685	72.15	± 0.21	-24.62	± 0.11	KIA42458	282147	5742537
	S	C-504	^{14}C	charcoal	4.10	1.20	2590	± 20			2690	72.43	± 0.18	-23.68	± 0.09	KIA42457	282147	5742537
	R	C-520	^{14}C	charcoal	4.70	1.00	3990	± 25			4410	60.86	± 0.19	-24.8	± 0.13	KIA42459	282147	5742537
	Q	C-373	^{14}C	charcoal	3.10	1.50	5085	± 25			5845	53.1	± 0.17	-24.98	± 0.09	KIA42453	282848	5742781
MLS	P		ip						5140	± 25	5900							
	O		ip						5190	± 25	5950							
	N	C-527	^{14}C	charcoal	4.30	5.00	5245	± 30			6005	52.06	± 0.18	-24.52	± 0.14	KIA43961	282147	5742537
	M	C-395	^{14}C	charcoal	3.20	2.50	5830	± 30			6600	48.41	± 0.17	-25.32	± 0.19	KIA42456	281492	5742917
	L	C-393	^{14}C	charcoal	3.30	3.00	6205	± 30			7125	46.2	± 0.18	-24.62	± 0.09	KIA42455	281492	5742917
	K		ip						6740	± 540	7635							
LLS	J	C-391	^{14}C	charcoal	3.60	3.00	7310	± 30			8140	40.25	± 0.16	-25.81	± 0.17	KIA43958	281492	5742917
	I	C-201	^{14}C	charcoal	0.55	4.00	7230	± 65			8175	40.67	± 0.32	-24.58	± 0.10	KIA41188	282656	5743080
	H	C_390	^{14}C	charcoal	5.10	3.50	7630	± 30			8440	36.68	± 0.15	-28.47	± 0.12	KIA43957	282568	5742788
	G	C-532	^{14}C	charcoal	4.70	4.00	8240	± 40			9220	35.84	± 0.17	-23.78	± 0.10	KIA43962	282147	5742788
	F		ip						8525	± 140	9525							
	E	C-389	^{14}C	charcoal	3.10	3.00	8810	± 40			9830	33.39	± 0.17	-24.09	± 0.10	KIA42454	282568	5742788
	D		ip						9150	± 175	10320							
	C		ip						9500	± 175	10810							
	B		ip						9850	± 175	11300							
	A	BB-15A★	^{14}C	org mat			10200★	± 70			11795							

★=radiometric age from Polanco (1998)
^=Navidad eruption 1988-1990 AD

^{14}C=radiocarbon
ip=interpolated
hr=historic

2.3.2 Chemical analyses

Homogeneous glass pellets, molten from finely ground sample powders with lithium tetraborate as fluxing agent, were used for analyses with wavelength dispersive XRF spectrometers (Philips X´Unique PW 1480 XRF at the XRF lab at GEOMAR, Kiel; Panalytical MagixPro PW 2450 VR at the Institute of Mineralogy and Petrography at the University of Hamburg). Achieved typical uncertainties are less than 0.01 wt% for major (Si, Al, Na, Ca, K, Ti, Mg, Fe, Mn, and P) and <5 ppm for most trace elements (Ce, La <20 ppm; Co <15 ppm; Ba, Nd <10 ppm).

In addition to the bulk rock chemistry, a JEOL JXA 8200 wave length-dispersive Electron Probe Microanalyzer (EPM) was used to conduct spot analyses for major element compositions of glasses and minerals. In order to ensure significant analytic results, representative juvenile clasts were chosen from each tephra sample. The clasts were crushed, embedded in resin, polished, and analyzed with EPM. Each tephra field given in Fig. 2.5 is defined by >20 spot analyses for the felsic compositions. Matrix glass analyses of mafic rocks were harder to perform and sometimes simply not possible due to devitrification or microcrystalline matrix of the samples. Thus, mafic fields are defined by less analyses (n>5) or even lacking for some samples. But since mafic glasses of the samples show more distinct compositions, these smaller sampling batches are sufficient for characterization. We performed all of our EPM analyses for the matrix glasses with the following setup: 15 kV accelerating voltage; defocused beam (5 μm) to avoid analytical Na-loss (Hunt and Hill, 1993; Nielsen and Sigurdsson, 1981); probe current was 10 nA for mafic and 6 nA for felsic glasses. International natural and synthetic glass standards were used to ensure a proper calibration during analysis runs. The typical analytical error (relative standard deviation) is less than 0.5% for major (Si, Al, Na, Ca, K, Ti, Mg, and Fe) and <3% for minor elements (Mn and P). All analytical data presented in this work are normalized to anhydrous compositions unless otherwise stated. The electronic supplement (LVC data) contains matrix glass compositions used for tephra correlation. A complete data set of bulk rock, mineral and matrix glass analyses of LVC samples will be presented elsewhere.

2.4 TEPHROSTRATIGRAPHY

2.4.1 Stratigraphic results

The stratigraphic record of LVC's explosive activity is an alternating sequence of widespread well-sorted fallout layers, poorly sorted charcoal bearing tuffs, and locally confined deposits of pyroclastic density flows. We have defined 23 stratigraphic units (Unit A-W, Fig. 2.3).

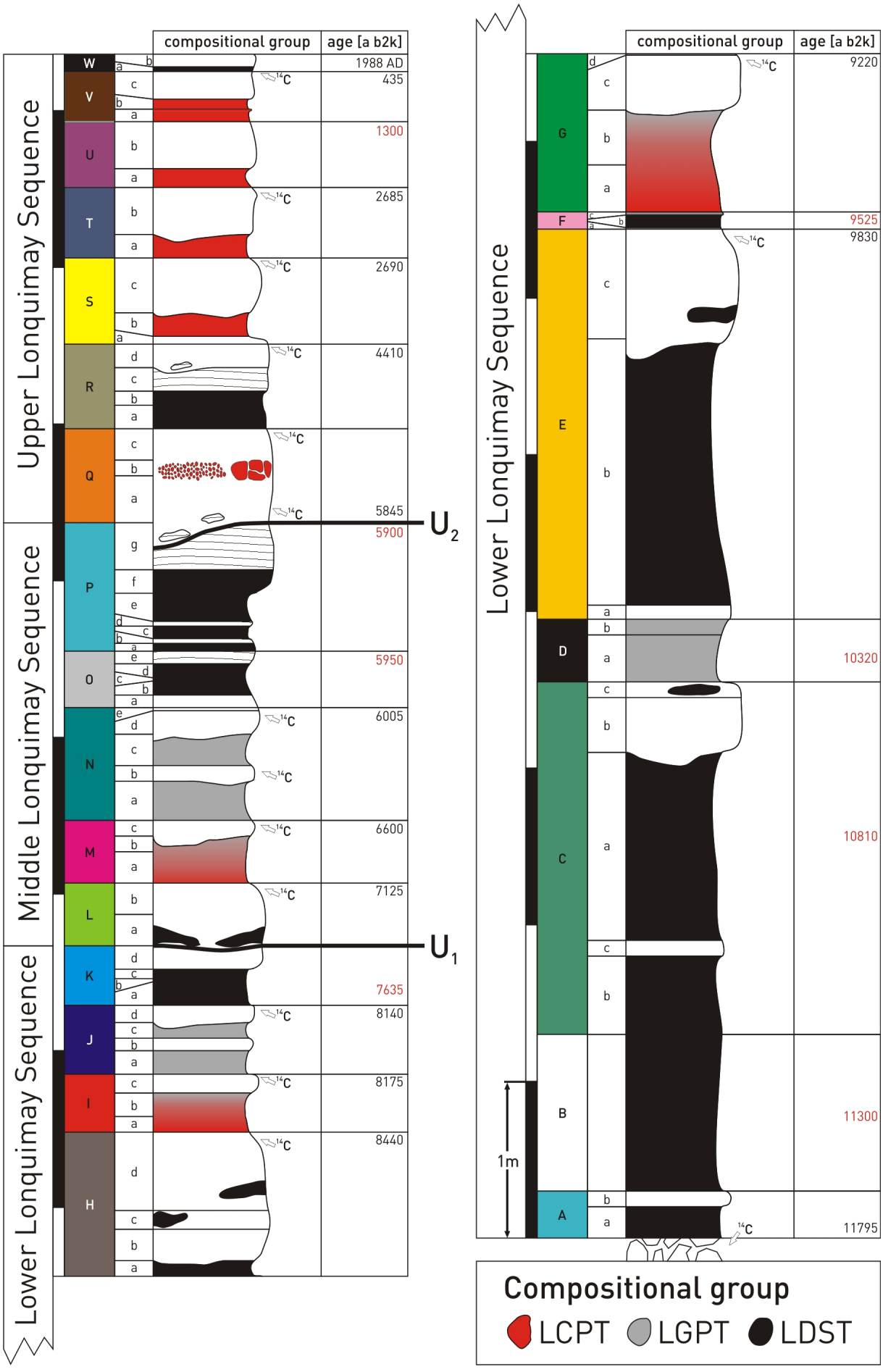
Upper Lonquimay Sequence
Middle Lonquimay Sequence
Lower Lonquimay Sequence
compositional group
age [a b2k]
W
V
U
T
S
R
Q
P
O
N
M
L
K
J
I
H
1988 AD
435
1300
2685
2690
4410
5845
5900
5950
6005
6600
7125
7635
8140
8175
8440
U2
U1
Lower Lonquimay Sequence
compositional group
age [a b2k]
G
F
E
D
C
B
A
9220
9525
9830
10320
10810
11300
11795
1m
Compositional group
LCPT
LGPT
LDST

Fig. 2.3 (previous page) Schematic composite column of the LVC stratigraphic succession with radiometric (black) and interpolated (red) ages. Two widespread unconformities (U1 & U2) divide the succession into Lower, Middle and Upper Lonquimay sequences. The color coding in the lithologic column marks the occurrence of the three petrographic groups throughout the stratigraphy. White deposits are tuffites intercalated between fallout deposits. Maximum thicknesses from several outcrops were used to compose this section. Note that deposits compositionally zoned from colored to grey pumice are restricted to deposits older than 6600 b2k. A more detailed profile is available in Appendix A.1.

Fig. 2.4 A) Interpreted photographs of outcrops C110 and C113. Outcrop C113 records LVC's eruptive history since 8175 b2k, whereas C110 documents the lowermost units (A-I) of the LVC-tephrostratigraphy. Stratigraphic units are marked as annotations. Note the prominent erosional unconformity that divides the Middle and Upper Lonquimay Sequences (turquois line). The unconformity that defines the boundary between Lower- and Middle Lonquimay Sequence (light blue line) is less prominent but marked as a paleosol horizon in almost all logged outcrops. B) Photographs of representative tephra beds defining the petrographic groups.

Most units are built up by a well-sorted basal pyroclastic fallout deposit, overlain by a poorly sorted tuff. In some cases such tuff contains juvenile clasts of the same composition as the underlying fallout and may be thin overbank facies of pyroclastic flow deposits (Polanco, 2010). However, most of these tuffs contain a heterogeneous population of volcanic clasts, all occur high on steep paleo-slopes, and there is little evidence for valley-filling pyroclastic flow deposits in this area.

Therefore, a pyroclastic flow origin seems unlikely in most cases despite the presence of charcoal fragments. The radiometric ages (Tab. 2.1) obtained from that charcoal (Fig. 2.3) constrain a minimum age of the respective underlying fallout deposits.

Two regional unconformities split the LVC stratigraphic succession into a Lower (LLS, Units A-K), Middle (MLS, Units L-P), and Upper Lonquimay Sequence (ULS, Units Q-W). LLS and MLS are separated by an unconformity (U1 in Fig. 2.3) with a widely distributed paleosol horizon at the top of Unit K. This originally grey massive medium-ash tuff contains sandy brown lenses of fine to medium lapilli and has a purple, slightly stratified base, followed by incipient soil transformation, whereas it's paleosol top shows traces of root penetration. MLS and ULS are divided by a widespread erosional unconformity that cuts variably deep into the underlying deposits, reaching the largest depths on lower valley walls (Fig. 2.4). This indicates that present valleys, which pre-existed during the LVC eruptions as evidenced by mantling fallout beds, experienced a phase of particularly strong erosion at around 5900 b2k (Fig. 2.4) prior to emplacement of Unit Q, which covers the unconformity.

2.4.2 Matrix glass compositions

The different tephra units of our stratigraphic succession have distinct major element compositions of matrix glasses. This allows us to use them as a tool to verify and refine field-based correlations between outcrops. Diagrams of K_2O/TiO_2 versus SiO_2 (Fig. 5) are most useful to distinguish between different units and correlate tephras of different, partly well established, stratigraphic successions with each other. In general, the diagrams show similar characteristics for ULS, MLS, and LLS in which felsic compositions show a wider scatter than mafic ones. Although a number of compositional fields are equivocal (e.g. Units U, T, and V in Fig. 2.5), these diagrams are valuable in combination with stratigraphic relations from fieldwork. In fact, this chemical ambiguity shows the importance of a proper field based correlation to establish the overall tephrostratigraphy for this particular volcanic center.

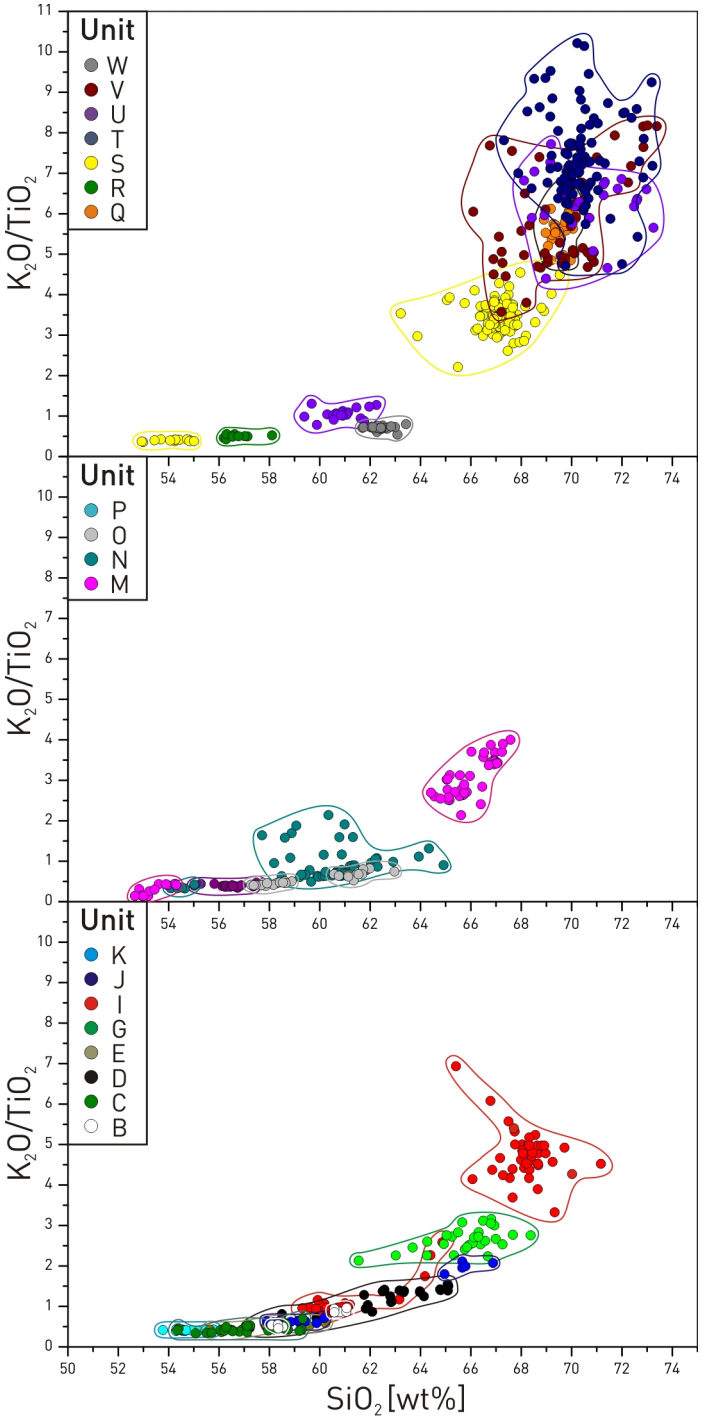

Fig. 2.5 K_2O/TiO_2 variation diagrams of juvenile-clast matrix glasses of LVC-units, for clarity shown separately for stratigraphic members. Color coding of units according to Figs. 2.3 and 2.4.

2.4.3 Time constraints

The dated tephras range in age between 9830 and 435 b2k (Tab. 2.1). The succession of radiometric ages generally agrees with the observed stratigraphic order. However, for the two pairs

of Units I+J and S+T the respective underlying tephra gave a slightly younger age than the overlying deposit although, in both cases, the radiometric ages overlap within analytical errors, suggesting that the respective deposits/units were emplaced during a time interval shorter than the ^{14}C-error range; it is also possible that unit pairs I+J and S+T each are the product of one multi-episodic eruption.

Statistical time series analyses demand for discrete events. Therefore, ages of fallout tephras that could not be radiometrically dated but represent distinct eruption events were approximated by equidistant linear interpolation between the bracketing ^{14}C-ages of the over- and underlying horizons (see Tab. 2.1). Naturally, this should be taken as an approximation, because the error may be as large as half the time span between the bracketing ^{14}C-ages.

In order to obtain age estimates for the stratigraphic units (Units A-D) older than 9830 b2k we used the oldest age (11795 b2k) from Polanco (1998) as the lower bracket for a linear interpolation. Polanco (1998) reported that the soil horizon rich in organic matter used for this dating was collected between fluvioglacial bedrock deposits and the oldest tephra deposit, giving a maximum age for the onset of LVC's post-glacial explosive activity.

2.4.4 Petrographic groups

The pyroclastic products of the LVC show a wide diversity in composition (Figs. 2.5 and 2.6) and thus appearance. In order to simplify descriptions and discussions, we divide the fallout tephras of the Lonquimay stratigraphic succession into three distinct petrographic groups based on the macroscopic and microscopic textures of the juvenile clasts, chemical compositions, and bed structures: 1) Dark grey to black scoria tephra, 2) grey pumice tephra, and 3) light colored pumice tephra. Detailed petrographic descriptions are reported in supplementary material Tab. A.2.

1) Lonquimay dark scoria tephras (LDST)

The well-sorted fallout deposits of basaltic andesitic dark juvenile clasts (Fig. 2.6; SiO_2: 52.67 to 55.27 wt%) occur throughout the LVC stratigraphic succession (11 fallout layers; Units: A, B, C, E, F, H, K, O, P, R, and W). However, those in the lower part of the LLS (Units A, B, C, E, and F) are dominated by slightly stratified and well-sorted deposits composed of black, microvesicular to dense juvenile clasts (Fig. 2.7d). Although the lithic contents of these layers are moderate to low, the dense texture indicates a phreatomagmatically influenced eruption mechanism. In contrast, deposits younger than 6000 b2k (Units O, P, R, and W) contain scoriae with higher vesicularity and commonly have grain sizes of coarse ash to fine lapilli (Fig. 2.7c); only units P and R reach medium-lapilli grain size in the exposed area.

The dense to microvesicular, black juvenile clasts of units A, B, C, E, and F show a porphyritic to glomerophyric rock texture. The matrix is mainly microcrystalline with minor hyaline domains (Fig. 2.8d), and exhibits some aligned microlites (plag, ol, and cpx) and devitrification products. The phenocryst assemblage comprises (in order of frequency): plagioclase (plag), clinopyroxene (cpx), olivine (ol), titanomagnetite (ti-mt), and ilmenite (ilm). The Fe-Ti-oxides commonly appear as intergrowths with mainly ol and cpx, only subordinately with plag crystals. Moreover, some clasts contain cumulate fragments composed of intergrown plag, ol, and Fe-Ti-oxide crystals (Fig. 2.8c1).

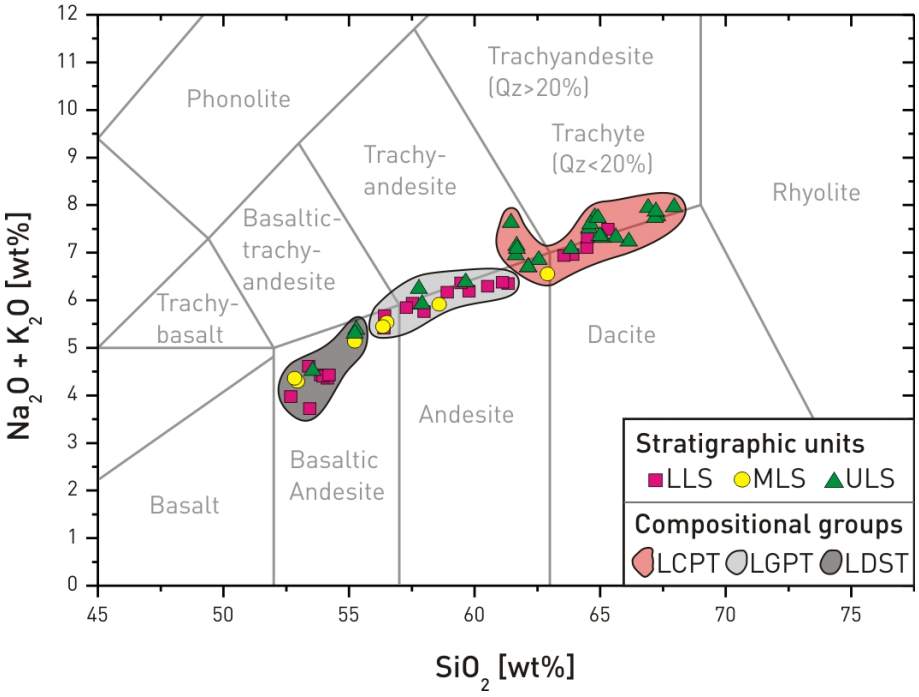

Fig. 2.6 Total alkali versus silica classification diagram after Le Bas et al., (1986) for LVC bulk-rock compositions. LDST, LGPT, and LCPT groups differ by their basaltic-andesitic, andesitic, and dacitic compositions.

The majority of the scoria clasts of Units H, K, O, P, R, and W have a moderate to high vesicularity with larger elongated bubbles (Fig. 2.8c); but some clasts with smaller microvesicular texture exist as well. The prevailing rock texture can be characterized as vitrophyric to glomerophyric. The matrix is partly vitreous, partly microcrystalline with microlites (plag, ol, and ti-mt) and devitrification products especially towards the rims. The lithic contents of these scoria layers account for about 5-10% and comprise colored and grey pumices, as well as dense lava fragments. A significant fraction of lithics and vitreous scoria clasts are hydrothermally altered and brownish weathered. Especially scoria clasts, overlying fine-ash beds (e.g. Unit K), show a yellow-brownish weathered alteration rim, probably related to the ash beds blocking downward percolating ground water. The phenocryst assemblage comprises (in order of frequency): pl, ol, cpx, ti-mt, and accessory hematite (hem) and apatite (ap). Most plagioclase phenocrysts are fragmented and show sieve textures as signs of chemical disequilibrium (Fig. 2.8c2). Some scoria

clasts contain cumulate fragments (plag, cpx, ol, ti-mt, and ap; see Fig. 2.8c1) resembling those observed in the dense juvenile clasts of the stratigraphically lower units.

Next to pure LDST fallout deposits as described above, LDST compositions occur as scattered mafic clasts in several LCPT (Units M, S, U, and V) and LGPT (Units J and N) deposits throughout the whole stratigraphy, indicating that mafic injections into more evolved magmas were common.

The well-sorted, dark brown scoria fallout of Unit P is a useful marker horizon at the transition from MLS to ULS (Fig. 2.4) because it differs from the other scoria deposits by being composed of strata of unusually large grain-size (medium to coarse lapilli) and higher scoria vesicularity. Grey fine-ash layers separate the lapilli beds, with the thick stratified top ash layer being the most prominent. The lithic content of these scoria lapilli beds is very low (<2%).

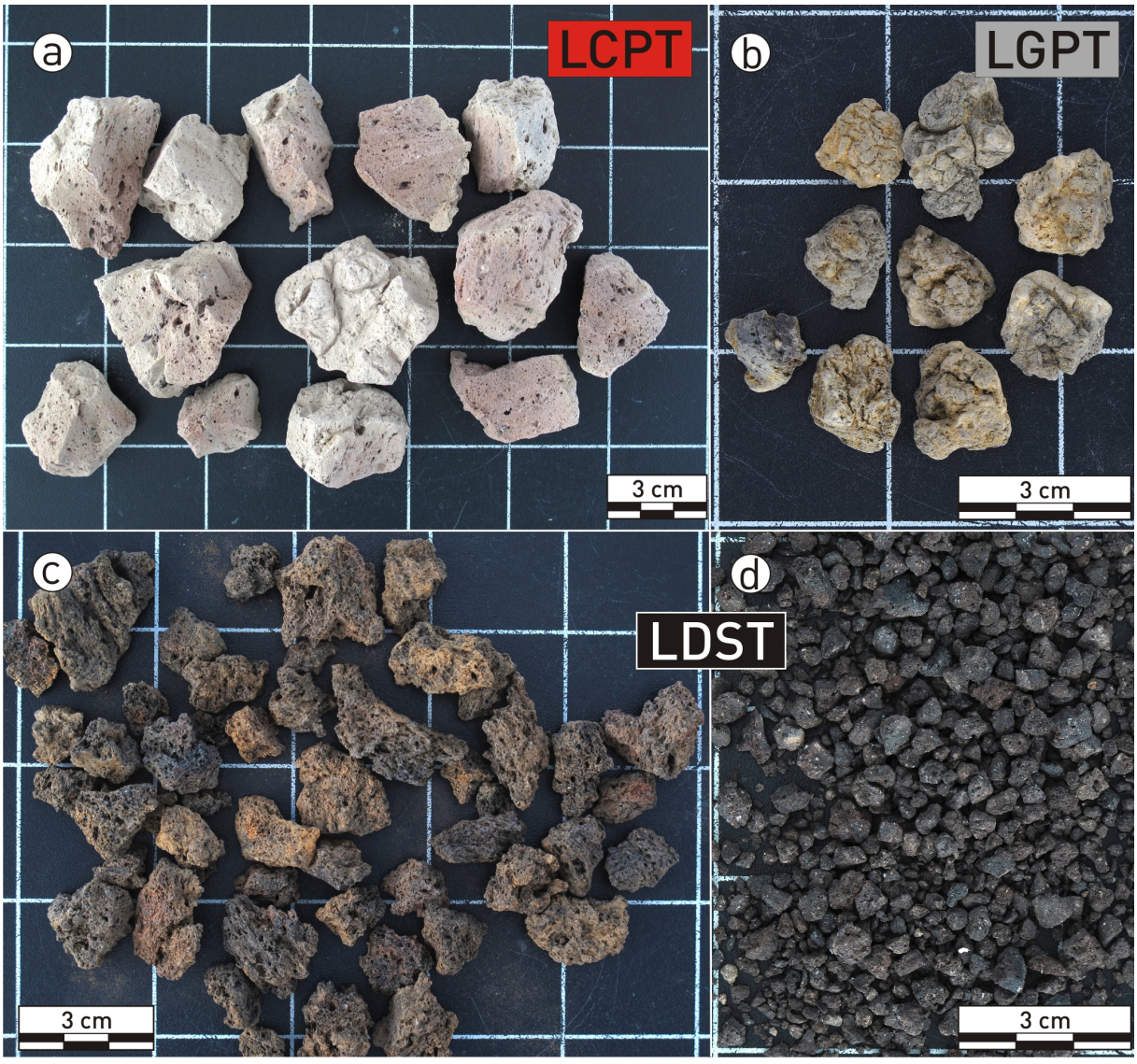

Fig. 2.7 Photographs of juvenile lapilli of the three petrographic groups of the LVC stratigraphic succession.

2) Lonquimay Grey Pumice Tephras (LGPT)

The stratigraphic record comprises six eruptive events that discharged grey pumice clasts: Layers Da, Gb, Ib, J, Mb, and N. Layers Da, J, and N are compositionally homogeneous fallouts of grey pumice clasts, whereas layers Gb, Ib, and Mb each form the grey-pumice upper part of compositionally zoned deposits composed of colored pumice at their base.

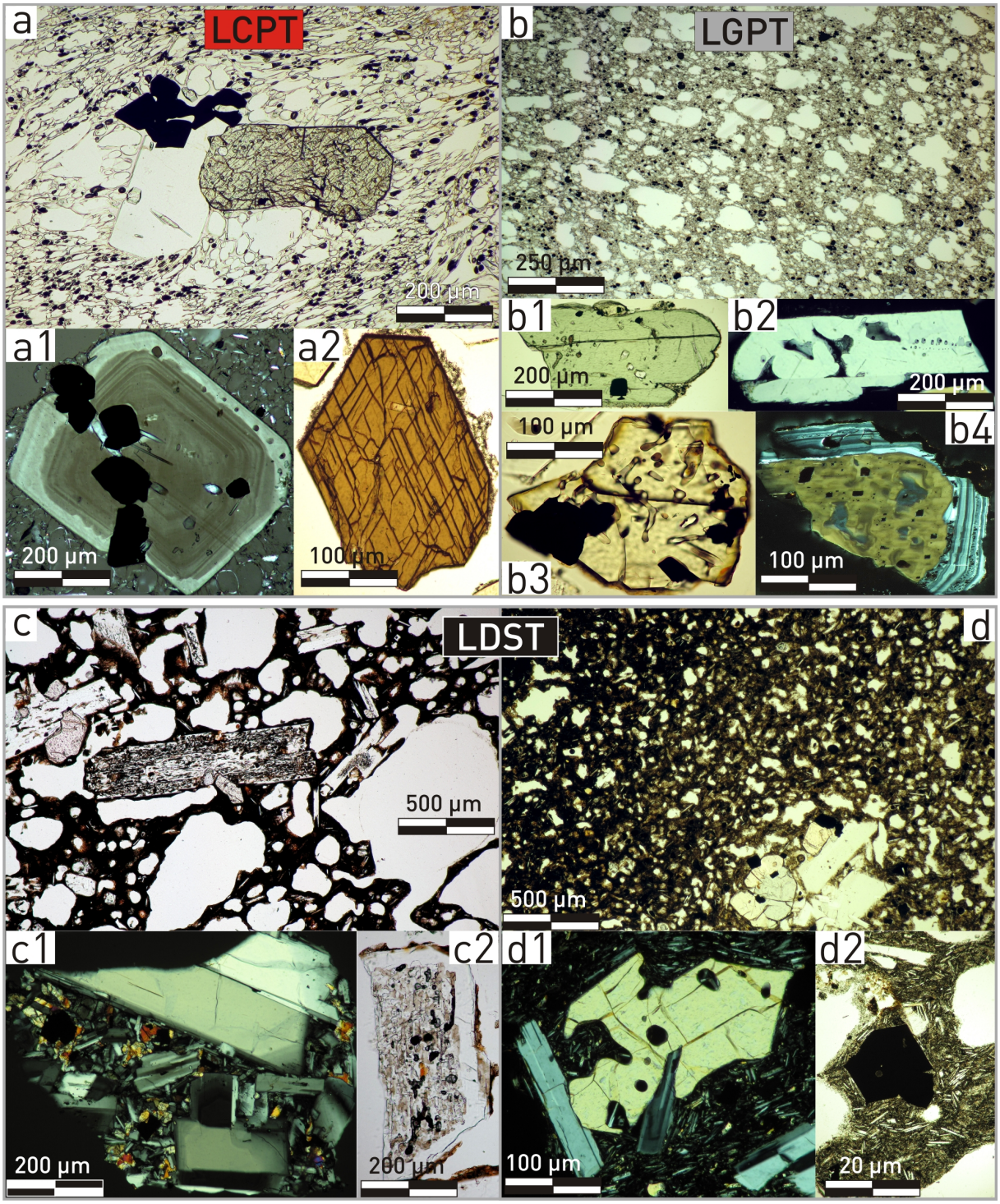

Fig. 2.8 (previous page) Photomicrographs of the three petrographic groups. LCPT: a) clinopyroxene, plagioclase, titanomagnetite cluster in pumiceous glass matrix with stretched vesicles. a1) zoned plagioclase with dissolution horizon covered by light colored rim contains inclusions of glass and titanomagnetite. a2) singular euhedral amphibole. LGPT: b) vesicle texture of grey pumice b1) cpx phenocryst with inclusions of apatite needles, ti-mt, and plag. b2) plagioclase with resorption embayments and melt inclusions. b3) olivine with resorption tubes intergrown with titanomagnetite. b4) resorbed plag core with intensely zoned overgrowth rim. LDST: c) texture of vesicular dark scoria with resorbed plag. c1) crystal cluster of plagioclase, clinopyroxene, olivine, and titanomagnetite. c2) plagioclase with strongly resorbed core covered by overgrowth rim. d) texture of poorly vesicular scoria with olivine, plagioclase, clinopyroxene, titanomagnetite cluster. d1) olivine with dissolution embayments intergrown with plagioclase. d2) singular euhedral titanomagnetite in microlite-rich matrix. Figs. a1, b2, b4, c1, d1 under crossed polarizers, all others in transmitted light.

Grey pumice clasts typically have a microvesicular to foamy texture (Fig. 2.8b), although some clasts have higher vesicularities with larger and more elongated vesicles. Several, especially larger, pumice fragments have a cracked surface (Fig. 2.7) resembling that of bread crust bombs. The bulk rock composition of grey pumice is andesitic to trachyandesitic with three samples plotting in the field of basaltic andesites (56.34 - 61.31 wt% SiO_2; Fig. 2.6).

The lithic contents of these fallout deposits are generally low (2-5%). The lithics are mainly hydrothermally altered, reddish, dense lava to foamy scoria clasts. The phenocryst parageneses comprise plag, cpx, ol, mt, ilm, ap, and hem (in order of frequency). Olivine crystals mostly have dissolution embayments indicative of disequilibrium with the melt (Fig. 2.8b3). Moreover, the grey pumice fallouts older than 6000 b2k (Layers Da, Gb, Ib, J, Mb, and N) contain significant amounts of euhedral amphibole (hbl) phenocrysts but comparably rare cpx-crystals.

3) Lonquimay Colored Pumice Tephras (LCPT)

The eight layers Ga, Ia, Ma, Q, Sb, Ta, Ua, and V are fallout deposits of colored pumice clasts that have more evolved, dacitic compositions (range in SiO_2: 61.43-67.91 wt%; Fig. 2.6). The medium to coarse pumice lapilli are typically light colored (beige, grey, reddish, violet), with an angular to subrounded shape. Some dispersed dark grey and banded pumice clasts occur in these deposits, too. Most of the colored pumice clasts have a high vesicularity with large and elongated vesicles (Figs. 2.7, 2.8a). However, some rather microvesicular colored clasts exist as well. The LCPT deposits can be further subdivided into two groups based on their depositional features: 1) Layers Ga, Ia, and Ma, all older than 6600 b2k, each form the basal parts of compositionally zoned deposits with grey pumice clasts at their top. 2) The colored-pumice deposits of the ULS (Units Q, S, T, U, and V, all younger than 5845 b2k) are compositionally homogeneous except for the subordinate occurrence of LDST components in Units S, U, and V.

Each of the compositionally zoned deposits starts with a massive, normally graded colored pumice lapilli layer at the base that gradually changes into grey pumice lapilli at its top (Gb, Ib, and Mb). The grey tops are slightly stratified; the most distinct stratification exists in Layer Mb (see Fig.

2.4A). In addition to the main component of eponymous colored pumices, minor grey and banded pumices do occur in the basal parts as well. Several grey pumice clasts in the colored-pumice-dominated lower part have bread crust-like surfaces indicating rapid cooling of these grey components (Fig. 2.7b). The colored pumice clasts host phenocrysts of plag, cpx, ol, hbl, mt, ilm, ap, and hem crystals (in order of abundance) which occur as scattered single crystals as well as mineral clusters (Fig. 2.8a). The Fe-Ti-oxides occur primarily as inclusions and intergrowths with ol- and cpx-crystals, and only rarely with plag (Fig. 2.8a1). Abundant ap is mostly included in ol, cpx, and plag. Most of the larger, oscillatory zoned plag phenocrysts are broken crystal fragments, sometimes preserved in a fitting position close to each other indicating in-situ fragmentation during the eruptive discharge. Amphibole crystals occur as fragments of euhedral to subhedral crystals only and are not intergrown with other mineral species (Fig. 2.8a2) suggesting they did not precipitate simultaneous with the other phenocryst phases.

The not compositionally zoned LCPT-layers of the ULS typically show similar phenocryst assemblages containing plag, cpx, ol, ilm, mt, ap, and hem-crystals (in order of frequency) as scattered single crystals (mostly fragments) and crystal clusters (Fig. 2.8a). These younger LCPT deposits do not contain amphibole (hbl). This contrasts with the older (>6000 b2k) compositionally zoned deposits, in which amphibole occurs in both the LCPT and the LGPT components.

2.5 ERUPTION TIME SERIES

In the following we investigate the LVC tephrochronology of explosive eruptive events by statistical methods in order to obtain a probabilistic eruption forecast. The purpose of this forecast is to contribute to the hazard assessment from explosive eruptions of the LVC.

2.5.1 Eruption Record

Probabilistic eruption forecast based on volcanic eruption histories has to handle two different types of data: "Historical" eruptions are usually defined as eruptions known from written or oral records. Eruptions of "geological magnitude" are typically referred to eruptive activity that can be reconstructed from volcanic deposits (e.g. Wehrmann and Dzierma, 2011). Typically, but not necessarily, these two types of eruption records cover different ranges of eruption magnitudes: the geologic record used here misses small explosive eruptions that failed to disperse tephra into the working area and near-vent lava effusion whereas the historic record of the LVC comprises such small events. Although we cannot determine specific values of magnitude or VEI (Newhall and Self, 1982) for the tephras studied here, a qualitative comparison of deposits from the geological

record with the 1988-1990 AD eruption (VEI=3) suggests that all tephras represent eruptions of VEI≥3. The historical eruptions of the LVC are reported by Naranjo et al. (1992) and Siebert and Simkin (2002). Wehrmann and Dzierma (2011) have shown that expanding the geological record with historical eruptive activity of similar magnitude performs similarly well as using the geological record alone. We included the historical events with filtering for VEI≥3 in our examined time series in order to add as much information about eruptive activity as available while conserving a valid data set. Nevertheless, we also investigated both datasets (geological and extended) independently for comparison. Henceforth, we use the terms "geological record" for tephrostratigraphically documented eruptions only and "extended record" for the combination of tephrostratigraphically and historically documented eruptions.

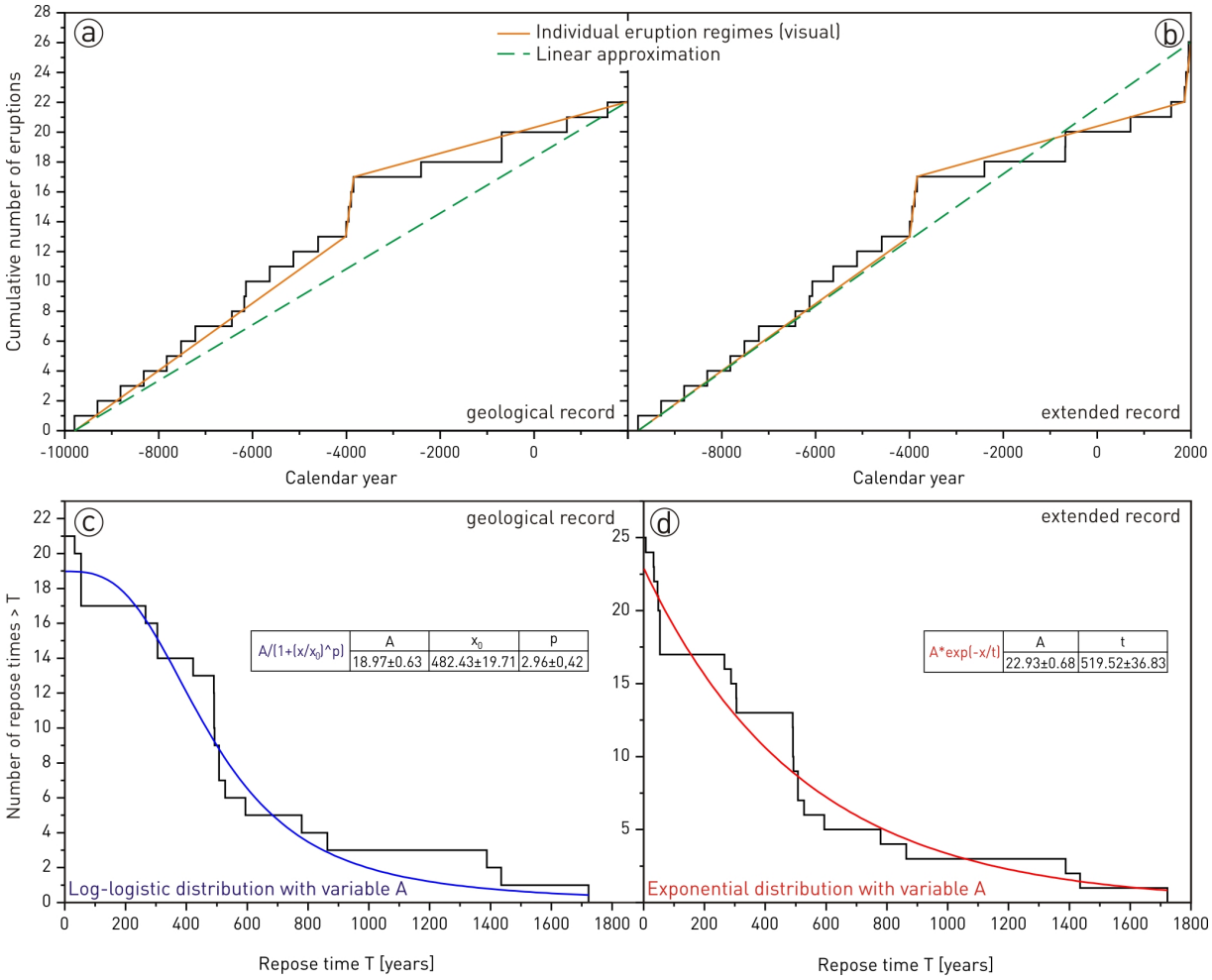

Fig. 2.9 a) Cumulative number of eruptions of a) geological record and b) extended record. Orange lines visually identify regimes of constant eruption rate; green dashed lines illustrate the constant eruption rate approximation to the total time interval. c) Repose time distribution of the geological record with its log-logistic distribution fit using variable scale factor A. d) Repose time distribution of the extended record with its exponential distribution fit using variable scale factor A.

2.5.2 Statistical analysis of eruption history

We use a similar procedure as described by Dzierma and Wehrmann (2010a) to assess the probability of future eruptions based on the tephrochronology presented in this work. The method is briefly outlined below (for more detailed information see Dzierma and Wehrmann, 2010a; 2010b; Wehrmann and Dzierma, 2011).

The repose times (Tab. 2.1 and Figs. 2.11b, 2.9a, b) inferred from the stratigraphic record can be described by several statistical distribution models that require to be applied to a stationary and independent data set. We performed tests for stationarity and independence according to Dzierma and Wehrmann (2010a). Extended and geologic records both satisfy the test for stationarity. The test for independence is passed after removal of the artificial diagonal elements caused by age determinations using equidistant interpolation.

As stationarity and independence were confirmed for the remaining events (see supplementary material Fig. A.1) we assume this holds true for the complete records as suggested by Wehrmann and Dzierma (2011). After fulfilling these prerequisites, both datasets were fitted with an exponential-, Weibull- and Log-logistic distribution each, applying the method of least squares fitting. We decided to use an approach with fixed and variable scale factor A, resulting in two fitting curves for each distribution and dataset. See Dzierma and Wehrmann (2010b) for a detailed discussion of this topic. All fit distributions pass the goodness of fit test at the 5% level (Kolmogorov-Smirnoff-Test, see supplementary Tab. A.3 for results). Based on the Akaike Information Criterion (AIC), we chose the best fitting distribution for each record from the six curves as suggested by Wehrmann and Dzierma (2011). The resulting parameters from fitting both data sets with the distribution functions are reported in supplementary material Tab. A.3.

The extended record is fitted best by an exponential distribution with variable A (Fig. 2.9d) whereas the geological record is best approached by a log-logistic distribution with variable A (Fig. 2.9c). The corresponding fitting parameters are given in the insets in Fig. 2.9c, d. Afterwards, the fitting parameters of the two best-fitting distributions were used to compute the probability of an eruption to occur within a given time interval as of 2011 for each dataset (Fig. 2.10).

The accumulation of events with time (Fig. 2.9a, b) suggests a change in slope at around 6000 b2k, which we will discuss further below in the context of changing magma-plumbing conditions. Therefore, we now perform a complementary statistical approach to determine eruption probability using the mixture of exponential distributions (MOED) as introduced by Mendoza-Rosas and De la Cruz-Reyna (2008; 2009). In contrast to the methods employed above, which assume stationarity, this method takes into account that eruption processes are possibly not stationary and result in different eruption regimes, i.e. time intervals each with roughly constant eruption rates. We determined these intervals visually from a plot of cumulative number of

eruptions vs. time (cf. Dzierma and Wehrmann, 2010a). In both the geological and extended records the regime prior to 6000 b2k is characterized by shorter repose times than that after 5845 b2k (Fig. 2.9a, b). The jump at 6000 b2k is an artifact of four fallout beds bracketed between dated tephras; the ages of these fallout beds have been interpolated but the geologic evidence is ambiguous to whether these really document four separate eruptions or possibly just four beds of a single, multi-episodic eruption. The historic eruptions from 1853 to 1988 in the extended record appear to define a period of higher eruption frequency. Thus there are three (geologic record) or four (extended record) eruption regimes which are used to determine the parameters of a matching mixture of exponential distributions following the procedure from Mendoza-Rosas and De la Cruz-Reyna (2008). Results are given in Tab. 2.2 and Fig. 2.10.

Regime	Start year [b2k]	End year [b2k]	Nr. erupt.	rate λi	weight wi
geological record					
1	5846	12	6	0.0010	0.2524
2	6005	5846	3	0.0188	0.4932
3	11794	6005	14	0.0024	0.2543
extended record					
1	146	12	4	0.0296	0.3295
2	5846	146	6	0.0011	0.1721
3	6005	5846	3	0.0188	0.3288
4	11794	6005	14	0.0024	0.1695

Tab. 2.2 Parameters for MOED of geological and extended record.

The curve for the log-logistic function based on the geological record leads to much higher probabilities than the exponential distribution for the extended record. The probability for a significant (VEI≥3) eruption within the next 100 years is 2.5 times higher (49% compared to 18%). Compared to the log-logistic fit of the geological record the MOED-approach results in overall lower hazard probabilities and approaches probabilities close to 100% relatively late. This late convergence is due to the fact that MOED, as a mixture of different exponential distributions, has a decreasing hazard rate (Marshall and Olkin, 2007). The MOED-fit for the extended record gives higher eruption probabilities for the near future and lower probabilities for the time larger 1500 years as of 2011. The diagrams and parameters for fit distributions and applicability tests as well as the probability curves not shown here are given as supplementary material Fig. A.1.

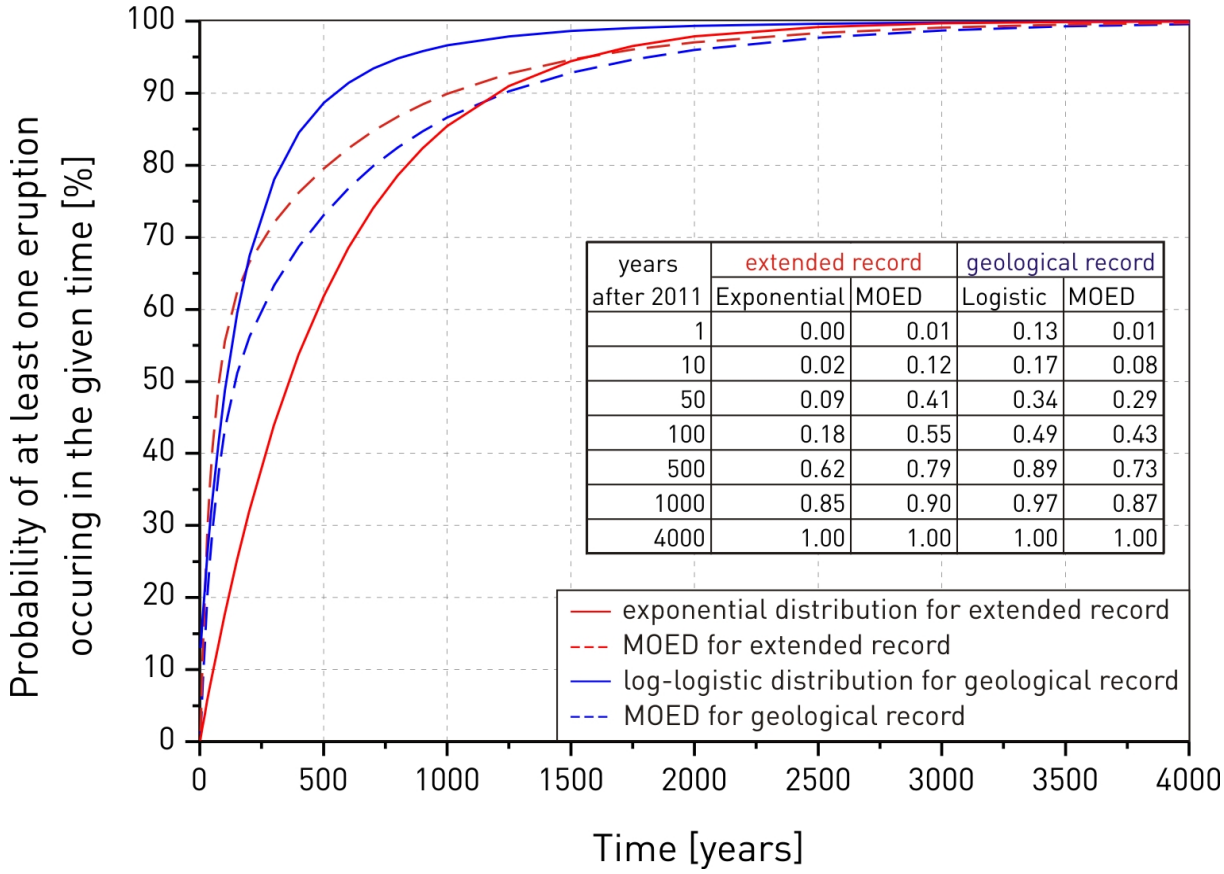

years after 2011	extended record		geological record	
	Exponential	MOED	Logistic	MOED
1	0.00	0.01	0.13	0.01
10	0.02	0.12	0.17	0.08
50	0.09	0.41	0.34	0.29
100	0.18	0.55	0.49	0.43
500	0.62	0.79	0.89	0.73
1000	0.85	0.90	0.97	0.87
4000	1.00	1.00	1.00	1.00

Fig. 2.10 Probabilities that at least one eruption (VEI≥3) will occur within a given time span as of 2011. The inset table lists probabilities as a function of time interval considered.

2.6 EVOLUTION OF THE PLUMBING SYSTEM

2.6.1 Repose time distribution

The repose time distribution (Fig. 2.9b) shows a distinctive dichotomy that corresponds with the systematic distribution of the petrographic groups and occurrence of amphiboles in the system. The lower part of the stratigraphy is dominated by quite uniform recurrence times between 200 and 800 years (RT_{mean}=417±169a) apparently without any coupling between repose time and erupted magma composition. In contrast, the upper part (<5845 b2k) of the stratigraphy is dominated by more evolved, dacitic LCPT deposits with subordinate intercalated mafic fallouts, and shows markedly longer repose times (RT_{mean}=1350±310a). The mafic layers are restricted to the base (Unit O (5950 b2k), P (5900 b2k), R (4410 b2k)), and uppermost top (Unit W (1988 AD)). The vesicular scoria clasts from these intercalated LDST-layers differ notably from the dense juvenile clasts of older LDST-layers. The relatively large grain size, high vesicularity (see Fig. 2.7c), and the thickness of the mafic fallout layers suggest different, more highly explosive and larger-magnitude, eruptions compared to the dense, juvenile clasts from LLS that are associated with eruptions of significantly shorter repose times. Thus, the mafic fallouts of Units O, P, and R appear to have formed by eruptions dynamically similar to those of the more evolved LCPT deposits (Units S, T, U, and V). The remarkable shift of the magmatic system at 6000 b2k from shorter to longer repose periods (see Fig. 2.9b) coincides with the transition from hbl-bearing LCPT and LGPT (Units D, G, I, J, M, and N) to hbl-free LCPT and LGPT (Units Q, S, T, U, and V) in the younger deposits.

2.6.2 Degree of differentiation over time

Potassium behaved as an incompatible element during differentiation of the LVC magmas. Therefore, a plot of K_2O vs. age can be used to visualize the course of the degree of differentiation in the stratigraphic record. The reasons for stratigraphic changes in K_2O-contents may be manifold: e.g. tapping of either mafic or felsic magma bodies, mafic replenishment of the system, and differentiation of the residual magma. The petrographic groups described above differ in their degree of differentiation (Fig. 2.6) and thus can be distinguished by their K_2O contents. The stratigraphic record (Fig. 2.3) shows that LDST-deposits dominate at the base and homogenous LCPT-deposits dominate at the top of the stratigraphic profile. LGPT-layers are restricted to

before 6000 b2k where they occur as individual layers as well as forming part of compositionally zoned tephras with LCPT-layers.

The plot of K_2O vs. age (Fig. 2.11a) shows six major events of tapping of mafic magma batches typically followed by eruptions of more evolved compositions. In the LLS and lower MLS, the latter are either LGPT tephras or, in three cases, compositionally zoned deposits (LCPT+LGPT). In contrast, the more evolved tephras in the ULS all have LCPT compositions. Upward through the entire LVC record, the maximum K_2O contents in both mafic LDST and felsic LCPT increase, indicating a general trend to reach higher degrees of differentiation of both magma types that may be related to the longer repose times after 6000 b2k.

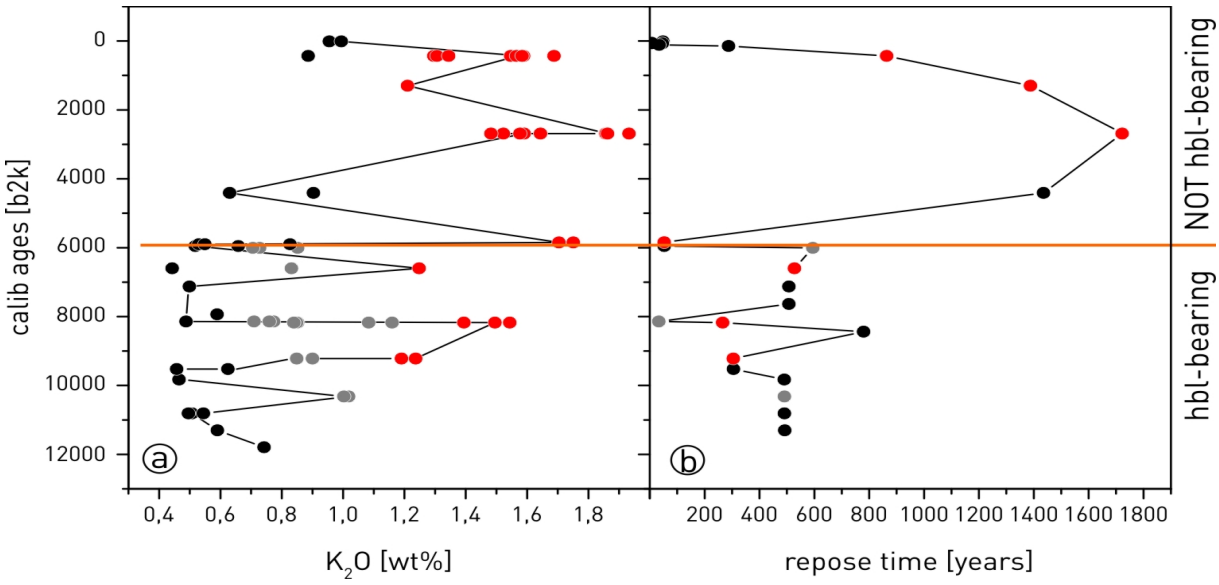

Fig. 2.11 Variation with tephra age of a) bulk rock K_2O-contents, b) repose time between eruptions. Red symbols represent LCPT, grey symbols are LGPT, and black symbols show LDST units.

2.6.3 Reservoir conditions

In order to check whether the observed changes in composition and eruptive behavior can be linked with changing parameters of magma storage, we computed pressure and temperature values based on cpx-liquid equilibria (Putirka, 2008) and hornblende compositions (Ridolfi et al., 2010.)

Cpx-liquid Thermobarometry

Numerous petrologic experiments and thermodynamic models (e.g. Nimis, 1999; Putirka et al. 1996; Putirka 2005) have calibrated the compositions of cpx and equilibrated melts as a function of crystallization pressure and temperature. We here used matrix-glass and cpx-rim compositions to calculate p-T conditions prevailing during differentiation; we note that cpx phenocrysts are typically not compositionally zoned. Mineral-melt pairs were checked to satisfy the equilibrium condition $K_D(Fe\text{-}Mg)_{cpx\text{-}liq}^{equ}=0.28\pm0.08$ calculated with the temperature compensated formula

(Eq. 35) of Putirka (2008). An additional check for equilibrium was performed by comparing observed (measured) and predicted cpx-components (derived from the corresponding melt composition). The observed cpx-components were calculated with the normative scheme of Putirka et al. (1996)_ENREF_20, whereas the predicted cpx-components were computed using Eq. 3.1a (DiHd), Eq. 3.2 (EnFs), Eq. 3.4 (CaTs), Eq. 3.5 (Jd), and Eq. 3.7 (CrCaTs) of Putirka (1999). Only cpx-liquid pairs that satisfy both equilibrium tests were used for thermobarometric calculations solving Eq. 31 for pressure and Eq. 33 for temperature (Putirka, 2008) simultaneously in an iterative procedure. Putirka (2008) gives the respective calibration standard error of estimate (SEE) as SEE(P)=±290 MPa and SEE(T)=±45°C. The results for a number of mineral-melt pairs per sample are reported as absolute ranges (P_{range} and T_{range}) that indicate calculated minimum and maximum values, and as averaged values (P_{mean} and T_{mean}) with their standard deviation, where the standard deviations are much smaller than the reported SEEs.

The results reveal different storage conditions for each of the petrographic groups introduced above. Cpx-liquid pairs from LDST yield the highest pressures and temperatures with P_{range}=145-640 MPa, P_{mean}=476±95 MPa, T_{range}=1015-1115°C, T_{mean}=1073±24°C. LCPT samples in contrast provide the lowest values (P_{range}=10-180 MPa, P_{mean}=86±49 MPa, T_{range}=896-957°C, T_{mean}=936±24°C), whereas LGPT samples deliver intermediate values (P_{range}=70-418 MPa, P_{mean}=239±100 MPa, T_{range}=997-1051°C, T_{mean}=1013±17°C). Representative clinopyroxene and matrix-glass pairs as well as computed pressure and temperature-values are given as supplementary material Tab. A.4.

Hornblende-Thermobarometry

Using different independent pressure estimates is by far the best quality check if the results fall within one standard deviation (Putirka, 2008). Therefore, we used the compositions of the amphiboles - which are restricted to the lower part of the stratigraphy - to apply the thermobarometric method of Ridolfi et al. (2010). Despite the range of bulk-rock compositions, LCPT and LGPT samples all share approximately identical compositions of their amphibole crystals which also lack any core-to-rim compositional zonation such that the derived pressure and temperature values are fairly uniform and seem to be independent of the host-rock composition. Mean values from all samples of pressure of 337±25 MPa and temperature of T_{mean}=929±18°C have small standard deviations although they are derived from >80 analyses of crystal rims and cores in nine different samples. The mean values per rock type are 313±10 MPa and 912±10°C for LCPT and 351±20 MPa and 939±13°C for LGPT. The standard deviations are again smaller than the reported SEEs (SEE_T=±22°C, SEE_P=±35-85 MPa) of the thermodynamic models.

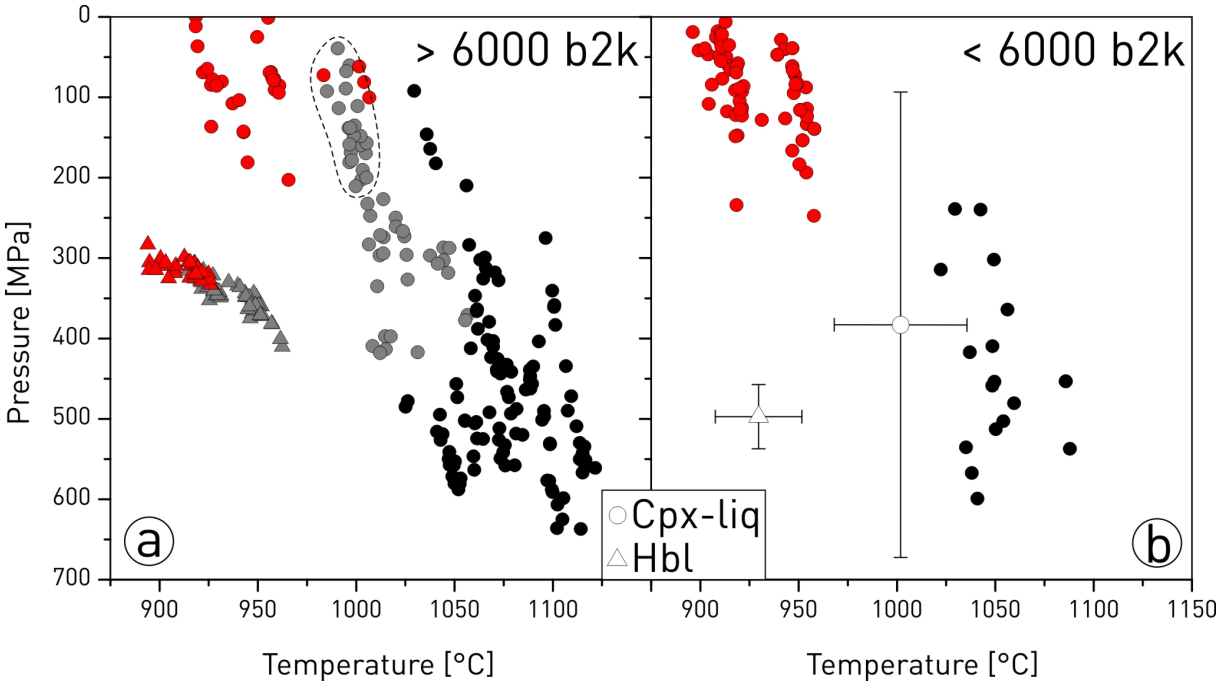

Fig. 2.12 P-T-variation diagrams for a) deposits older than 6000 b2k, b) deposits younger than 6000 b2k. For the LGPT, pressures are generally >200 MPa except for a sub-population of low-pressure cpx in units J and N that is enclosed by the dashed line. Red symbols represent LCPT, grey symbols are LGPT, and black symbols show LDST units.

2.6.4 Reservoir system over time

Because the thermobarometric results correlate largely with magmatic composition systematics, we interpret the data in Fig. 2.12 to reflect three distinct but interconnected levels of magma storage: a deep-seated (around 500 MPa) reservoir of basaltic-andesitic LDST magma, a shallow (around 100 MPa) reservoir of dacitic LCPT magma, and an intermediate storage level identified through mostly LGPT data. We will investigate the petrogenesis of these magma types in detail elsewhere; the summarizing conclusion that LCPT compositions are fractionated daughters of LDST compositions while LGPT compositions formed as hybrids of these two endmembers are here supported by bimodal glass compositions (Fig. 2.5) and petrographic observations of disequilibrium assemblages and textures (Fig. 2.8).

While these reservoirs and magma components provide a general framework for the LVC plumbing system, the details of magma transport differ between eruptions and through time. Depositional and petrographic features, as well as thermobarometric results and time series investigations suggest that the magmatic system experienced a two-tier evolution with a sudden change at 6000 b2k.

Eruptive history before 6000 b2k is characterized by the coexistence and interaction of all three connected reservoirs. The nature of erupted tephras depends on the paths through this system used by ascending magmas and how they mixed along these routes, as we illustrate by the four cases discussed below (cf. Fig. 2.12a).

1) Withdrawal directly from the deep seated mafic magma chamber to the surface led to the deposition of mafic fallouts (units A, B, C, E, H, K, and L; Fig. 2.13a - 1).

2) Mixing between LDST and LCPT magmas in the intermediate reservoir formed a pool of LGPT hybrid erupted as pure LGPT deposits such as units D and G in which all pyroxenes yield intermediate pressures (Fig. 2.13a-2a). In some cases such mixing extended to form LGPT in both the intermediate and the shallow reservoir, and withdrawal from both led to LGPT units J and N in which pyroxenes from both pressure levels coexist and scattered mafic clasts occur throughout the deposits (Fig. 2.13a-2b).

3) When hybridization remained incomplete, the intermediate reservoir became compositionally zoned from an LDST base through a hybrid LGPT center to an LCPT top. Withdrawal from this zoned reservoir always tapped the shallow LCPT reservoir, too (Fig. 13a - 3). The resulting compositionally zoned deposits (units G, I, and M) include a basal LCPT layer with pyroxenes from shallow level and amphibole from the intermediate level, and an upper LGPT layer with intermediate-pressure pyroxenes and infrequent scattered LDST components. The intermediate storage level was where all amphiboles were formed. The amphibole compositions are uniform and obviously independent from their host magma (LCPT and LGPT) but appear to have formed at temperatures typical of the LCPT (Fig. 2.12a). We thus conclude that amphiboles in LCPT have been inherited from magma mixing with LGPT at intermediate pressure level; such mixing probably occurred shortly prior to, or during the eruption because amphiboles show no signs of breakdown. We speculate that pressure in the upper LCPT reservoir was too low to stabilize amphibole.

Deposits younger than 6000 b2k only show evidences for an involvement of the deep LDST and shallow LCPT reservoirs. Amphibole does no longer occur, pyroxenes only record deep and shallow pressures, and no more hybrid LGPT was erupted (Fig. 2.12b); in other words, there is no longer any evidence for magmatic contributions from intermediate depth. However, different paths of magma withdrawal also operated during the younger history (cf. Fig. 2.13b):

1) Exclusive tapping of the deep LDST magma chamber resulted in the pure scoria deposits that dominate the lower part of the deposits younger than 6000 b2k (units O, P, and R; Fig. 2.13b - 1).

2) Unimodal low-pressure pyroxene populations (and absence of amphibole) demonstrate that all LCPT magma younger than 6000 b2k erupted from the shallow reservoir. Units Q and T are composed of pure LCPT (Fig. 2.13b - 2) but units S, U, and V contain scattered LDST clasts with

higher-pressure pyroxenes documenting recharge of the LCPT reservoir by mafic magma from the deep reservoir which probably served as an eruption trigger (Fig. 2.13b - 3).

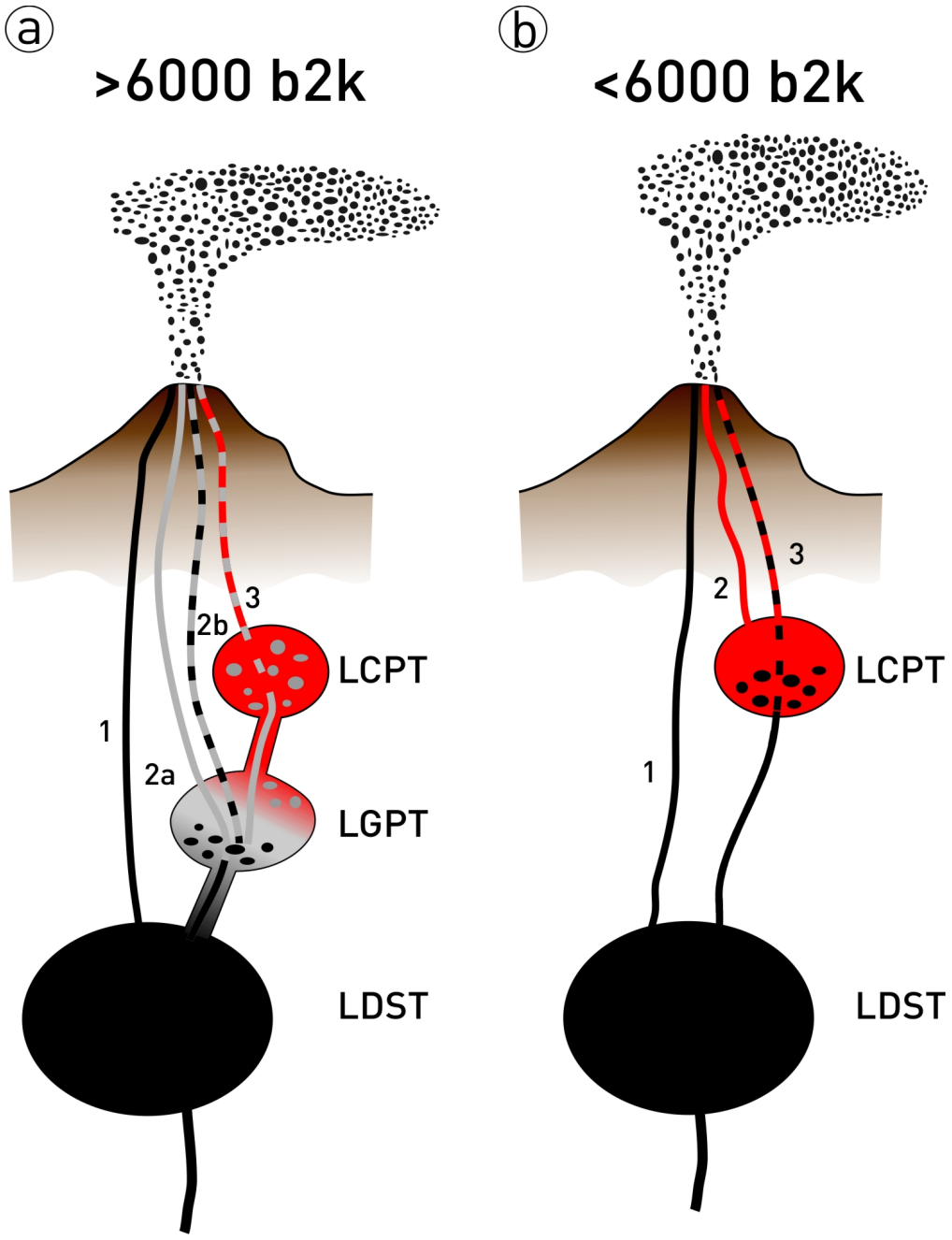

Fig. 2.13 Schematic illustration of the two-tier evolution of LVC´s plumbing system and pathways as discussed in the text.

While the deep mafic and the shallow felsic reservoirs seem to have persisted throughout the post-glacial evolution of the LVC, the intermediate reservoir ceased to exist at about 6000 b2k. The associated changes in repose times and eruption frequency (Figs. 2.11b, 2.9a, b) allow two important conclusions.

The first conclusion is that the older plumbing system involving three storage levels was able to erupt more frequently than the younger system with only two reservoirs left. Frequent eruptions during the older phase may have been facilitated by removal of the ice load (cf. Sigvaldason et al., 1992) after the glacial maximum at 17200 b2k (McCulloch et al., 2000). While this effect would diminish gradually with time, it cannot explain the sudden regime shift at 6000 b2k. Alternatively, a decrease in the production of parental melts may be invoked but, as we will demonstrate elsewhere, trace element systematics do not reveal any significant temporal change in melt generation and probably such a change would also occur gradually. Therefore, we interpret the change in eruption regime in terms of rearrangement of pathways to the surface.

A second conclusion (cf. Fig. 2.11) is that this change in plumbing regime occurred quite suddenly; it can be bracketed into a time interval of about 50 years (corresponding to the 2σ envelope of the radiometric dating of Unit N). We therefore favor the interpretation that this change in eruption regime via rearrangement of crustal magma pathways was provoked by a sudden external event. We speculate that a major earthquake, probably at the Liquiñe-Ofqui Fault Zone, may have disrupted the transport links between the reservoirs, such that the intermediate reservoir was no longer supplied while the (presumably larger) mafic and felsic reservoirs subsequently were less strongly coupled (Fig. 2.13b).

2.7 CONCLUSION

Our stratigraphic work revealed an eruptive history of the LVC that comprises 23 post-glacial explosive eruptions. Including the four historic events, a total of at least 27 explosive eruptions occurred in the last ~12000 years. Statistical analysis of the eruption time series yields probabilities of 20-50% that a VEI≥3 eruption will occur within the next 100 years.

Based on petrography and juvenile compositions, the tephra deposits can be subdivided into three groups: Poorly vesicular to dense mafic juvenile clasts of LDST-deposits dominate the Lower Lonquimay Sequence and were probably emplaced by phreatomagmatically influenced eruptions possibly related to extensive ice/snow cover during these early Holocene times. The intermediate (LGPT) to felsic (LCPT), compositionally zoned deposits of the Lower and Middle Lonquimay Sequence show evidence for pre- and syn-eruptive magma mixing indicating that intrusion of less evolved magma batches probably triggered these eruptions. The Upper Lonquimay Sequence is largely composed of felsic LCPT tephras with only rare scattered mafic clasts and mafic scoria fallouts.

Thermobarometric calculations reveal that the three petrographic groups derive from distinct magma storage levels. LDST deposits were discharged from a reservoir at 14-19 km depth and at temperatures of 1030-1120°C. The LCPT magmas were mainly stored at shallow depths between

1.5 and 6 km and at temperatures between 890 and 960°C. An intermediate magma chamber at 8.5 to 12.5 km depth stored most of the LGPT-magmas at temperatures between 1000 and 1050°C.

Although being dominated by contributions from the deep-seated mafic reservoir, the lower half of the Lonquimay tephra succession was built by magmas discharged from all three connected reservoirs. We speculate that tectonic conditions at that time facilitated frequent eruptions from the deep-seated mafic-reservoir and that these conditions favored magma transport through the system of connected reservoirs leading to intense magma mixing and eruption of compositionally zoned tephras. Repose times between eruptions then were relatively short (around 400 years). However, from 6000 b2k on, there is no more indication of any involvement of the intermediate-level reservoir. Most eruptions originated from the shallow felsic reservoir and were only rarely interrupted by eruption of mafic magma from the deep reservoir. Contemporaneously, repose time intervals between eruptions increased significantly (to around 1300 years). The change in eruptive behavior of the LVC at 6000 b2k occurred rather suddenly (within the time resolution of radiocarbon dating) and was not associated with changes in magma compositions that would indicate changes in the generation or evolution of the magmas. We therefore conclude that the change in regime was externally forced probably by a tectonic event that limited replenishments from depth and disrupted the plumbing pathways between the three reservoirs resulting in the cessation of the intermediate reservoir.

Acknowledgements

We owe thanks to J. Stix and S. Wulf for detailed reviews and helpful comments that greatly improved this manuscript. We gratefully acknowledge the support by the Leibniz-Labor für Altersbestimmung und Isotopenforschung at the University of Kiel who conducted our radiocarbon dating. Moreover, we thank E. Thun and S. Jung (University of Hamburg) for providing XRF analyses of our samples. M. Thöner facilitated our microanalytical investigations with helpful support during (EPMA) measurements and L. Lara of SERNAGEOMIN supported us by providing a copy of the unpublished thesis of E. Polanco (1998) and during our field campaigns in Chile. This publication is contribution no. 230 of the Sonderforschungsbereich 574 on "Volatiles and Fluids in Subduction Zones" at University of Kiel.

REFERENCES

Arancibia, G., Cembrano, J., and Lavenu, A., 1999, Transpresión dextral y partición de la deformación en la Zona de Falla Liquiñe-Ofqui, Aisén, Chile (44-45°S): Revista Geológica de Chile, v. 26, p. 3-22.

Barrientos, S.E., and Acevedo-Aránguiz, P.S., 1992, Seismological aspects of the 1988-1989 Lonquimay (Chile) volcanic eruption: Journal of Volcanology and Geothermal Research, v. 53, p. 73--87.

Cembrano, J., and Lara, L., 2009, The link between volcanism and tectonics in the southern volcanic zone of the Chilean Andes: A review: Tectonophysics, v. 471, p. 96-113.

Cembrano, J., Schermer, E., Lavenu, A., and Sanhueza, A., 2000, Contrasting nature of deformation along an intra-arc shear zone, the Liquiñe-Ofqui fault zone, southern Chilean Andes: Tectonophysics, v. 319, p. 129-149.

Clark, S.K., Reagan, M.K., and Trimble, D.A., 2006, Tephra deposits for the past 2600 years from Irazú volcano, Costa Rica: Geological Society of America Special Papers, v. 412, p. 225-234.

Dzierma, Y., and Wehrmann, H., 2010a, Eruption time series statistically examined: Probabilities of future eruptions at Villarrica and Llaima Volcanoes, Southern Volcanic Zone, Chile: Journal of Volcanology and Geothermal Research, v. 193, p. 82-92.

Dzierma, Y., and Wehrmann, H., 2010b, Statistical eruption forecast for the Chilean Southern Volcanic Zone: typical probabilities of volcanic eruptions as baseline for possibly enhanced activity following the large 2010 Concepción earthquake: Natural Hazards and Earth System Sciences, v. 10, p. 2093-2108.

Freundt, A., Hartmann, A., Kutterolf, S., and Strauch, W., 2010, Volcaniclastic stratigraphy of the Tiscapa maar crater walls (Managua, Nicaragua): implications for volcanic and seismic hazards and Holocene climate changes: International Journal of Earth Sciences, v. 99, p. 1453-1470.

Gevrek, A.İ., and Kazanci, N., 2000, A Pleistocene, pyroclastic-poor maar from central Anatolia, Turkey: influence of a local fault on a phreatomagmatic eruption: Journal of Volcanology and Geothermal Research, v. 95, p. 309-317.

Hildreth, W., and Moorbath, S., 1988, Crustal contributions to arc magmatism in the Andes of Central Chile: Contributions Mineralogy Petrology, v. 98, p. 455-489.

Hill, B.E., Connor, C.B., Jarzemba, M.S., La Femina, P.C., Navarro, M., and Strauch, W., 1998, 1995 eruptions of Cerro Negro volcano, Nicaragua, and risk assessment for future eruptions: Geological Society of America Bulletin, v. 110, p. 1231-1241.

Hill, D.P., 1977, A Model for Earthquake Swarms: Journal of Geophysical Research, v. 82, p. 1347-1352.

Hunt, J.B., and Hill, P.G., 1993, Tephra geochemistry: a discussion of some persistent analytical problems: The Holocene, v. 3, 3, p. 271 - 278.

Jones, G., Chester, D.K., and Shooshtarian, F., 1999, Statistical analysis of the frequency of eruptions at Furnas Volcano, São Miguel, Azores: Journal of Volcanology and Geothermal Research, v. 92, p. 31-38.

Kienle, J., Kyle, P.R., Self, S., Motyka, R.J., and Lorenz, V., 1980, Ukinrek Maars, Alaska, I. April 1977 eruption sequence, petrology and tectonic setting: Journal of Volcanology and Geothermal Research, v. 7, p. 11-37.

La Femina, P.C., Connor, C.B., Hill, B.E., Strauch, W., and Saballos, J.A., 2004, Magma–tectonic interactions in Nicaragua: the 1999 seismic swarm and eruption of Cerro Negro volcano: Journal of Volcanology and Geothermal Research, v. 137, p. 187-199.

Lara, L.E., Lavenu, A., Cembrano, J., and Rodríguez, C., 2006a, Structural controls of volcanism in transversal chains: Resheared faults and neotectonics in the Cordón Caulle–Puyehue area (40.5°S), Southern Andes: Journal of Volcanology and Geothermal Research, v. 158, p. 70-86.

Lara, L.E., Moreno, H., Naranjo, J.A., Matthews, S., and Pérez de Arce, C., 2006b, Magmatic evolution of the Puyehue-Cordón Caulle Volcanic Complex (40° S), Southern Andean Volcanic Zone: From shield to unusual rhyolitic fissure volcanism: Journal of Volcanology and Geothermal Research, v. 157, p. 343-366.

Lavenu, A., and Cembrano, J., 1999, Compressional and transpressional stress pattern for Pliocene and Quaternary brittle deformation in fore-arc and intra-arc zones (Andes of Central and Southern Chile): Journal of Structural Geology, v. 21, p. 1669-1691.

Le Bas, M.J., Le Maitre, R.W., Streckeisen, A., and Zanettin, B., 1986, A chemical classification of volcanic rocks based on the total alkali-silica diagram: Journal of Petrology, v. 27, p. 745 - 750.

Lindquist, K.G., Engle, K., Stahlke, D., and Price, E., 2004, Global topography and bathymetry grid improves research efforts: EOS Trans. AGU, v. 85.

López-Escobar, L., Cembrano, J., and Moreno, H., 1995, Geochemistry and tectonics of the chilean Southern Andes basaltic Quaternary volcanism (37°-46°S). Revista Geológica de Chile, v. 22, p. 219-234.

López-Escobar, L., Killian, R., Kempton, P., and Tagiri, M., 1993, Petrography and geochemistry of Quaternary rocks from the Southern Volcanic Zone between 41°30' and 46°00' S: Revista Geológica de Chile, v. 20, p. 35-55.

Lowrie, A., and Hey, R., 1981, Geological and geophysical variations along the western margin of Chile near latitude 33° to 36°S and their relation to Nazca Plate subduction. In Nazca Plate; crustal formation and Andean convergence: Geological Society of America Memoirs, v. 154, p. 741-754.

Marshall, A.W., and Olkin, I., 2007, Life Distributions: Structure of Nonparametric, Semiparametric, and Parametric Families: New York, Springer, 808 p.

McCormac, F.G., Hogg, A.G., Blackwell, P.G., Buck, C.E., Higham, T.F.G., and Reimer, P.J., 2004, SHCal04 Southern Hemisphere Calibration, 0–11.0 cal kyr BP: Radiocarbon, v. 46, p. 1087-1092.

McCulloch, R.D., Bentley, M.J., Purves, R.S., Hulton, N.R.J., Sugden, D.E., and Clapperton, C.M., 2000, Climatic inferences from glacial and palaeoecological evidence at the last glacial termination, southern South America: Journal of Quaternary Science, v. 15, p. 409-417.

Mendoza-Rosas, A.T., and De la Cruz-Reyna, S., 2008, A statistical method linking geological and historical eruption time series for volcanic hazard estimations: Applications to active polygenetic volcanoes: Journal of Volcanology and Geothermal Research, v. 176, p. 277-290.

Mendoza-Rosas, A.T., and De la Cruz-Reyna, S., 2009, A mixture of exponentials distribution for a simple and precise assessment of the volcanic hazard: Natural Hazards and Earth System Sciences, v. 9, p. 425-431.

Monaco, C., Catalano, S., Cocina, O., De Guidi, G., Ferlito, C., Gresta, S., Musumeci, C., and Tortorici, L., 2005, Tectonic control on the eruptive dynamics at Mt. Etna Volcano (Sicily)

during the 2001 and 2002–2003 eruptions: Journal of Volcanology and Geothermal Research, v. 144, p. 211-233.

Moreno Roa, H., and Gardeweg, M., 1989, La erupcion reciente en el complejo volcanico Lonquimay (diciembre 1988-), Andes del Sur: Revista geológica de Chile, v. 16, p. 93-117.

Naranjo, J.A., Sparks, R.S.J., Stasiuk, M.V., Moreno, H., and Ablay, G.J., 1992, Morphological, structural and textural variations in the 1988-1990 andesite lava of Lonquimay Volcano, Chile: Geological Magazine, v. 129, p. 657--678.

Newhall, C.G., and Self, S., 1982, The Volcanic Explosivity Index (VEI) An Estimate of Explosive Magnitude for Historical Volcanism: Journal of Geophysical Research, v. 87, p. 1231-1238.

Nielsen, C.H., and Sigurdsson, H., 1981, Quantitative methods of electron microprobe analysis of sodium in natural and synthetic glasses. : American Mineralogist, v. 66, p. 547–552.

Nimis, P., 1999, Clinopyroxene geobarometry of magmatic rocks. Part 2. Structural geobarometers for basic to acid, tholeiitic and mildly alkaline magmatic systems: Contributions to Mineralogy and Petrology, v. 135, p. 62-74.

Petrinovic, I.A., Riller, U., Brod, J.A., Alvarado, G., and Arnosio, M., 2006, Bimodal volcanism in a tectonic transfer zone: Evidence for tectonically controlled magmatism in the southern Central Andes, NW Argentina: Journal of Volcanology and Geothermal Research, v. 152, p. 240-252.

Polanco, E., 1998, Volcanismo Explosivo Postglacial de la Cuenca del Alto Biobío, Andes del Sur (37º45'-38º30') [Master thesis]: Santiago de Chile, Universidad de Chile.

Polanco, E., 2010, Volcanoestratigrafía, geoquímica y peligro volcánico del volcán Lonquimay (38º30'S), Andes del Sur (Chile): Barcelona, Universidad de Barcelona.

Putirka, K., 1999, Clinopyroxene + liquid equilibria to 100 kbar and 2450 K: Contributions to Mineralogy and Petrology, v. 135, p. 151-163.

Putirka, K.D., 2005, Igneous thermometers and barometers based on plagioclase + liquid equilibria: Tests of some existing models and new calibrations: American Mineralogist, v. 90, p. 336-346.

Putirka, K.D., 2008, Thermometers and Barometers for Volcanic Systems, *in* Putirka, K.D., and Tepley III, F.J., eds., Minerals, inclusions and volcanic processes, Volume 69: Reviews in Mineralogy and Geochemistry, The Mineralogical Society of America, p. 61-111.

Putirka, K.D., Johnson, M., Kinzler, R., Longhi, J., and Walker, D., 1996, Thermobarometry of mafic igneous rocks based on clinopyroxene-liquid equilibria, 0–30 kbar: Contributions to Mineralogy and Petrology, v. 123, p. 92-108.

Ridolfi, F., Renzulli, A., and Puerini, M., 2010, Stability and chemical equilibrium of amphibole in calc-alkaline magmas: an overview, new thermobarometric formulations and application to subduction-related volcanoes: Contributions to Mineralogy and Petrology, v. 160, p. 45-66.

Rosenau, M., Melnick, D., and Echtler, H., 2006, Kinematic constraints on intra-arc shear and strain partitioning in the southern Andes between 38°S and 42°S latitude: Tectonics, v. 25, p. TC4013.

Siebert, L., and Simkin, T., 2002, Volcanoes of the World: an Illustrated Catalog of Holocene Volcanoes and their Eruptions, internet database.

Sigvaldason, G.E., Annertz, K., and Nilsson, M., 1992, Effect of glacier loading/deloading on volcanism: postglacial volcanic production rate of the Dyngjufjöll area, central Iceland: Bulletin of Volcanology, v. 54, p. 385-392.

Stern, C.R., 2004, Active Andean volcanism: its geological and tectonic setting: Revista Geológica de Chile, v. Vol. 31, p. p. 161-206.

Stuiver, M., and Polach, H.A., 1977, Discussion: Reporting of ^{14}C Data: Radiocarbon, v. 19, p. 355-363.

Stuiver, M., and Reimer, P.J., 1993, Extended 14C Data Base and Revised Calib 3.0 14C Age Calibration Program: Radiocarbon, v. 35, p. 215-230.

Tormey, D.R., Hickey-Vargas, R., Frey, F.A., and López-Escobar, L., 1991, Recent lavas from the Andean front (33° to 42°S): interpretations of along-arc compositional variations. , *in* Harmon, R.S., and Rapela, C.W., eds., Andean Magmatism and its Tectonic Setting, Volume 265: Special Paper, Geological Society of America, p. 57-77.

Valentine, G.A., and Perry, F.V., 2007, Tectonically controlled, time-predictable basaltic volcanism from a lithospheric mantle source (central Basin and Range Province, USA): Earth and Planetary Science Letters, v. 261, p. 201-216.

Vergara Sáez, C.A., 2010, Petrogénesis de los centros eruptivos del complejo volcánico Lonquimay (CVL), IX región de la araucanía [Master thesis]: Santiago de Chile, Universidad de Chile.

Völker, D., Kutterolf, S., and Wehrmann, H., 2011, Comparative mass balance of volcanic edifices at the southern volcanic zone of the Andes between 33°S and 46°S: Journal of Volcanology and Geothermal Research, v. 205, p. 114-129.

Watanabe, T., Koyaguchi, T., and Seno, T., 1999, Tectonic stress controls on ascent and emplacement of magmas: Journal of Volcanology and Geothermal Research, v. 91, p. 65-78.

Wehrmann, H., and Dzierma, Y., 2011, Applicability of statistical eruption analysis to the geological record of Villarrica and Lanín volcanoes, Southern Volcanic Zone, Chile: Journal of Volcanology and Geothermal Research, v. 200, p. 99-115.

Chapter 3

Pre-eruptive equilibrium and disequilibrium conditions, and the volatile inventory of explosive eruptions of the Lonquimay Volcanic Complex

This chapter will be submitted to *Contributions to Mineralogy and Petrology*

Co-authors: A. Freundt, S. Kutterolf, R. Trumbull, H. Wehrmann

3.1 ABSTRACT

The Lonquimay Volcanic Complex (LVC) in the high Southern Andes comprises a stratocone and two NE-trending flank-cone alignments. Numerous effusive and explosive volcanic eruptions characterize its post-glacial eruptive activity. This study reveals that the post-glacial magmas experienced a complex history of interacting processes within the plumbing system that systematically affected the magma compositions as well as their volatile inventories and hence LVC's eruptive behavior.

During ascent, the LVC magmas reached two independent levels of volatile saturation. A first deep saturation level (~14 km) was reached by mafic melts. The resulting exsolution of a S-rich fluid phase led to a strong depletion in S of the melt. A second more shallow saturation level was reached between 1.5 and 6 km in a shallow reservoir. The stagnation of rhyodacitic magmas at this level resulted in their H_2O oversaturation and hence exsolution of an aqueous fluid phase.

The frequent injection of primitive melt batches into the deep LDST reservoir is recorded in the pheno- and xenocryst assemblage. These frequent replenishments may have triggered most mafic LDST eruptions. Prior to 6000 b2k, most of these mafic eruptions have been influenced by phreatomagmatic activity probably due to melt water from ongoing deglaciation, The occurrence of compositionally zoned, amphibole-bearing deposits that is limited to LCPT deposits older than 6000 b2k indicates the occurrence of compositionally zoned magma bodies and hence stronger interaction between the three distinct reservoirs prior to this threshold. In contrast, the matrix glass and crystal compositions of most felsic eruptions younger than 6000 b2k are homogeneous and reflect equilibrium conditions. We therefore conclude that these eruptions may not have been triggered by replenishments but H_2O saturation, giving a possible explanation for the longer repose times between these eruptions younger than 6000 b2k.

3.2 INTRODUCTION

Volatile species dissolve in silicate melts under high pressures, but form a vapor phase at low pressures. The exsolution of a fluid phase generates overpressures in magma reservoirs and drives magma ascent through buoyancy. Enrichment of fluid phased near the roofs of magma chambers might create overpressures that are sufficient to fracture wall rocks and trigger gas-driven, rapidly propagating fractures (e.g. Carrigan, 2000; Lister, 1990; Rubin, 1993). Such vapor-driven cracks may precede the transfer of magma from the storage level to the surface prior to the eruption (Menand and Tait, 2001). Instantaneous near-surface expansion of the fluid phase yields excess

kinetic energy, capable to sustain explosive eruptions. Therefore, magmatic volatiles exsolved during ascent provide the primary internal driving force for volcanic eruptions.

However, there is a growing amount of evidence (e.g. Cembrano and Lara, 2009) that external forcing may contribute to a significant amount of volcanic eruptions in arc settings. Arc volcanoes by nature lie in tectonically highly active regions where regional fault zones and large-magnitude earthquakes are common. Tectonic influence on volcanism is commonly based on observed spatial correlations between tectonic and volcanic features but may also be inferred from the pattern of temporal evolution of a volcano. The various ways in which such external tectonic forcing may affect magmatic systems depend strongly on the internal state of the system (i.e. pre-eruptive criticality due to volatile saturation; e.g. Manga and Brodsky, 2006; Watt et al., 2009). This study tries to identify the petrologic conditions and involved pre-eruptive petrogenetic processes in order to estimate pre-eruptive criticality and triggering mechanisms for post-glacial Lonquimay magmas.

3.3 GEOLOGICAL SETTING AND BACKGROUND

The Lonquimay Volcanic Complex (LVC, 38°22'S-71°35'W) is part of the volcanic front of the Quaternary Southern Volcanic Zone (SVZ) (López-Escobar et al., 1995; Hildreth and Moorbath, 1988; López-Escobar et al., 1993; Stern, 2004; Tormey et al., 1991) and is of Late Pleistocene to Holocene age. The Southern Volcanic Zone of the Andes results from the north-eastward subduction of the oceanic Nazca plate underneath the continental margin of the South American plate. Oblique convergence (22-30° NE) between the Chile Triple Junction and the Copahue volcano at 38°S (Rosenau et al., 2006) causes strain partitioning in the upper plate that leads to the formation of the arc-parallel (~10° NE) Liquiñe-Ofqui Fault Zone (Arancibia et al., 1999; Lavenu and Cembrano, 1999). This right lateral strike slip system affects the tectonic architecture of the intra-arc region and therefore controls the loci of most larger volcanic centers and smaller monogenetic centers in the CSVZ and SSVZ (López-Escobar et al., 1995; Cembrano and Lara, 2009).

Fig. 3.1 (next page) Overview map (data from GINA, Lindquist et al., 2004) of the Southern Volcanic Zone (SVZ) emphasizing the location of the Lonquimay Volcanic Complex. Based on petrographic, geochemical and tectonic observations the SVZ has been further subdivided into four domains: the Northern (NSVZ; 33°-34°30'S), Transitional (TSVZ; 34°30'-37° S), Central (CSVZ; 37°- 41°30'S), and Southern (SSVZ; 41°30'-46° S) Volcanic Zones. Black line LOFZ is the Liquiñe-Ofqui Fault Zone.

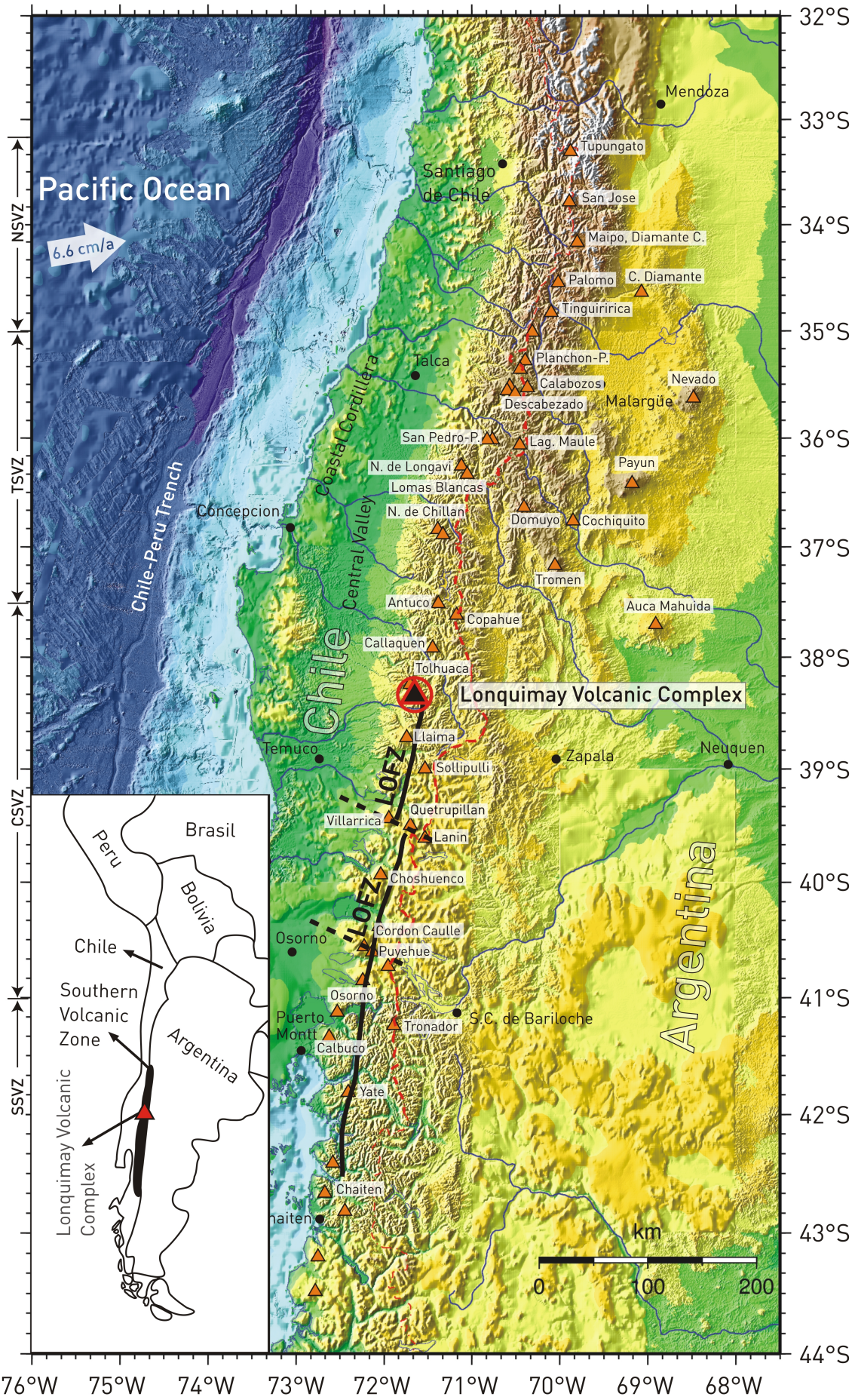
Pacific Ocean
6.6 cm/a
Chile-Peru Trench
Coastal Cordillera
Central Valley
Chile
Argentina
NSVZ
TSVZ
CSVZ
SSVZ
LOFZ
LOFZ
Mendoza
Tupungato
Santiago de Chile
San Jose
Maipo, Diamante C.
Palomo
C. Diamante
Tinguiririca
Planchon-P.
Talca
Calabozos
Descabezado
Nevado
Malargüe
San Pedro-P.
Lag. Maule
Payun
N. de Longavi
Lomas Blancas
N. de Chillan
Concepcion
Domuyo
Cochiquito
Tromen
Antuco
Copahue
Auca Mahuida
Callaquen
Tolhuaca
Lonquimay Volcanic Complex
Llaima
Temuco
Zapala
Neuquen
Sollipulli
Villarrica
Quetrupillan
Lanin
Choshuenco
Osorno
Cordon Caulle
Puyehue
Osorno
Puerto Monti
Tronador
S.C. de Bariloche
Calbuco
Yate
Chaiten
km
0
100
200
32°S
33°S
34°S
35°S
36°S
37°S
38°S
39°S
40°S
41°S
42°S
43°S
44°S
76°W
75°W
74°W
73°W
72°W
71°W
70°W
69°W
68°W
Peru
Brasil
Bolivia
Chile
Southern Volcanic Zone
Argentina
Lonquimay Volcanic Complex

The Lonquimay Volcanic System of Late Pleistocene to Holocene age is rather a volcanic complex than a single volcano. It comprises a principal stratocone - the Volcán Lonquimay - and several adjacent minor eruptive centers that sit astride two fissure zones (Moreno Roa and Gardeweg, 1989) and thus seem to be controlled by regional tectonics. The shape of Lonquimay's truncated stratocone is slightly elongated in WSW-ENE direction and elevates approximately 1420 m above its base (Völker et al., 2011) reaching 2865 m asl. Estimates of the volcanic edifice volume from Völker et al. (2011) using remote sensing techniques yield values between $Vol_{edifice}$=22km^3 and Vol_{max}=106.5 km^3. The large uncertainty results from the high relief underlying the Lonquimay Stratocone causing problems for the definition of a proper baseplane. Compared to other SVZ-volcanoes, these dimensions show that Lonquimay's edifice is quite small. The small size can mainly be attributed to its adolescent state of mainly postglacial evolution that is inferred from the absence of any traces of glacial erosion (Völker et al., 2011) and the tephrostratigraphy as established by Polanco (1998) and Gilbert et al. (2012). The oldest magmatic products dated so far document explosive magmatic activity since 10200±70 a BP (Polanco, 1998).

3.3.1 Post-glacial eruptive history

The record of eruptive history of the LVC shows both, explosive and effusive activity, involving a range of magmatic products ranging from basaltic andesite to dacite (Gilbert et al., 2012; Polanco, 1998; Vergara Sáez, 2010). The last eruptive phase of the "Navidad"-eruption from 1988-1990 was characterized by strombolian activity that discharged two andesitic lava flows (VEI=3; 58 wt% SiO_2; Moreno Roa and Gardeweg, 1989) and a widespread tephra blanket. A detailed investigation of the general tephrostratigraphy is given by Gilbert et al. (2012) revealing a post-glacial explosive eruption history of the LVC that comprises 23 explosive eruptions (Fig. 3.2). Juvenile components of the erupted tephras have been subdivided into three petrographic groups: a felsic group (Lonquimay Colored Pumice Tephra, LCPT), an intermediate population (Lonquimay Grey Pumice Tephra, LGPT) and a mafic member (Lonquimay Dark Scoria Tephra, LDST). The distribution of these petrographic groups through the LVC tephrostratigraphy (Fig. 3.2) is linked with an observed change in repose times. LDST deposits as well as deposits compositionally zoned from LCPT to LGPT dominate the lower part of the stratigraphy (>6000 b2k - years before 2000 AD) for which recurrence times are short (RT_{mean}=417±169 a). Deposits younger than 6000 b2k have dominantly LCPT and minor LDST compositions, no longer contain LGPT, and repose times are significantly longer (RT_{mean}=1350±310 a).

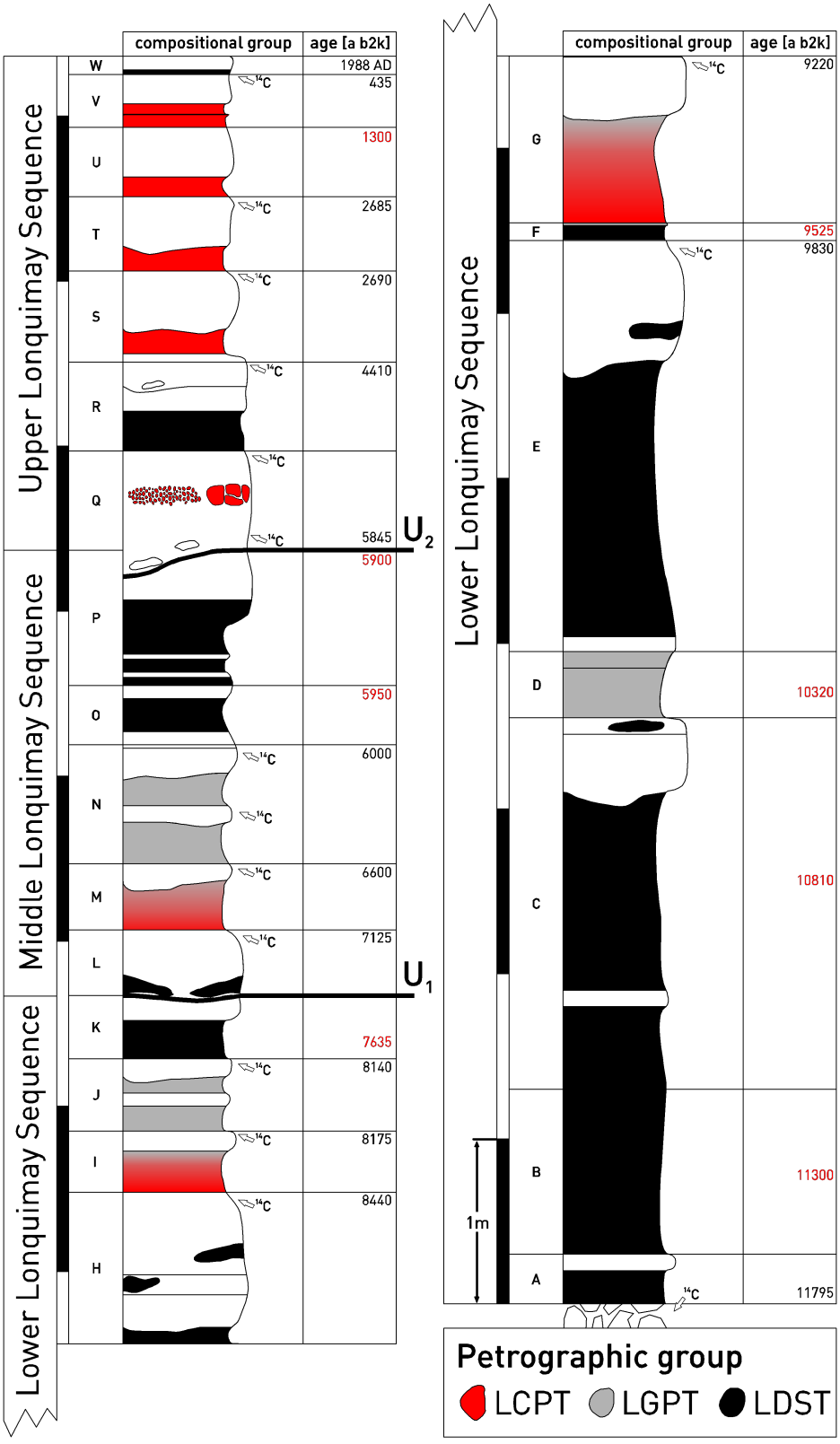

Fig. 3.2 Schematic composite column of the LVC stratigraphic succession with radiometric (black) and interpolated (red) ages (modified from Gilbert et al., 2012). The color coding in the lithologic column marks the occurrence of the three compositional groups (LCPT, LGPT, LDST) throughout the stratigraphy. Note that deposits compositionally zoned from colored to grey pumice and pure grey pumice deposits are older than 6000 b2k. U= major erosional unconformity.

Gilbert et al. (2012) further propose that the instant nature of this change in eruption regime resulted from a rearrangement in the magma storage and plumbing system that is probably linked with tectonic activity.

Thermobarometric calculations by Gilbert et al. (2012) revealed that the three petrographic groups derive from distinct crustal magma storage levels. LDST deposits were discharged from a reservoir at 14-19 km depth, the LCPT magmas were mainly stored at shallow depths between 1.5 and 6 km, and an intermediate magma chamber at 8.5 to 12.5 km depth stored most of the LGPT-magmas. Magma contributions from this intermediate reservoir are restricted to >6000 b2k when the Lonquimay plumbing system was in a regime of short repose times; disappearance of the intermediate reservoir coincides with the change to longer repose times between eruptions.

Here we investigate the thermobarometric conditions for the LVC magma types in more detail and compare them with analyses of dissolved volatile contents of the melts in order to constrain the magmatic degassing history and the driving forces of magma ascent and eruption. As we will show below, both volatile saturation in some magma batches and magma mixing in others were important controls on vertical magma movements.

3.4 SAMPLES AND ANALYTICAL TECHNIQUES

3.4.1 Sampling

The freshest tephra clasts from medial to distal outcrops downwind Lonquimay were collected for this study. The LVC tephrostratigraphy established in (Gilbert et al., 2012) was used to ensure that samples from all stages of LVC's post-glacial magmatic evolution were collected. Moreover, several lava and tephra samples from adjacent minor eruptive centers were sampled.

3.4.2 Chemical analyses

Matrix glasses

A JEOL JXA 8200 wave length-dispersive Electron Probe Microanalyzer (EPMA) was used to conduct spot analyses for major element compositions of glasses and minerals. In order to ensure significant analytic results, representative juvenile clasts were chosen from each tephra sample. The clasts were crushed, embedded in resin, polished, and analyzed with EPMA. To ensure representative results, matrix glass compositions are by >20 spot analyses for felsic compositions.

Mafic glass composition are determined by less analyses (n>5) or even lacking for some samples because they were harder to perform and sometimes simply not possible due to devitrification or microcrystalline matrix of the samples. But since glasses of mafic samples show more distinct compositions, these smaller sampling batches are sufficient for characterization. We performed all of our EPMA analyses for matrix glasses using the following setup: 15 kV accelerating voltage; defocused beam (5 μm) to avoid analytical Na-loss (Hunt and Hill, 1993; Nielsen and Sigurdsson, 1981); probe current was 10 nA for mafic and 6 nA for felsic glasses. International natural and synthetic glass standards were used to ensure a proper calibration during analysis runs. The typical accuracy is less than 0.5% for major (Si, Al, Na, Ca, K, Ti, Mg, and Fe) and <5% for minor elements (Mn and P). All analytical data presented in this work are normalized to anhydrous compositions unless otherwise stated.

Melt inclusions

Prior to analysis, melt inclusions were carefully examined for post-entrapment crystallization and the host crystals were subsequently polished until surface exposure of the inclusions. Major element compositions of melt inclusions hosted in plagioclase, olivine, spinel and pyroxene crystals were analyzed using a JEOL Superprobe JXA-8200 electron microprobe using the same analytical setup as described above for analysis of matrix compositions of the melt inclusions. Volatiles (Cl, S, and F) were determined using a 15 kV acceleration voltage, 30 nA beam current and 5 μm beam size. Typical accuracy derived from repeated analyses of International glass standards (KE3, KN18) is 0.4% for S, 3.6% for Cl, and 0.6% for F.

Mineral compositions

Analyses of mineral phenocrysts were performed at the GEOMAR | Helmholtz Centre for Ocean Research Kiel using a JEOL Superprobe JXA-8200 electron microprobe. All mineral species were analyzed at 15 kV accelerating voltage and adjusted primary beam current and beam diameter (olivine 80 nA and focused beam; plagioclase 20 nA, pyroxene 20nA, spinel 50nA, amphibole 20 nA, apatite 50 nA); ZAF correction routine was used to achieve true element concentrations. A set of reference materials (Kakanui Augite USNM 122142; San-Carlos Olivine USNM 111312/44; Natural Bridge Diopside USNM117733; Ilmenite Ilmen Mnts. USNM 96189; Minas Gerais Magnetite USNM 114887; Great Sitkin Island Anorthite USNM 137041; Lake County Plagioclase USNM115900; Jarosewich et al., 1980) were used for routine calibration and instrument stability monitoring.

H_2O measurements

Measured H_2O concentrations of LDST samples presented in this study were determined using a Cameca ims6f ion microprobe at the GFZ Helmholtz Centre Potsdam. As for EPMA, the plagioclase-hosted melt inclusions were carefully examined for post-entrapment modification, the host crystals were subsequently polished until surface exposure of the inclusions and ethanol-cleaned prior to analysis. The crystal wafers as well as the reference materials were subsequently mounted in indium metal contained on a single aluminum disk (adopting the procedure of Hauri et al., 2002). Sample mounts were stored for one week in an ultrahigh vacuum before being inserted into the instrument. The strict avoidance of epoxy allows for minimizing background values by preventing degradation of vacuum in the secondary ion source chamber, which remained stable at $\sim 1 \times 10^{-10}$ torr throughout the measurement campaign. A primary voltage of 12.5 kV was applied to the primary O^- source. A mass resolution of $M/\Delta M = 330$ was applied in order to eliminate isobaric molecular interferences. The area to be analyzed (25x25 μm) was pre-sputtered for three minutes. For analyses, the beam was set to raster this area using a 10 μm field-of-view aperture to avoid contamination from the rim. A set of natural basaltic and andesitic glasses (ALV519-4, Na23-6, A-46, TRD 80, P2-3) was used to calibrate the ion microprobe with H_2O contents from Danyushevsky et al. (1993) and Dixon and Clague (2001). For quantification, the intensities on the peaks of the secondary ion ^{1}H and ^{30}Si were recorded. The measured $^{1}H/^{30}Si$ ratios were calibrated versus the H/Si (atom%) ratios of reference materials. The data obtained on the reference glasses are presented in Appendix B in the auxiliary material and are used to constrain the calibration curve presented in Appendix B. The two main reference materials (TRD 80, A-46; Danyushevsky et al., 1993) were measured several times per day during the four day analytical campaign and proved highly reproducible with a relative repeatability of 3.1% (TRD 80, N = 10) and 8.7% (A-46, N = 13). Data quality was monitored by repeated measurements of complementary reference materials (ALV519-4, Na23-6, P2-3). The background of the instrument was monitored by two bracketing analyses of olivine supposed to contain water at the ppm level. The background remained below 0.29 wt%.

3.5 PETROGRAPHY OF LVC MAGMA TYPES

The tephra clasts from fallout deposits of the LVC cover a compositional range from basaltic andesite to rhyodacite. According to Gilbert et al. (2012) the pyroclastic deposits can be subdivided into three distinct petrographic groups: 1) Dark grey to black scoria tephra, 2) grey pumice tephra, and 3) light colored pumice tephra.

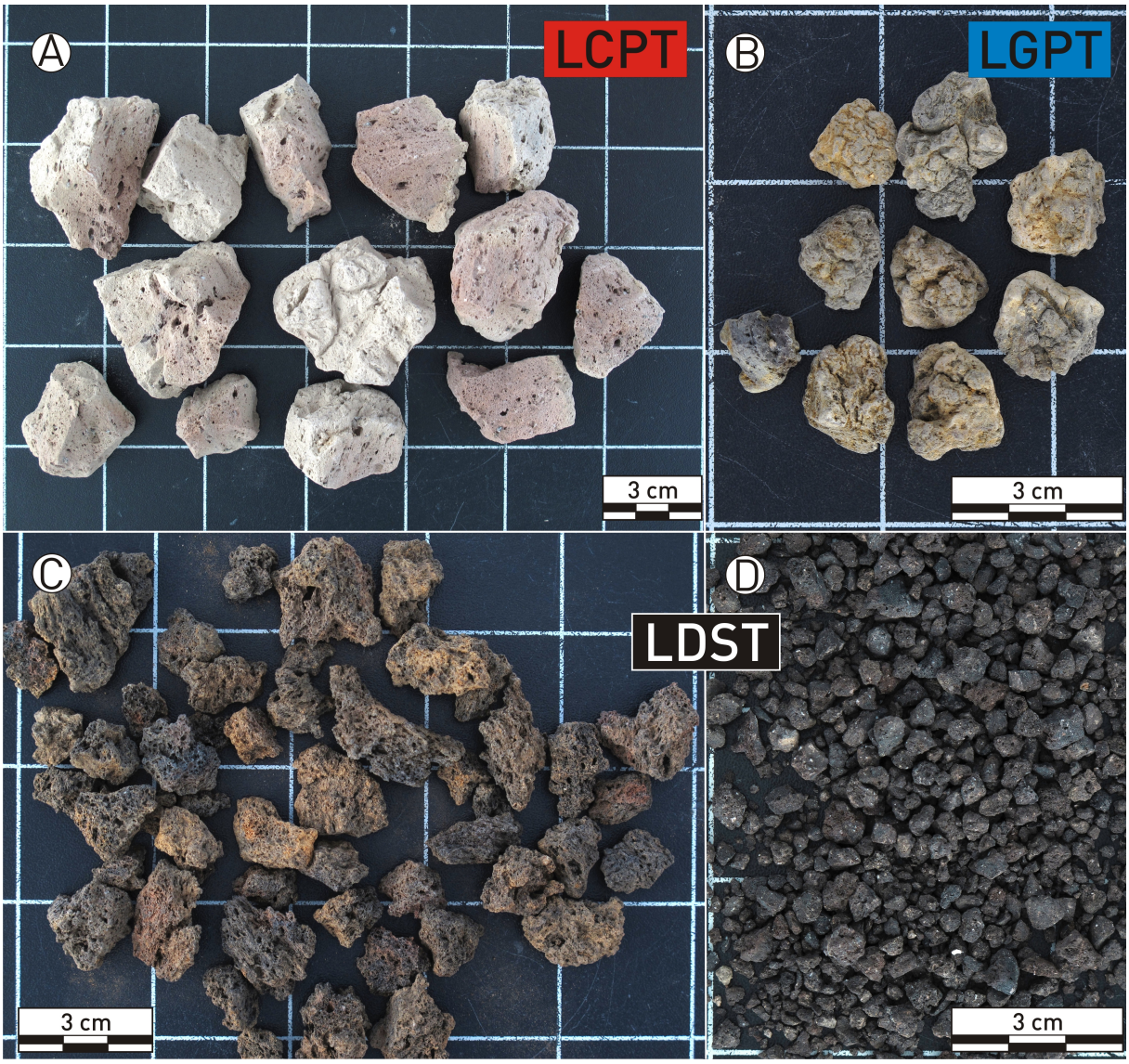

Fig. 3.3 Photographs of juvenile lapilli of the three compositional groups of the LVC stratigraphic succession. Modified from Gilbert et al. (2012).

1) Lonquimay dark scoria tephras (LDST)

The basaltic andesitic dark juvenile clasts (Fig. 3.3) occur throughout the LVC stratigraphic succession (11 fallout layers; Units: A, B, C, E, F, H, K, O, P, R, and W). The LDST tephras older 6000 b2k (Units A, B, C, E, and F) are composed of black, microvesicular to dense juvenile tachylitic clasts. Occurring phenocrysts are (in order of frequency): plagioclase (plag), clinopyroxene (cpx), olivine (ol), titanomagnetite (ti-mt), and ilmenite (ilm). The Fe-Ti oxides commonly appear as intergrowths with ferromagnesian minerals, only subordinately with plag crystals.

In contrast, vitrophyric to glomerophyric scoriae younger than 6000 b2k (Units O, P, R, and W) have higher vesicularity. The phenocryst assemblage comprises (in order of frequency): plag,

ol, cpx, ti-mt, and accessory apatite (ap) and hematite (hem). Most plagioclase phenocrysts are fragmented and show complex zoning patterns and sieve textures (Fig. 3.4). Beside their occurrence as pure LDST fallout deposits as described above, LDST products occur as scattered mafic clasts in several LCPT (units M, S, U, and V) and LGPT (units J and N) deposits throughout the whole stratigraphy, indicating that mafic injections into more evolved magmas were common.

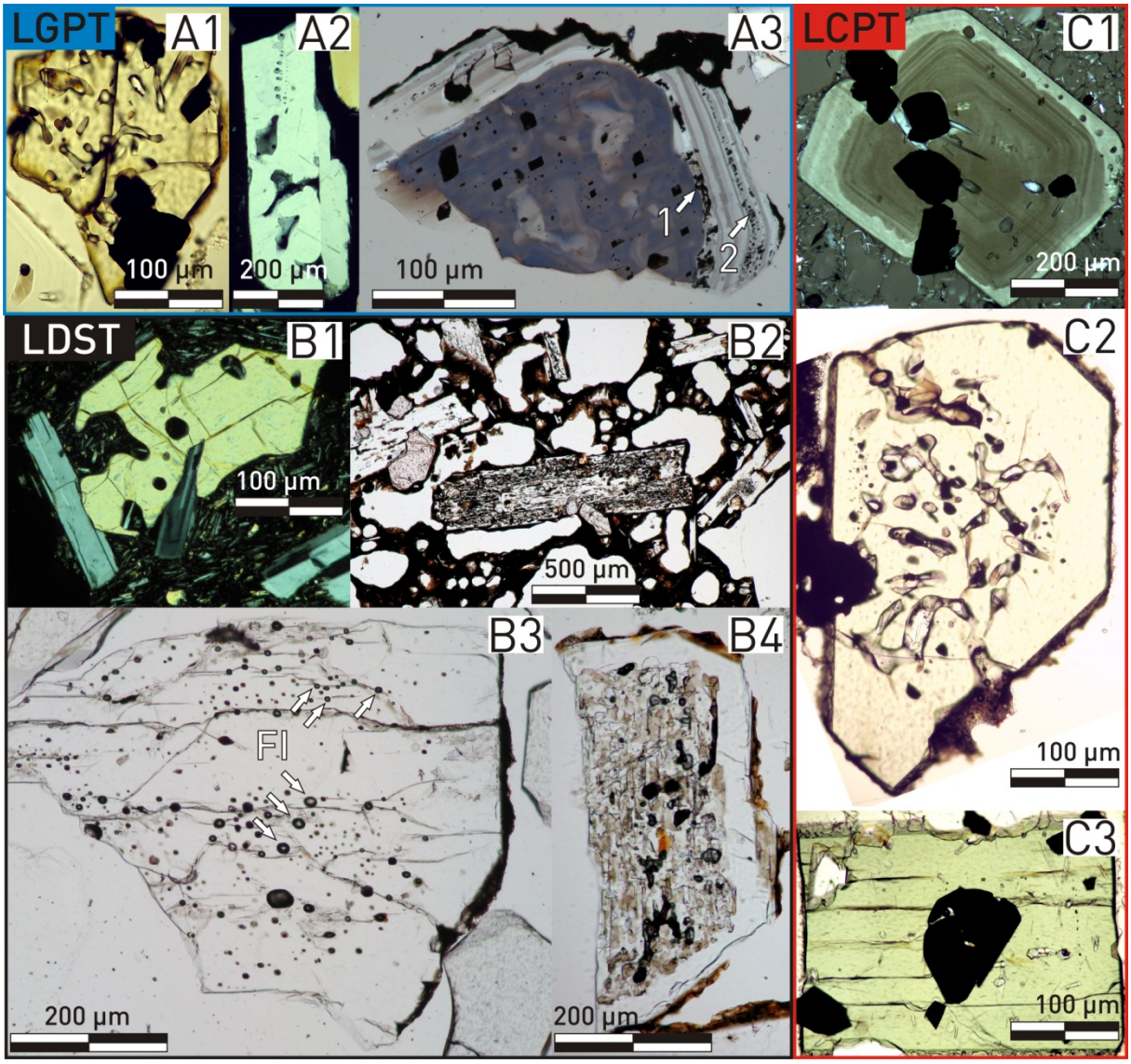

Fig. 3.4 Photomicrographs of the three compositional groups. LGPT: A1) olivine with resorption tubes intergrown with Ti-magnetite. A2) Plagioclase with resorption embayments and melt inclusions. A3) Resorbed plagioclase core with intensely zoned overgrowth rims. Two disequilibrium events are documented by incorporated melt inclusions (1&2). LDST: B1) Olivine with dissolution embayments intergrown with plagioclase. B2) Texture of vesicular dark scoria with resorbed plagioclase. B3) Plagioclase without zonation and numerous dispersed but decrepitated fluid inclusions (white arrows). B4) Plagioclase with strongly resorbed core covered by overgrowth rim. LCPT: C1) Zoned plagioclase with dissolution horizon covered by light colored rim contains inclusions of glassy melt and Ti-magnetite. C2) Euhedral olivine with corrosion tubes, C3) Euhedral clinopyroxene with apatite and Ti-magnetite inclusions. Figs. a1, a2, a3, b1, c1 under crossed polarizers, all others in transmitted light.

2) Lonquimay Grey Pumice Tephras (LGPT)

Six eruptive events, all older than 6000 b2k, discharged basaltic andesitic to trachyandesitic grey pumice clasts as either upper parts of compositionally zoned (Gb, Ib, and Mb) or homogeneous (Layers D, J, and N) fallouts. Grey pumice clasts are mostly microvesicular with some clasts having higher vesicularities. Several, especially larger, pumice fragments exhibit cracked surfaces (Fig. 3.3) resembling that of bread crust bombs. The phenocryst parageneses comprise plag, amphibole (hbl), ol, cpx, mt, ilm, ap, and hem (in order of occurrence). A significant amount of olivine and plagioclases crystals show textures indicative of disequilibrium with the surrounding melt (dissolution embayments and resorption tubes in plag and ol, resorbed plag cores; Fig. 3.4).

3) Lonquimay Colored Pumice Tephras (LCPT)

Eight layers (Ga, Ia, Ma, Q, Sb, Ta, Ua, and V) of light beige reddish colored angular pumice clasts (Fig. 3.3) with dacitic composition are recorded in the LVC tephrostratigraphy. Most colored pumice clasts show high vesicularities with large and elongated vesicles. The LCPT Layers Ga, Ia, and Ma, all older than 6000 b2k, each form the basal parts of compositionally zoned deposits with tops of LGPT or LDST clasts. In contrast, the colored-pumice deposits younger than 6000 b2k (Units Q, S, T, U, and V) are compositionally homogeneous except for the subordinate scattered occurrence of LDST clasts components in units S, U, and V. All colored pumice clasts contain plag, cpx, ol, mt, ilm, ap, and hem phenocrysts (in order of frequency) occurring as single crystals and mineral clusters (Fig. 3.4). Moreover, only pumice clasts older than 6000 b2k contain amphibole (hbl) minerals.

3.6 MINERAL COMPOSITIONS

Mineral phases were analyzed on polished uncovered petrographic thin sections as well as crystal grain mounts. In the following, mineral compositions are reported as mean values of corresponding populations with 1σ standard deviation.

3.6.1 Clinopyroxenes

Clinopyroxenes typically occur as euhedral to subhedral phenocrysts either as frequently scattered individual grains or as glomerocrysts. Clinopyroxene crystals are present in all samples from basaltic andesite to rhyodacite. Most phenocrysts are relatively homogeneous, with no systematic core-to-rim variations. Although the compositional range occupied by the phenocrysts

is pretty narrow in terms of Cpx-components ($DiHd_{0.73\pm0.08}$ $EnFs_{0.21\pm0.08}$ $CaTs_{0.02\pm0.02}$ $Jd_{0.02\pm0.00}$ $CaTi_{0.03\pm0.01}$; Tab. 3.1; Cpx-components are calculated using the normative scheme from Putirka et al., 1996), there are some variations in Mg numbers (Mg# = Mg/(Fe+Mg)) visible. Mg# vary systematically between the petrographic units (Fig. 3.5). Cpx crystals from LDST samples have in general the highest Mg# that correlate with highest Al_2O_3 and CaO contents. LDST cpx older than 6000 b2k show two distinct cpx populations centered at Mg# 73.9±1.5 and 81.3±2.4, whereas cpx from LDST deposits younger than 6000 b2k cluster around Mg# 67.6±5.7. LGPT samples have cpx phenocrysts with intermediate Mg# 69.7±3.2 and intermediate Al_2O_3 and CaO grades. The lowest Mg# and (lowest) Al_2O_3 and CaO contents are represented by LCPT samples, with samples older 6000 b2k peaking at Mg# 55.4±1.8 and LCPT samples younger 6000 b2k at Mg# 50.3±2.8.

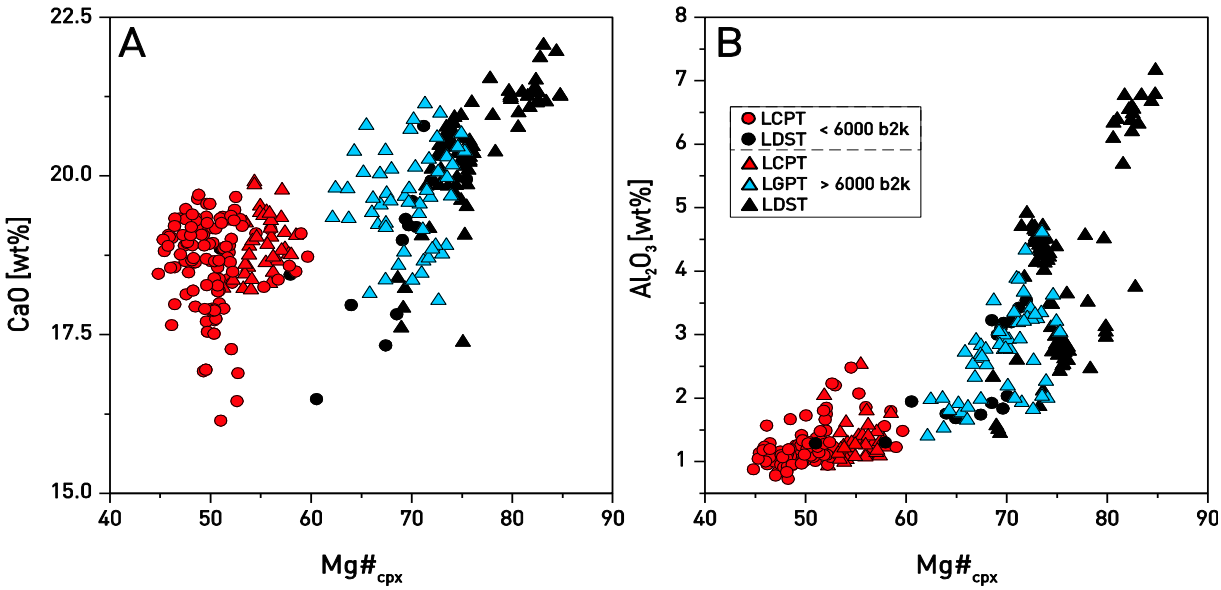

Fig. 3.5 Mg# of clinopyroxene crystals versus A) CaO-contents and B) Al_2O_3-contents.

3.6.2 Olivines

Subhedral to anhedral olivine is present in all petrographic groups as individual grains or glomerocrysts with other ferromagnesian minerals and significantly less frequently with plagioclase. LDST samples older than 6000 b2k feature three distinct Olivine populations ($Fo_{83\pm2}$ - approaching mantle values; $Fo_{72\pm1}$; $Fo_{42\pm2}$; Fig. 3.6), whereas LDST samples younger 6000 b2k show two olivine groups ($Fo_{72\pm2}$ and $Fo_{64\pm2}$). Most olivines but especially the high forsterite olivines show resorption embayments and tubes. Olivine compositions from LGPT units cover a wide range (Fo_{29}-Fo_{84}) with bimodal distribution peaking at $Fo_{63\pm4}$ and $Fo_{36\pm6}$. LCPT samples younger than 6000 b2k group into three distinct Fe-rich populations ($Fo_{39\pm1}$, $Fo_{31\pm0}$, $Fo_{24\pm1}$) and some rare scattered Mg-

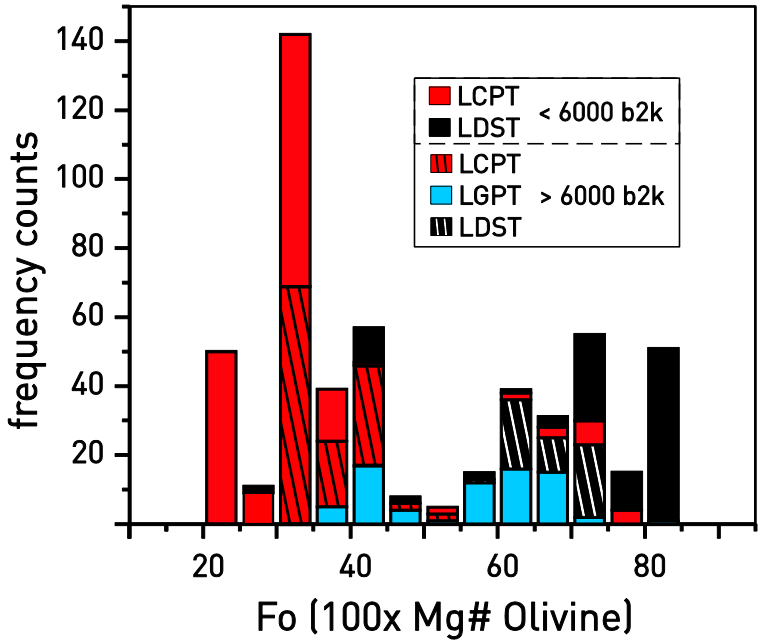

rich olivines ($Fo_{67\pm5}$) comparable to those from LDST samples. In contrast LCPT olivines older than 6000 b2k have only one olivine population peaking at $Fo_{36\pm4}$.

Fig. 3.6 Frequency histogram of olivine Mg# distinguished by petrographic group and eruptive age.

3.6.3 Amphiboles

Amphibole crystals are present in virtually all LCPT and LGPT samples older than 6000 b2k. The tschermakitic pargasite composition (Al#=0.05±0.01) shows only slight dependency from host rock petrographic group (LGPT: Mg# = 0.55±0.03; LCPT: Mg# = 0.49±0.02). Amphibole crystals occur as fragments of euhedral to subhedral crystals only and are not intergrown with other mineral species suggesting they did not precipitate simultaneous with the other phenocryst phases.

3.6.4 Fe-Ti-Oxides

In general, the Fe-Ti oxide crystals are subhedral to anhedral (Fig. 3.4). They occur as clusters of magnetite (X'Usp=0.51, Tab. 3.5), ilmenite (X'Ilm=0.92) and subordinately hematite crystals that are mainly intergrown or included in other ferromagnesian as well as plagioclase crystals. No core to rim compositional variations were identified within the oxides analyzed (Tab. 3.5).

3.6.5 Plagioclase

Plagioclase phenocrysts from all petrographic groups have euhedral to anhedral morphologies and exhibit zonation patterns including complex and oscillatory zoning (Fig. 3.7, Tab. 3.3). The phenocrysts range in composition from An_{95} to An_{30} and K_D(Ab-An) = 0.13±0.09 with surrounding matrix glass (Fig. 3.7, Tab. 3.3).

		Al_2O_3	CaO	Cr_2O_3	FeO	MgO	MnO	Na_2O	NiO	SiO_2	TiO_2	Mg#	N
< 6000 b2k	LCPT	1.22	18.63	0.01	17.98	10.20	0.71	0.28	0.02	50.66	0.32	50.2	130
	±STD	0.28	0.71	0.01	0.97	0.71	0.08	0.02	0.02	0.31	0.07	2.8	
	LDST	2.52	15.39	0.01	13.97	15.85	0.38	0.25	0.01	51.18	0.63	67.5	18
	±STD	1.01	6.76	0.01	4.83	3.07	0.14	0.13	0.02	0.66	0.21	5.7	
> 6000 b2k	LCPT	1.37	18.94	0.01	16.10	11.20	0.67	0.28	0.02	51.20	0.31	55.3	30
	±STD	0.39	0.48	0.01	0.71	0.42	0.09	0.02	0.03	0.29	0.06	1.8	
	LGPT	2.79	19.66	0.01	11.11	14.33	0.38	0.34	0.01	51.07	0.62	69.7	54
	±STD	0.74	0.79	0.01	1.19	0.77	0.10	0.06	0.02	0.45	0.14	3.2	
	LDST pop1	3.64	20.19	0.02	9.36	14.86	0.23	0.33	0.02	50.70	0.65	73.9	62
	±STD	0.94	0.63	0.03	0.67	0.54	0.06	0.04	0.03	0.85	0.13	1.5	
	LDST pop2	5.50	21.21	0.21	6.39	15.55	0.13	0.28	0.03	50.31	0.44	81.3	25
	±STD	1.58	0.43	0.13	1.00	0.28	0.06	0.02	0.04	0.84	0.08	2.4	

Tab. 3.1 Representative mean electron microprobe analyses of clinopyroxene phenocrysts from the post-glacial tephras of Lonquimay Volcano.

		Al_2O_3	CaO	Cl	Cr_2O_3	FeO	K_2O	MgO	MnO	Na_2O	NiO	SiO_2	TiO_2	Mg#	N
> 6000 b2k	LCPT	11.36	10.45	0.05	0.01	18.77	0.24	10.31	0.44	2.76	0.02	42.31	3.27	0.49	27
		0.16	0.15	0.02	0.01	0.72	0.02	0.48	0.05	0.09	0.01	0.29	0.16	0.02	
	LGPT	11.90	10.73	0.04	0.01	16.50	0.22	11.52	0.32	2.81	0.03	42.24	3.67	0.55	50
		0.26	0.18	0.01	0.02	1.11	0.01	0.61	0.05	0.05	0.01	0.19	0.20	0.03	

Tab. 3.2 Representative mean electron microprobe analyses of amphibole phenocrysts from the post-glacial tephras of Lonquimay Volcano.

		Al_2O_3	CaO	FeO	K_2O	MgO	Na_2O	SiO_2	TiO_2	Or	Ab	An	N
< 6000 b2k	LCPT	26.5	8.3	0.3	0.2	0.0	6.3	58.3	0.0	1.4	56.9	41.7	134
		0.6	0.7	0.1	0.1	0.0	0.5	0.9	0.0	0.3	3.8	3.9	
	LDST pop1	34.0	17.2	0.6	0.0	0.1	1.7	46.4	0.0	0.1	14.8	85.1	60
		0.7	0.8	0.1	0.0	0.0	0.4	1.0	0.0	0.1	3.8	3.9	
	LDST pop2	29.8	12.5	0.6	0.1	0.1	4.0	52.8	0.1	0.7	36.6	62.8	57
		0.9	1.0	0.1	0.0	0.0	0.5	1.2	0.0	0.3	4.7	4.9	
> 6000 b2k	LCPT	27.4	9.2	0.3	0.1	0.0	5.9	57.1	0.0	0.8	53.2	46.0	105
		0.7	0.8	0.0	0.0	0.0	0.5	1.1	0.0	0.1	3.9	4.0	
	LGPT pop1	28.4	10.4	0.4	0.1	0.0	5.2	55.4	0.0	0.8	47.1	52.1	167
		1.3	1.7	0.1	0.1	0.0	0.9	2.2	0.0	0.4	8.2	8.5	
	LGPT pop2	33.6	16.8	0.7	0.0	0.1	1.9	46.9	0.0	0.2	16.7	83.1	17
		1.1	1.1	0.3	0.0	0.0	0.6	1.4	0.0	0.2	5.2	5.3	
	LDST pop1	29.6	12.3	0.7	0.1	0.1	4.1	53.0	0.1	0.7	37.3	62.0	44
		1.6	1.9	0.3	0.1	0.1	0.9	2.5	0.0	0.5	8.7	9.1	
	LDST pop2	34.1	17.3	0.6	0.0	0.1	1.5	46.3	0.0	0.2	13.9	86.0	72
		0.8	0.9	0.4	0.0	0.0	0.4	1.1	0.0	0.2	3.9	4.0	

Tab. 3.3 Representative mean electron microprobe analyses of plagioclase phenocrysts from the post-glacial tephras of Lonquimay Volcano.

		Al_2O_3	CaO	Cr_2O_3	FeO	MgO	MnO	Na_2O	NiO	SiO_2	TiO_2	Mg#	K_D(Fe-Mg)	N
< 6000 b2k	LCPT pop1	0.01	0.20	0.00	48.10	17.15	1.32	0.02	0.00	33.17	0.02	38.85	0.34	16
		0.01	0.02	0.00	0.45	0.40	0.07	0.01	0.01	0.18	0.01	0.75	0.01	
	LCPT pop2	0.01	0.26	0.01	52.60	13.26	1.69	0.00	0.00	32.17		30.99	0.39	73
		0.00	0.03	0.01	0.42	0.15	0.21	0.00	0.01	0.41		0.31	0.18	
	LCPT pop3	0.01	0.26	0.01	55.69	10.06	2.10	0.00	0.01	31.86	0.01	24.23	0.40	53
		0.00	0.03	0.01	0.48	0.26	0.18	0.01	0.01	0.15	0.01	0.34	0.01	
	LDST pop1	0.03	0.19	0.01	25.41	36.66	0.44	0.00	0.02	37.24		71.15	0.17	34
		0.04	0.02	0.01	1.52	1.39	0.05	0.00	0.02	0.27		0.58	0.01	
	LDST pop2	0.02	0.21	0.00	31.24	31.66	0.59	0.00	0.01	36.26		64.24	0.23	35
		0.01	0.04	0.01	1.45	1.27	0.08	0.01	0.02	0.34		1.96	0.02	
> 6000 b2k	LCPT pop1	0.01	0.21	0.01	49.61	15.64	1.56	0.01	0.00	32.93	0.01	35.83	0.43	93
		0.01	0.16	0.01	1.12	0.90	0.22	0.01	0.01	0.29	0.02	4.07	0.13	
	LCPT pop2	0.02	0.19	0.01	25.22	34.82	0.45	0.00		35.46		64.24	0.23	
		0.01	0.03	0.01	3.88	3.14	0.12	0.00		0.84		1.96	0.02	
	LGPT pop1	0.02	0.20	0.01	31.97	31.00	0.69	0.00	0.01	36.11	0.00	63.24	0.23	50
		0.01	0.03	0.01	3.59	3.03	0.18	0.00	0.02	0.70	0.01	4.88	0.04	
	LGPT pop2	0.01	0.22	0.00	49.47	15.81	1.58	0.00	0.00	32.91		36.23	0.36	57
		0.00	0.05	0.00	3.32	2.98	0.29	0.00	0.00	0.66		5.84	0.06	
	LDST pop1	0.03	0.16	0.01	16.25	44.10	0.22	0.00	0.11	39.12		82.12	0.07	49
		0.00	0.02	0.01	1.36	1.12	0.02	0.00	0.03	0.31		2.29	0.01	
	LDST pop2		0.20	0.00	25.18	36.63	0.43	0.00	0.03	37.50		70.48	0.18	39
			0.02	0.01	2.79	2.28	0.08	0.00	0.03	0.56		0.22	0.03	
	LDST pop3	0.01	0.20	0.00	45.67	18.91	1.44	0.02	0.00	33.70	0.03	42.45	0.34	15
		0.01	0.04	0.00	1.27	1.01	0.10	0.02	0.00	0.28	0.04	1.98	0.02	

Tab. 3.4 Representative mean electron microprobe analyses of olivine phenocrysts from the post-glacial tephras of Lonquimay Volcano.

			Al_2O_3	Cr_2O_3	FeO	MgO	MnO	NiO	SiO_2	TiO_2	N
< 6000 b2k	LCPT	mgt	2.01	0.00	73.46	0.99	0.88	0.02	0.09	22.55	44
			0.15	0.01	0.73	0.18	0.06	0.02	0.01	0.58	
		ilm	0.14	0.01	46.97	1.50	1.00	0.02	0.01	50.34	11
			0.02	0.01	0.16	0.20	0.09	0.03	0.01	0.19	
	LDST	mgt	4.08	0.31	75.76	2.88	0.53	0.02	0.32	16.09	52
			1.71	1.25	4.42	1.39	0.20	0.03	1.10	5.26	
		ilm	0.15	0.00	46.84	1.61	1.02	0.00	0.00	50.38	1
> 6000 b2k	LCPT	mgt	2.51	0.00	74.02	1.35	0.83	0.02	0.09	21.18	84
			0.40	0.01	0.41	0.39	0.07	0.02	0.02	0.36	
		ilm	0.23	0.00	46.14	2.78	0.86	0.01	0.01	49.97	7
			0.06	0.01	0.48	0.83	0.14	0.03	0.01	0.36	
	LGPT	mgt	3.39	0.08	75.23	2.34	0.68	0.02	0.09	18.15	75
			1.39	0.32	2.94	1.03	0.19	0.03	0.03	3.96	
		ilm	0.22	0.01	46.19	2.85	0.84	0.02	0.01	49.86	30
			0.10	0.01	0.76	1.31	0.20	0.02	0.01	0.60	
	LDST pop1	mgt	5.76	0.07	79.04	4.03	0.35	0.03	0.11	10.61	30
			0.18	0.08	0.14	0.04	0.02	0.03	0.01	0.11	
	LDST pop2	mgt	3.79	0.06	77.97	3.65	0.51	0.01	0.09	13.89	6
			0.15	0.00	0.35	0.18	0.02	0.01	0.01	0.64	
	LDST pop3	mgt	2.60	0.01	74.39	1.54	0.87	0.01	0.08	20.47	11
			0.23	0.01	0.37	0.24	0.06	0.02	0.01	0.82	
	LDST	ilm	0.06	0.01	47.34	2.46	0.61	0.04	0.02	49.46	3
			0.02	0.01	0.32	0.10	0.03	0.06	0.02	0.26	

Tab. 3.5 Representative mean electron microprobe analyses of Fe-Ti oxide pairs from the post-glacial tephras of Lonquimay Volcano.

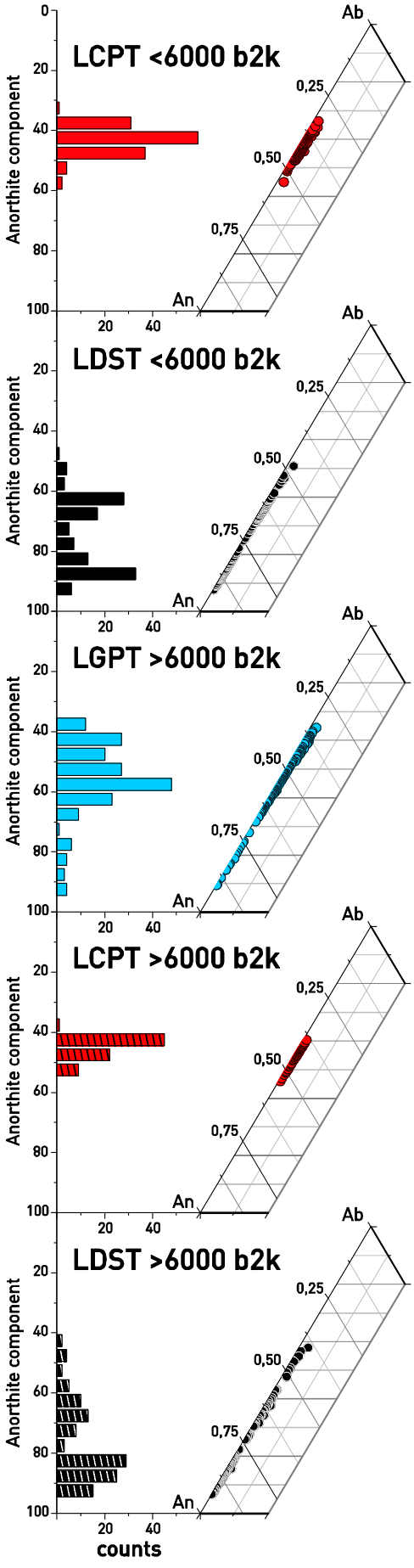

Plagioclase phenocrysts from LDST samples cover a large range in composition from An_{50} to An_{95} showing a clearly bimodal distribution (Fig. 3.7, Tab. 3.3). Samples older than 6000 b2k show distinct peaks centered at $An_{86\pm4}$ and $An_{66\pm5}$ and samples younger than 6000 b2k at $An_{85\pm4}$ and $An_{63\pm5}$. Phenocrysts mostly show complex or oscillatory zoning patterns but there are also plagioclase fragments with no obvious zonation in which decrepitated fluid inclusions are randomly dispersed (Fig. 3.4B3). Such crystals are commonly interpreted as metasomatically altered plutonitic wall rocks (e.g. Hansteen et al., 1998).

Plagioclase phenocrysts from LGPT samples have a similar range in composition with a broad peak (An_{70} to An_{35}; K_D(Ab-An)=0.10±0.02 with matrix glass) centered around $An_{59\pm10}$, and subordinate more Ca-rich compositions extending up to An_{95} (Fig. 3.8). Evidence for partial resorption (i.e. dissolution zones and embayments) and sieve textures are common in phenocrysts from LDST and LGPT (Fig. 3.4). However, disequilibrium textures, in particular the exsolved cores, are more pronounced in LDST plagioclase crystals. In contrast, feldspars from all LCPT samples (older and younger than 6000 b2k) occupy a significantly narrower compositional range (An_{60} to An_{30}, K_D(Ab-An)=0.11±0.02 with matrix glass; Fig. 3.7) with a distinct peak around An_{45} ($LCPT_{>6000b2k}$ $An_{46\pm4}$; $LCPT_{<6000b2k}$ $An_{43\pm6}$). Disequilibrium textures only occur in a minor portion of LCPT crystals.

Fig. 3.7 Ternary projections of plagioclase compositions of Lonquimay volcanic products by petrographic group and eruptive age. Histograms on the left show the frequency distribution of plagioclase compositions in 5 mol% classes.

		SiO_2	Al_2O_3	CaO	FeO	K_2O	MgO	MnO	Na_2O	P_2O_5	TiO_2	F	S	Cl	N
< 6000 b2k	LCPT	66.62	16.78	3.43	4.76	1.42	0.64	0.16	5.64	0.13	0.43	0.1015	0.0164	0.3148	305
	±STD	1.61	0.99	0.59	1.00	0.25	0.29	0.07	0.71	0.05	0.10				
	LDST	58.70	13.98	5.96	11.30	1.10	2.54	0.26	3.81	0.36	1.93	0.0888	0.0471	0.3706	118
	±STD	3.27	1.30	1.22	2.05	0.28	0.99	0.05	0.63	0.10	0.41				
> 6000 b2k	LCPT	68.99	15.46	2.58	4.59	1.99	0.37	0.15	5.36	0.09	0.40	0.1211	0.0277	0.7713	99
	±STD	2.05	1.07	0.66	1.28	0.32	0.24	0.06	0.69	0.06	0.14				
	LGPT	59.96	15.95	5.29	8.93	1.14	2.07	0.22	4.68	0.35	1.38	0.1156	0.0125	0.3415	71
	±STD	3.19	1.53	1.28	2.31	0.47	1.30	0.07	0.86	0.07	0.39				
	LDST	56.64	14.49	6.71	12.01	0.95	3.03	0.25	3.72	0.29	1.87	0.0850	0.0557	0.2104	59
	±STD	2.70	2.09	0.99	2.05	0.34	1.49	0.06	0.66	0.09	0.28				

Tab. 3.6 Representative mean electron microprobe analyses of matrix glasses from the post-glacial tephras of Lonquimay Volcano.

		SiO_2	Al_2O_3	CaO	FeO	K_2O	MgO	MnO	Na_2O	P_2O_5	TiO_2	F	S	Cl	N
< 6000 b2k	LCPT	67.95	15.70	2.97	5.48	1.75	0.56	0.16	4.77	0.15	0.52	0.1022	0.0387	0.4338	244
	±STD	2.42	0.87	0.89	1.28	0.33	0.68	0.06	0.90	0.43	0.27				
	LDST	54.99	16.44	7.30	10.51	0.77	3.88	0.20	4.27	0.22	1.41	0.1007	0.1443	0.1534	52
	±STD	2.26	2.45	1.36	1.92	0.25	1.43	0.06	0.60	0.08	0.30				
> 6000 b2k	LCPT	67.95	15.70	2.97	5.48	1.75	0.56	0.16	4.77	0.15	0.52	0.1022	0.0387	0.4338	244
	±STD	2.42	0.87	0.89	1.28	0.33	0.68	0.06	0.90	0.43	0.27				
	LGPT	61.55	15.67	4.97	8.23	1.32	2.04	0.20	4.80	0.21	1.01	0.1434	0.1248	0.3219	166
	±STD	6.20	1.42	2.11	3.19	0.58	1.96	0.08	0.71	0.14	0.54				
	LDST	55.52	16.85	7.99	9.92	0.65	3.78	0.19	3.72	0.18	1.21	0.0785	0.1463	0.2079	63
	±STD	2.90	2.61	2.58	2.72	0.25	2.06	0.11	1.17	0.06	0.25				

Tab. 3.7 Representative mean electron microprobe analyses of inclusion glasses from the post-glacial tephras of Lonquimay Volcano.

3.7 MATRIX GLASS COMPOSITIONS

The compositional variation in matrix glasses from the least evolved LDST basaltic andesites to the most evolved LCPT trachydacite display distinct trends on bivariate major element versus SiO_2 diagrams. The trends are defined by increasing K_2O but decreasing MgO, FeO, CaO, and TiO2 with increasing SiO2 contents (Fig. 3.8; Tab. 3.6). P2O5 and Al_2O_3 increase up to ~63 wt% SiO_2 and then decrease with a comparably sharp bend. Na2O contents of matrix glasses increase towards even higher SiO_2 contents (~68 wt%) before decreasing afterwards.

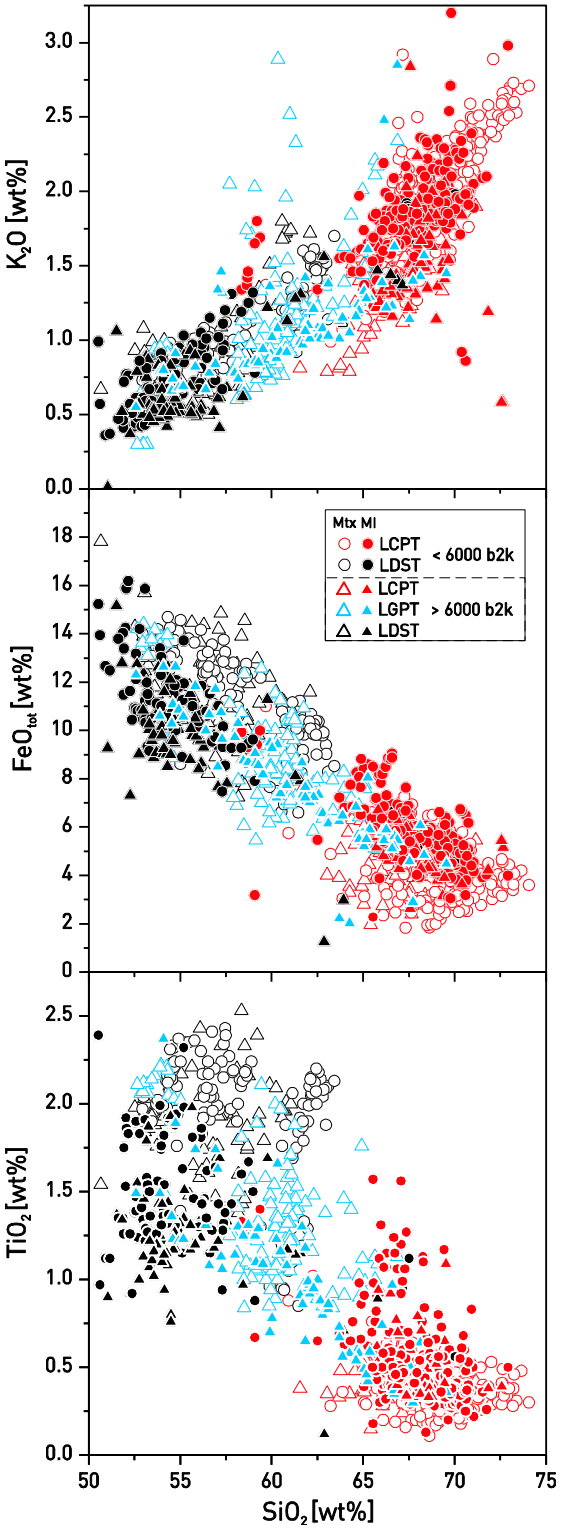

LCPT glasses occupy a compositional range in the dacite-rhyolite field. Although there is some overlap, LCPT glasses younger than 6000 b2k have higher SiO_2 contents (65-75 wt%) than LCPT samples older than 6000 b2k (62.5-70 wt%). LDST and LGPT glasses are more diverse in composition than those from LCPT samples. The melt phase of the LDST eruptions - marking the most mafic compositions - was basaltic andesite, with some compositional diversity towards andesite. Although there is considerable overlap, the LDST melts (52-63 wt% SiO_2) were generally less evolved than the intermediate LGPT magmas (57.5-65 wt% SiO_2) that dominate the andesite field (Fig. 3.8; Tab. 3.6). However, the matrix glass compositions from the rare LDST-clasts scattered in the LCPT-deposits younger than 6000 b2k form a distinct narrow field of intermediate compositions (61-63 wt% SiO_2).

Fig. 3.8 (previous page) Major element variation diagrams of matrix glass (Mtx; open symbols) and melt inclusions (MI; filled symbols) from the post-glacial explosive eruptions at Lonquimay volcano. Note that - although there is some considerable overlap - MI are less evolved than Mtx for LCPT and LDST samples. LGPT MI occupy a wide array of compositions extending to even more evolved compositions than corresponding matrix glasses.

3.8 MELT INCLUSION COMPOSITIONS

Light to dark brown plagioclase-, clinopyroxene- and olivine-hosted melt inclusions are common in the magmatic products from the 23 eruptions investigated. No significant compositional variations were found between plagioclase or olivine hosted melt inclusions.

The LDST basalt-andesite melt inclusions encompass a relatively narrow compositional range ($LDST_{<6000b2k}$ 50-60 wt% SiO2, $LDST_{>6000b2k}$ 52-58 wt% SiO2) and are typically less evolved than the surrounding matrix glass (Fig. 3.8; Tab. 3.7). Melt inclusions from the intermediate LGPT eruptions occupy a comparably wide SiO2 range (LGPT 52.5-70 wt% SiO_2), and in general they are either similar to, or more evolved than their co-existing matrix glasses (Fig. 3.8; Tab. 3.7). The most evolved compositions of LCPT samples are reflected by the most evolved melt inclusion compositions, too. The samples older than 6000 b2k encompass a narrow compositional range ($LCPT_{>6000b2k}$ 65-70 wt% SiO_2). In contrast, the LCPT melt inclusions younger than 6000 b2k occupy a broader compositional range ($LCPT_{<6000b2k}$ 63-72 wt% SiO_2) but the majority extends to more evolved compositions, just like the corresponding matrix glasses.

3.8.1 Volatile inventory of melt inclusions

A total of 450 plagioclase and olivine-hosted melt inclusions, from representative samples of each petrographic group, were analyzed for their chlorine (Cl) and sulfur (S) contents in order to determine pre-eruptive Cl and S melt contents. In general, there is no observable dependency between host mineral and volatile content.

Chlorine

Fig. 3.9A shows the chlorine concentrations against MgO contents as indicator for the degree of differentiation. In general, chlorine contents increase curvilinearly towards higher degrees of differentiation (i.e. lower MgO contents). Nevertheless, melts before and after 6000 b2k behaved slightly different. The LDST melt inclusions older than 6000 b2k have lower chlorine contents than comparable samples younger than 6000 b2k. In contrast, chlorine contents are comparable for all LCPT samples although samples younger than 6000 b2k are generally more evolved.

Sulfur

Sulfur contents of melt inclusions (Fig. 3.9B) decrease linearly with declining MgO contents, resulting in highest S-contents for LDST, intermediate contents for LGPT and lowest contents for LCPT samples. LDST samples younger than 6000b2k show a wide range in S for a given MgO content (e.g. S (<6000 b2k)=100-1200 ppm at MgO=4 wt%). In contrast, samples older than 6000 b2k have mostly retained relatively high S-contents (e.g. S (>6000 b2k)=900-1200 ppm at MgO=4 wt%).

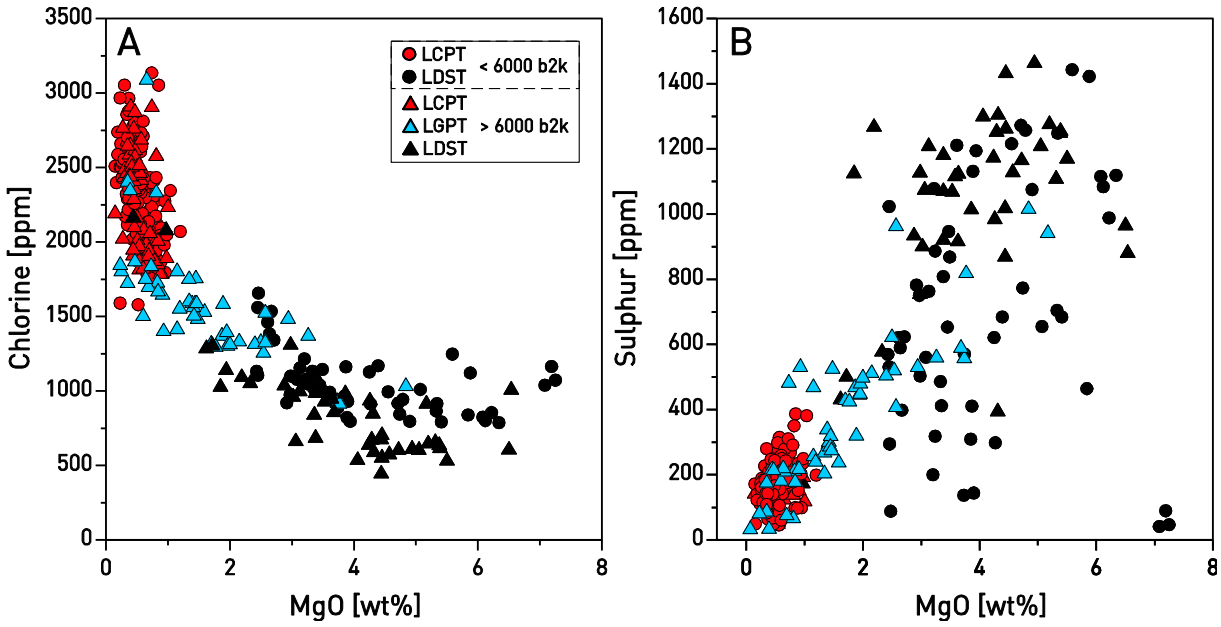

Fig. 3.9 A) Measured chlorine and MgO contents of melt inclusions B) Measured sulfur (S) compositions of melt inclusions. Note the strong decrease in S already at the beginning of the differentiation leading to a strong depletion in S for the differentiated LCPT/LGPT samples. This strong depletion of S suggests an early separation of a S-rich fluid phase, that is also documented as (decrepitated) fluid inclusions in LDST crystals.

H_2O

H_2O-contents of nine representative melt inclusions from LDST samples were determined by SIMS measurement. The results (Tab. 3.8; Fig. 3.12) vary between 0.2 and 4.0 wt% (H_2O_{mean}=3.1±0.7 wt%, samples with H_2O<0.2 wt% are excluded from average).

Tab. 3.8 Measured H_2O contents of representative melt inclusions from LDST samples.

	host mineral	rock sample	SiO_2 EPMA	H_2O [wt%]
< 6000 b2k	ol	C-399	56.16	3.14
	plag	C-399	56.16	0.13
	plag	C-501	52.28	0.15
> 6000 b2k	plag	C-196	53.75	0.97
	plag	C-196	53.89	1.88
	plag	C-196	53.75	2.90
	plag	C-196	53.75	3.06
	ol	C-196	53.49	2.87
	ol	C-375	63.93	3.57
	ol	C-377	54.76	4.04

3.9 PRE-ERUPTIVE INTENSIVE PARAMETERS

Based on its tephrostratigraphic record (Gilbert et al., 2012), LVC is one of the most explosive centers in the Central Southern Volcanic Zone. However, little is yet known about the underlying plumbing system and resulting consequences for LVC's petrogenesis. Gilbert et al. (2012) made a first attempt to investigate the magmatic system beneath the volcano using clinopyroxene-liquid thermobarometry. We here use several complementary mineralogical thermobarometers and volatile component analysis in order to evaluate these results and better constrain physicochemical magma chamber conditions prevailing prior to the eruptions.

To ensure that the obtained parameters are representative, we used mineral and glass compositions (both matrix- and melt inclusion glasses as available) that fulfill equilibrium criteria (e.g. Putirka, 2008). Especially melt inclusions paired with mineral compositions from the immediately overgrown crystal, as well as crystal rims and matrix glass compositions give very good (equilibrated) results and allow for insights into LVC's magmatic system. All intensive parameters are reported as averages and standard deviations of obtained populations. In general, the standard deviations are typically much smaller than the System Estimation Error (SEE) of the models used for the calculations. P-T-X results and SEEs are given in Tab. 3.3.2. As a further check on our thermobarometric estimates, we compared our results from different independent models for compliance (Fig. 3.11).

3.9.1 Clinopyroxene-liquid thermobarometry

Based on numerous petrologic experiments and thermodynamic models (e.g. Nimis, 1999; Putirka et al., 1996; Putirka, 2005) the compositions of cpx and equilibrated melts can be used to model crystallization pressure and temperature. We here used matrix-glass and cpx-rim compositions - of the typically not compositionally zoned cpx phenocrysts - to calculate pre-eruptive p-T. Used mineral-melt pairs were checked to satisfy the equilibrium condition $K_D^{cpx\text{-}liq}(Fe\text{-}Mg)^{equ}=0.28\pm0.08$ ($K_D^{cpx\text{-}liq}(Fe\text{-}Mg)=[MgO_{liq}FeO_{cpx}]/[MgO_{cpx}FeO_{liq}]$) calculated with the temperature compensated formula (Eq. 35) of Putirka (2008). An additional check for equilibrium was performed by comparing observed (i.e. measured) and predicted cpx-components (based on the corresponding melt composition). Cpx-components are calculated using the normative scheme of Putirka et al. (1996), whereas the predicted cpx-components were computed using Eq. 3.1a (DiHd), Eq. 3.2 (EnFs), Eq. 3.4 (CaTs), Eq. 3.5 (Jd) and Eq. 3.7 (CrCaTs) of Putirka (1999). Only cpx-liquid pairs that satisfy equilibrium tests were used for thermobarometric calculations

solving Eq. 31 (System Estimation Error (SEE)=290 MPa) for pressure and Eq. 33 (SEE=45°C) for temperature (Putirka, 2008) simultaneously in an iterative procedure.

The results (Tab. 3.9) reveal different storage conditions for each of the petrographic groups. Cpx-liquid pairs from LDST yield the highest pressures and temperatures (Pmean≈440±100 MPa; Tmean≈1065±25°C). LCPT samples in contrast provide the lowest values (Pmean≈80±25 MPa; Tmean=935±20°C), whereas LGPT samples deliver intermediate values (Pmean=240±110 MPa, Tmean=1010±15°C). In order to verify the previous estimates we computed cpx-saturation temperatures from melt compositions (matrix glasses and melt inclusions) using Eq. 34 (SEE=51°C) of Putirka (2008). The results (given in Tab. 3.9) converge very well with the cpx-liquid results indicating valid estimates.

3.9.2 Olivine-liquid thermometry

Olivine-liquid (ol-liq) equilibria were used to estimate crystallization temperatures from crystal rims and matrix glasses using Eq. 22 from Putirka (2008). The following input parameters were used: pressures derived from cpx-liq thermobarometry (Eq. 31; Putirka, 2008), H_2O_{melt} from plag-liq thermohygrometer (Eq. 25b; Putirka, 2008). Only olivine-melt pairs that fulfill the equilibrium criterium $K_D(Fe\text{-}Mg)_{ol\text{-}liq}^{equ}=0.30\pm0.03$ (Roeder and Emslie, 1970) are included in the temperature estimates. The rigorous filtering for equilibrium conditions yielded valid estimates for LCPT samples only (T_{mean}(<6000 b2k)=878±24°C, T_{mean}(>6000 b2k)=893±34°C) when using olivine-matrix glass pairs. We therefore used melt inclusion and host crystal compositions for additional temperature estimates. Again LCPT results (T_{mean} (<6000 b2k)=885±21°C, T_{mean}(>6000 b2k)=902±12°C) yield the lowest, LGPT results (T_{mean} (>6000 b2k)=995±8°C) are intermediate and LDST values (T_{mean}(>6000 b2k)=1076±14°C) mark the top end. In general, T calculated from olivine phenocrysts (Putirka, 1997) matches T from clinopyroxene phenocrysts to within 1σ model error. Olivines yield somewhat lower T values (average -39°C) compared to clinopyroxenes (Tab. 3.9) for LCPT samples, but this difference probably reflects the late-stage precipitation of Fe-rich olivine in these evolved samples. However, the ol-liq temperatures for LGPT and LDST samples (as available) coincide very precisely with our cpx-derived T estimates (Tab. 3.9).

3.9.3 Amphibole-thermobarometry

The compositions of the amphiboles - which are restricted to the lower part of the stratigraphy - are used to apply the thermobarometric method of Ridolfi et al. (2010). Because the amphibole crystals lack any systematic compositional core-to-rim zonation, the derived pressure and

temperature values are fairly uniform and seem to be independent of the host-rock composition (LCPT and LGPT). Although more than 80 analyses of crystal rims and cores from nine different samples were used, mean values (P_{mean}=337±25 MPa, SEE=40-70 MPa; T_{mean}=929±18°C, SEE=22°C) have comparably small standard deviations. The mean values per rock type are P_{mean}=313±10 MPa and T_{mean}=912±10°C for LCPT, and P_{mean}=351±20 MPa and T_{mean}=939±13°C for LGPT. The standard deviations are again smaller than the reported SEEs (Tab. 3.9) of the thermodynamic models. Although the temperatures quitely matches results from other used thermometers, the pressure estimates are significantly higher than cpx-liq estimates (Tab. 3.9). fO_2-estimates from amphibole compositions (Tab. 3.9) yield oxygen fugacity (fO_2) conditions between the NNO- and FMQ-buffers for most LCPT and LGPT samples (Fig. 3.10).

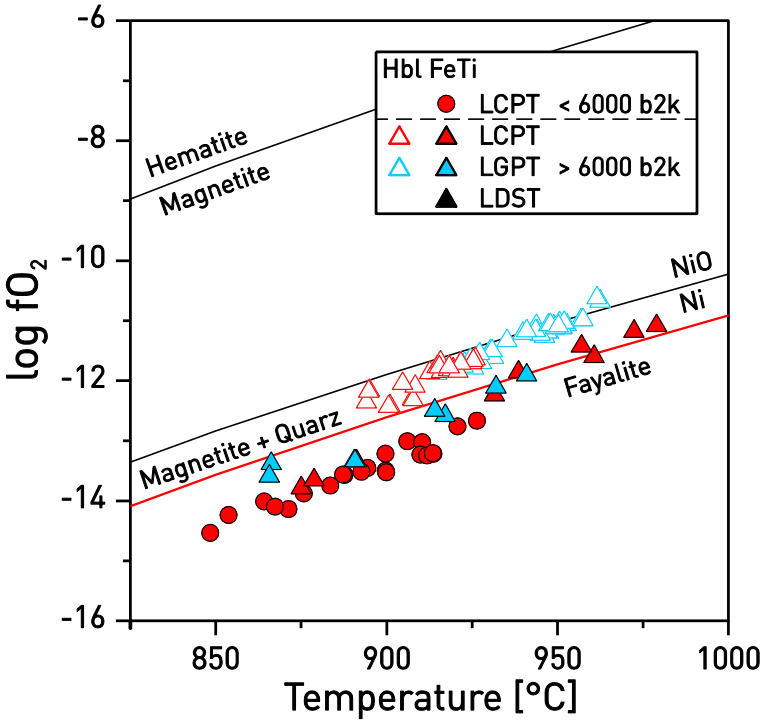

Fig. 3.10 Comparison between absolute fO_2 calculated from Fe-Ti oxides (closed symbols) and amphiboles (open symbols) and temperature-dependent oxygen buffer reactions.

3.9.4 Fe-Ti-oxide thermometry

Fe-Ti oxide geothermometry was used to estimate equilibration temperatures and oxygen fugacities. The Mg/Mn equilibrium test after Bacon and Hirschmann (1988) was only passed by ilmenite-magnetite pairs from LCPT and LGPT samples. Equilibrium temperature and fO_2 were computed according to the geothermometer of Andersen & Lindsley (1985) using the method from Stormer (1983) to calculate ulvöspinel and ilmenite components. The results yield T_{mean}=893±22°C and fO_2=-13.5±0.5 for samples younger 6000 b2k. Samples older than 6000 b2k yield temperatures around 932±43°C and fO_2=-12.2±1.2 indicating fO_2-conditions below the FMQ-buffer for most LCPT and LGPT samples (Fig. 3.11). The temperatures fall again well within the results from complementary methods. The oxygen fugacities, however, are slightly lower than values obtained from amphibole barometry.

	Parameter	Reference	Eqn	SEE	Unit	< 6000 b2k		> 6000 b2k		
						LCPT	LDST	LCPT	LGPT	LDST
Plagioclase	T_plag-liq	Putirka (2008)	Eqn 24a	36	°C	889±23	1147±29	921±27	1008±40	1115±46
	T_plag-sat	Putirka (2008)	Eqn 26	37	°C	915±20	1148±22	942±22	1019±39	1117±44
	H2O_melt	Putirka (2008)	Eqn 25b	1.1	wt%	5.0±0.5	1.0±0.8	4.9±0.5	3.2±0.9	2.4±1.3
		Lange et al. 2009		0.32	wt%	4.6±0.5	1.5±0.4	4.2±0.4	3.0±0.9	2.4±0.9
	P_plag-liq	Putirka (2008)	Eqn 25a	380	Mpa	60±80	292±29	64±78	−120±157	250±127
Clinopyroxene	P_cpx_liq	Putirka (2008)	Eqn 31	290	Mpa	96±43	444±109	72±10	241±108	437±125
	T_cpx-liq	Putirka (2008)	Eqn 33	45	°C	927±19	1056±21	941±24	1011±15	1074±27
	T_cpx-sat	Putirka (2008)	Eqn 34	51	°C	926±23	1029±54	945±35	1018±12	1065±25
Olivine	T_ol-sat	Putirka (2008)	Eqn 22	43	°C	878±24		893±34		
		Putirka (2008)	Eqn 22	43	°C	⋆885±21		⋆902±12	⋆995±8	⋆1076±14
Fe-Ti-Oxides	T [°C]	Andersen & Lindsley (1985); X'Usp & X'Ilm from: Stormer (1983)			°C	893±22		932±43		
	log10 fO2					−13.52±0.50		−12.24±1.15		
Amphibole	T [°C]	Ridolfi et al. 2010		22	°C			912±10	939±13	
	P [MPa]			40-70	Mpa			313±10	351±20	
	log 10 fO2			0.4				−11.95±0.26	−11.32±0.32	
	ΔNNO							−0.33±0.14	−0.16±0.11	
	H2O_melt			1	wt%			6.8±0.3	6.6±0.2	

⋆= derived from MI

Tab. 3.9 Summary of the pre-eruptive conditions for the post-glacial eruptions of Lonquimay Volcano. Asterisk marks data derived from melt inclusions

3.9.5 Plagioclase-liquid-thermohygrometry

Because plagioclase crystallization depends strongly on the H_2O activity of the melt, plagioclase-liquid (plag-liq) equilibria can further be used as a thermo-hygrometer to estimate H_2O contents and temperature during crystallization. Crystal rim-matrix glass pairs were used to perform calculations using formulations from Putirka (2008) and Lange et al. (2009).

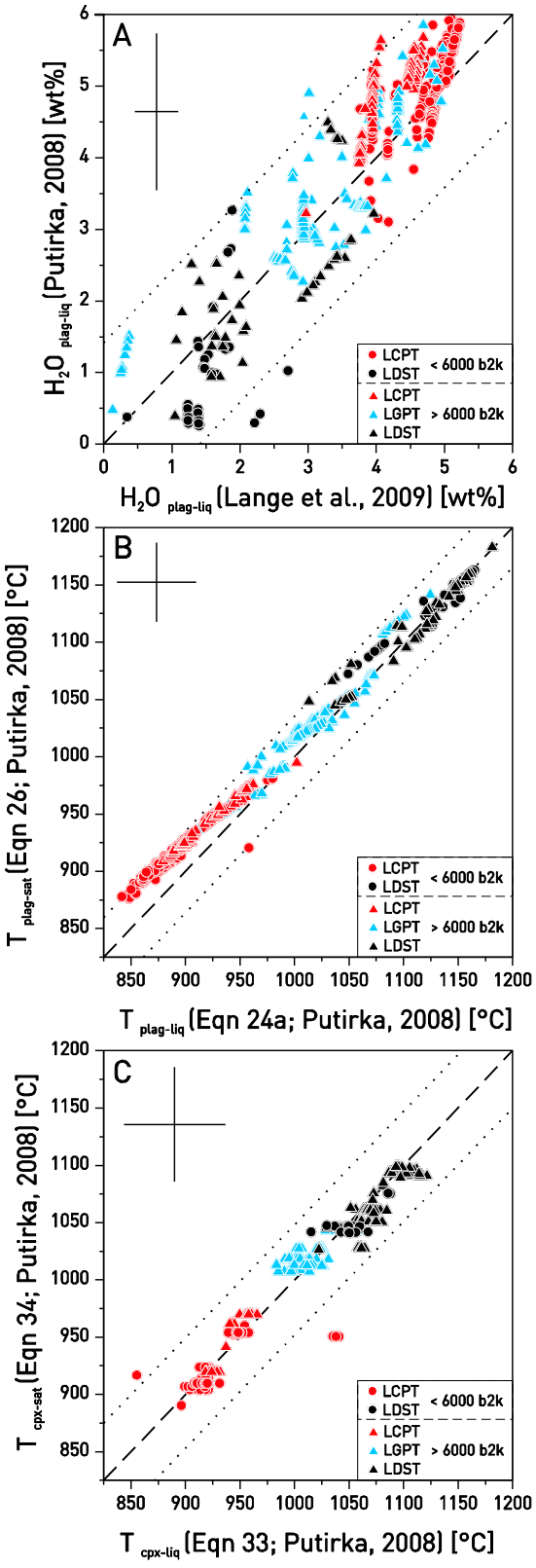

Pressure estimates from clinopyroxene-liquid equilibria and H_2O_{liq} from Eq. 25b (Putirka, 2008) were used to solve the thermometer (Eq. 24a; SEE=36°C) and hygrometer (Eq. 25b, SEE=1.1wt%) iteratively. Only liquid-mineral pairs that fulfill the equilibrium partitioning K_D(Ab-An)= 0.1±0.05 for T<1050°C and K_D(Ab-An)= 0.27±0.11 for T>1050°C (Putirka, 2008) are included in the final temperature and H_2O estimates. Results for each petrographic group are given in Tab. 3.9. LCPT samples result in the lowest temperatures and highest H_2O_{melt}-values (T_{mean} ≈ 900°C, H_2O_{mean} ≈ 5 wt%). LGPT estimates for temperature and pressure are intermediate (T_{mean} ≈ 982±40°C, H_2O_{mean} = 3.2±0.9 wt%) while LDST results mark highest temperatures and lowest H_2O_{melt} (T_{mean} ≈ 1125°C, H_2O_{mean} ≈ 2 wt%). Temperatures calculated from plagioclase saturation (Eq. 26, SEE=37°C, Putirka, 2008) give results (Tab. 3.9; Fig. 3.11) that are very similar to those obtained from plag-liq equilibria.

Fig. 3.11 (previous page) A) Comparison of H_2O contents modeled after Putirka (2008) and Lange et al. (2009) B) Plagioclase saturation (Eq. 26, Putirka, 2008) compared to phenocryst crystallization (Eq. 24a, Putirka, 2008) temperatures for Lonquimay tephras. C) Clinopyroxene saturation (Eq. 34, Putirka, 2008) vs. phenocryst crystallization (Eq. 33, Putirka, 2008) temperatures for Lonquimay tephras. Saturation T is calculated using calculated p (Eq. 31, Putirka, 2008) and matrix glass composition as input. Generally all estimates yield good correlations since all values lie within 1σ errors (dotted lines) of estimation models.

We further used the hygrometer-formulation of Lange et al. (2009) to calculate H_2O_{melt} (SEE=0.32 wt%) based on temperature from plag-liq equilibrium (Eq. 24a , Putirka, 2008) and pressure estimates from cpx-liq thermobarometry (Eq. 31). LCPT samples yield highest H_2O_{melt}-values (H_2O_{mean}=4.4±0.9 wt%). LDST estimates result in the lowest values (H_2O_{mean}=1-3 wt%) and LGPT samples give intermediate H_2O melt contents (H_2O_{mean}=3.0±0.9 wt%). When comparing both hygrometer models, the results fall well within the SEE boundaries (Fig. 3.11) indicating valid estimates. Nevertheless, values computed after Lange et al. (2009) seem to be systematically lower than estimates obtained after Putirka (2008).

Based on the effort we put into the evaluation of equilibrium conditions, we suggest that the multiple correlations between independently calculated thermobarometric results (Fig. 3.11 and Tab. 3.9) are not just coincidental. We therefore conclude that our results give robust estimates for the P-T-X-conditions prevailing in LVC's magmatic system.

3.10 DISCUSSION

3.10.1 Implications from equilibrium conditions

Mineral melt equilibria allow us to model P-T-X conditions prevailing in the magma chamber prior to most LVC explosive eruptions. The good agreement with H_2O contents in LDST melt inclusions measured by SIMS analyses shows (Fig. 3.13) that H_2O contents calculated from both the Lange et al. (2009) and Putirka (2008) hygrometers are valid estimates for mafic LVC samples. Moreover, the higher H_2O contents in the more evolved LCPT rocks are just as would be expected from the enrichment of H_2O as an incompatible element during fractional crystallization. Temperatures obtained by various thermometers agree well and follow a systematic pattern of cooling with increasing degree of fractionation. The pressure data confirm the earlier results that the LDST, LGPT and LCPT magma types were largely distributed in three crustal storage levels.

Fig. 3.12 shows pre-eruptive H_2O contents compared to P-estimates from clinopyroxene-liquid barometry. The H_2O solubilities calculated after Newman and Lowenstern (2002) for rhyolitic and basaltic compositions and temperatures representative for LCPT (900°C) and LDST

(1100°C) are given as dashed lines. Samples plotting above the corresponding line experienced H_2O-oversaturation whereas samples falling below the solubility curve were H_2O-undersaturated at reservoir depths. Pre-eruptive H_2O contents imply that LCPT melts were water-saturated at their storage pressure whereas the mafic LDST melts were clearly H_2O-undersaturated (Fig. 3.12). Lower H_2O/K_2O of LCPT compared to the less evolved LDST rocks supports that some water (possibly 1-2 wt%) had exsolved at the LCPT reservoir level.

Chlorine has been enriched during differentiation along roughly constant Cl/K_2O; minor partitioning of Cl ($K_D^{fluid\text{-}melt}(Cl)=8.1\pm0.2$; Bureau et al., 2000) into a fluid phase coexisting with LCPT melt would be compatible with the scatter observed in Cl concentrations of the LCPT melt inclusions (Fig. 3.9).

All LDST samples yield H_2O-undersaturation at reservoir depths. The poorly vesicular to dense nature of LDST-deposits older than 6000b2k is, however, not related to such undersaturation but results from phreatomagmatically influenced eruptions possibly related to extensive ice cover during these early Holocene times. The LDST deposits younger than 6000b2k, derived from the same undersaturated conditions, are highly vesicular because water could exsolve and expand during magma ascent in these magmatic eruptions. Yet the question remains, why those LDST magmas ascended at all when they were not initially driven by water saturation?

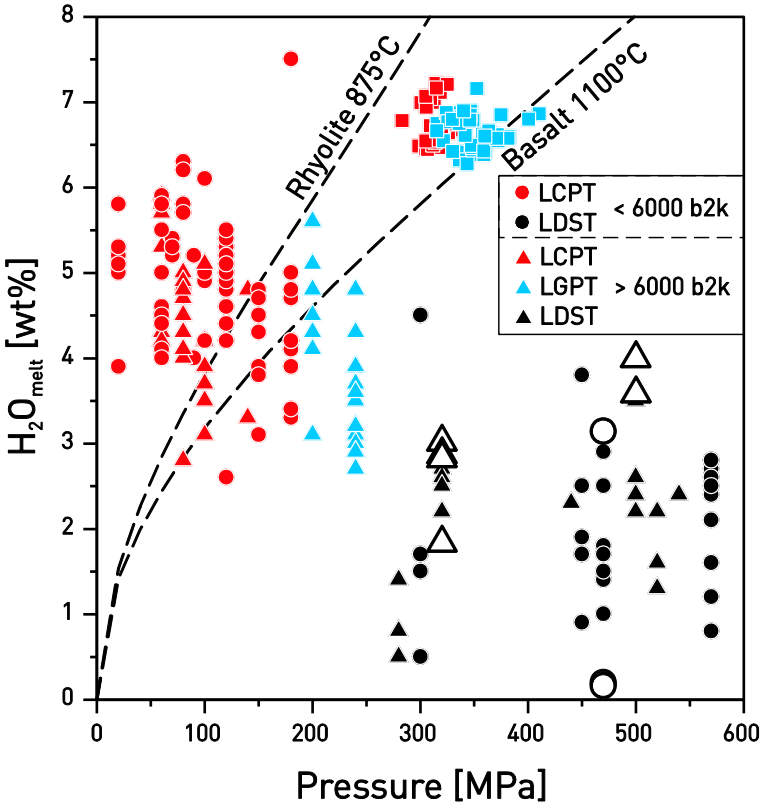

Fig. 3.12 Volatile Plot of H_2O contents of melts versus crystallization pressures. Crystallization pressures have been obtained from cpx-liquid equilibria (Eq. 31; Putirka 2008) and hbl-barometry (Ridolfi, 2010). The H_2O contents of the corresponding melts were calculated using compositions of plagioclase (Eq. 25b; Putirka 2008) and the amphibole-hygrometer of Ridolfi (2010). Water solubilities are calculated after Newman and Lowenstern (2002) for rhyolite (875°C) and basalt (1100°C) using temperatures that are representative for LCPT and LDST samples. Large open symbols represent SIMS H_2O-measurements.

The strong depletion of sulfur during differentiation (Fig. 3.9) indicates syn-crystallization S-degassing at LDST reservoir depth. In principle, sulfur may be lost from silicate melt either by unmixing into a sulfide phase or by partitioning into a fluid phase (Keppler, 1999). The interpretation of partitioning of S into a fluid phase would be supported by the observed occurrence of primary fluid inclusions (Fig. 3.4B3) in plagioclase crystals of LDST samples. These are somewhat unexpected in the light of the H_2O-undersaturation determined for the LDST magmas. On the other hand, the oxygen fugacities (for LCPT compositions, but by inference also for LDST compositions) near NNO are just in the region where sulfur speciation dramatically changes from S^{2-} to S^{6+} (e.g. Witham et al., 2012) and where sulfur solubility in silicate melt is at its minimum (Carroll and Webster, 1994). We have not found sulfide minerals in the thin sections but sulfur loss from silicate melt may have been forced by minor changes in fO_2. The stabilization of Fe-rich olivine supports a decrease in fO_2 below FMQ (cf. Fig. 3.10) for LCPT compositions that may also have occurred in LDST magmas. However, further analyses (of fluid inclusions and of CO_2 in melt inclusions) are needed to elucidate the problem of early sulfur loss at H_2O-undersaturated conditions.

3.10.2 Implications from disequilibrium conditions

The Rhodes diagram (Rhodes et al., 1979) in Fig. 3.13A allows for a visual test of olivine-liquid equilibrium. If olivine crystals are in equilibrium with a coexisting melt composition, then the putative olivine-liquid pair should plot along the solid line defined by $K_D(Fe\text{-}Mg)^{ol}_{liq}=0.3\pm0.03$. An additional utility of this diagram is that deviations from equilibrium can be explained by various forms of open system behavior (e.g. Putirka, 2008).

Regarding the LDST samples, nearly all olivine-melt pairs deviate from equilibrium conditions towards higher Mg# of the olivines. The $Fo_{82\pm2}$ olivine population of LDST samples deviate strongly from the equilibrium liquid composition as shown by both $K_D(Fe\text{-}Mg)=0.07\pm0.01$ and petrographic disequilibrium textures (Fig. 3.4), indicating that these olivines are in strong compositional contrast to their surrounding matrix glass and crystallized from much more mafic melts. The putatively equilibrated liquid compositions are required to have Mg# 56-62 compared to measured Mg# 18-22 of the matrix glass. The LDST olivine populations clustering around $Fo_{64\pm2}$ and $Fo_{71\pm1}$ are not as strongly in disequilibrium as the $Fo_{82\pm2}$ olivines. Nevertheless, the $K_D(Fe\text{-}Mg)$ values ($K_D(Fe\text{-}Mg)=0.23\pm0.02$ and $K_D(Fe\text{-}Mg)=0.18\pm0.03$ respectively) of these olivines indicate an origin from more mafic melt compositions (Mg# 33-44) than most of the coexistent matrix glasses (Mg# 26-34). In contrast, the comparably small population of olivines

with $Fo_{42\pm2}$ (K_D(Fe-Mg)=0.34±0.02) indicate equilibrium or only marginal disequilibrium with the matrix glass.

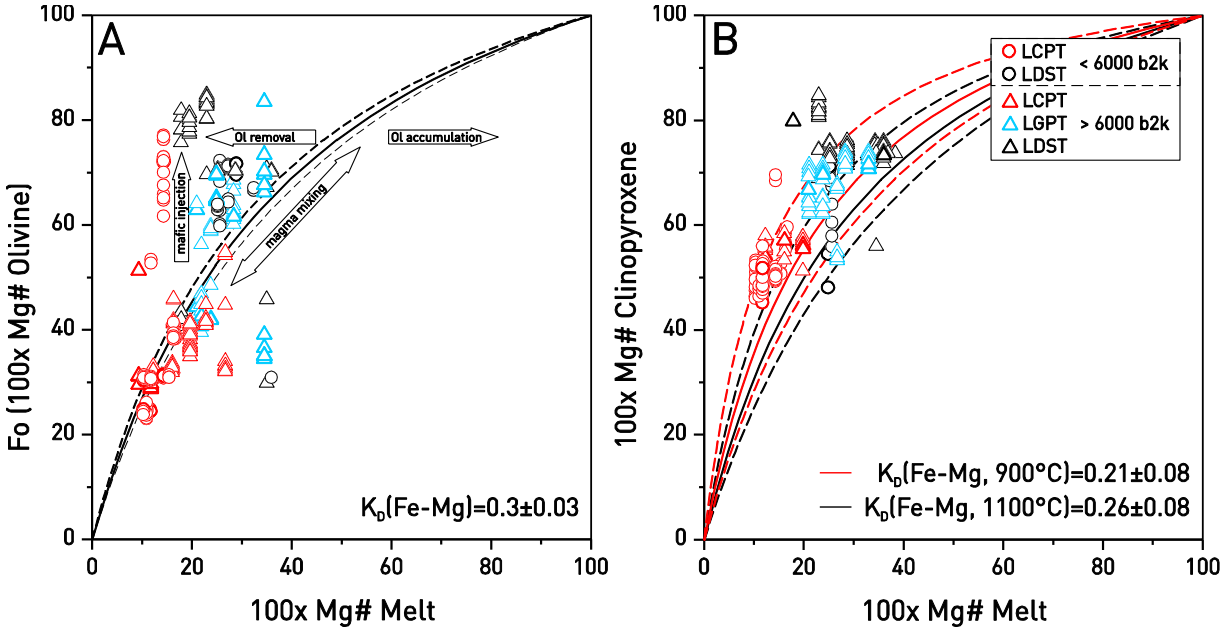

Fig. 3.13 A) Rhodes diagram (Rhodes et al., 1979) showing olivine-liquid relations in Lonquimay samples using matrix glass compositions as liquids. If olivines are in equilibrium with the coexisting melt, then the supposed melt-olivine pair should lie along the solid line within some established error ($K_D(Fe\text{-}Mg)^{ol\text{-}liq}$=0.30±0.03; Roeder and Emslie, 1970). B) Rhodes diagram (Rhodes et al., 1979) showing clinopyroxene-liquid relations in Lonquimay samples using matrix glass compositions as liquids. If clinopyroxenes are in equilibrium with the coexisting melt, then the supposed melt-clinopyroxene pair should lie along the solid line within some established error. Because $K_D(Fe\text{-}Mg)^{cpx\text{-}liq}$ are slightly invariant with temperature (Putirka, 2008), two K_D-values (LDST, 1100°C: K_D(Fe-Mg)=0.26±0.08; and LCPT, 900°C: K_D(Fe-Mg)=0.22±0.08) are used to check for equilibrium.

Although originally designed for olivine-liquid equilibrium, the Rhodes diagram is applicable for other crystal-melt equilibria with established K_D-values. Fig. 14b shows the diagram for clinopyroxene-liquid pairs and K_D(Fe-Mg). As already described in the thermobarometry section above K_D(Fe-Mg) for clinopyroxene and liquid varies slightly with temperature. Therefore, we use two different K_D-values - calculated for temperatures that are representative for LCPT and LDST components - to check for equilibrium conditions (LDST, 1100°C: K_D(Fe-Mg)=0.26±0.08; and LCPT, 900°C: K_D(Fe-Mg)=0.22±0.08). In general, clinopyroxene-melt pairs show the same features as olivine crystals: LDST samples show a population of clinopyroxene-crystals (Mg# 81.3±2.4) that is highly disequilibrated K_D=0.07±0.01. The population centered at Mg# 73.9±1.5 (K_D(Fe-Mg)=0.18±0.03) as well as clinopyroxenes from LDST deposits younger than 6000 b2k clustering around 67.6±5.7 (K_D(Fe-Mg)=0.21±0.07) are on the edge of equilibrium or slightly disequilibrated.

Although ilmenite and magnetite crystals occur in some samples, the equilibrium test after Bacon and Hirschmann (1988) yields that both Fe-Ti phases are not in equilibrium for LDST samples. The strong disequilibrium conditions not only apply to ferromagnesian minerals but also to the LDST plagioclase population which has K_D(Ab-An)=0.13±0.09 with matrix glass, much lower than the equilibrium value of K_D(Ab-An)=0.27±0.11). Most of the plagioclase crystals have heavily corroded cores (sieve textures) and overgrown crystal rims that are apparently in equilibrium K_D(Ab-An)=0.23±0.1 with the surrounding melt phase.

Olivine compositions from LGPT units cover a wide range (Fo_{29}-Fo_{84}) with bimodal distribution peaking at $Fo_{64±4}$ (K_D(Fe-Mg)=0.23±0.04) and $Fo_{37±6}$ (K_D(Fe-Mg)=0.36±0.06). According to the argumentation for the LDST samples above, the $Fo_{64±4}$ is inherited from mixing with more mafic magma batches, whereas the $Fo_{37±6}$ crystallized from the resulting hybridized LGPT magmas. LGPT samples have cpx phenocrysts with intermediate Mg# of 69.7±3.2 (K_D (Fe-Mg)=0.19±0.06) yielding equilibrium crystallization for most crystals. However, evidence of chemical disequilibrium is not only restricted to some ferromagnesian mineral populations but also affects the appearance of plagioclase crystals. A significant amount of plagioclase phenocrysts show dissolved cores and/or resorption embayments (Fig. 3.4), although not as heavily dissolved as those from LDST samples.

Olivine crystals from LCPT samples are mostly Fe-rich and in large part in equilibrium (K_D(Fe-Mg)≈0.3-0.4) with the surrounding matrix. K_D(Fe-Mg) values from clinopyroxene-matrix glass pairs of LCPT samples older 6000 b2k peaking at Mg# 55.4±1.8 (K_D(Fe-Mg)=0.19±0.06) and LCPT samples younger 6000 b2k (Mg# 50.3±2.8; KD(Fe-Mg)=0.15±0.02) indicate equilibrium or only marginal disequilibrium for most samples. However, the shift of K_D values towards the lower end of equilibrium range suggests crystallization from slightly less evolved melts. Although some zoned plagioclase crystals with resorbed cores are existent, the vast majority shows no to only slight evidences for chemical disequilibrium with the surrounding LCPT matrix. This is further supported by K_D(Ab-An)=0.11±0.01 with the surrounding melt phase yielding equilibrium crystallization (K_D(Ab-An)=0.10±0.05) for most plagioclase crystals.

In summary, a significant amount of ferromagnesian (olivine and clinopyroxene) and plagioclase minerals in LDST samples have high Mg# or An-contents, respectively, exceeding the equilibrium compositions. These highly mafic crystals are apparently inherited from melt batches with more mafic compositions, suggesting the frequent injection of such batches into the LDST magma chamber. The only subordinate occurrence of olivines, clinopyroxenes and plagioclases that are in equilibrium with the coexisting melt and the incomplete resorption of crystals despite strong chemical contrast with the surrounding liquid indicate that the admixing of the primitive

magma batches must have occurred shortly prior to the corresponding LDST eruptions. We therefore suggest that frequent replenishment events may have triggered the comparably frequent mafic LDST eruptions. However, after a while hybridization also re-established equilibrium conditions such that precipitation of mineral populations in equilibrium continued.

Mineral parageneses of LCPT samples are dominated by mineral populations (Fe-rich olivines and clinopyroxenes, low An-plagioclase) that are apparently in equilibrium with the coexisting dacitic melt. However, some LCPT samples contain olivine crystals with higher Mg# that apparently crystallized in more mafic magma batches before being injected together into the LCPT magma chamber. This finding is further supported by the existence of bimodal matrix-glass compositions in some but not all LCPT deposits as well as olivine phenocrysts that have Fe-contents even exceeding equilibrium contents with surrounding rhyodacitic matrix glasses (Fig. 3.13). This indicates that these crystals may have formed in an even more evolved melt that was afterwards contaminated by the injection of a mafic melt batch. Subsequent hybridization followed by equilibrium crystallization led to the formation of the LCPT magma that was finally tapped during eruption.

Based on its mainly bimodal distribution of mineral compositions, LGPT tephras are most likely in large parts hybridized from LDST magma with more evolved melts. This is further supported by the wide range of melt inclusions (Fig. 3.8) that cover the whole range of LVC compositions including LDST and LCPT compositions. This may indicate that the host minerals were inherited from more evolved as well as more mafic magma batches than the intermediate matrix glass compositions of LGPT pumice clasts. Beside these apparently xenocrystic mineral populations, there are some plagioclase, clinopyroxene and olivine crystals that crystallized from the re-homogenized melt within the LGPT magma chamber.

3.11 CONCLUSIONS

This study reveals that LVC's magmatic products experienced a complex history of interacting processes within the plumbing system that systematically affected the involved magmas and their volatile inventories and hence LVC's eruptive behavior.

During ascent, the magmas reached two independent levels of volatile saturation. A first deep level in the reservoir occupied by LDST melts (~14 km), leading to the formation of a S-rich fluid phase and therefore strong depletion in S of the melt. This fluid phase may have caused the metasomatic alteration of wall rocks as is suggested by plagioclase xenocrysts containing dispersed decrepitated fluid inclusions (plutonic texture). A second saturation level was reached between 1.5

and 6 km in the shallow reservoir. The stagnation of LCPT melts at this level led to their H_2O-oversaturation and hence exsolution of an aqueous fluid phase as is documented by primary fluid inclusions.

The frequent injection of primitive melt batches into the LDST reservoir, as documented in the pheno- and xenocryst assemblage, may have triggered the mafic LDST eruptions. Prior to 6000 b2k, most of these mafic eruptions have been influenced through phreatomagmatic activity probably due to melt water from ongoing deglaciation, The occurrence of compositionally zoned, amphibole-bearing deposits that is limited to LCPT deposits older 6000 b2k indicates the occurrence of compositionally zoned magma bodies and hence stronger interaction between the three distinct reservoirs prior to this threshold. In contrast, the matrix glass and crystal records of most felsic eruptions younger than 6000 b2k do not show the influence of mafic replenishment. We therefore conclude that these eruptions may have been triggered by H_2O-saturation, giving a possible explanation for the longer repose times between these eruptions (Gilbert et al., 2012).

Acknowledgements

We gratefully acknowledge the support of M. Thöner (EPMA) during EPMA analyses. L. Lara (SERNAGEOMIN) supported us during our field campaigns in Chile and provided invaluable information. Maxim Portnyagin kindly provided reference material for SIMS analyses. This publication is contribution no. 249 of the Sonderforschungsbereich 574 on "Volatiles and Fluids in Subduction Zones" at University of Kiel.

REFERENCES

Andersen, D.J., and Lindsley, D.H., 1985, New (and final!) models for the Ti-magnetite/ilmenite geothermometer and oxygen barometer - Abstract AGU 1985 Spring Meeting.

Arancibia, G., Cembrano, J., and Lavenu, A., 1999, Transpresión dextral y partición de la deformación en la Zona de Falla Liquiñe-Ofqui, Aisén, Chile (44-45°S): Revista Geológica de Chile, v. 26, p. 3-22.

Bacon, C.R., and Hirschmann, M.M., 1988, Mg/Mn partitioning as a test for equilibrium between coexisting Fe-Ti oxides: American Mineralogist, v. 73, p. 57-61.

Bureau, H., Keppler, H., and Métrich, N., 2000, Volcanic degassing of bromine and iodine: experimental fluid/melt partitioning data and applications to stratospheric chemistry: Earth and Planetary Science Letters, v. 183, p. 51-60.

Carrigan, C.R., 2000, Plumbing systems, *in* Sigurdsson, H., Houghton, B.F., McNutt, S.R., Rymer, H., Stix, J., and McBirney, A.R., eds., Encyclopedia of Volcanoes, Volume 53: San Diego, USA, Academic Press, p. 149-170.

Carroll, M.R., and Webster, J.D., 1994, Solubilities of sulfur, noble gases, nitrogen, chlorine, and fluorine in magmas: Reviews in Mineralogy and Geochemistry, v. 30, p. 231-279.

Cembrano, J., and Lara, L., 2009, The link between volcanism and tectonics in the southern volcanic zone of the Chilean Andes: A review: Tectonophysics, v. 471, p. 96-113.

Danyushevsky, L.V., Falloon, T.J., Sobolev, A.V., Crawford, A.J., Carroll, M., and Price, R.C., 1993, The H_2O content ot basalt glasses from Southwest Pacific back arc basins: Earth and Planetary Science Letters, v. Vol. 117, p. p. 347-362.

Dixon, J.E., and Clague, D.A., 2001, Volatiles in Basaltic Glasses from Loihi Seamount, Hawaii: Evidence for a Relatively Dry Plume Component: Journal of Petrology, v. 42, p. 627-654.

Gilbert, D., Freundt, A., Kutterolf, S., and Burkert, C., 2012, Post-glacial time series of explosive eruptions and associated changes in the magma plumbing system of Lonquimay Volcano, south central Chile: International Journal of Earth Sciences, p. 1-20.

Hansteen, T.H., Klügel, A., and Schmincke, H.-U., 1998, Multi-stage magma ascent beneath the Canary Islands: evidence from fluid inclusions: Contributions to Mineralogy and Petrology, v. 132, p. 48-64.

Hauri, E.H., Kent, A.J.R., and Arndt, N., 2002, Melt inclusions at the millenium: toward a deeper understanding of magmatic processes: Chemical Geology, v. 183, p. 1-3.

Hildreth, W., and Moorbath, S., 1988, Crustal contributions to arc magmatism in the Andes of Central Chile: Contributions Mineralogy Petrology, v. 98, p. 455-489.

Hunt, J.B., and Hill, P.G., 1993, Tephra geochemistry: a discussion of some persistent analytical problems: The Holocene, v. 3, 3, p. 271 - 278.

Jarosewich, E., Nelen, J.A., and Norberg, J.A., 1980, Reference Samples for Electron Microprobe Analysis*: Geostandards Newsletter, v. 4, p. 43-47.

Keppler, H., 1999, Experimental Evidence for the Source of Excess Sulfur in Explosive Volcanic Eruptions: Science, v. 284, p. 1652-1654.

Lange, R.A., Frey, H.M., and Hector, J., 2009, A thermodynamic model for the plagioclase-liquid hygrometer/thermometer: American Mineralogist, v. 94, p. 494-506.

Lavenu, A., and Cembrano, J., 1999, Compressional and transpressional stress pattern for Pliocene and Quaternary brittle deformation in fore-arc and intra-arc zones (Andes of Central and Southern Chile): Journal of Structural Geology, v. 21, p. 1669-1691.

Lindquist, K.G., Engle, K., Stahlke, D., and Price, E., 2004, Global topography and bathymetry grid improves research efforts: EOS Trans. AGU, v. 85.

Lister, J.R., 1990, Buoyancy-driven fluid fracture: the effects of material toughness and of low-viscosity precursors: Journal of Fluid Mechanics, v. 210, p. 263-280.

López-Escobar, L., Cembrano, J., and Moreno, H., 1995, Geochemistry and tectonics of the chilean Southern Andes basaltic Quaternary volcanism (37°-46°S). Revista Geológica de Chile, v. 22, p. 219-234.

López-Escobar, L., Killian, R., Kempton, P., and Tagiri, M., 1993, Petrography and geochemistry of Quaternary rocks from the Southern Volcanic Zone between 41°30' and 46°00' S: Revista Geológica de Chile, v. 20, p. 35-55.

Manga, M., and Brodsky, E., 2006, Seismic Triggering of Eruptions in the Far Field: Volcanoes and Geysers. : Annual Review of Earth and Planetary Sciences, v. 34, p. 263-291.

Menand, T., and Tait, S.R., 2001, A phenomenological model for precursor volcanic eruptions: Nature, v. 411, p. 678-680.

Moreno Roa, H., and Gardeweg, M., 1989, La erupcion reciente en el complejo volcanico Lonquimay (diciembre 1988-), Andes del Sur: Revista geológica de Chile, v. 16, p. 93-117.

Newman, S., and Lowenstern, J.B., 2002, VC: a silicate melt-H2O-CO2 solution model written in Visual Basic for excel: Computers & Geosciences, v. 28, p. 597-604.

Nielsen, C.H., and Sigurdsson, H., 1981, Quantitative methods of electron microprobe analysis of sodium in natural and synthetic glasses. : American Mineralogist, v. 66, p. 547–552.

Nimis, P., 1999, Clinopyroxene geobarometry of magmatic rocks. Part 2. Structural geobarometers for basic to acid, tholeiitic and mildly alkaline magmatic systems: Contributions to Mineralogy and Petrology, v. 135, p. 62-74.

Polanco, E., 1998, Volcanismo Explosivo Postglacial de la Cuenca del Alto Biobío, Andes del Sur (37º45'-38º30') [Master thesis]: Santiago de Chile, Universidad de Chile.

Putirka, K., 1999, Clinopyroxene + liquid equilibria to 100 kbar and 2450 K: Contributions to Mineralogy and Petrology, v. 135, p. 151-163.

Putirka, K.D., 2005, Igneous thermometers and barometers based on plagioclase + liquid equilibria: Tests of some existing models and new calibrations: American Mineralogist, v. 90, p. 336-346.

Putirka, K.D., 2008, Thermometers and Barometers for Volcanic Systems, *in* Putirka, K.D., and Tepley III, F.J., eds., Minerals, inclusions and volcanic processes, Volume 69: Reviews in Mineralogy and Geochemistry, The Mineralogical Society of America, p. 61-111.

Putirka, K.D., Johnson, M., Kinzler, R., Longhi, J., and Walker, D., 1996, Thermobarometry of mafic igneous rocks based on clinopyroxene-liquid equilibria, 0–30 kbar: Contributions to Mineralogy and Petrology, v. 123, p. 92-108.

Rhodes, J.M., Dungan, M.A., Blanchard, D.P., and Long, P.E., 1979, Magma mixing at mid-ocean ridges: Evidence from basalts drilled near 22° N on the Mid-Atlantic Ridge: Tectonophysics, v. 55, p. 35-61.

Ridolfi, F., Renzulli, A., and Puerini, M., 2010, Stability and chemical equilibrium of amphibole in calc-alkaline magmas: an overview, new thermobarometric formulations and application to subduction-related volcanoes: Contributions to Mineralogy and Petrology, v. 160, p. 45-66.

Roeder, P.L., and Emslie, R.F., 1970, Olivine-liquid equilibrium: Contributions to Mineralogy and Petrology, v. 68, p. 325 - 334.

Rosenau, M., Melnick, D., and Echtler, H., 2006, Kinematic constraints on intra-arc shear and strain partitioning in the southern Andes between 38°S and 42°S latitude: Tectonics, v. 25, p. TC4013.

Rubin, A.M., 1993, On the thermal viability of dikes leaving magma chambers: Geophysical Research Letters, v. 20, p. 257-260.

Stern, C.R., 2004, Active Andean volcanism: its geological and tectonic setting: Revista Geológica de Chile, v. Vol. 31, p. p. 161-206.

Stormer Jr, J.C., 1983, The effects of recalculation on estimates of temperature and oxygen fugacity from analyses of multicomponent iron-titanium oxides: American Mineralogist, v. 68, p. 586-594.

Tormey, D.R., Hickey-Vargas, R., Frey, F.A., and López-Escobar, L., 1991, Recent lavas from the Andean front (33° to 42°S): interpretations of along-arc compositional variations. , *in* Harmon, R.S., and Rapela, C.W., eds., Andean Magmatism and its Tectonic Setting, Volume 265: Special Paper, Geological Society of America, p. 57-77.

Vergara Sáez, C.A., 2010, Petrogénesis de los centros eruptivos del complejo volcánico Lonquimay (CVL), IX región de la araucanía [Master thesis]: Santiago de Chile, Universidad de Chile.

Völker, D., Kutterolf, S., and Wehrmann, H., 2011, Comparative mass balance of volcanic edifices at the southern volcanic zone of the Andes between 33°S and 46°S: Journal of Volcanology and Geothermal Research, v. 205, p. 114-129.

Watt, S.F.L., Pyle, D.M., and Mather, T.A., 2009, The influence of great earthquakes on volcanic eruption rate along the Chilean subduction zone: Earth and Planetary Science Letters, v. 277, p. 399-407.

Witham, F., Blundy, J., Kohn, S.C., Lesne, P., Dixon, J., Churakov, S.V., and Botcharnikov, R., 2012, SolEx: A model for mixed COHSCl-volatile solubilities and exsolved gas compositions in basalt: Computers & Geosciences, v. 45, p. 87-97.

Chapter 4

Puyehue-Cordón Caulle: a history of critical magma chambers due to volatile oversaturation

This chapter was submitted to *GEOLOGY*

Co-authors: A. Freundt, S. Kutterolf, T. Hansteen, A. Amigo

4.1 ABSTRACT

Since its 1960 eruption, Puyehue-Cordón Caulle Volcanic Complex (PCCVC) is one of the most renowned volcanoes thought to be susceptible to seismic triggering. The 2011 eruption raised the question if it was possibly related to the M_W 8.8 Maule earthquake. We present estimates for crystallization temperatures and pressures as well as pre-eruptive H_2O contents based on several independent methods for the 2011, 1960 and four older post-glacial explosive eruptions. Clinopyroxene-liquid thermobarometry reveals crystallization pressures between 250 and 50 MPa (P_{mean}=154±40 MPa) suggesting shallow magma chambers at depths of 2-9 km and magma temperatures of 885-915°C (T_{mean}=899±12°C) for all eruptions. Pre-eruptive H_2O contents of 4-5 wt% and the occurrence of water-dominated magmatic fluid inclusions indicate the exsolution of a chlorine-bearing fluid phase ($salinity_{mean}$=3.2±0.1 wt% NaCl equivalent) at pressures of ~135 MPa. Such pre-eruptive H_2O-saturation in relatively shallow reservoirs appears to be typical of explosive eruptions at this volcanic system. We imply that due to volatile supersaturation the system was due to erupt when it was eventually triggered by seismic activity. PCCVC's ability to repeatedly restore critical magmatic conditions and its position astride a NW fissure zone of the arc-wide Liquiñe-Ofqui Fault Zone system, along which seismic energy/strain may be transmitted particularly effectively, probably are the two factors that facilitate tectonic triggering of eruptions this particular volcanic system.

4.2 INTRODUCTION

On June 4th 2011 the Puyehue-Cordon Caulle volcanic complex (40°35'S, 72°7'W) in South Central Chile woke after 51 years of dormancy. The rhyodacitic eruption produced an ash plume that reached altitudes of ~12 km, causing severe problems for civil aviation in the Southern hemisphere. During June 2nd and 3rd, the eruption announced itself by mostly hybrid and long-period earthquakes located in the SE sector of the Cordón Caulle rift zone at depths of 2-5 km. Seismicity increased to an average of 230 earthquakes per hour on June 4th, revealing dike propagation at depths of 1-4 km (OVDAS, 2011).

While statistically significant correlations between major regional earthquakes and eruptions within days or even months have been reported by several studies (e.g. Eggert and Walter, 2009; Linde and Sacks, 1998; Watt et al., 2009), the 1960 eruption of the PCCVC is one of the most famous examples because it occurred only 37h after the largest ever instrumentally recorded earthquake (M_S=9.5) (Cembrano and Lara, 2009; Lara et al., 2004; Manga and Brodsky, 2006; Walter and Amelung, 2007; Watt et al., 2009). Most studies (Hill et al., 2002; Manga and

Brodsky, 2006; Walter and Amelung, 2007; Watt et al., 2009) coping with feedback mechanisms between tectonic forcing and volcanic activity stress that the pre-eruptive volatile saturation state is the most important factor ruling the susceptibility of the magmatic system. However, until today a study about the volatile inventory, the saturation state of the magmatic system and its contribution to the eruptive potential of PCCVC is missing. Therefore, we performed thermobarometric and volatile studies for the remarkably homogeneous rhyodacitic 2011, 1960 and older post-glacial eruptions. The use of several independent methods allows us to give robust estimates of pre-eruptive P-T-X-conditions and how the volatile saturation state evolved over time.

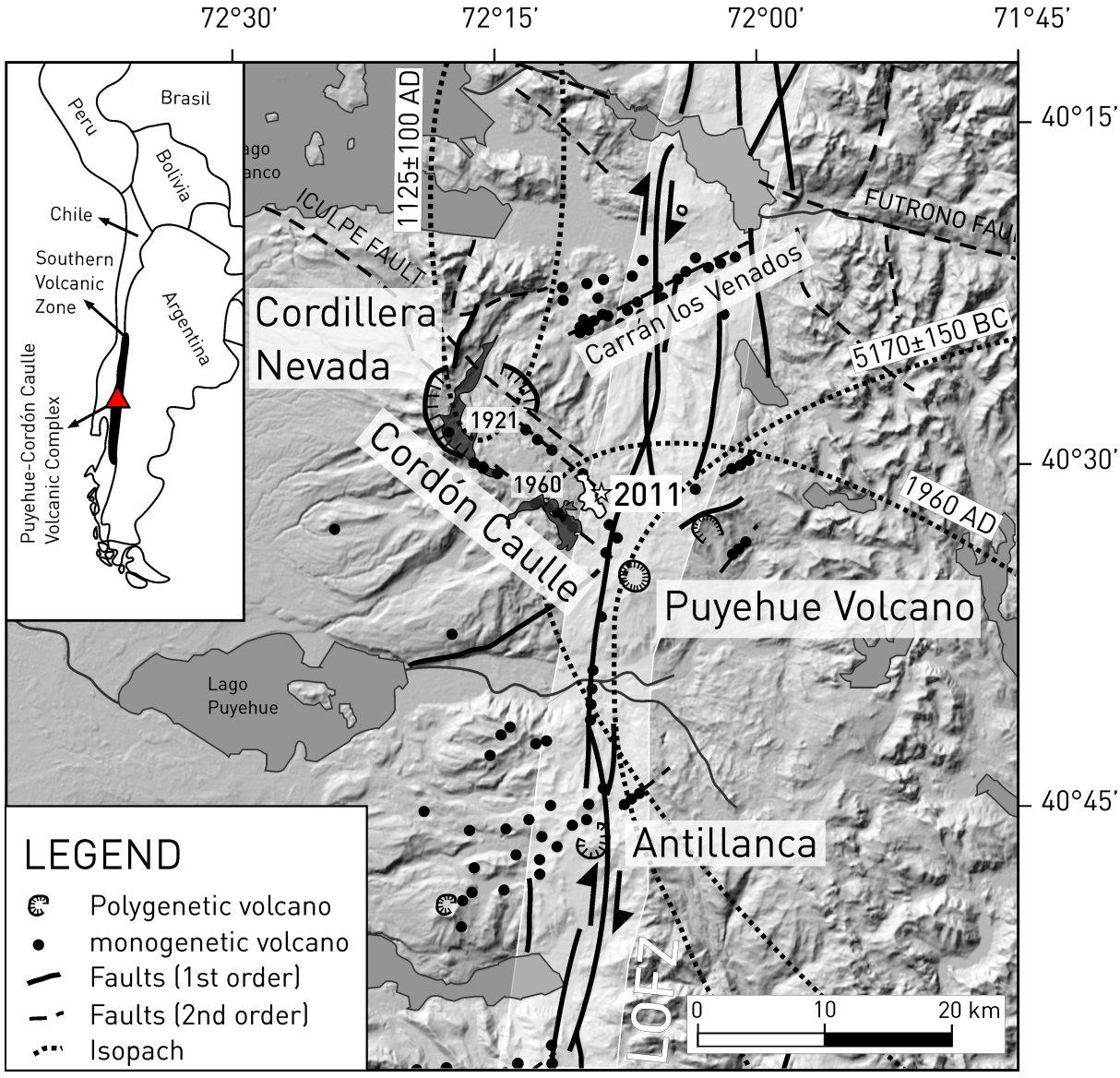

Fig. 4.1 Overview map of the Puyehue-Cordón Caulle Volcanic Centre highlighting the tectonic features, loci of eruptive centers (Sepúlveda et al., 2005) and tephra dispersal (dotted lines, Lara et al., 2006) in this region.

4.2.1 Geological setting of the Lonquimay Volcanic Complex

The Puyehue-Cordón Caulle Volcanic Complex, an assemblage of eruptive centers, is part of the Quaternary Volcanic front of the Southern Volcanic Zone (SVZ) of the Andes that formed in response to the subduction of the 0-45 Ma old oceanic Nazca plate beneath the continental South American plate. The oblique convergence (22-30° NE) causes dextral slip along the arc-parallel (~10° NE) Liquiñe-Ofqui Fault Zone (e.g. Arancibia et al., 1999; Cembrano et al., 2000; Rosenau et al., 2006). This major right lateral strike slip system controls the architecture of the intra-arc region and the position of most volcanoes in the Central and Southern SVZ (López-Escobar et al., 1995; Cembrano and Lara, 2009). The magmatic products of PCCVC (lavas, tephras and pyroclastic density currents) of the last 200 ka cover a wide range from basaltic to rhyolitic compositions (Gerlach et al., 1988), with rhyolites dominating the last post-glacial stage (<10.47±0.15 ka BP; Singer et al., 2008).

4.2.2 Methods

Juvenile pumice clasts from the post-glacial tephrostratigraphic sequence of PCCVC (Lara et al., 2006) were analyzed for their matrix glass, mineral, and melt inclusion compositions by electron microprobe (EPMA; cf. ESM1 for more detailed information about analytical procedures).

P-T-X conditions were calculated by several independent mineral-liquid equilibria (plagioclase-liquid, clinopyroxene-liquid and orthopyroxene-liquid; Putirka, 2008; Lange et al., 2009) using adjacently measured mineral-glass pairs (matrix glasses and crystal rims; melt inclusions and immediately overgrown host minerals; Fig. 4.3B) that were rigorously checked to satisfy equilibrium conditions (cf. ESM3 for procedures and formulas used).

A microscope-mounted heating and cooling stage was used to investigate magmatic fluid inclusions (small droplets of an exsolved fluid phase) in doubly polished wafers of plagioclase-crystals (cf. ESM4). Based on inclusion salinity and density, isochores were calculated using the FLUIDS software package (Bakker, 2003). We assume that agreement between fluid-inclusion and various mineral-based hygro- and thermobarometers (cf. ESM4) is not coincidental but validates the robustness of our estimates for pre-eruptive P-T-X conditions.

We collected our samples at tephra sections downwind of the PCCVC using the tephrostratigraphy established by Lara et al. (2006). The fallout deposits preserved in this region were formed by eruptions typically larger than Volcanic Explosivity Index (VEI) 3. The radiometric ages (Lara et al., 2006; Singer et al., 2008) were converted to calibrated ages using the

software Calib 6.01 (Stuiver and Reimer, 1993) with Southern hemisphere correction according to McCormac et al. (2004). The resulting calibrated ages are given in Fig. 4.2 and Tab. C.6.1 (appendix) and are reported as calibrated years BC/AD below.

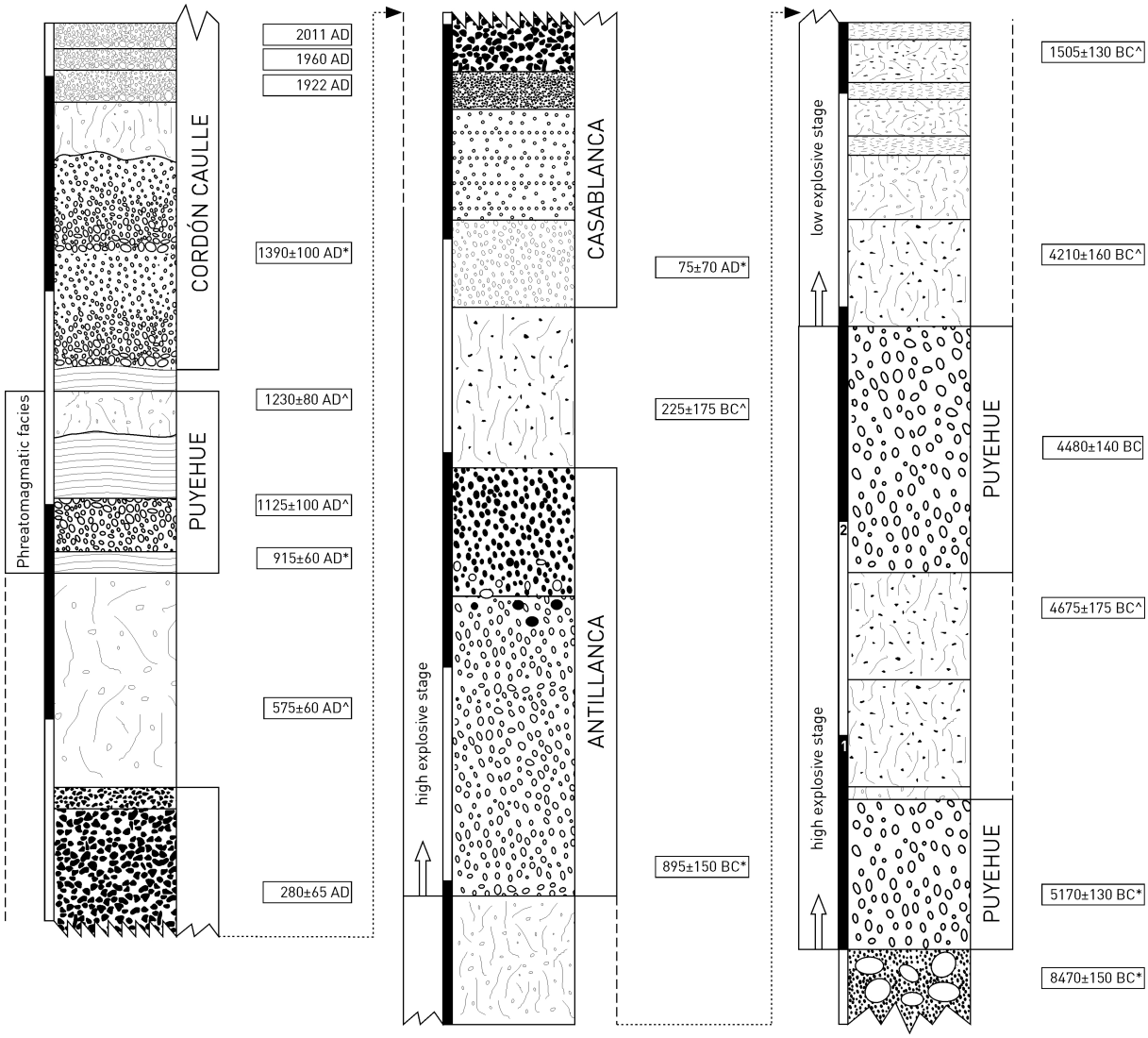

Fig. 4.1 General tephrostratigraphic profile of the Puyehue-Cordón Caulle region. Note that pyroclastic products at 895±150 BC and 75±70 AD originated not from PCCVC but from Antillanca and Casablanca volcanoes respectively. Ages are from Lara et al. (2006=^) and Singer et al. (2008=*) and are given as calibrated ages.

4.3 RESULTS

PCCVC rocks span a continuous medium K-series ranging from basalt (8-9 wt% MgO) to rhyolite (up to 72 wt% SiO_2) and cover the entire compositional range found in the Southern SVZ (Singer et al., 2008). In contrast, post-glacial volcanic activity discharged magmas of monotonous rhyodacitic compositions that can be derived by fractional crystallization from a common basaltic parental magma (Gerlach et al., 1988; Lara et al., 2006).

4.3.1 Matrix glasses

The geochemical composition of matrix glass shards reflects the composition of the melt at the time of eruption of a tephra (e.g. Ortega-Guerrero and Newton, 1998). Post-glacial PCCVC matrix glass compositions (cf. Appendix C, Tab. C.5.1) show the compositional homogeneity already noted by Gerlach et al. (1988) and Singer et al. (2008).

	2011 AD	1960 AD	1922 AD	1390 AD	915 AD	4480 BC
2011 AD	-	-	-	-	-	-
1960 AD	0.81	-	-	-	-	-
1922 AD	0.87	0.93	-	-	-	-
1390 AD	0.90	0.89	0.96	-	-	-
915 AD	0.91	0.88	0.95	0.98	-	-
4480 BC	0.89	0.77	0.81	0.83	0.83	-

Tab. 4.1 Multi-element comparison (similarity coefficients, SC) of mean matrix glass compositions (given in appendix Tab. C.5.1) of the PCCVC tephras after Borchardt et al. (1972). SC >0.92 identify nearly identical compositions (Froggatt, 1992).

In order to quantify geochemical similarity between the tephras, we calculated Similarity Coefficients (SC) from the matrix glass compositions after Borchardt et al. (1972), normally used in tephrostratigraphy for correlating tephras from drill cores (Tab. 1). SC is a single parameter reporting multivariate similarity considering the analytical precision and sample homogeneity of the underlying dataset. SCs approaching 1.0 represent chemical equality whereas values ≥0.92 are generally taken as indicative of correlation between tephra samples (e.g. Froggatt, 1992) taking into account scatter in natural glass compositions. SCs of PCCVC matrix glasses are mostly >0.9 indicating a very close similarity in pre-eruptive melt chemistry between different eruptions. Only the oldest tephra (4480 a BC) yields significantly lower SCs mainly due to the higher SiO_2 contents.

4.3.2 Minerals

PCCVC's post-glacial rhyodacitic lavas and tephas are typically crystal poor (5-13%) and show similar mineral parageneses comprising plagioclase ($An_{44.2\pm3.8}$), clinopyroxene (Mg# 62.7±1.9), orthopyroxene (Mg# 57.9±2.4), magnetite (53.7±0.9 mol% ulvöspinel), ilmenite (89.2±1 mol% ilmenite), and apatite (see ESM2). The observed similarity of core and rim compositions suggests that most crystals are nearly unzoned. However, the oldest tephra (4480 BC) that also differs in matrix-glass composition has mineral compositions slightly distinct from the younger tephras with plagioclase ($An_{37.7\pm2.6}$), clinopyroxene (Mg# 47.4±4.9), orthopyroxene (Mg# 67.4±3.4), and

magnetite (61.71±4.7 mol% ulvöspinel). The two oldest tephras (4480 a BC and 915 BC) - contrary to the younger ones - contain olivine xenocrysts (Mg# 0.83±0.01) corresponding to basaltic melt compositions, and are thus chemically out of equilibrium (K_D(Fe-Mg)=0.3±0.03; Roeder and Emslie, 1970) with their host-melt compositions. The oldest tephra (4480 a BC), however, additionally contains more Fe-rich olivines (Mg# 0.23±0.01) that are apparently in equilibrium with the surrounding melt.

4.3.3 Thermobarometry

Thermobarometric calculations using clinopyroxene-liquid equilibrium yield fairly uniform pressure estimates for all tephras ($P_{mean}^{cpx\text{-}liq}$=154±40 MPa) and indicates magma chamber depths of 5.8±1.5 km, which fits the observation of magma-ascent earthquakes between 0-5 km depth prior to the 2011 eruption. Orthopyroxene-liquid derived pressures are systematically higher ($P_{mean}^{opx\text{-}liq}$= 240±50 MPa) but correlate with clinopyroxene-liquid well within error bounds (cf. ESM 3).

Calculated clinopyroxene-liquid temperatures of $T_{mean}^{cpx\text{-}liq}$=899±12°C for tephras from 915 to 2011 AD have an overall standard deviation only slightly larger than the scatter of temperatures for single tephras. The oldest tephra (4480 BC) gives slightly lower temperatures $T_{mean}^{cpx\text{-}liq}$=848±8°C. These results are in good agreement with temperature-estimates based on plagioclase-liquid equilibria that reveal slightly lower temperatures ($T_{mean}^{plag\text{-}liq}$=889±11°C for 915 to 2011 AD tephras with standard deviation akin to the scatter in single tephras; $T_{mean}^{plag\text{-}liq}$=826±11°C is again slightly lower for 4480 BC). Temperatures from orthopyroxene-liquid equilibria show similar values and spreading properties ($T_{mean}^{opx\text{-}liq}$=893±11°C for 915 to 2011 AD, $T_{mean}^{opx\text{-}liq}$=812±6°C for 4480 BC).

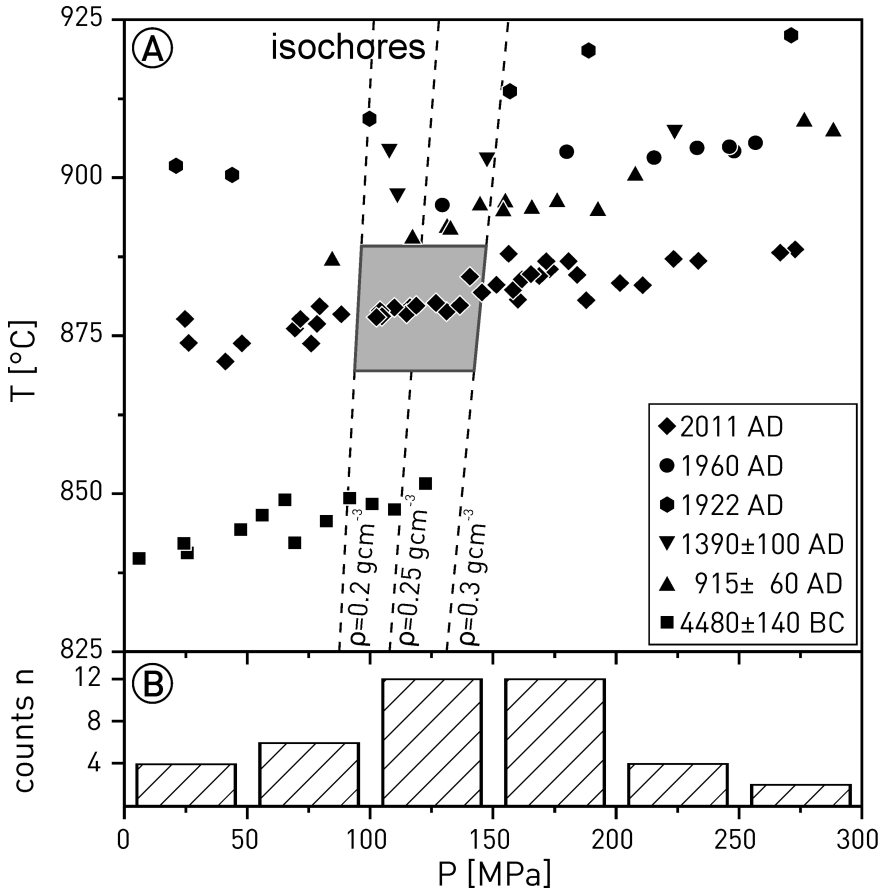

Fig. 4.2 A) Pre-eruptive clinopyroxene-liquid pressures vs. temperatures. Dashed lines are isochors for fluid inclusion compositions from the 2011 eruption. Isochors indicate the exsolution of the fluid phase between 95-150 MPa. B) Histogram of clinopyroxene-liquid pressures for the 2011 tephra. The pressure range derived from fluid inclusions (2-4 wt% NaCl) coincides with the mode of mineral-based pressures.

4.3.4 Magmatic volatile inventory

Magmatic volatiles such as H_2O dissolve in silicate melts at high pressures but may form a free vapor phase at lower pressures, thereby facilitating eruption. The pressure where degassing begins depends on the dissolved concentration and the solubility in a given melt of the volatile species considered. Here we constrain volatile contents by plagioclase-melt hygrometry and by analysis of fluid inclusions trapped in minerals.

Applying the hygrometers of Putirka (2008) and Lange et al. (2009) to adjacently measured plagioclase-melt pairs (matrix glasses and crystal-rims; melt inclusions and immediately overgrown host plagioclase, Fig. 4.3B) yields H_2O_{mean}=4.4±0.3 wt% and H_2O_{mean}=4.1±0.2 wt%, respectively, which agree within 1σ error (cf. Appendix C; Fig. C.2.1). To constrain the composition of the exsolved fluid phase, we investigated fluid inclusions in the 2011 AD tephra by microthermometry.

In all inclusions, the following two phase transitions were observed: (1) Initial melting (T_i) of ice crystals in the temperature interval -35 to -21°C, (2) final melting of ice (T_m) at -2.1 to -1.3°C, implying an average salinity of ca. 3.2 wt% NaCl equivalents (Bodnar and Vityk, 1994). No CO_2-clathrate was formed during the microthermometry experiments such that the total CO_2 contents in the inclusions are below about 2.5 wt% (Perry, 1936). The average salinity of 3.2 wt% NaCl of the fluid inclusions and the chlorine concentrations (Cl_{mean}=2140 ppm) of the 2011 melt inclusions yield a mean partition coefficient Kd_{mean}=9.1±1.5 (K_D^{range}=7.3-11.2) that matches the experimental results of Bureau et al. (2000).

Isochores calculated from fluid inclusion salinity and density estimates (see ESM4) yield exsolution pressures of 95-150 MPa at the temperature range (875-890°C) obtained from mineral-melt thermometry; this pressure range agrees reasonably well with the pressures obtained from clinopyroxene-liquid equilibria.

4.4 DISCUSSION

The susceptibility of a magmatic system to triggering by remote seismic events depends mainly on the criticality of the system at the time of excitation, i.e. how close the system is to the point of eruption. Such criticality is primarily controlled by the nature and abundance of exsolved fluids and the overpressure they generate in the system. On the other hand, triggering also depends on the tectonic parameters such as type, size and distance of the earthquake. This intrinsic complexity in magmatic systems and associated feedback mechanisms, probably causes seismically-triggered eruptions to occur with a time lag of days to years after the earthquake.

Our mineral-thermobarometric calculations reveal magma storage at temperatures around 900°C in the upper third of the crust (Fig. 4.2; P_{mean}=154±40 MPa, equals 5.8±1.5 km; for comparison, MOHO-depth is 35 km; Völker et al., 2011). In order to constrain the depth of fluid oversaturation for the PCCVC eruptions, H_2O concentrations based on melt inclusion - host plagioclase pairs combined with crystallization pressures obtained from chemical thermobarometry were compared with the H_2O solubility model of Newman and Lowenstern (2002). Data from all eruptive units lie close to the range of water saturation (Fig. 4.3a). Matrix glass - plagioclase rim pairs yield a tendency to even higher H_2O concentrations implying that some supersaturation may have developed in the melt (or else solubility may have slightly increased with changing composition). Such fluid oversaturation is further corroborated by the occurrence of primary magmatic fluid inclusions in the same host minerals in the 2011 tephra (Fig. 4.3c). Furthermore, the pressure mode of 120 to 130 MPa obtained for the 2011 eruption overlaps very well with the

fluid-inclusion based pressures of 95 to 150 MPa, providing strong evidence for fluid oversaturation at depths less than about 6 km, corresponding to the upper portion of the magma feeding system.

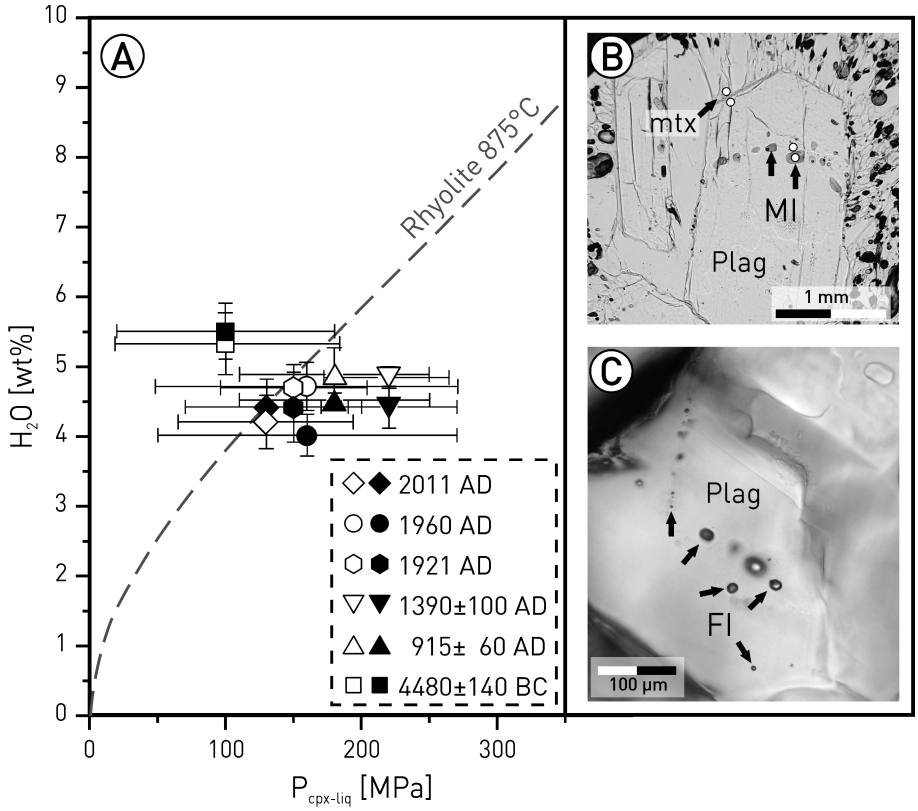

Fig. 4.2 A) Calculated H_2O contents (Eq. 25b from Putirka, 2008) and pressures compared to H_2O-solubility calculated after Newman and Lowenstern (2002). Open symbols represent matrix glass, filled symbols melt inclusion derived values. The error bars represent the range of computed values. For all PCCVC tephras melts appear to have reached H_2O-saturation before eruption. B) Plagioclase phenocryst with melt inclusions (MI) and adherent matrix glass (mtx). White dots figuratively mark data pairs (matrix glasses and crystal-rims; melt inclusions and immediately overgrown host minerals) as used for P-T-X estimates. C) Fluid inclusions (black arrows) hosted in a plagioclase phenocryst from the 2011 eruption.

Addressing a possible eruption triggering mechanism, we modeled the pressure increase for closed system crystallization for H_2O-saturated melts using the formulation of Tait et al. (1989) (ESM5). The results indicate that 5-10% of crystallization (i.e. the phenocryst contents of the pumice clasts) after H_2O saturation is reached yield an increase in pressure of 10-20% above the saturation pressure (5% crystals → 14 MPa, 10% crystals → 30 MPa). Therefore, only ~5% of fractional crystallization are required with a pure H_2O gas phase to cause overpressures exceeding the fracture criterion for pristine granitic country rock (13.8±2.1 MPa, Touloukian et al., 1981) such as the granite plutons that occur in the vicinity of the PCCVC (Sepúlveda et al., 2005); sedimentary country rock would be considerably weaker.

4.5 CONCLUSION

Thermobarometry suggests a shallow magma chamber (2-10 km depth, 50-250 MPa pressure) at 865 to 890°C temperature for the 2011 eruption. Volatile concentrations (4-5 wt% H_2O) and occurrence of water-dominated, low-salinity magmatic fluid inclusions indicate that H_2O-saturation prevailed in the upper portions of the feeding system (above about 6 km depth) during crystallization and significantly prior to eruption.

Relatively shallow reservoirs and pre-eruptive H_2O-saturation were typical features also of the older post-glacial explosive eruptive events at PCCVC. Our investigations suggest that the system repeatedly resumed a critical state throughout its whole (documented) post-glacial evolution. Thus, in principle, the PCCVC system was susceptible to seismic triggering but still eruptive activity and large earthquakes show quite distinct time series behavior (e.g. Watt et al., 2009). When the critical state generated an internally triggered eruption, criticality and susceptibility may have been temporarily lost for a subsequent large regional earthquake. On the other hand, tectonic conditions of some earthquakes may have been insufficient for them to serve as eruption trigger. While we can reasonably assume that PCCVC will again be in a critical state, seismic eruption triggering still requires sufficient strength and proper timing and location of a future large earthquake. Although being a case study based on particular PCCVC conditions, the general implication from this study may be applicable to other volcanic systems with similar prerequisites. Especially in silicic subduction-related systems shallow storage and volatile saturation are common features (e.g. Pinatubo, Scaillet and Evans, 1999; Novarupta, Hammer et al., 2002), as are arc-wide fault systems in the upper plate due to oblique convergence in other subduction zones (e.g. Sumatra-Andaman; McCarthy and Elders, 1997). We therefore infer that seismic triggering of volcanic eruptions may be more common than usually assumed.

Acknowledgements

We gratefully acknowledge the support of M. Thöner during EPMA measurements. This publication is contribution no. 248 of the Sonderforschungsbereich 574 on "Volatiles and Fluids in Subduction Zones" at Kiel University.

REFERENCES

Arancibia, G., Cembrano, J., and Lavenu, A., 1999, Transpresión dextral y partición de la deformación en la Zona de Falla Liquiñe-Ofqui, Aisén, Chile (44-45°S): Revista Geológica de Chile, v. 26, p. 3-22.

Bakker, R.J., 2003, Package FLUIDS 1. Computer programs for analysis of fluid inclusion data and for modelling bulk fluid properties: Chemical Geology, v. 194, p. 3-23.

Bodnar, R.J., and Vityk, M.O., 1994, Interpretation of microthermometric data for NaCl-H2O inclusions, *in* De Vivo, B., and Frezzotti, M.L., eds., Fluid inclusions in minerals: Methods and applications. Short course of the working group (IMA) "Inclusions in Minerals": Blacksburg, Virginia, USA, Virginia Polytechnic Institute and State University, p. 117-131.

Borchardt, G.A., Aruscavage, P.J., and Millard, H.T., 1972, Correlation of the Bishop Ash, a Pleistocene marker bed, using instrumental neutron activation analysis: Journal of Sedimentary Research, v. 42, p. 301-306.

Bureau, H., Keppler, H., and Métrich, N., 2000, Volcanic degassing of bromine and iodine: experimental fluid/melt partitioning data and applications to stratospheric chemistry: Earth and Planetary Science Letters, v. 183, p. 51-60.

Cembrano, J., and Lara, L., 2009, The link between volcanism and tectonics in the southern volcanic zone of the Chilean Andes: A review: Tectonophysics, v. 471, p. 96-113.

Cembrano, J., Schermer, E., Lavenu, A., and Sanhueza, A., 2000, Contrasting nature of deformation along an intra-arc shear zone, the Liquiñe-Ofqui fault zone, southern Chilean Andes: Tectonophysics, v. 319, p. 129-149.

Eggert, S., and Walter, T.R., 2009, Volcanic activity before and after large tectonic earthquakes: Observations and statistical significance: Tectonophysics, v. 471, p. 14-26.

Froggatt, P.C., 1992, Standardization of the chemical analysis of tephra deposits. Report of the ICCT Working Group: Quaternary International, v. 13-14, p. 93--96.

Gerlach, D.C., Frey, F.A., Moreno-Roa, H., and Lopez-Escobar, L., 1988, Recent Volcanism in the Puyehue--Cordon Caulle Region, Southern Andes, Chile (40·5°S): Petrogenesis of Evolved Lavas: Journal of Petrology, v. 29, p. 333-382.

Hammer, J., Rutherford, M., and Hildreth, W., 2002, Magma storage prior to the 1912 eruption at Novarupta, Alaska: Contributions to Mineralogy and Petrology, v. 144, p. 144-162.

Hill, D.P., Pollitz, F., and Newhall, C., 2002, Earthquake-Volcano Interactions: Physics Today, v. 55, p. 41-47.

Lange, R.A., Frey, H.M., and Hector, J., 2009, A thermodynamic model for the plagioclase-liquid hygrometer/thermometer: American Mineralogist, v. 94, p. 494-506.

Lara, L.E., Moreno, H., Naranjo, J.A., Matthews, S., and Pérez de Arce, C., 2006, Magmatic evolution of the Puyehue-Cordón Caulle Volcanic Complex (40° S), Southern Andean Volcanic Zone: From shield to unusual rhyolitic fissure volcanism: Journal of Volcanology and Geothermal Research, v. 157, p. 343-366.

Lara, L.E., Naranjo, J.A., and Moreno, H., 2004, Rhyodacitic fissure eruption in Southern Andes (Cordón Caulle; 40.5°S) after the 1960 (Mw:9.5) Chilean earthquake: a structural interpretation: Journal of Volcanology and Geothermal Research, v. 138, p. 127-138.

Linde, A.T., and Sacks, I.S., 1998, Triggering of volcanic eruptions: Nature, v. 395, p. 888-890.

López-Escobar, L., Cembrano, J., and Moreno, H., 1995, Geochemistry and tectonics of the chilean Southern Andes basaltic Quaternary volcanism (37°-46°S). Revista Geológica de Chile, v. 22, p. 219-234.

Manga, M., and Brodsky, E., 2006, Seismic Triggering of Eruptions in the Far Field: Volcanoes and Geysers. : Annual Review of Earth and Planetary Sciences, v. 34, p. 263-291.

McCarthy, A.J., and Elders, C.F., 1997, Cenozoic deformation in Sumatra: oblique subduction and the development of the Sumatran Fault System: Geological Society, London, Special Publications, v. 126, p. 355-363.

McCormac, F.G., Hogg, A.G., Blackwell, P.G., Buck, C.E., Higham, T.F.G., and Reimer, P.J., 2004, SHCal04 Southern Hemisphere Calibration, 0–11.0 cal kyr BP: Radiocarbon, v. 46, p. 1087-1092.

Newman, S., and Lowenstern, J.B., 2002, VC: a silicate melt-H2O-CO2 solution model written in Visual Basic for excel: Computers & Geosciences, v. 28, p. 597--604.

Ortega-Guerrero, B., and Newton, A.J., 1998, Geochemical Characterization of Late Pleistocene and Holocene Tephra Layers from the Basin of Mexico, Central Mexico: Quaternary Research, v. 50, p. 90-106.

OVDAS, 2011, Complejo Volcánico Puyehue-Cordón Caulle - Región de Los Ríos, Reporte Especial de Actividad Volcánica Volume 26: Temuco, SERNAGEOMIN.

Perry, R.H., 1936, Chemical engineers' handbook: New York, McGraw-Hill Professional, 674 p.

Putirka, K.D., 2008, Thermometers and Barometers for Volcanic Systems, *in* Putirka, K.D., and Tepley III, F.J., eds., Minerals, inclusions and volcanic processes, Volume 69: Reviews in Mineralogy and Geochemistry, The Mineralogical Society of America, p. 61-111.

Roeder, P.L., and Emslie, R.F., 1970, Olivine-liquid equilibrium: Contributions to Mineralogy and Petrology, v. 68, p. 325 - 334.

Rosenau, M., Melnick, D., and Echtler, H., 2006, Kinematic constraints on intra-arc shear and strain partitioning in the southern Andes between 38°S and 42°S latitude: Tectonics, v. 25, p. TC4013.

Scaillet, B., and Evans, B.W., 1999, The 15 June 1991 Eruption of Mount Pinatubo. I. Phase Equilibria and Pre-eruption P–T–fO2–fH2O Conditions of the Dacite Magma: Journal of Petrology, v. 40, p. 381-411.

Sepúlveda, F., Lahsen, A., Bonvalot, S., Cembrano, J., Alvarado, A., and Letelier, P., 2005, Morpho-structural evolution of the Cordón Caulle geothermal region, Southern Volcanic Zone, Chile: Insights from gravity and 40Ar/39Ar dating: Journal of Volcanology and Geothermal Research, v. 148, p. 165-189.

Singer, B.S., Jicha, B.R., Harper, M.A., Naranjo, J.A., Lara, L.E., and Moreno-Roa, H., 2008, Eruptive history, geochronology, and magmatic evolution of the Puyehue-Cordon Caulle volcanic complex, Chile: Geological Society of America Bulletin, v. 120, p. 599-618.

Stuiver, M., and Reimer, P.J., 1993, Extended 14C Data Base and Revised Calib 3.0 14C Age Calibration Program: Radiocarbon, v. 35, p. 215-230.

Tait, S., Jaupart, C., and Vergniolle, S., 1989, Pressure, gas content and eruption periodicity of a shallow, crystallising magma chamber: Earth and Planetary Science Letters, v. 92, p. 107-123.

Touloukian, Y.S., Judd, W.R., and Roy, R.F., 1981, Physical Properties of Rocks and Minerals: New York, McGraw Hill.

Völker, D., Kutterolf, S., and Wehrmann, H., 2011, Comparative mass balance of volcanic edifices at the southern volcanic zone of the Andes between 33°S and 46°S: Journal of Volcanology and Geothermal Research, v. 205, p. 114-129.

Walter, T.R., and Amelung, F., 2007, Volcanic eruptions following M ≥ 9 megathrust earthquakes: Implications for the Sumatra-Andaman volcanoes: Geology, v. 35, p. 539-542.

Watt, S.F.L., Pyle, D.M., and Mather, T.A., 2009, The influence of great earthquakes on volcanic eruption rate along the Chilean subduction zone: Earth and Planetary Science Letters, v. 277, p. 399-407.

ACKNOWLEDGEMENTS

I am deeply grateful to all people that supported and promoted me during the last three and a half years while I worked on this thesis. I want to mention and thank a number of people in particular:

First of all, I would like to thank **Armin Freundt**, my thesis supervisor. His enthusiasm and experience, and our lively discussions about volcanology and my work were always stimulating for me. His critical but always benevolent treatment of my analytical results, my approaches and of writing manuscripts trained me to become a concise scientist. I really appreciate the freedom he gave me to develop my own ideas, and finally steering the sometimes resulting nonsense into the right direction. I especially want to thank him for the time he put into giving advice and correcting drafts for this thesis as well as for supporting me during all my efforts to establish my future career.

I am in great debt to **Steffen Kutterolf**, who led me into the scientific realm of tephra layers, facilitated lots of my lab tasks and was always willing for discussions, advices, correcting drafts and sharing a laugh.

Thor Hansteen was always available for discussions and cracking Friday jokes – even on Mondays. Furthermore, he introduced me to the secrets of microthermometry and processing of fluid inclusion data and was of great help during the last weeks of my PhD work.

I want to thank **Kaj Hoernle** for his willingness to read my thesis and act as my co-referee. I greatly appreciate his effort.

Cosima Burkert joined me during my first two field campaigns and greatly contributed to solve the quest of establishing a general tephrostratigraphy of the Lonquimay volcano by her willingness for discussing the same tephra layers over and over again.

I want to thank my coauthors: **Alvaro Amigo** for sharing observations and providing samples to investigate the 2011 eruption of Puyehue-Cordón Caulle. **Heidi Wehrmann** did a great job guiding me through the preparation for and during SIMS-analyses at GFZ Potsdam. **Robert Trumbull** made the SIMS campaign possible by calibrating the machine early in the morning and shutting it down late at night.

Apart from the people mentioned above, my analytical work for this thesis was greatly facilitated by the following people: **Julie Schindlbeck, Karen Strehlow** and **Kathrin Laeger** were reliable helping hands during various preparation steps. **Dagmar Rau, Elisabeth Thun** and **Stefan Jung** provided XRF data for all my tephra samples. **Ulrike Westernströer** was of great

help during acid pressure digestion and subsequent ICP-MS analyses of my samples. **Dieter Garbe-Schönberg** introduced me into the principles and specialties of ICP-MS analytics as well as processing of trace element data. He also joined me during my last field campaign together with **Maren Wanke** and **Guillaume Jacques.** All three of them made especially the guitar and wine sessions in the evening a memorable experience. I want to extend a special word of thanks to **Mario Thöner**. He greatly facilitated my research by taking care for all of my calibrations during several thousand EPMA analyses that build the spine of this thesis. The LA-ICP-MS group at GEOMAR, **Jan Fietzke, Matthias Frische** and **Dagmar Rau** are thanked for being so patient with the first steps to get trace element information out of tiny melt inclusions.

Apart from this "scientific" support mentioned above, I owe thanks to the many persons that made my PhD time a particular exciting period of my life: **Felix, Lukas, Dirk, Anke** and all other members of the Kivelo and Vapiano training groups for an enjoyable time in the saddle. The members of the SFB574 and particularly my colleagues from building 8A for the positive and stimulating atmosphere.

Rauno, Anna and the **Rohde family** for drinks, barbecues or just hanging out and talking our way through thesis problems. **Vera, Dirk, Katha** and **Benny** for their enduring friendship. I particularly want to thank Dirk for critically correcting parts of this thesis.

I especially want to thank **my parents** for all their support and believe in me, especially during the sometimes unexpected changes in my personal life and during my studies. They helped me to become the person that I am now.

Last, not least my dear **Julia** for all her patience and support, especially during the last months of finishing this thesis. Your love and joy in life made my work so much easier.

CURRICULUM VITAE

DAVID JOHANN GILBERT

Date of birth:	*05.08.1980*
Place of birth:	*Karlsruhe, Germany*
Nationality:	*German*

ACADEMIC EDUCATION

2009 – 2011 PhD student within the Collaborative Research Center (SFB) 574 at GEOMAR | Helmholtz-Centre for Ocean Research Kiel, Germany

2003 – 2008 Studies of Earth Sciences, University of Stuttgart, Germany

2001 – 2003 Studies of Aerospace Engineering, University of Stuttgart, Germany

Appendix A

Supplementary material for Chapter 2

Post-glacial time series of explosive eruptions and associated changes in the magma plumbing system of Lonquimay volcano, south central Chile

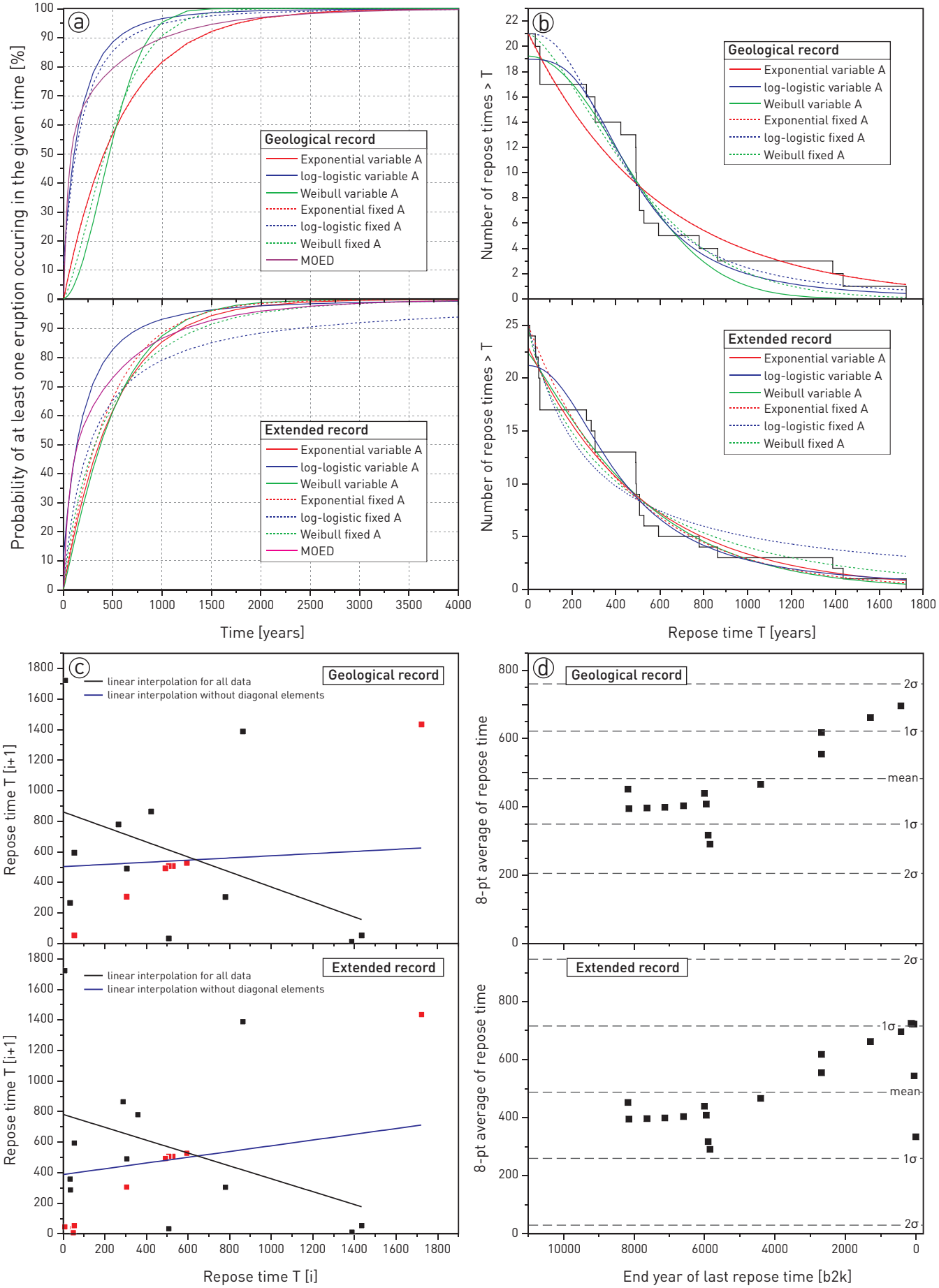

Fig. A.1 a) Eruption probabilities for the different fit-distributions for geological and extended records.
b) All distribution functions used to fit the observed repose time distribution using both variable and fixed scale factor A.
c) Scatter plots of observed repose times versus preceding repose times used to check the independence of the data sets for the extended and geological record. The black lines show the results of linear regression if the independence test is performed indiscriminately in the "standard" way. The blue line results from the test after deleting the diagonal elements (red), that are artifacts from interpolated ages.
d) Variation of moving-average repose time versus end date of repose periods used to test for stationarity for geological and extended records.

Unit	sample	Al2O3	STD	CaO	STD	FeO	STD	K2O	STD	MgO	STD	MnO	STD	Na2O	STD	P2O5	STD	SiO2	STD	TiO2	STD	Total	N
B	C-375	**12.67**	0.51	**5.32**	0.38	**12.20**	1.40	**1.51**	0.27	**2.04**	0.23	**0.26**	0.05	**3.44**	0.63	**0.43**	0.05	**59.88**	1.41	**2.11**	0.19	100.00	11
C	C-376	**16.78**	0.98	**7.41**	0.35	**10.32**	0.68	**0.65**	0.06	**2.33**	0.57	**0.23**	0.04	**3.95**	0.25	**0.19**	0.02	**56.52**	0.96	**1.61**	0.21	100.00	7
C	C-377_pop1	**15.12**	1.86	**6.98**	0.42	**10.57**	1.65	**0.80**	0.09	**1.99**	0.43	**0.25**	0.07	**3.42**	0.76	**0.24**	0.04	**58.65**	0.42	**1.87**	0.30	100.00	6
C	C-377_pop2	**14.81**	2.11	**8.41**	0.61	**11.36**	2.08	**0.58**	0.09	**3.32**	1.41	**0.24**	0.06	**3.56**	0.27	**0.20**	0.03	**55.70**	0.53	**1.65**	0.33	100.00	4
C	C-379	**13.08**	2.46	**6.62**	0.73	**12.34**	1.44	**0.91**	0.22	**3.88**	1.74	**0.29**	0.06	**3.79**	0.76	**0.31**	0.05	**57.02**	1.43	**1.76**	0.18	100.00	7
D	C-374a	**15.18**	1.34	**3.93**	0.45	**7.95**	1.76	**1.24**	0.21	**1.90**	1.60	**0.23**	0.09	**4.95**	0.70	**0.37**	0.05	**63.33**	1.78	**0.92**	0.06	100.00	11
E	C-388	**14.80**	2.09	**6.45**	0.77	**10.94**	2.35	**0.95**	0.13	**2.37**	0.76	**0.21**	0.05	**4.23**	0.66	**0.27**	0.05	**57.87**	1.52	**1.89**	0.32	100.00	9
F	C-188	**17.14**	0.19	**3.44**	0.15	**5.29**	0.24	**1.36**	0.10	**0.64**	0.08	**0.19**	0.02	**5.39**	0.09	**0.18**	0.03	**65.91**	0.31	**0.47**	0.03	100.00	8
G	C-197a	**16.71**	0.62	**3.53**	0.28	**5.17**	0.51	**1.31**	0.11	**0.70**	0.16	**0.17**	0.05	**5.54**	0.32	**0.18**	0.03	**66.19**	0.66	**0.51**	0.05	100.00	11
G	C-359a	**16.01**	0.76	**3.41**	0.30	**5.63**	0.60	**1.33**	0.13	**0.93**	0.14	**0.21**	0.05	**5.71**	0.24	**0.18**	0.02	**66.07**	0.52	**0.52**	0.04	100.00	11
G	C-359b	**17.16**	1.17	**3.41**	0.55	**4.00**	0.89	**1.34**	0.22	**0.44**	0.19	**0.16**	0.04	**6.11**	0.39	**0.16**	0.04	**66.80**	1.44	**0.44**	0.10	100.00	14
I	C-200	**16.11**	1.33	**2.81**	0.62	**4.11**	0.55	**1.78**	0.33	**0.32**	0.06	**0.09**	0.04	**5.58**	0.67	**0.11**	0.02	**68.72**	1.76	**0.36**	0.06	100.00	6
I	C-202	**15.83**	1.59	**4.40**	0.89	**6.91**	2.71	**1.43**	0.29	**1.15**	0.62	**0.17**	0.07	**5.29**	0.70	**0.36**	0.16	**63.23**	3.31	**1.24**	0.65	100.00	9
I	C-358a	**16.15**	0.76	**2.89**	0.25	**4.41**	0.66	**1.63**	0.21	**0.47**	0.10	**0.12**	0.05	**5.68**	0.50	**0.08**	0.02	**68.21**	0.53	**0.36**	0.04	100.00	20
I	C-358b	**16.78**	1.05	**5.00**	0.38	**8.21**	1.15	**1.04**	0.18	**1.67**	0.32	**0.22**	0.05	**5.32**	0.59	**0.42**	0.06	**60.26**	0.51	**1.08**	0.13	100.00	16
I	C-368b	**16.94**	1.07	**3.01**	0.47	**3.95**	0.94	**1.53**	0.26	**0.39**	0.11	**0.12**	0.05	**5.59**	1.32	**0.08**	0.02	**68.07**	1.27	**0.32**	0.06	100.00	15
J	C-203a	**16.68**	1.61	**5.84**	0.41	**8.13**	1.64	**0.85**	0.14	**2.36**	1.48	**0.17**	0.06	**5.10**	0.50	**0.31**	0.04	**59.20**	1.22	**1.36**	0.16	100.00	8
J	C-370_pop1	**16.59**	2.36	**6.08**	0.51	**8.79**	2.12	**0.97**	0.25	**1.95**	0.82	**0.19**	0.09	**4.73**	0.77	**0.30**	0.07	**58.85**	0.74	**1.57**	0.33	100.00	10
J	C-370_pop2	**15.17**	0.37	**3.70**	0.31	**5.28**	0.18	**2.17**	0.11	**1.45**	0.46	**0.14**	0.03	**4.93**	0.10	**0.28**	0.02	**65.79**	0.62	**1.09**	0.05	100.00	5
K	C-500	**13.55**	0.29	**7.07**	0.20	**13.73**	0.43	**0.92**	0.05	**3.65**	0.36	**0.28**	0.03	**3.57**	0.41	**0.32**	0.02	**54.68**	0.46	**2.24**	0.10	100.00	15
M	C-356	**16.80**	0.21	**3.60**	0.31	**5.22**	0.54	**1.43**	0.13	**0.75**	0.14	**0.18**	0.04	**5.45**	0.29	**0.14**	0.04	**65.97**	0.90	**0.46**	0.05	100.00	13
M	C-371a	**16.86**	0.62	**3.65**	0.40	**5.19**	0.60	**1.36**	0.16	**0.71**	0.12	**0.17**	0.06	**5.70**	0.34	**0.15**	0.03	**65.74**	0.87	**0.47**	0.07	100.00	25
M	C-394	**14.59**	0.13	**7.30**	0.37	**13.78**	0.35	**0.64**	0.27	**4.07**	0.10	**0.27**	0.05	**3.46**	0.59	**0.31**	0.02	**53.44**	0.53	**2.14**	0.06	100.00	11
N	C-355	**15.85**	1.12	**4.56**	0.50	**8.53**	1.38	**1.17**	0.26	**1.49**	0.66	**0.22**	0.07	**5.05**	0.48	**0.37**	0.05	**61.38**	1.48	**1.39**	0.18	100.00	24
N	C-396_pop1	**16.42**	1.08	**4.80**	0.56	**8.39**	1.33	**1.54**	0.68	**1.25**	0.40	**0.20**	0.05	**4.68**	0.49	**0.35**	0.04	**60.88**	0.60	**1.32**	0.24	100.00	11
N	C-396_pop2	**15.59**	1.09	**8.54**	0.64	**9.72**	0.69	**0.67**	0.11	**5.44**	0.72	**0.27**	0.07	**2.97**	0.35	**0.27**	0.01	**54.53**	0.31	**1.90**	0.20	100.00	4
N	C-396_pop3	**16.08**	1.10	**5.43**	0.51	**9.42**	1.01	**1.74**	0.32	**3.00**	0.58	**0.22**	0.04	**4.00**	0.29	**0.28**	0.02	**58.62**	0.48	**1.10**	0.08	100.00	4
N	C-397	**16.64**	1.83	**5.94**	0.57	**8.41**	1.41	**0.88**	0.17	**1.56**	0.43	**0.22**	0.05	**4.56**	0.52	**0.30**	0.05	**59.95**	0.83	**1.43**	0.25	100.00	8
O	C-501	**13.66**	0.54	**5.00**	0.68	**10.45**	0.93	**1.20**	0.21	**2.02**	0.48	**0.28**	0.05	**4.32**	0.46	**0.43**	0.07	**60.76**	1.49	**1.88**	0.13	100.00	13
O	C-502	**13.12**	0.49	**6.31**	0.58	**12.39**	0.75	**1.03**	0.13	**2.60**	0.26	**0.27**	0.03	**3.11**	0.30	**0.32**	0.07	**58.54**	1.20	**2.18**	0.12	100.00	14
P	C-503	**13.83**	0.73	**7.04**	0.24	**12.64**	0.92	**0.84**	0.09	**2.88**	0.34	**0.26**	0.04	**3.43**	0.55	**0.26**	0.03	**56.55**	0.54	**2.17**	0.13	100.00	15
Q	C-190	**15.38**	0.18	**2.60**	0.13	**4.82**	0.15	**1.95**	0.05	**0.35**	0.03	**0.16**	0.05	**4.72**	0.16	**0.07**	0.02	**69.60**	0.26	**0.36**	0.02	100.00	15
Q	C-352	**15.39**	0.11	**2.51**	0.05	**4.77**	0.21	**1.99**	0.03	**0.35**	0.03	**0.14**	0.04	**5.06**	0.10	**0.06**	0.02	**69.36**	0.25	**0.36**	0.02	100.00	15
Q	C-372a	**15.24**	0.19	**2.33**	0.10	**4.35**	0.21	**1.97**	0.14	**0.30**	0.03	**0.14**	0.06	**5.45**	0.27	**0.06**	0.02	**69.82**	0.19	**0.34**	0.01	100.00	12

Unit	sample	Al2O3	STD	CaO	STD	FeO	STD	K2O	STD	MgO	STD	MnO	STD	Na2O	STD	P2O5	STD	SiO2	STD	TiO2	STD	Total	N
R	C-199	**14.44**	0.59	**5.11**	0.27	**11.62**	0.78	**1.42**	0.19	**2.19**	0.32	**0.18**	0.03	**3.81**	0.37	**0.43**	0.04	**58.89**	0.42	**1.91**	0.13	100.00	12
R	C-399	**14.40**	0.30	**6.13**	0.25	**12.36**	0.46	**0.98**	0.07	**3.32**	0.40	**0.31**	0.02	**3.47**	0.25	**0.31**	0.01	**56.77**	0.56	**1.96**	0.08	100.00	8
S	C-189	**15.18**	0.14	**3.10**	0.10	**6.12**	0.22	**1.88**	0.06	**0.57**	0.03	**0.16**	0.06	**4.74**	0.18	**0.14**	0.03	**67.57**	0.22	**0.55**	0.02	100.00	15
S	C-191a	**15.49**	0.51	**3.03**	0.13	**5.70**	0.22	**1.89**	0.10	**0.56**	0.04	**0.17**	0.06	**4.91**	0.19	**0.13**	0.02	**67.57**	0.65	**0.55**	0.02	100.00	18
S	C-348a	**15.24**	0.51	**3.07**	0.19	**5.92**	0.52	**1.91**	0.19	**0.55**	0.06	**0.19**	0.06	**5.35**	0.49	**0.14**	0.02	**67.08**	0.37	**0.55**	0.05	100.00	18
S	C-348b	**13.98**	0.57	**7.74**	0.15	**13.04**	0.73	**0.79**	0.05	**4.10**	0.44	**0.23**	0.06	**3.82**	0.26	**0.25**	0.04	**54.06**	0.63	**1.99**	0.09	100.00	14
S	C-349	**15.48**	0.11	**3.25**	0.09	**6.11**	0.24	**1.80**	0.03	**0.62**	0.04	**0.20**	0.06	**4.66**	0.20	**0.13**	0.02	**67.19**	0.33	**0.56**	0.03	100.00	17
S	C-350	**15.25**	0.64	**3.01**	0.26	**6.13**	0.60	**1.97**	0.29	**0.57**	0.09	**0.19**	0.05	**4.80**	0.59	**0.13**	0.03	**67.38**	0.57	**0.56**	0.05	100.00	25
S	C-367a	**15.17**	0.43	**3.04**	0.23	**5.73**	0.42	**1.84**	0.14	**0.54**	0.06	**0.17**	0.05	**5.27**	0.26	**0.12**	0.02	**67.59**	0.42	**0.53**	0.03	100.00	18
S	C-367b	**15.52**	0.92	**3.07**	0.48	**5.32**	0.71	**1.81**	0.34	**0.50**	0.10	**0.16**	0.06	**5.57**	0.40	**0.12**	0.02	**67.44**	0.86	**0.48**	0.08	100.00	15
S	C-380	**15.52**	0.50	**3.12**	0.20	**5.96**	0.50	**1.79**	0.12	**0.59**	0.09	**0.20**	0.07	**5.36**	0.24	**0.14**	0.02	**66.76**	0.50	**0.55**	0.07	100.00	13
T	C-192	**15.51**	0.76	**2.14**	0.27	**3.71**	0.46	**2.06**	0.21	**0.24**	0.05	**0.16**	0.07	**5.44**	0.58	**0.05**	0.01	**70.40**	0.93	**0.29**	0.04	100.00	13
T	C-346a	**15.61**	0.54	**2.20**	0.24	**3.90**	0.28	**2.04**	0.18	**0.27**	0.02	**0.14**	0.06	**5.18**	0.39	**0.05**	0.02	**70.31**	0.70	**0.29**	0.03	100.00	20
T	C-346b	**14.91**	0.84	**1.80**	0.38	**3.45**	0.46	**2.39**	0.31	**0.16**	0.06	**0.10**	0.04	**5.47**	0.54	**0.06**	0.01	**71.33**	1.15	**0.33**	0.10	100.00	9
T	C-347	**16.02**	1.76	**2.34**	0.51	**3.04**	1.25	**1.94**	0.37	**0.19**	0.25	**0.14**	0.11	**5.68**	1.48	**0.04**	0.02	**70.38**	2.34	**0.22**	0.05	100.00	9
T	C-366	**15.53**	0.43	**2.18**	0.23	**3.95**	0.51	**2.04**	0.18	**0.26**	0.06	**0.16**	0.06	**5.71**	0.34	**0.06**	0.03	**69.80**	0.69	**0.31**	0.05	100.00	31
T	C-381a	**15.38**	0.30	**2.11**	0.10	**3.84**	0.35	**2.02**	0.16	**0.26**	0.04	**0.13**	0.05	**5.82**	0.21	**0.05**	0.01	**70.07**	0.29	**0.30**	0.04	100.00	15
T	C-381b	**15.59**	1.42	**2.00**	0.53	**2.96**	0.72	**2.13**	0.36	**0.10**	0.06	**0.10**	0.04	**6.07**	0.67	**0.05**	0.02	**70.73**	1.49	**0.26**	0.07	100.00	16
U	C-382a	**15.06**	1.31	**2.30**	0.44	**3.75**	0.85	**2.20**	0.29	**0.28**	0.11	**0.14**	0.03	**5.51**	0.61	**0.11**	0.10	**70.31**	1.14	**0.35**	0.08	100.00	18
U	C-382b	**15.11**	1.55	**2.14**	0.71	**3.75**	0.71	**2.22**	0.41	**0.21**	0.09	**0.12**	0.05	**4.53**	0.76	**0.08**	0.02	**71.28**	1.86	**0.33**	0.07	100.00	8
U	C-382c	**16.15**	1.68	**5.15**	0.50	**8.64**	1.53	**1.13**	0.20	**1.60**	0.70	**0.23**	0.06	**4.54**	0.43	**0.44**	0.07	**60.85**	0.65	**1.11**	0.16	100.00	15
V	C-194	**15.07**	1.20	**3.15**	0.29	**5.39**	1.09	**1.72**	0.20	**0.46**	0.14	**0.20**	0.08	**5.47**	0.58	**0.19**	0.10	**67.77**	0.59	**0.57**	0.13	100.00	11
V	C-204a	**15.29**	0.99	**2.69**	0.41	**5.17**	0.77	**1.88**	0.23	**0.58**	0.25	**0.17**	0.04	**5.15**	0.55	**0.16**	0.03	**68.39**	1.29	**0.53**	0.07	100.00	11
V	C-204b	**15.42**	0.85	**2.83**	0.44	**5.38**	0.85	**1.84**	0.21	**0.59**	0.30	**0.16**	0.07	**5.30**	0.41	**0.14**	0.03	**67.79**	0.96	**0.55**	0.05	100.00	12
V	C-205a	**14.15**	0.63	**2.17**	0.21	**5.32**	0.87	**2.11**	0.12	**0.59**	0.31	**0.18**	0.07	**4.88**	0.42	**0.15**	0.03	**69.87**	0.77	**0.57**	0.08	100.00	13
V	C-342	**15.39**	1.57	**2.32**	0.66	**3.87**	0.86	**2.15**	0.35	**0.25**	0.15	**0.13**	0.04	**4.98**	0.76	**0.10**	0.04	**70.46**	1.91	**0.34**	0.08	100.00	25
V	C-343	**15.51**	1.31	**2.47**	0.51	**4.35**	0.96	**2.06**	0.31	**0.33**	0.16	**0.15**	0.06	**5.69**	0.58	**0.09**	0.03	**68.94**	1.34	**0.41**	0.08	100.00	21
W	C-206	**14.60**	2.17	**4.64**	0.64	**9.69**	1.69	**1.33**	0.25	**2.16**	0.73	**0.21**	0.03	**4.33**	0.54	**0.49**	0.09	**60.93**	0.81	**1.63**	0.29	100.00	11
W	C-510	**13.20**	0.48	**4.67**	0.21	**9.82**	0.62	**1.47**	0.12	**1.68**	0.10	**0.27**	0.04	**3.80**	0.34	**0.46**	0.03	**62.43**	0.39	**2.07**	0.09	100.00	24

Tab. A.1 Matrix-glass analyses of LVC samples from chapter 2. Compositions are reported as mean values and standard deviation of compositions obtained from n spot analyses.

Stratigraphic Unit	Sample	compositional group	phenocrysts																											mineral clusters	cumulates	matrix	rock texture	vesicle texture	comments		
			plagioclase						clinopyroxene						olivine						Fe-Ti-oxides				Amphibole				apatite								
			euhedral	subhedral	anhedral	oscillatory zoning	fragments	sieve texture	euhedral	subhedral	anhedral	fragments	embayments	sieve texture	euhedral	subhedral	anhedral	fragments	embayments	sieve texture	euhedral	subhedral	anhedral	whisker	euhedral	subhedral	anhedral	clasts									
Va	C-204	LCPT	x	x		x	x	r	x	x				x	x	x	x		x		x	x							x	x		vitric	vitrophyric to glomerophyric	highly vesicular		ores as "inclusions"/intergrowths with ol/cpx, rare but existent intergrowths of ores and plag	hbl-free
	C-342					x	x	r	x	x					x				x		x	x								x					pleochroitic Cpx		
	C-343		x	x		x	x	x	x						x	x			x		x	x							x	x							
Ua	C-382		x	x		x	x		x	x				x	x	x	x		x	x				x					r	x	x						
Ta	C-346		x	x		r	x		x					x	x				x		x	x								x					ap as needles in cpx		
	C-347		x	x		r	x			x						x	x				x	x							x	x							
Sb	C-191b		x	x			x		x	x					x														x	x					lots of MI in cpx + ol		
	C-349		x	x		x	x			x		x		x	x	x					x	x							x	x					ap in ol + cpx, lots of MI in cpx + ol		
	C-350		x	x		x	x			x	x	x		x		x			x		x	x							x	x					lots of MI in cpx + ol		
Qb	C-190		x	x		x	x	r	x	x		x				x			x											x							
	C-372		x	x			x	r	x	x		x				x			x		x	x							x	x	x				LDS-clast as incl. (pic)		
Ma	C-371	LCPT	x			x	x		x	x		x			x	x			x		x	x			x	x		x	x	x					ap in cpx + ol, large fe-ti-oxides		hbl-bearing
Ia	C-358a		x	x			x	r	x	x		x				x			x	x	x	x							x	x							
	C-358b		x	x		x	x		x	x		x			x	x			x	n					x	x		x	x	x	x				hbl as single crystals, no ores or other intergrowths, very rare plag intergrowths		
	C-200		x	x		x	x		x	x		x		x	x	x			x		x	x			x	x		x	x	x							
Ga	C-359a		x	x		x	x								x	x			x		x	x			x	x		x	x								
	C-359b		x	x		x	x								x	x			x	x	x	x			x	x		x	x	x							
Na	C-397	LGPT	x	x		r	x	x	x	x	x	x			x	x		x	x		x									x		vitric >> microcrystalline	vitrophyric to glomerophyric	microvesicular to vesicular	devitrified MI, rare fe-ti - only as intergrowth	no Fe-Ti-intergrowth with Plag. Only Cpx + Ol	Ol >> Cpx
Mb	C-394		x	x			x	x								x		x	x		x								r	x					Fe-Ti-oxides only as cluster with ol, rare		
Ja	C-203a		x	x			x			x					x	x		x	x		r					x		x		r					hbl as single crystals, no ores or other intergrowths, very rare plag intergrowths		
	C-370		x	x		r	x		x	x		x				x			x	x	r				x	x		x		x							
Ib	C-202		x	x			x			x		x	x		x	x			x		x									x	x				Fe-Ti-oxides as IG with ol		
	C-369		x	x			x	x		x		x	x			x		x	x		x									x					Fe-Ti-oxides as IG with ol		
Gb	C-198a		x			r	x	x							x	x		x	x	x	x					x		x	r								
	C-198b		x	x		r	x	x							x	x		x	x	x	x	x			x	x		x	r	x	x						
Da	C-374		x	x			x														x	x				x		x	r								
Wa	C-510	LDST		x			x									x	x		x		x			x					r			vitric = microcrystalline	vitrophyric to glomerophyric	vesicular	Fe-Ti-oxides in mtx, not as cluster	Fe-Ti oxides as single phenocryst in mtx	rare cpx
Rb	C-199		x	x			x	x		r							x	x	x		x	x								x	x						
	C-399		x	x	x		x	xx		r						x			x		x								r	x	x				Fe-Ti-oxides in mtx, not as cluster		
Pe	C-503		x	x			x	xx		r	r	x			x	x			x		x	x								x	x						
O	C-501		x	x			x	xx		r		x				x	x	x	x		r	r								x	x				Fe-Ti-oxides as cluster with Cpx + Ol, single phenocrysts in mtx		
	C-502		x	x			x	xx								x		x	x		x	x	x						r	x	x				Fe-Ti-oxides as cluster with Cpx + Ol, single phenocrysts in mtx		
Kb	C-500		x	x			x	x								x			x		x	x								x							
B	C-375	LDST		x			x	x		x	x	x	x			x			x		r									x	x	microcrystalline >> vitric	porphyritic to glomerophyric	dense to microvesicular			with cpx
Cc	C-379		x	x			x	x	x	x		x			x	x			x		x	x								x	x				cluster of Fe-Ti + Cpx + Ol		
Cb	C-377		x				x	x	x	x		x			x	x			x		x									x	x				cluster of Fe-Ti + Cpx + Ol		
Ca	C-376		x	x			x	x	x	x		x				x			x		x	x								x					Fe-Ti-oxides as inc in cpx + ol		

LCP=Lonquimay colored pumice
LGP=Lonquimay grey pumice

LVS=Lonquimay vitric scoria
LDS=Lonquimay dense scoria

r= rare
x=existent
n=numerous

Tab. A.2 Petrographic descriptions of representative samples for each stratigraphic unit and petrographic group.

extended record			Fit-tests				Parameter											
Model	Equation	Scale factor	KS-Test	AIC_c	R^2	χ^2/DOF	A	error	t	error	d	error	k	error	x_0	error	p	error
Exponential	A*exp(-x/t)	fixed	0.18	41.05	0.93	4.24	25.00		462.72	28.44								
		variable	0.16	35.15	0.95	3.19	22.93	0.68	519.52	36.83								
Weibull	A*exp(-(k/x)^d)	fixed	0.17	38.47	0.94	3.62	25.00				0.79	0.07	0.00217	1.49E-04				
		variable	0.17	37.61	0.94	3.28	22.36	0.91			1.14	0.19	0.00188	1.26E-04				
Logistic	$A/(1+(x/x_0)^p)$	fixed	0.18	48.17	0.91	5.26	25.00								259.37	26.57	1.03	0.11
		variable	0.19	40.84	0.94	3.72	21.19	0.68							419.11	26.71	2.18	0.35

geological record			Fit-tests				Parameter											
Model	Equation	Scale factor	KS-Test	AIC_c	R^2	χ^2/DOF	A	error	t	error	d	error	k	error	x_0	error	p	error
Exponential	A*exp(-x/t)	fixed	0.15	29.30	0.92	3.21	21.00		591.88	37.40								
		variable	0.15	32.00	0.92	3.37	19.23	0.70	589.46	50.98								
Weibull	A*exp(-(k/x)^d)	fixed	0.18	27.13	0.94	2.71	21.00				1.47	0.21	0.00177	8.14E-05				
		variable	0.21	24.72	0.95	2.22	21.07	0.91			1.98	0.31	0.00172	7.28E-05				
Logistic	$A/(1+(x/x_0)^p)$	fixed	0.20	28.74	0.93	2.91	21.00								440.91	18.19	2.47	0.36
		variable	0.21	22.65	0.95	2.03	18.97	0.63							482.43	19.71	2.96	0.42

Tab A.3 Fit parameters of Exponential, Log-logistic and Weibull distributions fitted to the repose time distributions of geological and extended records used in Chapter 2.

		Clinopyroxene										Liquid										Results					
		SiO_2	TiO_2	Al_2O_3	FeO_t	MnO	MgO	CaO	Na_2O	K_2O	P_2O_5	SiO_2	TiO_2	Al_2O_3	FeO_t	MnO	MgO	CaO	Na_2O	K_2O	P_2O_5	K_D(Fe-Mg)	P_{mean}	STD_P	T_{mean}	STD_T	N
Unit	Samples	[wt%]										[wt%]										Eqn 35*	[MPa] Eqn 31*		[°C] Eqn 33*		
A	C-378	52.05	0.54	2.42	9.30	0.27	15.89	19.07	0.33	0.00	0.12	52.04	2.14	14.47	12.76	0.26	3.82	7.32	3.06	1.33	0.34	0.260	472	37	1109	3	3
B	C-355_pop2	51.15	0.70	2.92	10.63	0.36	14.05	20.89	0.30	0.00	0.01	61.38	1.39	15.85	8.53	0.22	1.49	4.56	5.05	1.17	0.37	0.234	294	70	997	7	5
	C-375_pop1	51.99	0.44	1.50	12.21	0.40	15.36	17.91	0.19	0.00	0.01	59.88	2.11	12.67	12.20	0.26	2.04	5.32	3.44	1.51	0.43	0.242	146	39	1036	5	3
	C-375_pop2	51.25	0.57	3.11	9.35	0.20	15.25	19.85	0.33	0.00	0.09	59.88	2.11	12.67	12.20	0.26	2.04	5.32	3.44	1.51	0.43	0.246	502	37	1055	4	3
	C-375	49.80	0.40	6.55	5.95	0.12	15.38	21.37	0.28	0.00	0.15	59.88	2.11	12.67	12.20	0.26	2.04	5.32	3.44	1.51	0.43	0.244	553	26	1048	4	16
C	C-376_pop1	51.84	0.46	2.74	8.61	0.24	15.44	20.35	0.30	0.00	0.00	56.52	1.61	16.78	10.32	0.23	2.33	7.41	3.95	0.65	0.19	0.248	299	41	1065	5	6
	C-376_pop2	49.94	0.77	4.47	9.39	0.21	14.37	20.47	0.35	0.00	0.01	56.52	1.61	16.78	10.32	0.23	2.33	7.41	3.95	0.65	0.19	0.251	440	36	1074	5	15
	C-377_pop1	51.64	0.46	2.59	8.77	0.12	15.65	20.46	0.30	0.00	0.00	58.65	1.87	15.12	10.57	0.25	1.99	6.98	3.42	0.80	0.24	0.248	366	17	1061	1	4
	C-377_pop2	49.77	0.79	4.14	9.64	0.21	14.56	20.48	0.37	0.01	0.02	58.65	1.87	15.12	10.57	0.25	1.99	6.98	3.42	0.80	0.24	0.251	526	28	1073	8	9
	C-377_pop1	51.64	0.46	2.59	8.77	0.12	15.65	20.46	0.30	0.00	0.00	55.70	1.65	14.81	11.36	0.24	3.32	8.41	3.56	0.58	0.20	0.257	361	17	1101	1	4
	C-377_pop2	50.03	0.76	4.40	9.29	0.22	14.43	20.47	0.37	0.00	0.01	55.70	1.65	14.81	11.36	0.24	3.32	8.41	3.56	0.58	0.20	0.260	543	22	1115	3	9
	C-379_pop1	51.60	0.50	2.84	8.84	0.23	15.35	20.32	0.30	0.00	0.01	57.02	1.76	13.08	12.34	0.29	3.88	6.62	3.79	0.91	0.31	0.254	456	18	1089	3	8
	C-379_pop2	49.98	0.73	4.17	9.17	0.24	14.68	20.66	0.35	0.00	0.00	57.02	1.76	13.08	12.34	0.29	3.88	6.62	3.79	0.91	0.31	0.257	577	64	1097	12	9
F	C-188	51.75	0.52	3.04	7.12	0.19	15.84	21.23	0.27	0.00	0.03	65.91	0.47	17.14	5.29	0.19	0.64	3.44	5.39	1.36	0.18	0.219	143	32	943	2	3
I	C-200a	51.25	0.30	1.30	16.31	0.65	10.82	18.98	0.31	0.01	0.02	68.72	0.36	16.11	4.11	0.09	0.32	2.81	5.58	1.78	0.11	0.214	65	40	924	5	9
	C-358b_pop1	50.96	0.62	2.62	11.95	0.43	13.88	19.19	0.32	0.00	0.00	60.26	1.08	16.78	8.21	0.22	1.67	5.00	5.32	1.04	0.42	0.239	267	50	1004	3	5
	C-358b_pop2	51.18	0.25	1.20	16.51	0.67	10.66	19.26	0.26	0.00	0.00	60.26	1.08	16.78	8.21	0.22	1.67	5.00	5.32	1.04	0.42	0.235	81	19	1024	2	2
J	C-370_pop1	50.80	0.70	3.32	9.79	0.39	14.71	20.99	0.30	0.00	0.00	58.85	1.57	16.59	8.79	0.19	1.95	6.08	4.73	0.97	0.30	0.243	318	36	1047	6	8
	C-370_pop2	51.96	0.52	2.26	9.63	0.33	15.30	19.68	0.31	0.00	0.00	65.79	1.09	15.17	5.28	0.14	1.45	3.70	4.93	2.17	0.28	0.237	335	88	1011	8	3
	C-370_pop3	51.15	0.70	2.93	10.15	0.46	14.17	21.14	0.30	0.00	0.00	65.79	1.09	15.17	5.28	0.14	1.45	3.70	4.93	2.17	0.28	0.235	379	42	1012	7	6
M	C-371a	51.41	0.29	1.34	15.44	0.61	11.86	18.77	0.27	0.00	0.00	65.99	0.47	16.83	5.25	0.17	0.73	3.60	5.43	1.38	0.14	0.222	79	50	958	4	10
	C-394	50.68	0.65	3.62	9.04	0.25	14.89	20.45	0.35	0.00	0.02	53.44	2.14	14.59	13.78	0.27	4.07	7.30	3.46	0.64	0.31	0.257	530	42	1099	4	4
N	C-355_pop1	51.18	0.45	1.97	13.69	0.57	12.77	19.81	0.25	0.00	0.01	61.38	1.39	15.85	8.53	0.22	1.49	4.56	5.05	1.17	0.37	0.233	148	57	1002	7	10
	C-396	51.33	0.30	2.32	12.11	0.50	13.70	20.03	0.30	0.00	0.00	60.88	1.32	16.42	8.39	0.20	1.25	4.80	4.68	1.54	0.35	0.235	232	39	1006	6	3
	C-397	50.39	0.76	3.89	10.86	0.29	14.89	18.47	0.44	0.00	0.02	59.95	1.43	16.64	8.41	0.22	1.56	5.94	4.56	0.88	0.30	0.249	524	24	1062	2	5
O	C-501	51.24	0.69	1.95	15.57	0.35	13.40	16.48	0.29	0.00	0.00	60.76	1.88	13.66	10.45	0.28	2.02	5.00	4.32	1.20	0.43	0.247	302	62	1049	7	4
P	C-503	51.59	0.50	2.91	8.98	0.19	15.46	19.95	0.32	0.00	0.06	56.55	2.17	13.83	12.64	0.26	2.88	7.04	3.43	0.84	0.26	0.254	453	48	1086	1	3
Q	C-352	50.42	0.32	1.29	19.10	0.71	9.30	18.56	0.28	0.00	0.01	69.36	0.36	15.39	4.77	0.14	0.35	2.51	5.06	1.99	0.06	0.213	69	50	918	4	6
	C372a	50.77	0.35	1.20	18.75	0.74	9.90	17.94	0.29	0.00	0.01	69.82	0.34	15.24	4.35	0.14	0.30	2.33	5.45	1.97	0.06	0.213	62	20	918	2	4
R	C-199	50.57	0.90	3.09	11.18	0.36	14.23	19.32	0.33	0.00	0.01	58.89	1.91	14.44	11.62	0.18	2.19	5.11	3.81	1.42	0.43	0.245	454	36	1050	7	6
S	C-348a	52.43	0.38	1.92	19.25	0.46	23.48	2.01	0.05	0.00	0.02	67.08	0.55	15.24	5.92	0.19	0.55	3.07	5.35	1.91	0.14	0.243	567	32	1038	3	2
	C-349	51.02	0.36	1.24	17.83	0.67	10.36	18.19	0.27	0.01	0.01	67.19	0.56	15.48	6.11	0.20	0.62	3.25	4.66	1.80	0.13	0.221	124	10	954	0	2
	C-350	50.80	0.40	1.33	18.66	0.66	10.35	17.55	0.24	0.00	0.00	67.38	0.56	15.25	6.13	0.19	0.57	3.01	4.80	1.97	0.13	0.220	84	39	948	5	19
T	C-346a	50.95	0.28	1.05	18.02	0.71	9.16	19.48	0.32	0.01	0.00	70.31	0.29	15.61	3.90	0.14	0.27	2.20	5.18	2.04	0.05	0.209	84	46	906	7	4
U	C-382a_pop1	51.05	0.33	1.19	18.19	0.75	9.55	18.63	0.27	0.00	0.03	70.31	0.35	15.06	3.75	0.14	0.28	2.30	5.51	2.20	0.11	0.211	37	16	911	2	9
	C-382a_pop2	50.37	0.45	1.80	17.48	0.66	10.54	18.38	0.29	0.00	0.01	70.31	0.35	15.06	3.75	0.14	0.28	2.30	5.51	2.20	0.11	0.213	105	30	920	5	7
V	C204b1	50.88	0.46	1.79	15.31	0.63	12.10	18.49	0.31	0.01	0.00	67.79	0.55	15.42	5.38	0.16	0.59	2.83	5.30	1.84	0.14	0.221	184	44	950	6	5
	C-342	50.32	0.47	1.75	18.14	0.67	11.06	17.27	0.27	0.00	0.00	70.46	0.34	15.39	3.87	0.13	0.25	2.32	4.98	2.15	0.10	0.213	118	71	914	7	5

*=all equations are from Putirka (2008)

Tab. A.4 Representative clinopyroxene and matrix-glass compositions that were used in chapter 2 to compute the listed P-T-conditions and K_D-values as a test for equilibrium.

Unit	Sample	representative Amphibole compositions												P-T conditions			
		SiO_2	TiO_2	AL_2O_3	Cr_2O_3	FeO	MnO	MgO	CaO	Na_2O	K_2O	F	Cl	T (°C)	SEE	P (MPa)	SEE
D	hbl_C-374a	41.57	3.78	11.76	0.01	15.18	0.34	11.62	10.60	2.77	0.21		0.0324	947	22	358	39
	hbl_C-374b	41.15	3.74	11.61	0.00	15.51	0.35	11.60	10.61	2.77	0.21		0.0318	949	22	349	38
I	hbl_C-200a	42.38	2.87	11.31	0.01	19.50	0.33	9.83	10.02	2.50	0.27			895	22	315	79
G	hbl_C-359a	40.96	3.24	11.14	0.00	17.97	0.42	10.24	10.04	2.68	0.22		0.0556	918	22	321	35
	hbl_C-359b	41.09	3.27	11.07	0.03	18.29	0.46	10.21	10.20	2.75	0.23		0.0568	919	22	312	34
	hbl_C-198a	41.46	3.40	11.55	0.00	17.91	0.36	10.40	10.39	2.72	0.23	0.0162	0.0505	927	22	342	38
	hbl_C-198b	41.98	3.40	11.62	0.00	17.92	0.37	10.56	10.21	2.79	0.22	0.0095	0.0551	922	22	338	85
M	hbl_C-371a	41.52	3.03	11.05	0.00	20.17	0.50	9.03	10.19	2.67	0.27		0.0711	901	22	310	77
N	hbl_C-396	42.03	3.40	11.28	0.00	17.66	0.36	10.65	10.62	2.73	0.22	0.0218	0.0428	922	22	315	35

formulation of Ridolfi et al. 2010

Tab. A.5 Representative amphibole compositions and calculated thermobarometric results for each amphibole-bearing sample.

Appendix B

Supplementary material for Chapter 3

Pre-eruptive equilibrium and disequilibrium conditions, and the volatile inventory of explosive eruptions of the Lonquimay Volcanic Complex

reference material	cycles	counts per second 1H+/30Si+	given H2O (wt%)	SiO2 (wt.%)	measured H2O (wt%)
TRD 80	20	0.18780	2.1	55.0	2.2
TRD 80	20	0.18710	2.1	55.0	2.1
TRD 80	20	0.19130	2.1	55.0	2.2
TRD 80	20	0.18760	2.1	55.0	2.2
TRD 80	20	0.18380	2.1	55.0	2.1
TRD 80	20	0.19060	2.1	55.0	2.2
TRD 80	20	0.17550	2.1	55.0	2.0
TRD 80	20	0.18760	2.1	55.0	2.2
TRD 80	20	0.18190	2.1	55.0	2.1
TRD 80	20	0.17500	2.1	55.0	2.0
mean		**0.18482**			**2.12**
SD		**0.00575**			**0.07**
RSD %		**3.1**			**3.11**
A-46	20	0.35400	4.1	56.5	4.2
A-46	20	0.35870	4.1	56.5	4.2
A-46	20	0.35290	4.1	56.5	4.2
A-46	20	0.35790	4.1	56.5	4.2
A-46	20	0.36440	4.1	56.5	4.3
A-46	20	0.28170	4.1	56.5	3.3
A-46	20	0.30890	4.1	56.5	3.6
A-46	20	0.30290	4.1	56.5	3.6
A-46	20	0.32370	4.1	56.5	3.8
A-46	20	0.36000	4.1	56.5	4.2
A-46	20	0.33180	4.1	56.5	3.9
A-46	20	0.29830	4.1	56.5	3.5
mean		**0.33293**			**3.9**
SD		**0.02899**			**0.3**
RSD %		**8.7**			**8.7**
ALV519-4	20	0.03941	0.224	43.8	0.42
P2-3	20	0.06487	0.47	50.3	0.68
KL-2	20	0.02147	0.01	50.3	0.23
Na-23-6	20	0.32880	0.98	42	2.88
SC-1	20	0.53340			
SC-1	20	0.53220			

Tab. B.1 Raw data and given element concentration values of reference materials for calibration of the SIMS instrument.

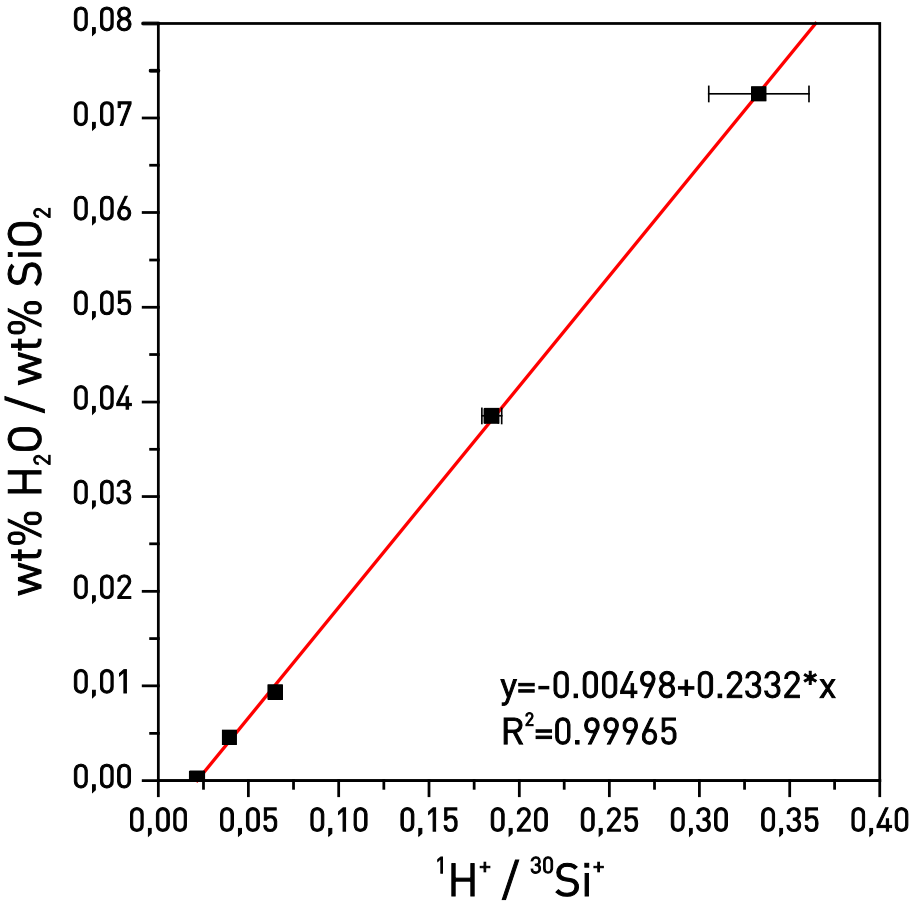

Fig. B.1 SIMS calibration curve for abundances of H_2O.

Appendix C

Supplementary material for Chapter 4

Puyehue-Cordón Caulle: a history of critical magma chambers due to volatile oversaturation

C.1 Analytical conditions

Major element compositions of matrix glasses, mineral phenocrysts (plagioclase, olivine, pyroxenes) and melt inclusions were analyzed using a JEOL Superprobe JXA-8200 electron microprobe at the GEOMAR | Helmholtz Center for Ocean Research Kiel. In order to ensure significant analytic results, representative juvenile clasts were chosen from each tephra sample. The clasts were crushed, separated into corresponding phases, embedded in resin, polished, and analyzed with EPMA.

C.1.1 Glass analyses

To ensure representative results, matrix glass compositions are defined by >20 spot analyses for each tephra. We performed all of our EPMA analyses for matrix glasses using the following setup: 15kV accelerating voltage; defocused beam (5μm) to avoid analytical Na-loss (Hunt and Hill, 1993; Nielsen and Sigurdsson, 1981); probe current was 6 nA. International natural glass standards (Lipari, VG2, A-99, VG-568; Jarosewich et al., 1980) were used to ensure a proper calibration during analysis runs. The typical accuracy is 0.5-1% for major- (Si, Al, Na, Ca, K, Ti, Mg, Fe) and less than 5% for minor elements (Mn, P) based on bracketing measurements of reference materials (Lipari obsidian, N=217; VG-568, N=95; VG-2, N=33). All glass data presented in this study are normalized to anhydrous compositions unless otherwise stated.

Melt inclusions were, prior to analysis, carefully examined for post-entrapment crystallization and the host crystals were subsequently polished until surface exposure of the inclusions. We used the same analytical setup as described above for analysis of glass compositions. In addition, volatiles (Cl, S, F) were determined using a 15 kV acceleration voltage, 30 nA beam current and 5 μm beam size. Typical accuracy derived from repeated analyses of International glass standards (KE3, KN18, N=112) is 0.4% for S, 3.6% for Cl, 0.6% for F.

C.1.2 Mineral analyses

Analyses of mineral phenocrysts were performed at 15 kV accelerating voltage and adjusted primary beam current and beam diameter (Olivine 80nA and focused beam; Plagioclase 20 nA, Pyroxene 20nA, Spinel 50nA, Amphibole 20nA, Apatite 50nA); ZAF correction routine was used to achieve true element concentrations. A set of reference materials (Kakanui Augite USNM 122142; San-Carlos Olivine USNM 111312/44; Natural Bridge Diopside USNM117733; Ilmenite Ilmen Mnts USNM 96189; Minas Gerais Magnetite USNM 114887; Great Sitkin Island

Anorthite USNM 137041; Lake County Plagioclase USNM115900; Jarosewich et al., 1980) were used for routine calibration and instrument stability monitoring.

References

Hunt, J.B., and Hill, P.G., 1993, Tephra geochemistry: a discussion of some persistent analytical problems: The Holocene, v. 3, 3, p. 271 - 278.

Jarosewich, E., Nelen, J.A., and Norberg, J.A., 1980, Reference Samples for Electron Microprobe Analysis*: Geostandards Newsletter, v. 4, p. 43-47.

Nielsen, C.H., and Sigurdsson, H., 1981, Quantitative methods of electron microprobe analysis of sodium in natural and synthetic glasses. : American Mineralogist, v. 66, p. 547–552.

C.2 Thermobarometry

C.2.1 Pyroxene-Liquid Thermobarometry

Numerous petrologic experiments and thermodynamic models (e.g. Nimis, 1999; Putirka et al. 1996; Putirka 2005) have calibrated the compositions of clinopyroxene (cpx) and orthopyroxene (opx) with equilibrated melts as a function of crystallization pressure and temperature. We here used matrix-glass and clinopyroxene-rim compositions, which are indicative for the last stage state of evolution of the magma chamber, to calculate pre-eruptive p-T conditions using Eqn. 31 (P) and Eqn. 33 (T) from Putirka (2008). Corresponding orthopyroxene-liquid equilibrium formulations (Eqn. 28b for T, Eqn. 29a for P) from Putirka (2008) were computed as well. To ensure that employed mineral-melt pairs are indeed equilibrated, we used Fe-Mg exchange coefficients $K_D^{cpx\text{-}liq}$(Fe-Mg) = 0.28±0.08 ($K_D^{min\text{-}liq}$(Fe-Mg) =[$MgO_{liq}FeO_{min}$]/[$MgO_{min}FeO_{liq}$]; Putirka, 2008) and $K_D^{opx\text{-}liq}$ (Fe-Mg) = 0.29±0.06. Because K_D-values are slightly invariant ($K_D^{cpx\text{-}liq}$ (Fe-Mg) is temperature dependant; $K_D^{opx\text{-}liq}$ (Fe-Mg) depends on the silica content of the equilibrium liquid; Putirka, 2008) we used the appropriately corrected formulations of Putirka (2008) to check that matrix glass compositions represent matching liquids. As a complementary check for clinopyroxene-liquid equilibrium we calculated T_{cpx_sat} (Eqn 3.8; Putirka, 1999) for clinopyroxene saturation using $P_{cpx\text{-}liq}$ as input.

C.2.2 Feldspar-Liquid-Thermohygrometry

Because plagioclase crystallization depends strongly on the H_2O activity of the melt, plagioclase-liquid equilibria can further be used as a hygrothermometer to estimate H_2O contents and temperature during crystallization. Adjacently measured crystal rim-matrix glass as well as melt inclusion-overgrown host crystal pairs were used to perform calculations using formulations from Putirka (2008) and Lange et al. (2009).

Pressure estimates from clinopyroxene-liquid equilibria and H_2O_{liq} from Eqn. 25b (Putirka, 2008) were used to solve the thermometer (Eqn. 24a) and hygrometer (Eqn. 25b) from Putirka (2008) iteratively. Only liquid-mineral pairs that fulfill the equilibrium criterium K_D(Ab-An)= 0.1±0.05 for T<1050°C (Putirka, 2008) are included in the final temperature estimates. Temperatures calculated from plagioclase saturation (Eq. 24a, Putirka, 2008) give results (Tab. ESM3.1 and ESM3.2) that are very similar to those obtained from plagioclase-liquid equilibria.

We further used the hygrometer-formulation of Lange et al. (2009) to calculate H_2O_{melt}. Used input-parameters are: Temperature from plag-liq equilibrium (Eq. 24a , Putirka, 2008) and pressure estimates from cpx-liq thermobarometry (Eq. 31). When comparing both models, the results fall well within the SEE boundaries (Fig.9) indicating valid estimates. Nevertheless, values computed after Lange et al. (2009) seem to be substantially lower than estimates obtained with equations from Putirka (2008).

C.2.3 Olivine-Liquid Thermometry

Olivine-liquid equilibria were used to estimate crystallization temperatures from crystal rims and matrix glasses using Eqn 22 from Putirka (2008). The following input parameters were used: pressures derived from cpx-liq Thermbarometry (Eqn 31; Putirka, 2008), H_2O_{melt} from plag-liq Thermohygrometer (Eqn 25b; Putirka, 2008). Only Olivine-melt pairs that fulfill the equilibrium criterium $K_D^{ol\text{-}liq}$(Fe-Mg)=0.30±0.03 (Roeder and Emslie, 1970) are included in the temperature estimates.

C.2.4 Fe-Ti-oxide Thermometry

Fe-Ti oxide geothermometry was used to estimate equilibration temperatures and oxygen fugacities. We only used Ilmenite-Magnetite pairs that fulfill the Mg/Mn equilibrium test after Bacon and Hirschmann (1988). Equilibrium temperature and fO_2 were computed according to the Geothermometer of Andersen & Lindsley (1985) using the method from Stormer (1983) to calculate Ulvöspinel and Ilmenite components. The temperatures fall again well within the results from complementary methods.

matrix glasses - crystal rims																				
method	cpx-liq				cpx-sat		plag-liq								opx-liq					
reference	Putirka 2008				Putirka 1999		Putirka 2008				Lange et al. 2009				Putirka 2008					
equation	33		31		3.8		24a		25b						28a		28b		29a	
SEE	45°C		2.9 kbar		51°C		36°C		1.1wt%		0.32wt%				36°C		48°C		210 MPa	
parameter	T	STD T	P	STD P	T	STD T	T	STD T	H2O	STD H2O	H2O	STD H2O			T	STD T	T	STD T	P	STD P
unit	[°C]		[MPa]		[°C]		[°C]		[wt%]		[wt%]				[°C]		[°C]		[MPa]	
2011 AD	880	4	127	64	867	2	872	13	4.2	0.4	5.1	0.2			913	8	876	3	307	51
1960 AD	913	10	157	111	912	4	888	12	4.7	0.3	4.2	0.2			943	11	906	4	209	67
1922 AD	903	4	148	54	901	2	878	12	4.7	0.3	4.6	0.2			925	12	896	2	298	28
1390 AD	903	3	216	46	895	2	866	5	4.8	0.2	4.8	0.1			921	8	895	4	210	56
915 AD	896	6	177	70	885	2	873	13	4.9	0.4	4.7	0.4			916	7	892	4	227	66
4480 BC	848	8	101	85	840	1	834	13	5.3	0.4	5.8	0.2			946	7	812	6	203	93
mean	899	12	154	40	892	17	876	8	4.7	0.3	4.7	0.3			927	12	893	11	242	49

Tab. C.2.1: Estimates of pre-eruptive intensive parameters using matrix glass-crystal rim pairs. References and used equations as well as corresponding SEEs are given in each field.

	melt inclusion - host mineral								crystal pairs			
method	plag-liq						ol-liq		Fe-Ti-oxides			
reference	Putirka 2008				Lange et al. 2009		Putirka et al. 2007		Andersen & Lindsley (1985)			
equation	24a		25b				22		X'Usp&X'Ilm	Lindsley & Spencer (1982)		
SEE	36°C		1.1wt%		0.32wt%		43°C					
parameter	T	STD T	H2O	STD H2O	H2O	STD H2O	T	STD T	T	STD T	fO2	STD fO2
unit	[°C]		[wt%]		[wt%]		[°C]		[°C]			
2011 AD	881	11	3.7	0.3	4.4	0.4			923	3	-12.0	0.1
1960 AD	907	7	4.0	0.3	3.8	0.4			937	10	-11.5	0.2
1922 AD	885	19	4.4	0.5	3.8	0.2			933	7	-11.7	0.2
1390 AD	880	4	4.5	0.1	4.0	0.1			936	11	-11.7	0.3
915 AD	890	24	4.4	0.3	3.9	0.2			929		-11.8	
4480 BC	826	11	5.6	0.4	4.6	0.3	885	8				
mean	889	11	4.4	0.3	4.1	0.2			931	6	-11.7	0.2

Tab. C.2.2: Estimates of pre-eruptive intensive parameters using melt inclusion-host mineral and crystal pairs. References and used equations as well as corresponding SEEs are given in each field.

C.2.4 Validity of P-T-X estimates

Using different independent pressure estimates is by far the best quality check if the results fall within one standard deviation (Putirka, 2008). $T_{cpx\text{-}liq}$ match $T_{opx\text{-}liq}$ and $T_{plag\text{-}liq}$ calculated from orthopyroxene and plagioclase phenocryst-liquid equilibria within 1σ model error.

Although $P_{opx\text{-}liq}$ from orthopyroxenes yields systematically higher pressures than $P_{cpx\text{-}liq}$ (ΔP_{mean} = 90 MPa), the variation falls within 1σ error of used models.

Fig. C.2.1: (next page) Comparison of P-T-X estimates from different models.

A) Phenocryst crystallization (Eqn 31; Putirka, 2008) versus clinopyroxene saturation (Eqn 3.8; Putirka, 1999) temperatures.
B) Pressure estimates based on cpx-liq (Eqn 31; Putirka, 2008) and opx-liq (Eqn 29a; Putirka, 2008) equilibria.
C) Clinopyroxene (Eqn 33; Putirka, 2008) against plagioclase (Eqn 25b; Putirka, 2008) crystallization temperatures.
D) H_2O melt contents computed with formulations of Putirka (Eqn 25b; 2008) versus Lange et al. (2009)
E) Comparison of plagioclase crystallization (Eqn 24a; Putirka, 2008) and clinopyroxene saturation temperatures (Eqn 3.8; Putirka, 1999)
F) Clinopyroxene phenocryst crystallization temperatures (Eqn 33; Putirka, 2008) versus orthopyroxene crystallization temperatures (Eqn 28b; Putirka, 2008)

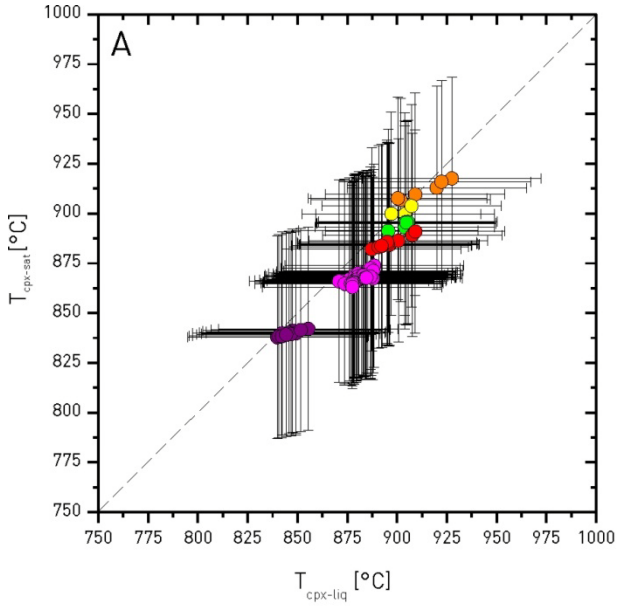
A
$T_{cpx-sat}$ [°C]
$T_{cpx-liq}$ [°C]

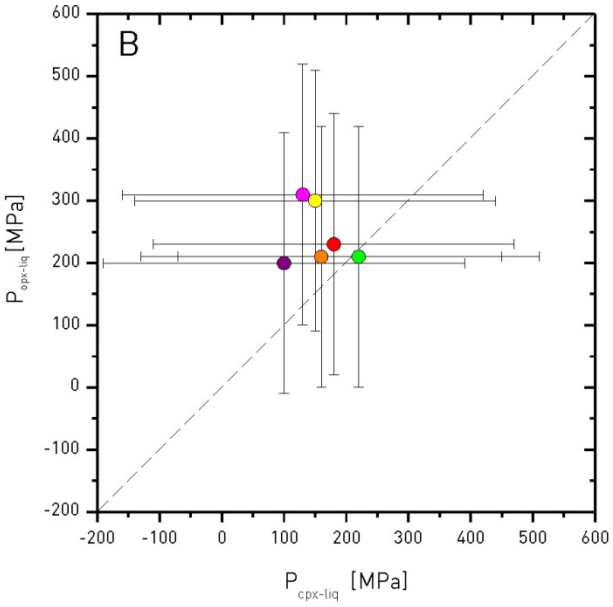
B
$P_{opx-liq}$ [MPa]
$P_{cpx-liq}$ [MPa]

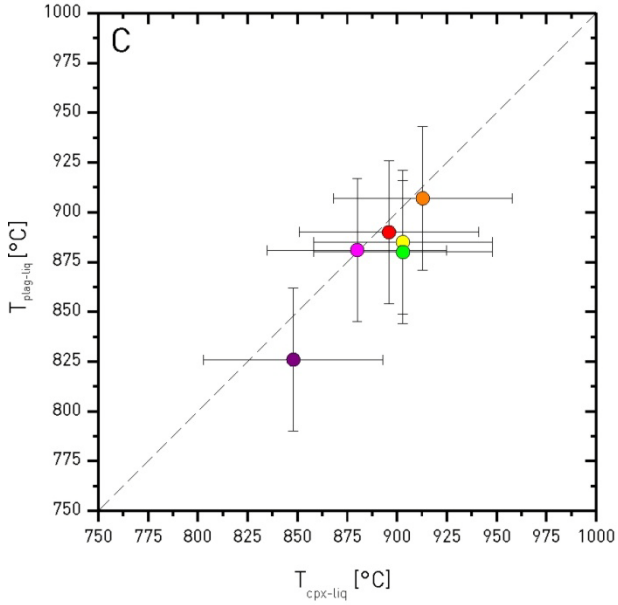
C
$T_{plag-liq}$ [°C]
$T_{cpx-liq}$ [°C]

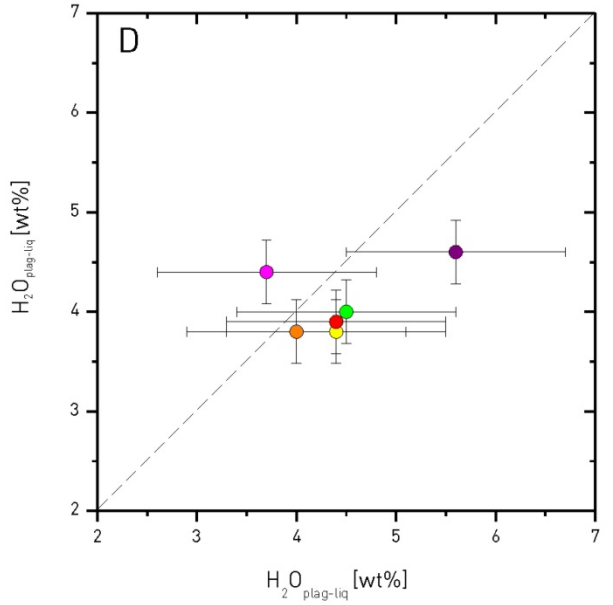
D
$H_2O_{plag-liq}$ [wt%]
$H_2O_{plag-liq}$ [wt%]

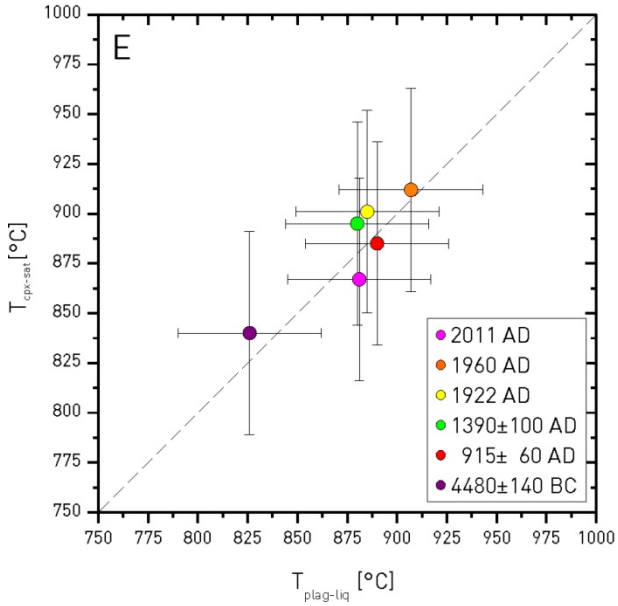
E
$T_{cpx-sat}$ [°C]
$T_{plag-liq}$ [°C]
2011 AD
1960 AD
1922 AD
1390±100 AD
915± 60 AD
4480±140 BC

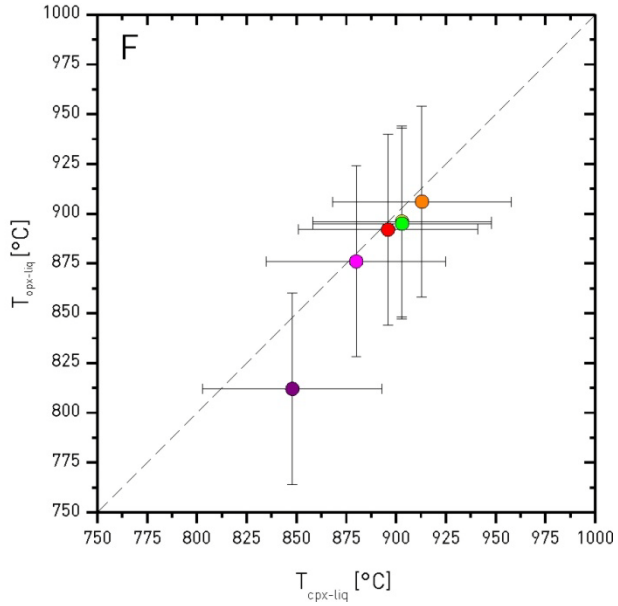
F
$T_{opx-liq}$ [°C]
$T_{cpx-liq}$ [°C]

References

Andersen, D.J., and Lindsley, D.H., 1985, New (and final!) models for the Ti-magnetite/ilmenite geothermometer and oxygen barometer - Abstract AGU 1985 Spring Meeting.

Lange, R.A., Frey, H.M., and Hector, J., 2009, A thermodynamic model for the plagioclase-liquid hygrometer/thermometer: American Mineralogist, v. 94, p. 494-506.

Nimis, P., 1999, Clinopyroxene geobarometry of magmatic rocks. Part 2. Structural geobarometers for basic to acid, tholeiitic and mildly alkaline magmatic systems: Contributions to Mineralogy and Petrology, v. 135, p. 62-74.

Putirka, K., 1999, Clinopyroxene + liquid equilibria to 100 kbar and 2450 K: Contributions to Mineralogy and Petrology, v. 135, p. 151-163.

Putirka, K.D., 2005, Igneous thermometers and barometers based on plagioclase + liquid equilibria: Tests of some existing models and new calibrations: American Mineralogist, v. 90, p. 336-346.

Putirka, K.D., 2008, Thermometers and Barometers for Volcanic Systems, *in* Putirka, K.D., and Tepley III, F.J., eds., Minerals, inclusions and volcanic processes, Volume 69: Reviews in Mineralogy and Geochemistry, The Mineralogical Society of America, p. 61-111.

Putirka, K.D., Johnson, M., Kinzler, R., Longhi, J., and Walker, D., 1996, Thermobarometry of mafic igneous rocks based on clinopyroxene-liquid equilibria, 0–30 kbar: Contributions to Mineralogy and Petrology, v. 123, p. 92-108.

Roeder, P.L., and Emslie, R.F., 1970, Olivine-liquid equilibrium: Contributions to Mineralogy and Petrology, v. 68, p. 325 - 334.

Stormer Jr, J.C., 1983, The effects of recalculation on estimates of temperature and oxygen fugacity from analyses of multicomponent iron-titanium oxides: American Mineralogist, v. 68, p. 586-594.

C.3 Fluid inclusion analyses

The compositions of magmatic fluid inclusions from the 2011 eruption were measured by microthermometry of doubly polished wafers from plagioclase-crystals, using a Linkam ® THMS 600 heating and cooling stage.

Upon cooling, all fluid inclusions froze to aggregates of ice and vapor when cooled to -35 to -45 °C. Further cooling to about -90 to -110 °C produced no visible phase changes. During heating of the inclusions from about -100 °C, no phase changes occurred at temperatures close to the triple point of CO_2 (-56.6 °C), implying that the vapor bubbles contain no or negligible amounts of CO_2.

Final homogenization experiments of liquid + vapor (L + V) into liquid or vapor (T_{hl} and T_{hv}, respectively), were not performed, as the high temperatures required would have destroyed the plagioclase-hosted fluid inclusions. Salinity (Tab. C.3.2) H_2O-NaCl was calculated after Bodnar and Vityk (1994).

Densities of fluid inclusions were calculated from visual estimates of phase proportions of the liquid and gas phase within each single fluid inclusion. The accuracy of the visual identification of phase proportions was estimated at ca. 5 vol%. Density estimates of single fluid inclusions are shown in Tab. C.3.1.

Isochores (Tab C.3.3) were calculated using the formulations of Bowers and Helgeson (1983) and the FLUIDS software package from Bakker (2003) using inclusion composition and density as input parameters.

Plag #	Incl. #	Water %	Density
1	1	25	0.25
	2	25	0.25
	3	20	0.2
	4	30	0.3
	5	25	0.25
	6	25	0.25
	7	30	0.3
	8	25	0.25
	9	20	0.2
	10	20	0.2
	11	20	0.2
	12	30	0.3
	13	25	0.25
2	1	20	0.2
	2	20	0.2
	3	25	0.25
	4	30	0.3
	5	30	0.3
	6	25	0.25
	7	25	0.25
	8	25	0.25
3	1	20	0.2
	2	25	0.25
	3	25	0.25
	4	25	0.25
	5	20	0.2
	6	20	0.2
	7	25	0.25
mean	N=28	24.29	0.24

Tab . C.3.1: Estimated densities of fluid inclusions from 2011 samples

Incl. #	T_{melt} Ice [°C]		T_{melt} mean [°C]	$Salinity_{FI}$ [eq. NaCl]	Cl_{FI} [ppm]	Cl_{MI} [ppm]	$D=Cl_{FI}/Cl_{MI}$
1	-2.0		-2.0	3.7	22695	2136	10.6
2	-2.1		-2.1	3.9	23889	2136	11.2
3	-1.8	-1.9	-1.9	3.4	20915	2136	9.8
4	-1.6		-1.6	3.0	17976	2136	8.4
5	-1.5	-1.3	-1.4	2.6	15651	2136	7.3
6	-2.1		-2.1	3.9	23889	2136	11.2
7	-1.9		-1.9	3.5	21506	2136	10.1
8	-1.4		-1.4	2.6	15651	2136	7.3
9	-2.0		-2.0	3.7	22695	2136	10.6
10	-1.6		-1.6	3.0	17976	2136	8.4
11	-1.5		-1.5	2.8	16811	2136	7.9
12	-1.5		-1.5	2.8	16811	2136	7.9
13	-1.4		-1.4	2.6	15651	2136	7.3
	PY2011		Mean	3.2	19394	2136	9.1
			STD	0.5	3270		1.5

Tab. C.3.2: Melting points, salinity and chlorine concentrations for 2011 fluid inclusions. Salinity H_2O-NaCl calculated after Bodnar and Vityk (1994)

Isochores [pressures in Mpa for a given temperature]			
Temperature °C	800	900	1000
Density 0.2			
Bowers and Helgeson	80	92	104
Bakker	84	98	112
Density 0.25			
Bowers and Helgeson	98	114	130
Bakker	103	123	142
Density 0.3			
Bowers and Helgeson	116	137	158
Bakker	125	150	174

Tab. C.3.3: Isochores calculated for 2011 fluid inclusion data using the assumptions: pure H_2O-NaCl fluids, $Salinity_{mean}$ 3.2 wt% NaCl. Isochores are computed using the formulations of Bowers and Helgeson (1983) and Bakker (2003).

References

Bakker, R.J., 2003, Package FLUIDS 1. Computer programs for analysis of fluid inclusion data and for modelling bulk fluid properties: Chemical Geology, v. 194, p. 3-23.

Bodnar, R.J., and Vityk, M.O., 1994, Interpretation of microthermometric data for NaCl-H2O inclusions, *in* De Vivo, B., and Frezzotti, M.L., eds., Fluid inclusions in minerals: Methods and applications. Short course of the working group (IMA) "Inclusions in Minerals": Blacksburg, Virginia, USA, Virginia Polytechnic Institute and State University, p. 117-131.

Bowers, T.S., and Helgeson, H.C., 1983, Calculation of the thermodynamic and geochemical consequences of nonideal mixing in the system H2O-CO2-NaCl on phase relations in geologic systems: Equation of state for H2O-CO2-NaCl fluids at high pressures and temperatures: Geochimica et Cosmochimica Acta, v. 47, p. 1247-1275.

C.4 ΔP-crystallization modeling

In chapter 4, the pressure increase through crystallization in a H_2O-saturated magma chamber similar to PCCVC was modeled using Eqn 19 from Tait et al (1989).

$$\frac{m_c}{M} = \frac{1 - \left(\frac{P_i}{P}\right)^n + \left(\frac{P}{P_i} - 1\right)\left[\frac{PP_i}{\frac{R}{m}T\rho_l s P^n}\left(\frac{1}{\mu} + \frac{1}{\beta}\right)\right]}{\left[1 + \frac{1}{\frac{R}{m}TsP^n}\left(\frac{1}{\rho_c} + \frac{1}{\rho_l}\right)\right]}$$

The parameters used to model the pressure increase through crystallization for PCCVC are given in Tab. C.4.1 below.

Eqn 19 from Tait el a. (1989)	parameters used		unit
melt density	ρ_l	2300	kg/m^3
crystal density	ρ_c	2600	kg/m^3
temperature	T	1130	K
parameter from H2O solubility*	s	4.11E-06	
	n	0.5	
rigidity of surrounding rocks	μ	10	GPa
bulk modulus of silicate liquids	β	10	GPa
perfect gas constant	R	8.31447	J/Kmol
molar mass H2O	m	18.01528	g/Mol
mass of fractionate crystals	m_c		
total mass of the system	M		
pressure	P		
initial pressure	P_i		

Tab. C.4.1: Parameters for Eqn 19 of Tait et al. (1989). * H2O solubility in granitic melts from Burnham and Jahns, 1962

The computed pressure increase is plotted in Fig. C.4.1. the fracture criterion of pristine granitic country rock (13.8±2.1 MPa; Touloukian et al., 1981) is reached with 5% crystallization. Nevertheless, it is apparent, that rocks around PCCVC are most likely pervasively torn from seismic or explosive events. Therefore, several studies suggest significantly lower overpressures to cause failure (1-4 MPa, Einarsson and Brandsdottir, 1978; 3-11 MPa, Rubin and Pollard, 1988; 8 MPa, Tait et al., 1989). We therefore conclude that crystallization of 2-3% could cause sufficiently large overpressures to burst the roof of the magma chamber.

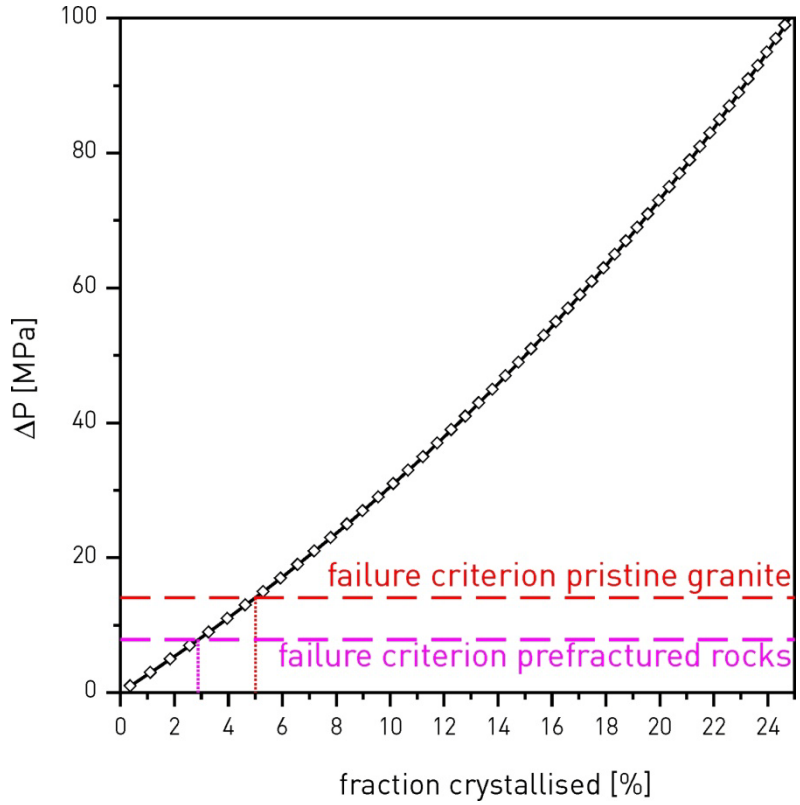

Fig. C.4.1: Pressure increase through crystallization in closed system using the model of Tait et al. (1989). Parameters used for calculation are given in Tab ESM5.1. The failure criterion for pristine granitic host rock is reached with 5% crystallization, more realistic assumptions of prefractured country rocks yield even lower crystallization fractions to reach the failure criterion.

References

Burnham, C.W., and Jahns, R.H., 1962, A method for determining the solubility of water in silicate melts: American Journal of Science, v. 260, p. 721-745.

Einarsson, P., and Brandsdottir, B., 1978, Seismological evidence for Lateral magma intrusion during the July 1978 deflation of the Krafla volcano in NE-Iceland, p. Medium: ED.

Rubin, A.M., and Pollard, D.D., 1988, Dike-induced faulting in rift zones of Iceland and Afar: Geology, v. 16, p. 413-417.

Tait, S., Jaupart, C., and Vergniolle, S., 1989, Pressure, gas content and eruption periodicity of a shallow, crystallising magma chamber: Earth and Planetary Science Letters, v. 92, p. 107-123.

Touloukian, Y.S., Judd, W.R., and Roy, R.F., 1981, Physical Properties of Rocks and Minerals: New York, McGraw Hill.

C.5 Analytical results

	SiO2	TiO2	Al2O3	FeO	MnO	MgO	CaO	Na2O	K2O	P2O5	N
2011AD_mtx	71.45	0.51	14.08	3.58	0.10	0.43	1.84	5.01	2.92	0.08	75
± STD	0.47	0.05	0.17	0.24	0.04	0.06	0.14	0.14	0.08	0.02	
1960AD_mtx	68.97	0.80	14.83	4.49	0.09	0.82	2.70	4.51	2.63	0.17	21
± STD	0.63	0.08	0.16	0.35	0.04	0.13	0.20	0.15	0.08	0.04	
1921AD_mtx	70.21	0.70	14.49	4.22	0.09	0.64	2.27	4.49	2.75	0.13	23
± STD	0.85	0.06	0.25	0.33	0.04	0.09	0.23	0.17	0.09	0.03	
1390AD_mtx	70.88	0.67	14.41	3.89	0.11	0.59	2.15	4.37	2.82	0.12	47
± STD	0.50	0.06	0.34	0.28	0.06	0.08	0.15	0.16	0.08	0.03	
915AD_mtx	71.05	0.64	14.39	3.82	0.11	0.57	2.11	4.37	2.85	0.11	61
± STD	0.49	0.02	0.18	0.24	0.05	0.06	0.10	0.48	0.05	0.03	
4480BC_mtx	72.41	0.33	14.17	3.52	0.13	0.22	1.69	4.55	2.93	0.04	30
± STD	0.29	0.02	0.13	0.23	0.05	0.03	0.08	0.12	0.06	0.02	

Tab. C.5.1 Mean matrix glass compositions and standard deviations calculated from N analyses of representative pumice clasts of post-glacial PCCVC eruptions

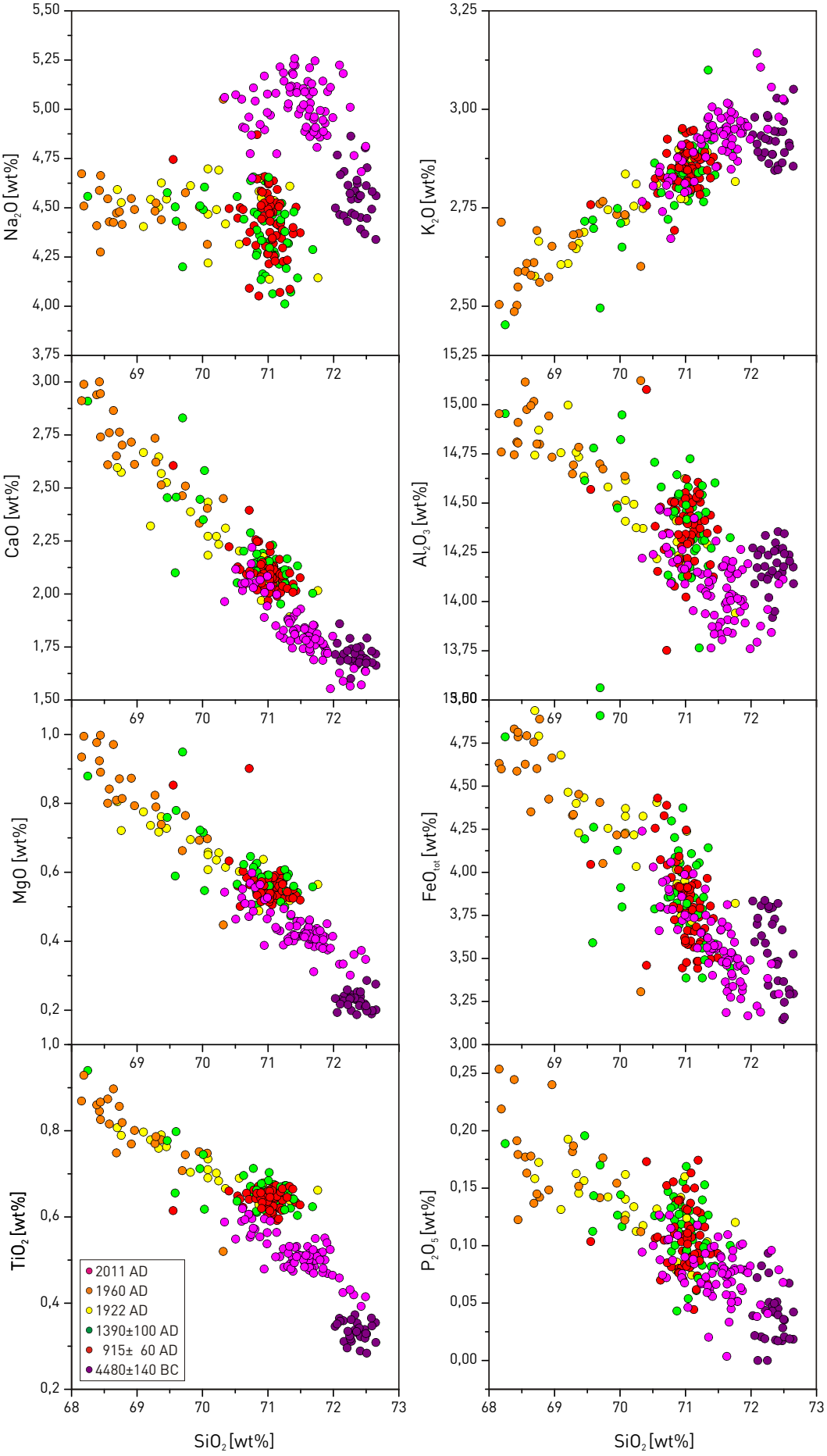

Fig. C.5.1 Matrix glass major element variation diagrams for PCCVC post-glacial eruptions.

sample		SiO2	TiO2	Al2O3	FeO	MgO	CaO	Na2O	K2O	An mol%	Ab mol%	Or mol%	N
plag_PY2011_core		58.76	0.04	25.97	0.43	0.03	8.11	6.19	0.47	40.8	56.4	2.8	40
	± STD	0.87	0.01	0.49	0.06	0.01	0.67	0.29	0.05	3.2	2.8	0.3	
plag_PY2011_rim		58.79	0.04	25.94	0.41	0.03	8.08	6.23	0.47	40.6	56.6	2.8	39
	± STD	1.07	0.01	0.69	0.05	0.01	0.80	0.41	0.06	3.9	3.6	0.4	
plag_PY1960_core		57.79	0.05	26.68	0.47	0.04	8.85	5.78	0.34	44.9	53.1	2.0	11
	± STD	1.05	0.01	0.67	0.04	0.01	0.80	0.42	0.05	4.0	3.9	0.3	
plag_PY1960_rim		58.42	0.04	26.31	0.44	0.04	8.41	5.96	0.38	42.8	54.9	2.3	11
	± STD	0.86	0.01	0.54	0.04	0.01	0.66	0.32	0.09	3.3	3.0	0.5	
plag_PY1922_core		58.89	0.04	26.05	0.44	0.03	8.02	6.10	0.42	41.0	56.5	2.6	16
	± STD	1.07	0.01	0.67	0.04	0.01	0.81	0.37	0.10	4.0	3.6	0.6	
plag_PY1922_rim		58.79	0.04	26.12	0.45	0.03	8.09	6.05	0.43	41.4	56.0	2.6	18
	± STD	0.92	0.01	0.57	0.06	0.01	0.66	0.32	0.08	3.3	3.0	0.5	
plag_PY1390_core		58.75	0.03	26.35	0.44	0.03	8.08	5.92	0.39	41.9	55.6	2.4	17
	± STD	1.20	0.02	0.78	0.06	0.01	0.87	0.37	0.11	4.3	3.8	0.7	
plag_PY1390_rim		58.84	0.04	26.39	0.42	0.03	8.16	5.75	0.37	43.3	54.4	2.3	17
	± STD	0.94	0.01	0.81	0.04	0.01	0.85	0.91	0.09	7.2	7.0	0.6	
plag_PY915_core		58.13	0.04	26.82	0.41	0.03	8.42	5.78	0.36	43.6	54.1	2.2	11
	± STD	0.44	0.02	0.26	0.03	0.01	0.28	0.11	0.08	1.2	1.0	0.5	
plag_PY915_rim		59.09	0.04	26.21	0.40	0.03	7.73	6.08	0.43	40.2	57.2	2.7	9
	± STD	0.51	0.01	0.34	0.06	0.01	0.31	0.13	0.09	1.5	1.3	0.6	
plag_PY4480BC_core		60.28	0.02	25.46	0.34	0.02	6.90	6.55	0.43	35.8	61.5	2.7	17
	± STD	0.72	0.01	0.31	0.10	0.01	0.53	0.24	0.11	2.4	1.9	0.7	
plag_PY4480BC_rim		60.81	0.02	25.26	0.30	0.01	6.49	6.65	0.46	34.1	63.1	2.9	16
	± STD	0.82	0.01	0.51	0.05	0.01	0.59	0.38	0.08	3.0	3.0	0.5	

Tab. C.5.2 Mean plagioclase compositions and standard deviations calculated from N analyses for post-glacial PCCVC eruptions

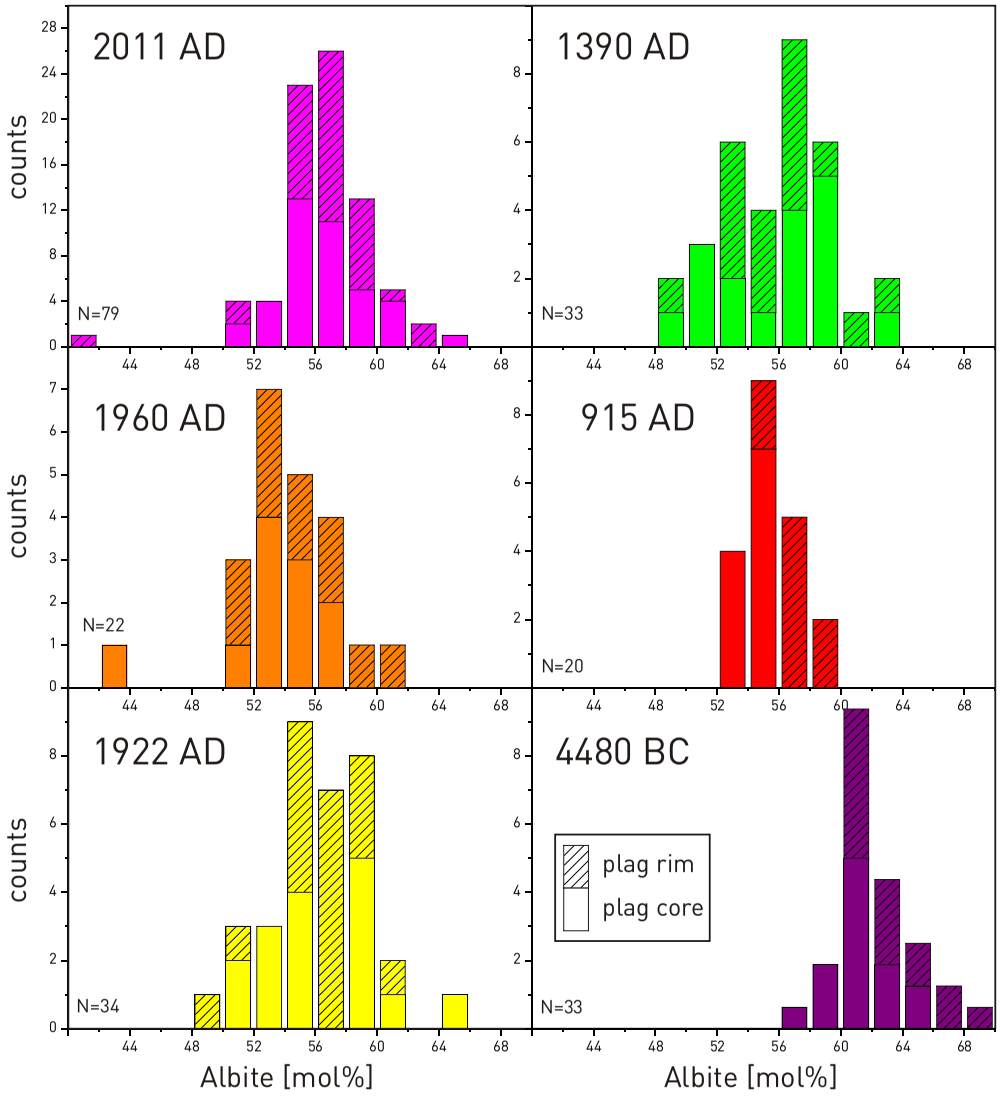

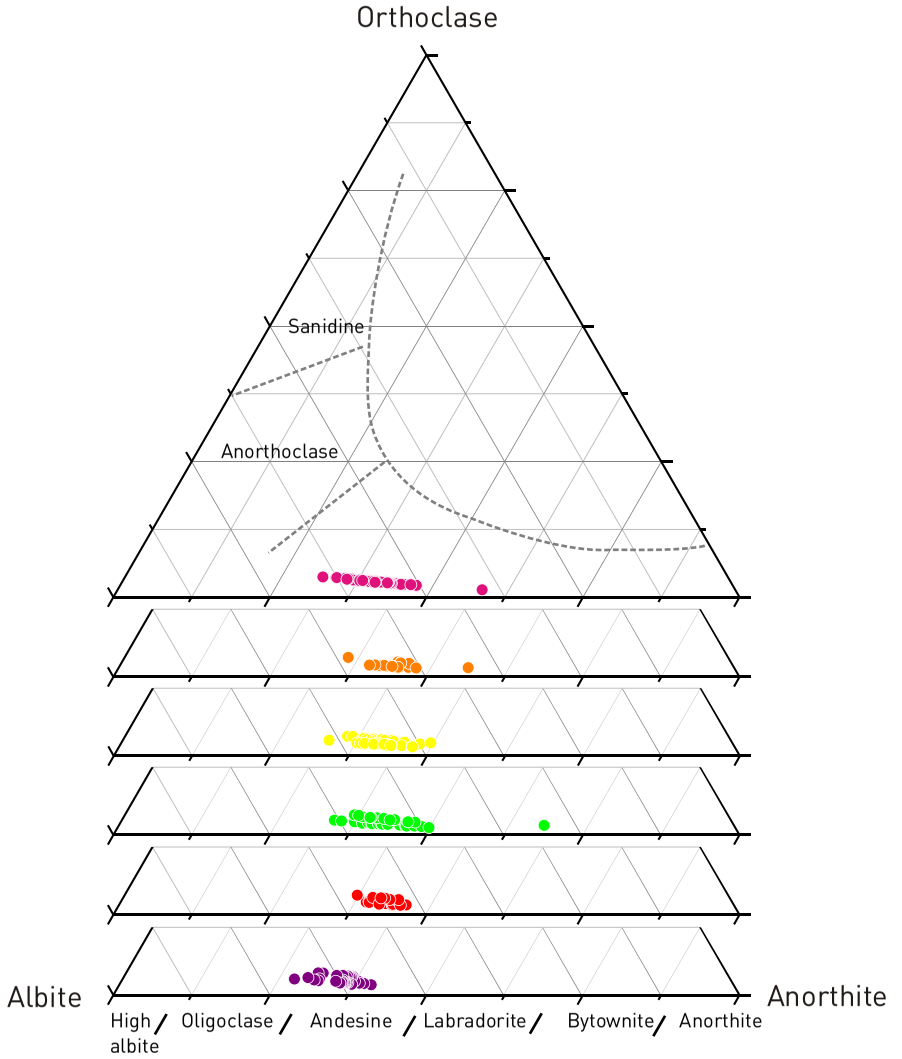

Fig. C.5.2 Compositions and frequency distributions of plagioclase rim and core compositions. Compositions overlap for all tephras but 4480 BC which is more albitic.

sample	SiO_2	TiO_2	Al_2O_3	Cr_2O_3	Fe_2O_3	FeO	MnO	MgO	CaO	NiO	Na_2O	K_2O	Total	En%	Fs%	Wo%	Mg#	N
cpx_PY2011_core	51.71	0.35	1.10	0.01	0.47	13.30	0.57	12.94	18.56	0.02	0.30		99.33	38.4	23.1	38.5	62.7	21
± STD	0.21	0.07	0.23	0.01	0.31	0.86	0.05	0.44	0.42	0.03	0.02		0.28	1.3	1.5	0.9	2.1	
cpx_PY2011_rim	51.62	0.36	1.14	0.01	0.58	13.11	0.58	13.10	18.42	0.02	0.29		99.23	39.0	22.8	38.2	63.1	19
± STD	0.27	0.07	0.31	0.02	0.37	0.81	0.07	0.42	0.38	0.03	0.01		0.31	1.3	1.3	0.8	1.7	
cpx_PY1960_rim	51.68	0.44	1.33	0.00	1.08	12.55	0.67	13.36	18.49	0.00	0.31		99.92	40.0	22.2	37.8	63.8	4
± STD	0.24	0.03	0.09	0.00	0.45	1.01	0.07	0.31	0.46	0.00	0.01		0.33	0.9	1.8	0.9	1.9	
cpx_PY1960_core	51.70	0.41	1.20	0.02	1.28	13.01	0.68	13.33	18.21	0.01	0.30		100.15	39.8	23.0	37.3	62.6	3
± STD	0.21	0.06	0.20	0.02	0.15	0.45	0.09	0.15	0.49	0.01	0.01		0.23	0.1	0.8	0.9	0.6	
cpx_PY1922_core	51.46	0.45	1.37	0.00	1.30	12.86	0.66	13.93	17.42	0.00	0.27		99.74	41.8	22.7	35.5	63.8	2
± STD	0.42	0.12	0.46	0.00	0.68	1.41	0.01	1.51	1.22	0.00	0.03		0.28	5.4	1.9	3.6	3.8	
cpx_PY1922_rim	51.82	0.40	1.18	0.02	1.12	12.93	0.65	13.74	17.93	0.02	0.27		100.07	40.7	22.6	36.7	63.7	2
± STD	0.35	0.08	0.30	0.02	0.16	1.70	0.15	0.91	0.40	0.03	0.04		0.07	2.4	3.3	0.9	4.6	
cpx_PY1390_core	51.58	0.42	1.15	0.01	1.06	13.00	0.72	13.00	18.59	0.01	0.28		99.82	38.7	22.9	38.3	62.4	5
± STD	0.70	0.03	0.10	0.01	1.18	0.96	0.09	0.42	0.16	0.00	0.02		0.36	1.6	1.3	0.3	1.7	
cpx_PY1390_rim	51.55	0.38	1.04	0.02	1.25	12.97	0.70	13.09	18.46	0.01	0.29		99.75	38.9	22.8	38.3	62.3	7
± STD	0.87	0.02	0.09	0.01	1.88	1.80	0.05	0.26	0.42	0.01	0.02		0.39	1.6	2.6	1.1	1.3	
cpx_PY915_core	51.66	0.43	1.22	0.01	0.81	13.22	0.68	13.07	18.41	0.01	0.29		99.81	38.8	23.1	38.1	62.5	6
± STD	0.25	0.10	0.29	0.01	0.25	0.69	0.07	0.32	0.31	0.01	0.02		0.34	1.1	1.2	0.7	1.6	
cpx_PY915_rim	51.64	0.36	1.02	0.01	0.69	13.91	0.72	12.76	18.19	0.01	0.29		99.63	38.0	24.4	37.6	61.0	6
± STD	0.38	0.06	0.19	0.02	0.65	0.95	0.05	0.39	0.36	0.01	0.01		0.45	1.4	1.5	0.5	1.6	
cpx_PY4480BC_core	50.92	0.29	0.90	0.01	0.67	18.10	0.94	9.88	18.03	0.01	0.27		100.01	29.8	32.3	38.0	48.4	8
± STD	0.53	0.05	0.09	0.01	0.50	1.62	0.12	1.23	0.40	0.01	0.03		0.47	3.4	3.1	0.9	5.1	
cpx_PY4480BC_rim	50.78	0.28	0.85	0.01	0.70	18.58	0.96	9.42	18.21	0.01	0.26		100.07	28.4	33.1	38.4	46.6	13
± STD	0.49	0.03	0.08	0.01	0.54	1.52	0.11	1.07	0.34	0.02	0.02		0.46	3.0	2.8	0.7	4.7	

Tab. C.5.3 Mean clinopyroxene compositions and standard deviations calculated from N analyses for post-glacial PCCVC eruptions

sample		SiO_2	TiO_2	Al_2O_3	Cr_2O_3	Fe_2O_3	FeO	MnO	MgO	CaO	NiO	Na_2O	K_2O	Total	En%	Fs%	Wo%	Mg#	N
opx_PY2011_core		52.06	0.24	0.54	0.01	0.57	24.51	0.94	19.34	1.73	0.03	0.05		100.04	55.9	41.3	2.8	57.9	19
	± STD	0.35	0.02	0.08	0.01	0.44	1.46	0.08	1.04	0.07	0.04	0.02		0.44	2.8	2.6	0.2	2.5	
opx_PY2011_rim		51.96	0.23	0.52	0.01	0.22	25.55	0.96	18.68	1.72	0.02	0.04		99.90	54.0	43.0	2.9	56.4	18
	± STD	0.26	0.02	0.06	0.01	0.24	0.79	0.07	0.61	0.04	0.03	0.01		0.39	1.5	1.5	0.2	1.6	
opx_PY1960_core		52.31	0.28	0.64	0.01	1.50	23.98	1.05	19.82	1.80	0.00	0.03		101.39	57.0	40.4	2.7	58.2	4
	± STD	0.53	0.03	0.09	0.01	0.55	0.54	0.02	0.52	0.15	0.00	0.02		0.70	1.0	1.0	0.2	1.5	
opx_PY1960_rim		52.82	0.25	0.60	0.02	1.29	22.43	0.97	21.07	1.74	0.02	0.04		101.24	60.0	37.4	2.6	61.4	5
	± STD	0.50	0.02	0.07	0.03	0.41	0.77	0.10	0.72	0.03	0.02	0.01		0.58	1.6	1.6	0.2	1.9	
opx_PY1922_rim		52.13	0.28	0.64	0.00	2.15	22.96	1.00	20.32	1.71	0.01	0.04		101.25	58.7	38.8	2.5	59.2	4
	± STD	0.19	0.06	0.15	0.00	0.76	3.20	0.09	1.75	0.04	0.02	0.01		0.78	5.4	5.1	0.3	4.5	
opx_PY1922_core		52.16	0.26	0.53	0.01	1.79	24.46	1.04	19.44	1.75	0.01	0.05		101.48	56.0	41.2	2.8	57.0	6
	± STD	0.36	0.01	0.07	0.01	0.82	2.11	0.10	1.43	0.03	0.01	0.01		0.28	3.9	3.7	0.2	3.2	
opx_PY1390_rim		52.34	0.26	0.59	0.01	0.89	24.18	1.11	19.67	1.75	0.01	0.03		100.83	56.5	40.8	2.8	58.4	16
	± STD	0.49	0.03	0.09	0.01	0.73	1.29	0.11	0.94	0.04	0.02	0.01		0.45	2.5	2.3	0.2	2.4	
opx_PY1390_core		52.33	0.29	0.63	0.01	1.04	24.10	1.07	19.71	1.81	0.01	0.04		101.04	56.6	40.6	2.8	58.4	14
	± STD	0.32	0.04	0.11	0.01	0.78	1.36	0.10	0.85	0.07	0.01	0.01		0.37	2.4	2.3	0.3	2.0	
opx_PY915-rim		52.38	0.28	0.61	0.01	0.56	24.81	1.06	19.42	1.76	0.02	0.02		100.96	55.6	41.6	2.8	57.8	4
	± STD	0.37	0.05	0.10	0.02	0.42	0.46	0.05	0.28	0.03	0.03	0.02		0.68	0.6	0.8	0.2	0.9	
opx_PY915_core		52.45	0.26	0.56	0.00	0.77	24.32	1.09	19.64	1.80	0.01	0.04		100.96	56.3	40.9	2.9	58.3	4
	± STD	0.23	0.05	0.14	0.00	0.52	1.38	0.10	0.89	0.06	0.03	0.01		0.25	2.5	2.4	0.3	2.1	
opx_PY4480BC_core		53.55	0.14	0.64	0.04	1.31	19.24	0.94	22.68	2.57	0.00	0.05		101.16	63.9	32.0	4.1	66.3	3
	± STD	0.95	0.01	0.12	0.05	0.58	1.50	0.10	2.70	1.52	0.00	0.03		0.35	6.3	3.3	3.0	4.8	
opx_PY4480BC_rim		54.09	0.14	0.59	0.01	0.95	18.38	0.88	24.24	1.69	0.00	0.03		101.01	67.5	30.1	2.4	69.2	2
	± STD	0.16	0.01	0.12	0.01	0.48	0.37	0.07	0.33	0.14	0.01	0.01		0.43	0.7	0.6	0.2	0.2	

Tab. C.5.4 Mean orthopyroxene compositions and standard deviations calculated from N analyses for post-glacial PCCVC eruptions

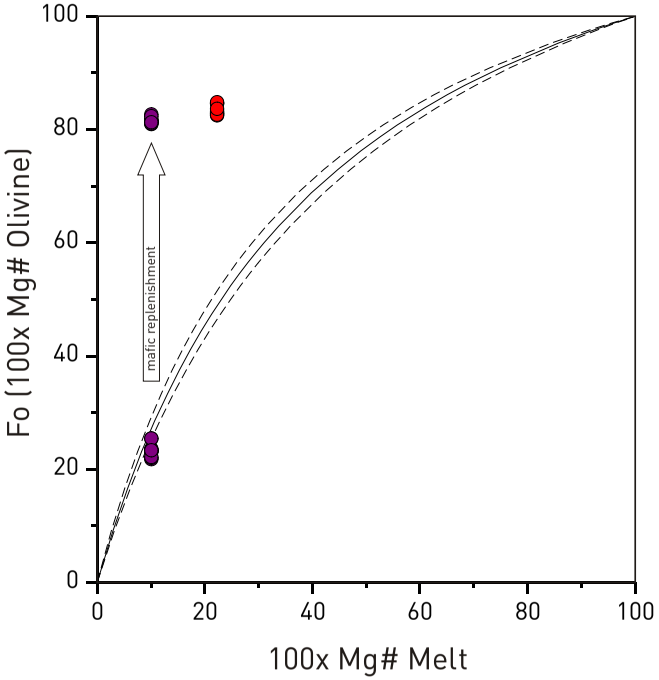

Fig. C.5.3 Rhodes diagram of PCCVC samples. The diagram yields tests of olivine-liquid equilibrium. Olivine-melt pairs that are in equilibrium should lie along the solid line or within some established error. The lines are here given as $K_D(Fe\text{-}Mg)^{ol\text{-}liq}$ = 0.3±0.03 (Roeder and Emslie, 1970)

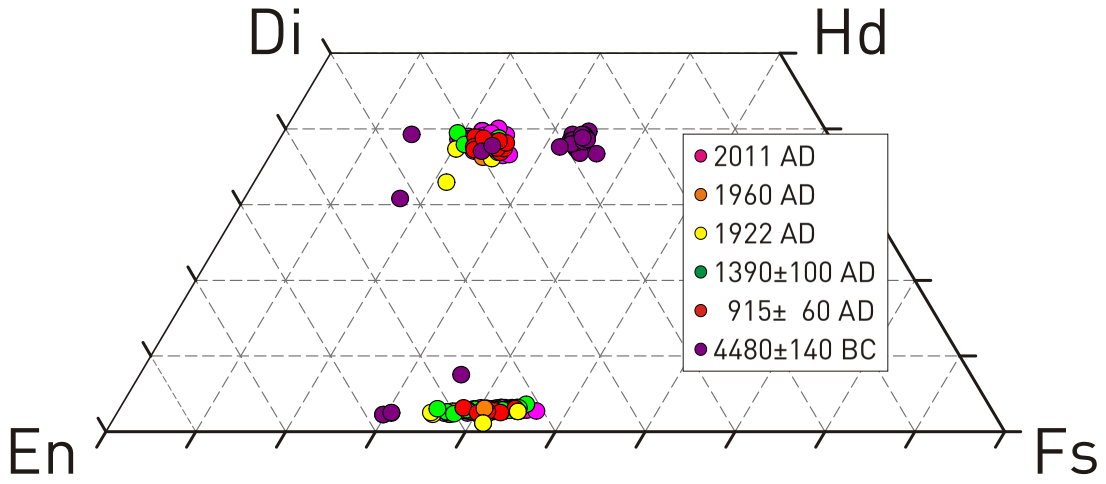

Fig. C.5.4 Pyroxene compositions of phenocrysts from post-glacial PCCVC eruptions.

Sample		SiO_2	TiO_2	Al_2O_3	Cr_2O_3	Fe_2O_3	FeO	MnO	MgO	CaO	NiO	Na_2O	K_2O	Total	Mg #	N
ol_PY915_core		39.51	0.01	0.03	0.03	1.62	14.48	0.24	44.96	0.18	0.16	0.01		101.23	83.41	9
	± STD	0.20	0.01	0.01	0.01	0.81	0.92	0.03	0.66	0.01	0.06	0.01		0.55	0.92	
ol_PY915_rim		39.50	0.01	0.02	0.02	1.37	14.75	0.25	44.74	0.19	0.12	0.00		100.98	83.30	10
	± STD	0.25	0.01	0.01	0.02	0.65	0.74	0.02	0.58	0.01	0.04	0.01		0.42	0.81	
ol_PY4480BC_core1		39.28	0.01	0.03	0.03	1.86	16.03	0.27	43.82	0.23	0.11	0.01		101.67	81.52	9
	± STD	0.32	0.01	0.01	0.01	0.84	0.82	0.02	0.50	0.02	0.03	0.01		0.31	0.65	
ol_PY4480BC_rim1		39.74	0.01	0.11	0.02	0.64	16.69	0.28	43.60	0.26	0.12	0.00		101.47	81.82	9
	± STD	0.34	0.01	0.25	0.01	0.85	1.13	0.03	0.81	0.13	0.02	0.01		0.29	0.75	
ol_PY4480BC_core2		31.97	0.04	0.01	0.01	0.97	56.79	2.12	9.86	0.28	0.02	0.02		102.08	23.36	9
	± STD	0.67	0.01	0.02	0.01	1.39	1.58	0.07	0.42	0.01	0.02	0.02		0.66	0.86	
ol_PY4480BC_rim2		32.08	0.03	0.01	0.01	0.71	57.01	2.11	9.79	0.28	0.02	0.01		102.06	23.24	10
	± STD	0.76	0.03	0.01	0.02	1.66	1.75	0.09	0.48	0.01	0.02	0.02		0.58	0.99	

Tab. C.5.5 Mean olivine compositions and standard deviations calculated from N analyses

		Al_2O_3	CaO	Cr_2O_3	FeO	MgO	MnO	NiO	SiO_2	TiO_2	Total	N
ilm_PY2011		0.17	0.04	0.00	46.28	2.53	1.04	0.01	0.01	47.76	97.85	10
	± STD	0.01	0.03	0.01	0.16	0.17	0.05	0.02	0.02	0.21	0.21	
mgt_PY2011		1.93	0.03	0.02	72.99	1.66	0.87	0.02	0.07	18.24	95.84	23
	± STD	0.07	0.05	0.01	0.18	0.11	0.04	0.02	0.01	0.22	0.20	
ilm_PY1960		0.21	0.02	0.01	47.04	2.89	0.85	0.01	0.00	47.20	98.22	6
	± STD	0.02	0.01	0.01	0.12	0.18	0.04	0.01	0.00	0.38	0.23	
mgt_PY1960		2.13	0.04	0.05	73.57	2.01	0.73	0.01	0.08	17.69	96.32	13
	± STD	0.13	0.06	0.02	1.02	0.20	0.03	0.02	0.01	0.39	1.41	
ilm_PY1922		0.19	0.03	0.01	46.71	2.85	0.86	0.01	0.01	47.49	98.15	4
	± STD	0.02	0.02	0.01	0.24	0.18	0.02	0.02	0.01	0.45	0.36	
mgt_PY1922		2.00	0.02	0.06	73.43	1.94	0.75	0.01	0.08	18.23	96.52	8
	± STD	0.09	0.01	0.01	0.55	0.11	0.02	0.01	0.01	0.25	0.77	
ilm_PY1390		0.19		0.01	47.14	2.75	0.87	0.00	0.01	47.76	98.75	6
	± STD	0.01		0.01	0.73	0.10	0.03	0.00	0.01	0.18	0.78	
mgt_PY1390		1.95		0.02	73.22	1.91	0.75	0.01	0.07	18.28	96.22	11
	± STD	0.09		0.01	0.33	0.13	0.02	0.01	0.01	0.29	0.22	
mgt_PY915		1.99		0.02	73.21	1.87	0.82	0.02	0.08	18.54	96.55	8
	± STD	0.03		0.01	0.21	0.03	0.02	0.02	0.01	0.20	0.29	
mgt_PY4480BC		1.65		0.01	72.04	1.35	0.89	0.01	0.08	21.06	97.09	9
	± STD	0.24		0.01	0.48	1.03	0.15	0.01	0.01	1.41	0.66	

Tab. C.5.6 Mean Fe-Ti-oxide compositions and standard deviations calculated from N analyses